FATIGUE OF COMPOSITE MATERIALS

STP 569

AMERICAN SOCIETY FOR TESTING AND MATERIALS

FATIGUE OF COMPOSITE MATERIALS

A symposium
presented at
December Committee Week
AMERICAN SOCIETY FOR
TESTING AND MATERIALS
Bal Harbour, Fla., 3–4 Dec. 1973

ASTM SPECIAL TECHNICAL PUBLICATION 569
J. R. Hancock, symposium chairman

List price $31.00
04-569000-33

American Society for Testing and Materials
1916 Race Street, Philadelphia, Pa. 19103

Library of Congress Catalog Card Number: 74-28976

NOTE

The Society is not responsible, as a body,
for the statements and opinions
advanced in this publication.

Printed in Rahway, N.J.
March 1975

Foreword

The symposium on Fatigue of Composite Materials was presented at December Committee Week of the American Society for Testing and Materials held in Bal Harbour, Fla., 3–4 Dec. 1973. Committee E-9 on Fatigue sponsored the symposium in cooperation with the Institute of Metals Division Composites Committee of the American Institute of Mining, Metallurgical, and Petroleum Engineers. J. R. Hancock, Midwest Research Institute, presided as symposium chairman.

Related ASTM Publications

Composite Materials: Testing and Design (Third Conference), STP 546 (1974), $39.75 (04-546000-33)

Applications of Composite Materials, STP 524 (1973), $16.75 (04-524000-33)

Analysis of the Test Methods for High Modulus Fibers and Composites, STP 521 (1973), $30.75 (04-521000-33)

Contents

FATIGUE DEFORMATION AND DAMAGE

FATIGUE FRACTURE MECHANISMS AND ENVIRONMENTAL EFFECTS

Introduction

This publication on Fatigue of Composite Materials is the first to focus on the critical problem of fatigue failure in composite materials. There is a discussion of fatigue, in all kinds of heterogeneous materials, promoting a better understanding of how to achieve improved fatigue resistance in composite materials and producing a broadly based contemporary reference on current and future problems.

Because of the presence of interfaces and the anisotropy and heterogeneity inherent in composite materials, the mechanisms of fatigue fracture in these materials are extremely complex and are not fully understood. It is these complexities which offer exciting and unprecedented opportunities to design more fatigue-resistant materials.

The publication focuses on phenomena rather than on the type of material in order to bring an interdisciplinary prospective to the fatigue problem in heterogeneous materials. Implicit in this approach is the belief that fatigue problems are not fundamentally different in the various materials and that unifying concepts of fatigue behavior would be useful.

The publication is divided into four sections: (1) Fatigue Crack Growth and Interfaces, (2) Fatigue Deformation and Damage, (3) Fatigue Fracture Mechanisms and Environmental Effects, and (4) Prediction, Reliability, and Design.

ASTM Committee E-9 on Fatigue sponsored the symposium on which this publication is based, in cooperation with the Institute of Metals Division Composites Committee of the American Institute of Mining, Metallurgical, and Petroleum Engineers.

Fatigue Crack Growth and Interfaces

W. J. Mills [1] *and R. W. Hertzberg* [1]

Fatigue Crack Propagation Behavior of the Ni-Ni_3Cb Eutectic Composite

REFERENCE: Mills, W. J. and Hertzberg, R. W., "**Fatigue Crack Propagation Behavior of the Ni-Ni_3Cb Eutectic Composite**," *Fatigue of Composite Materials, ASTM STP 569,* American Society for Testing and Materials, 1975, pp. 5–27.

ABSTRACT: Room temperature four-point-bending fatigue studies of the unidirectionally solidified Ni-Ni_3Cb eutectic composite have been conducted to better understand fatigue behavior in composite materials. Fatigue crack propagation (FCP) data for this eutectic composite alloy revealed a power relationship between the stress intensity factor range and the crack growth rate from 10^{-7} to 10^{-4} in./cycle. This application of fracture mechanics concepts to FCP data represents the first such reported information of its kind for eutectic composites. Fatigue behavior of this eutectic alloy was found to be sensitive to solidification parameters, thermal history, and the mean stress intensity level.

Metallographic and electron fractographic examination of the fatigue fracture revealed the FCP mechanism to be a function of the prevailing stress intensity factor at the crack tip with a fatigue fracture mechanism transition occurring between 5×10^{-6} and 1.5×10^{-5} in./cycle. At low growth rates, the Ni(γ) phase exhibited faceting indicative of Stage I propagation along active slip planes, while above 5×10^{-6} in./cycle, the γ fracture surface was characterized by the presence of fatigue striations which laid parallel to the Ni-Ni_3Cb interface. At both high and low growth rates, the fatigue response of the Ni-Ni_3Cb composite was controlled by the γ lamellae.

KEY WORDS: composite materials, cracking (fracturing), fatigue (materials), crack propagation, eutectic composites, unidirectional solidification, fatigue mechanism transition, metallography, fractography

Unidirectionally solidified eutectic alloys have recently emerged as a class of fiber reinforced composites that appear to meet the stringent requirements of high temperature applications and space age demands [*1–5*].[2] Although the monotonic behavior of unidirectionally controlled eutectic systems has been extensively investigated, their cyclic

[1] Research assistant and professor, respectively, Department of Metallurgy and Materials Science, Lehigh University, Bethlehem, Pa. 18015.

[2] The italic numbers in brackets refer to the list of references appended to this paper.

response has not been fully characterized. A few fatigue studies have been conducted on the Al-Al_3Ni [*6–8*], Al-$CuAl_2$ [*6*], Ni-Cr [*9*], Fe-Fe_2B [*10*], Ni-Ni_3Cb [*11*], Ni_3Al-Ni_3Cb [*12*], and Ni(Cr)-TaC [*13*] eutectic alloys in an attempt to generate engineering fatigue data and to better understand crack growth mechanisms in composite materials. However, no investigation has reported the application of fracture mechanics to fatigue crack propagation (FCP) data for controlled eutectic composites.

The Ni-Ni_3Cb system was selected for the current investigation for two primary reasons. First, this composite had been investigated previously, and it has exhibited attractive mechanical properties: a tensile strength of approximately 110 ksi and a uniform tensile elongation greater than 11 percent [*14–18*]. Second, the binary Ni-Ni_3Cb composite serves as a prototype model for similar but more complex nickel, columbium, aluminum, and chromium multicomponent systems now being examined for future engineering applications [*19*]. Unidirectional solidification of the Ni-Ni_3Cb system produces a lamellar eutectic consisting of a face centered cubic (fcc) nickel-columbium solid solution matrix (γ) reinforced by 32 volume percent of an ordered orthorhombic ($D_{2h}{}^{13}$) Ni_3Cb intermetallic phase (δ) [*14*]. Hoover [*11*] found that the Ni-Ni_3Cb composite exhibited several interesting fatigue properties. The ability of the composite to notch strengthen allowed the material to withstand several hundred load cycles at net section stresses above the smooth bar tensile strength. Also, the aligned eutectic exhibited a notched bar endurance limit of 55 percent of the smooth bar tensile strength which is considered outstanding for nickel-based alloys. Hoover also reported that a fracture mechanism transition occurred between high-cycle and low-cycle fatigue conditions. Under high stress-low cycle fatigue conditions, δ lamellae fractured ahead of the advancing crack tip by twin boundary cracking thereby creating long voids adjacent to the γ lamellae. Crack propagation into the unbroken γ lamellae occurred by ". . . cyclically induced void growth and coalescence . . . ," and produced fatigue striations, characteristic of Stage II FCP, parallel to the γ/δ interface. Low stress-high cycle fatigue resistance was found to be controlled by the Stage I crack propagation along active slip planes in the γ lamellae.

The objectives of this research were threefold: (1) to characterize fatigue crack propagation in the Ni-Ni_3Cb composite in terms of fracture mechanics concepts; (2) to determine what effect solidification and heat treatment parameters have on the fatigue crack propagation; and, (3) to elaborate on the fatigue fracture mechanisms reported by Hoover [*11*] and to define a growth rate range where the fatigue fracture mechanism transition occurred.

Experimental Procedures

Solidification and Heat Treatment

Master heats, 2000 g, of Ni-23Cb using high purity starting material (99.95 percent nickel and 99.87 percent columbium) were induction melted in an aluminum oxide (Al_2O_3) crucible under a vacuum purged, positive argon pressure atmosphere. The molten charge was homogenized for 5 min after which it was poured into a magnesium oxide (MgO) coated, steel split mold to produce eight ½-in.-diameter, 8-in.-long pins. The as-cast pins were cleaned as outlined by Gangloff [*16*] and then controlled in ⁹⁄₁₆-in. inside diameter 95.5 percent pure aluminum oxide thermocouple tubes under a vacuum purged, positive argon pressure at a growth rate of 4.7 cm/h. Solidification of the as-cast pins was performed in a vertical induction coil inside a vacuum chamber using the same techniques employed by Hoover [*15*] and Gangloff [*16*].

In order to ascertain the effect of heat treatment on FCP behavior, a precipitation strengthened matrix was obtained when as-controlled ingots were solution treated at 1220°C for 3 h in an air environment, quenched in a 10 percent brine solution, and aged for 2 h at 1000°C [*20,21*]. (The severity of the 10 percent brine quench resulted in lamellar interphase boundary separation in some regions; however, these localized separations did not appear to influence the fatigue response of the composite.)

Fatigue Testing

Test Specimen and Fatigue Apparatus—A number of different testing configurations can be employed to obtain FCP data. However, due to the size of the unidirectionally solidified ingot, approximately ⁹⁄₁₆ diameter by 6 in. long, conventional fatigue specimens could not be used. Consequently, a four-point bending configuration was used in the fatigue test program. Test specimens, ½ by ¹⁄₁₀ by 4½ in. as shown in Fig. 1, were electrodischarge machined from cylindrical as-grown ingots. A starting notch, approximately 0.05 in. deep, was introduced normal to the long dimension in the middle of the slab. Note that four steel tabs were epoxy-bonded to the extremities of the specimen to prevent buckling and damage to the specimen during cycling.

Loads were applied to the fatigue specimen in a four-point bend apparatus with the major span equal to 4 in. and the minor span equal to 3 in. (Fig. 2). Cyclic tests were performed on an MTS electrohydraulic closed loop testing machine under tension-tension loading conditions with a cyclic frequency of 10 and 20 Hz. Cycling was interrupted periodically in order to measure the increment of crack extension (about 0.005 in.) and to record the associated number of cycles.

Test Specimen and Loading Fixture Design Verification—Before fatigue tests were conducted on the eutectic composite, it was first necessary to prove that valid data could be obtained from the previously described loading fixture. T-1 steel was chosen for this test since its mechanical properties were similar to those of the Ni-Ni_3Cb composite and the FCP of T-1 steel had been previously investigated [*22*]. Specimens of T-1 steel were prepared to the same dimensions as was described previously. The FCP rates of the conventional steel alloy when tested in the four-point bending fixture were slightly greater than the crack growth rates previously observed by Parry [*22*], with the largest error being associated with higher stress intensity factor range conditions.

This discrepancy can be accounted for by applying plasticity corrections to the crack propagation data. By taking into account the plastic zone at the actual crack tip, the effective crack length may be approximated by the actual crack length plus the plastic zone size, r_y

$$a_{\text{eff}} \approx a_{\text{actual}} + r_y \tag{1}$$

where

$$r_y = \frac{1}{2\pi} \frac{K^2}{{\sigma_{ys}}^2} \tag{2}$$

K = stress intensity factor, and
σ_{ys} = material yield strength.

Thus, an effective stress intensity factor range

$$\Delta K_{\text{eff}} = Y\left[\frac{a_{\text{eff}}}{W}\right] \Delta\sigma \sqrt{\pi(a_{\text{eff}})} \tag{3}$$

where

$Y\left[\frac{a_{\text{eff}}}{W}\right]$ = geometrical correction factor,
W = specimen width, and
$\Delta\sigma$ = stress range

was determined by an iterative process since the plastic zone size is dependent on the stress intensity level. When the plasticity corrections

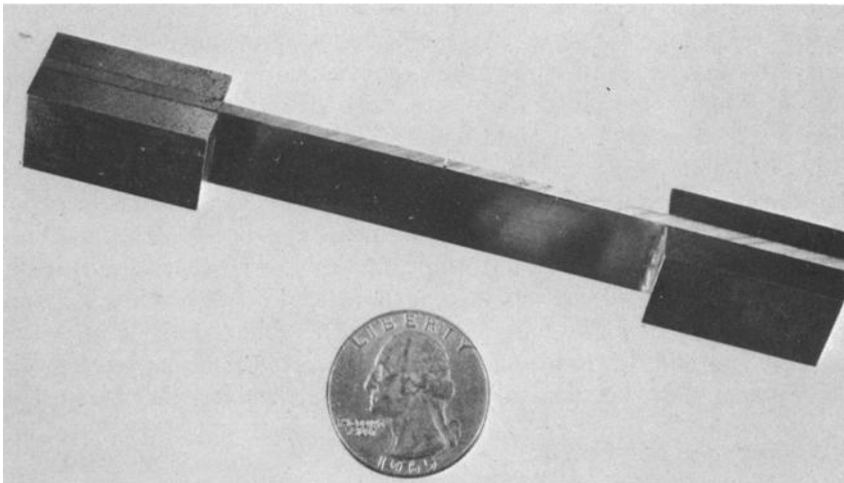

FIG. 1—*Four-point bending specimen.*

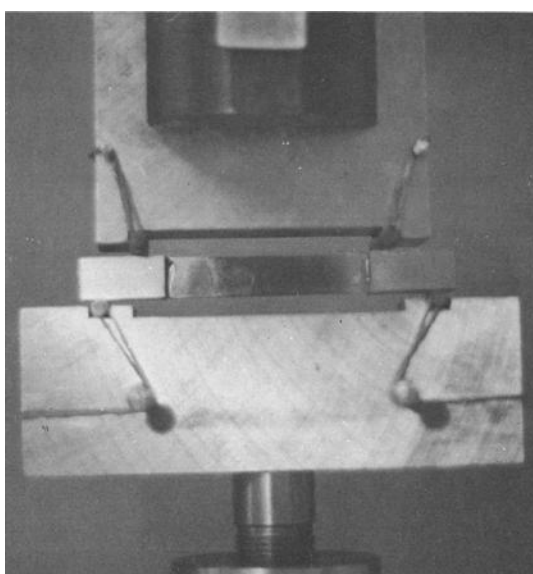

FIG. 2—*A photograph showing the four-point bending fixture and specimen taken during an actual fatigue test* ($X^1/_2$).

were introduced to fatigue data obtained during the current investigation, crack propagation rates were in much better agreement with those reported by Parry [22]. It is important to note that in conventional fatigue testing of larger specimens the plastic zone size is usually much smaller than the total crack length and is often ignored in computations of ΔK. However, with the specimen and testing fixture design employed during the current investigation, it was necessary to make the adjustment for plasticity at the crack tip since the ratio of plastic zone size to crack length was significantly larger, while the value of Y increased rapidly with relatively small increases in a/W in four-point bending. Having established that accurate fatigue data could be obtained using this specimen configuration in four-point bending when plastic zone size corrections are applied, specimens of the Ni-Ni_3Cb composite were tested.

Metallographic Techniques

Metallographic specimens were wet ground through 600 grit paper, rough polished with 6 and 1 μ diamond paste, and final polished with a Linde B slurry. For excellent contrast between the γ and δ phases, specimens were immersion etched from 4 to 8 s in a Modified Marbles Reagent (Etchant A: 20-g copper sulfate ($CuSO_4$), 299-ml ethanol, 100-ml concentrated hydrochloric acid (HCl) and 100-ml water (H_2O) and viewed under both white and polarized light. A drawback of this etch was its inability to reveal the twinning present within the δ phase.

To reveal the δ phase twins, metallographic specimens were immersion etched for 1 min in a solution of 35-ml nitric acid (HNO_3), 2-ml hydrofluoric acid (HF), and 63 ml water (H_2O) (designated as Etchant B). Because the effectiveness of the etch decreased in a short period of time, it was necessary to prepare the solution immediately before etching the sample.

All fatigue fractures were nickel plated to keep the fracture profile intact during metallographic preparation.

Electron Microscopy Techniques

In order to study the fatigue mechanisms operating in the Ni-Ni_3Cb composite, electron microscope replicas were made from appropriate fracture surfaces. Standard two-stage carbon replicas, shadowed parallel to the direction of crack propagation with a platinum-carbon mixture, were cut into small strips approximately 1 mm wide. Extreme care was taken in measuring the distance from the crack origin to each replica in an effort to relate the features found on the fracture surface to a corresponding growth rate and ΔK level.

Electron microscopic examination of the replicas was conducted in an RCA-EMU-3G electron microscope operated at an accelerating potential of 50 kV and in a Philips EM300 electron microscope operated at accelerating potentials of 60 and 80 kV.

Presentation and Discussion of Results

Microstructure

The aligned microstructure obtained during the current investigation (Fig. 3*a*) consisted of alternating lamellae of nickel-rich (γ) and intermetallic Ni_3Cb (δ) phases with an interlamellar spacing (λ) ranging from 6 to 9 μ. (The γ platelets were approximately twice as thick as those of the δ phase.) As-controlled microstructures were essentially free of δ phase precipitation; however, solution treating and aging produced a uniform distribution of δ phase precipitation with Widmanstätten morphology on all four variants of the $\{111\}$ habit plane within the γ matrix as shown in Fig. 3*b*. (Specific physical and mechanical characteristics of the age hardened composite are reported in Refs *20* and *21*.)

Fatigue Crack Propagation in the Ni-Ni₃Cb Composite: A Fracture Mechanics Approach

FCP in the Unidirectionally Solidified Ni-Ni₃Cb Composite—Fracture mechanics concepts have been applied successfully to crack growth during cyclic loading in face centered cubic (fcc), body centered cubic (bcc), and hexagonal closed packed (hcp) metals as shown by Paris [*23,24*]

$$\frac{da}{dN} = C\ \Delta K^n \tag{4}$$

where

ΔK = stress intensity factor range, $K_{max} - K_{min}$ (Eq 3),
σ = gross stress,
a = crack length,
W = panel width,
Y = geometrical correction factor, and
C, n = material constants which have been shown to depend on mean load.

The data shown in Fig. 4, which characterize the FCP response of the aligned eutectic at a load ratio (R = minimum load/maximum load) of less than 0.1, represent the first such reported information for eutectic

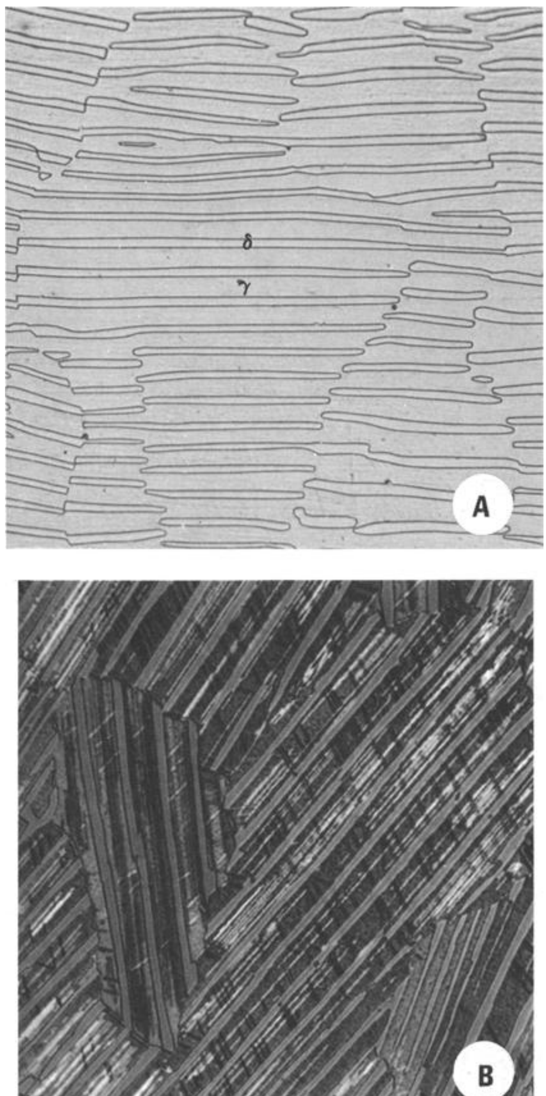

FIG. 3—*Microstructure of Ni-Ni_3Cb eutectic composite.* (a) *Aligned lamellar microstructure illustrating the absence of* δ *phase precipitation in as-grown ingots* (*X533*) (b) δ *phase precipitation of Widmanstätten morphology present after heat treatment* (*X533*).

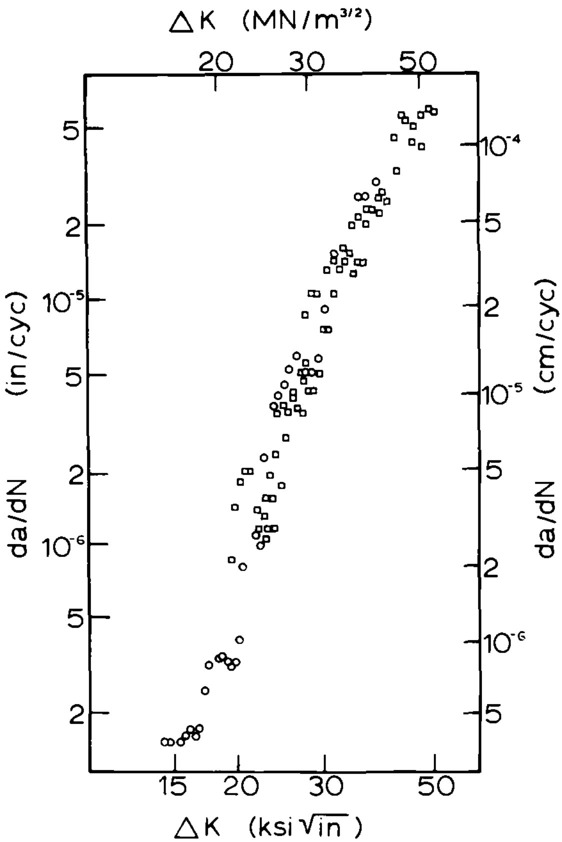

FIG. 4—*Fatigue crack growth rate versus* ΔK *for the Ni-Ni$_3$Cb eutectic composite* (R < *0.1*). (○: *10Hz*, □: *10 Hz*).

composites. Note that an excellent correlation exists between the stress intensity factor range and the fatigue crack growth rates in this *in situ* composite. From Eq 4, the experimental constants are found to be

$$C = 4 \times 10^{-13} \quad (\Delta K\text{: ksi } \sqrt{\text{in.}} \text{ units})$$
$$n = 4.9$$

for growth rates between 10^{-7} and 10^{-4} in./cycle. The value of n for the composite was slightly higher than that found in most conventional alloys, 4.9 versus 4.0.

The FCP response of the Ni-Ni$_3$Cb composite was similar to that of steel alloys with a comparable elastic modulus. This result was expected since Pearson [*25*] has illustrated that the crack growth rates of various

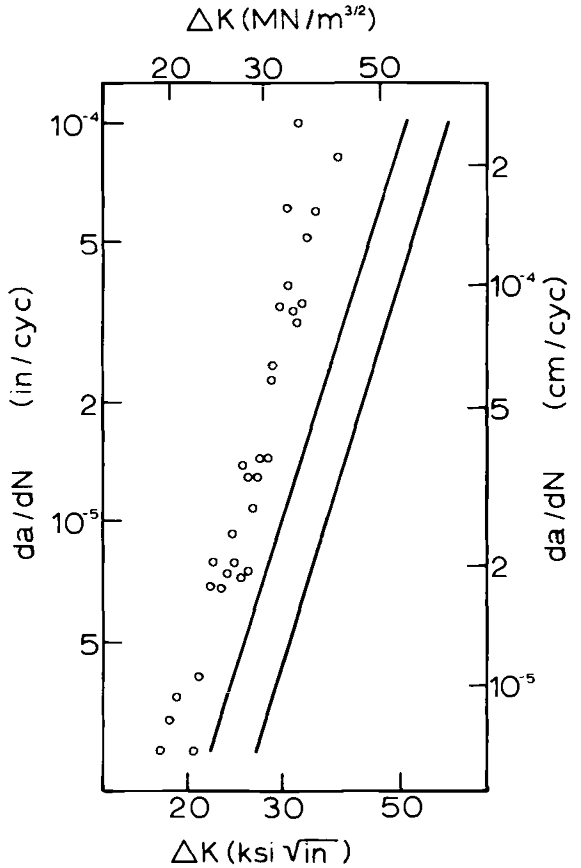

FIG. 5—*Fatigue crack propagation rates versus* ΔK *for the Ni-Ni$_3$Cb eutectic composite* (R = *0.5*). *Data band represents* R < *0.1 data range from Fig. 4.*

metals may be normalized by plotting da/dN versus $\Delta K/E$ where E is the modulus of elasticity.

Effect of Test Variables on FCP—The results of additional fatigue testing conducted at a load ratio of $R = 0.5$ were compared with the previous results (data band) as seen in Fig. 5. As expected [*24*] a small shift in crack growth rates resulted from the elevated mean stress intensity. It is important to note that ΔK rather than K_{mean} was the most important factor controlling crack propagation since an increase in K_{mean} by a factor of three only caused da/dN to triple, while doubling the value of ΔK caused a thirtyfold increase in da/dN.

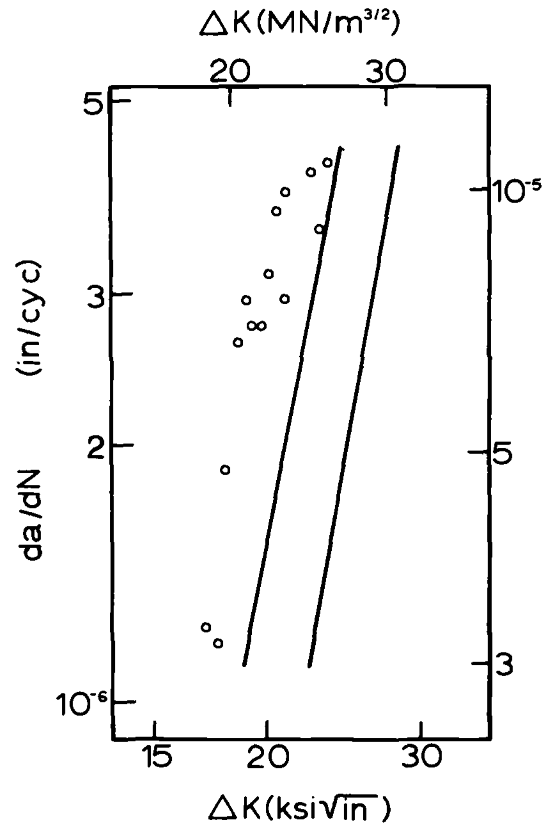

FIG. 6—*Fatigue crack growth rate versus* ΔK *for the non-controlled alloy.* (R < *0.1.*) *Data band represents the data range for the as-controlled composite.*

Effect of Metallurgical Variables on FCP—Metallurgical variables such as crystallographic texture and thermo-mechanical processing usually have little effect on the FCP response of conventional alloys. However, the fatigue growth rates of the nonaligned eutectic alloy were greater than that of the unidirectionally solidified composite (Fig. 6). Furthermore, the as-cast alloy underwent static fracture at a much lower stress intensity factor than did the as-controlled eutectic indicating that the nonaligned structure possessed much lower toughness. Therefore, the properly aligned eutectic composite was found to possess superior fatigue and fracture toughness behavior to the noncontrolled alloy. This inferior performance of the as-cast alloy was believed due to large and randomly oriented particles of δ which presumably failed prematurely.

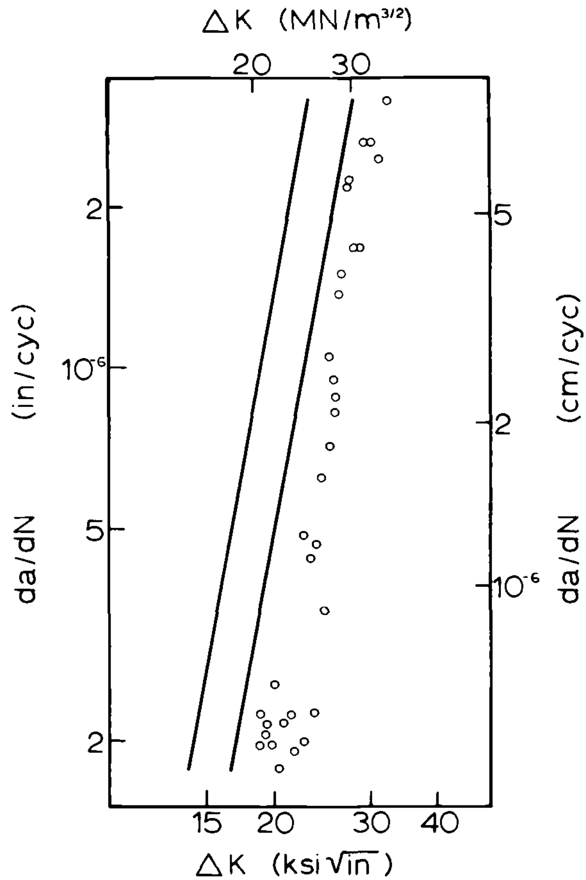

FIG. 7—*Fatigue crack growth rate versus* ΔK *for the age hardened Ni-Ni_3Cb eutectic composite.* (R < *0.1*) *Data band represents the data range for the as-grown composite.*

Thermal treatment of the unidirectionally solidified Ni-Ni_3Cb eutectic composite produced an improvement in the fatigue response of the alloy. Fatigue tests conducted on the age-hardened composite revealed a decrease in the crack propagation rates when compared to the fatigue behavior of the as-grown alloy (data band) as shown in Fig. 7. The presence of δ phase Widmanstätten precipitation in the γ matrix appears to have retarded crack growth in the γ phase thereby improving the fatigue behavior of the composite. This effect has important implications since the age hardening of the aligned structure can lead both to an improvement in strength [*20,21*] and an enhancement of fatigue performance as shown in Fig. 7.

Fatigue Fracture Mechanisms

Fractographic Observations: High FCP Rates (greater than 1.5 $\times$ 10^{-5} in./cycle)—Under high stress intensity range conditions, Stage II crack propagation occurred by fatigue striation formation in the γ phase (Fig. 8). Figure 9 illustrates that the microscopic growth rates, striation spacings, in the γ phase (broken lined boxes) were in good agreement with the macroscopic growth rates (data band) over a range of growth rates from 3×10^{-6} to 2×10^{-5} in./cycle. Striations always formed parallel to the γ/δ interface independent of the δ platelet orientation with respect to the crack front as shown in Fig. 8*b* which reveals two δ platelets surrounded by the striated γ matrix. Note that the direction of crack growth was normal to the interphase boundary as evidenced by the fact that striations always remained parallel to the γ/δ interface, suggesting that the γ lamellae had fractured ahead of the advancing crack front as reported by Hoover [*11*].

Delta platelets fractured as a result of $\{211\}_\delta$ type twinning and subsequent twin boundary cracking at all growth rates. Tongues and steps observed on the δ-phase fracture surface (Fig. 10) were found to be related to the four variants of the $\{211\}_\delta$ type twin. Twin boundary fracture occurred along one variant of the $\{211\}_\delta$ twin, while the other three variants intersected the fracture surface. Steps resulted from a change in orientation of the fracture surface due to the intersecting secondary $\{211\}_\delta$ twin while tongues were caused by localized crack plane deviations.

Fractographic Observations: Low FCP Rates (below 5×10^{-6} in./cycle)—As Hoover [*11*] had reported, at low growth rates the γ matrix fractured in a faceted manner indicative of Stage I FCP along active slip planes. The electron fractograph shown in Fig. 11*a* illustrates very crisp facets present at low growth rates. The observation of Stage I facets on the γ matrix fracture surface is consistent with Gell and Leverant's low stress-high cycle fatigue findings in the nickel-base superalloy, Mar-M200 [*26–28*].

Under low stress intensity range conditions in the Ni-Ni_3Cb composite, distinctive parallel fracture markings were often observed superimposed on facets as illustrated in Fig. 11*b*. Gell and Leverant [*27*] also found distinct markings on the fracture surfaces of the nickel-base superalloy, Mar-M200, which were not obliterated by rubbing. Based on these findings, they proposed a model for Stage I FCP where the weakening of slip planes by reversed shear deformation resulted in subsequent fracture of these weakened planes by local normal stresses. Consequently, the distinct features, such as crisp facets and parallel fracture markings, which were not obliterated on the fracture surface of the eutectic composite,

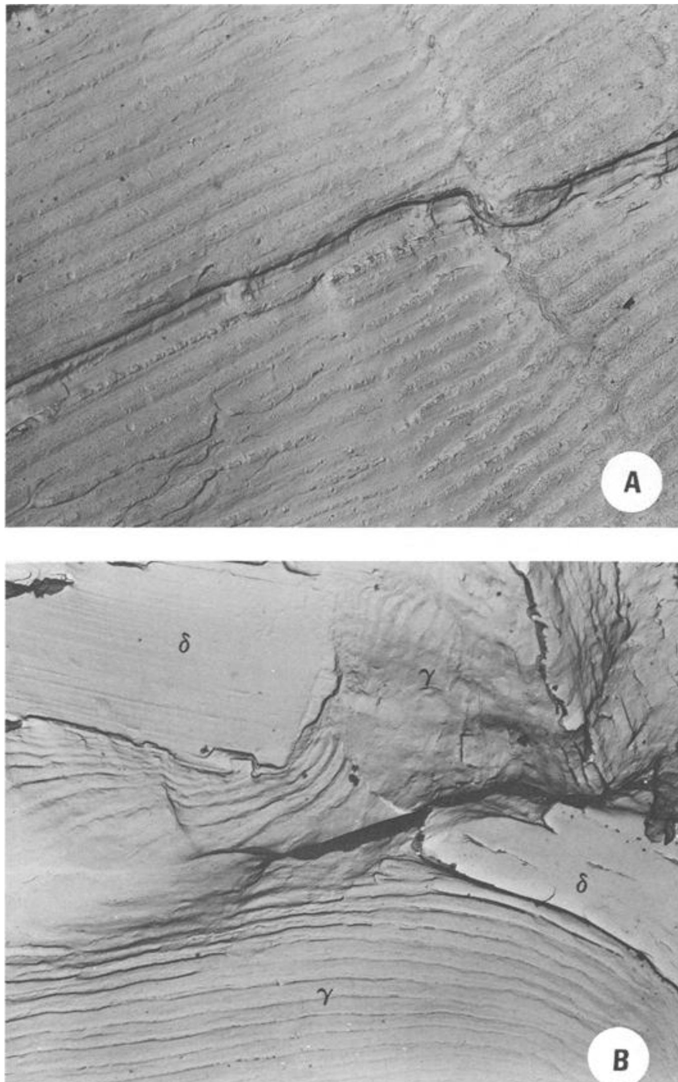

FIG. 8—*Electron fractographs revealing the fracture surface appearance under high* ΔK *conditions.* (a) *Typical striations found on the* γ *matrix fracture surface (X5300).* (b) *Striations remain parallel to the* γ/δ *interface irrespective of the* δ *platelet orientation (X6600).*

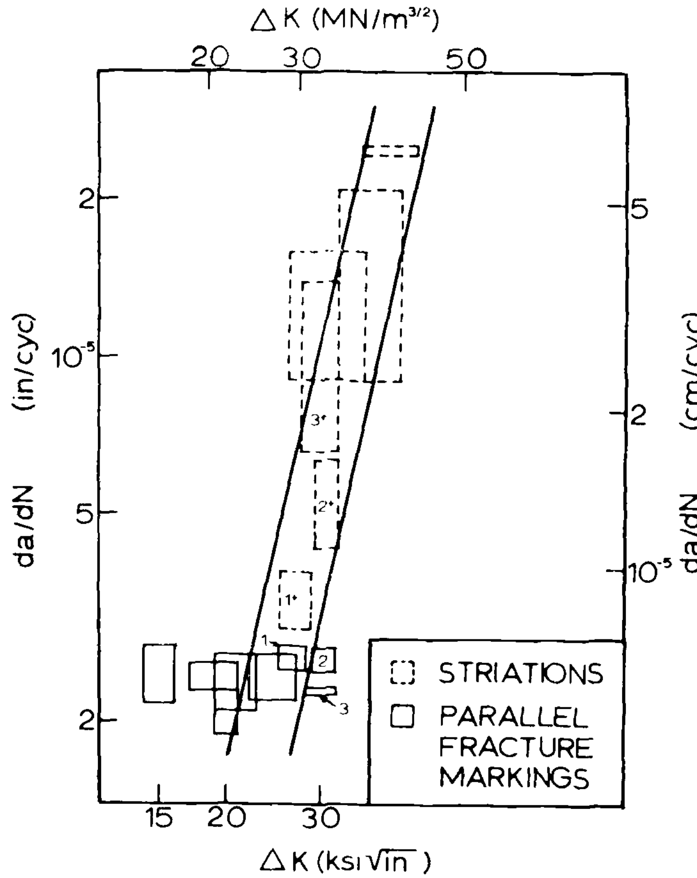

FIG. 9—*Plot representing the macroscopic (data band) and microscopic (striation spacing,* ⬚*) growth rates of the Ni-Ni_3Cb eutectic composite as a function of* ΔK. *The solid boxes represent the spacing of the parallel fracture markings found superimposed on the Stage I fracture surface. Boxes labelled 1-1*, 2-2*, and 3-3* correspond to the spacing of the parallel fracture markings and the striations, respectively, observed on a given replica.*

suggest that local shear and normal stresses control Stage I crack propagation in the γ matrix, consistent with Gell and Leverant's [*27*] hypothesis.

The spacing of these parallel markings (Fig. 11*b*), approximately 600Å, was independent of the applied stress intensity range as shown in Fig. 9 (solid boxes) which indicates that the parallel fracture markings were definitely not fatigue striations. Furthermore, when fracture markings and striations appeared in the same region, the spacing of the fracture

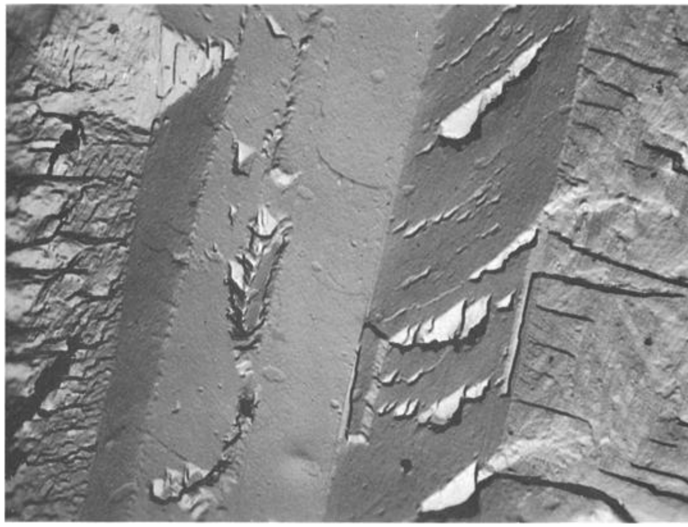

FIG. 10—*Electron fractograph of the fracture surface revealing twin related steps and tongues found at the δ fracture surface (X9000).*

markings was always two or three times smaller than that of the striations as indicated on Fig. 9 where the boxes labelled 1-1*, 2-2* and 3-3* correspond to the spacing of fine lines and striations, respectively. The parallel markings were always observed parallel to the γ/δ interface, which also corresponds to a trace of the $\{111\}_\gamma$ plane (the slip plane in fcc metals). This suggests that the fracture markings may be the result of slip offsets formed as a result of the severe stresses present at the crack tip [*26*].

Straight slip lines are usually found in low stacking fault energy materials that exhibit planar slip. While the stacking fault energy of pure nickel is very high, approximately 250 erg/cm^2 [*29*], the addition of columbium to the nickel causes a significant decrease in the stacking fault energy. In fact, Annarumma and Turpin [*17*] and Hill [*30*] have estimated the stacking fault energy of the γ-phase from dissociated threefold nodes to be less than 50 erg/cm^2. These low values for the stacking fault energy are consistent with the very straight slip lines observed in the γ-phase during the current investigation.

Fracture Mechanism Transition: (5×10^{-6} to 1.5×10^{-5} in./cycle)—At intermediate growth rates, a transition from Stage I to Stage II FCP occurred as evidenced by the fact that regions containing both facets (*F*) and striations were observed on the γ phase fracture surface as shown

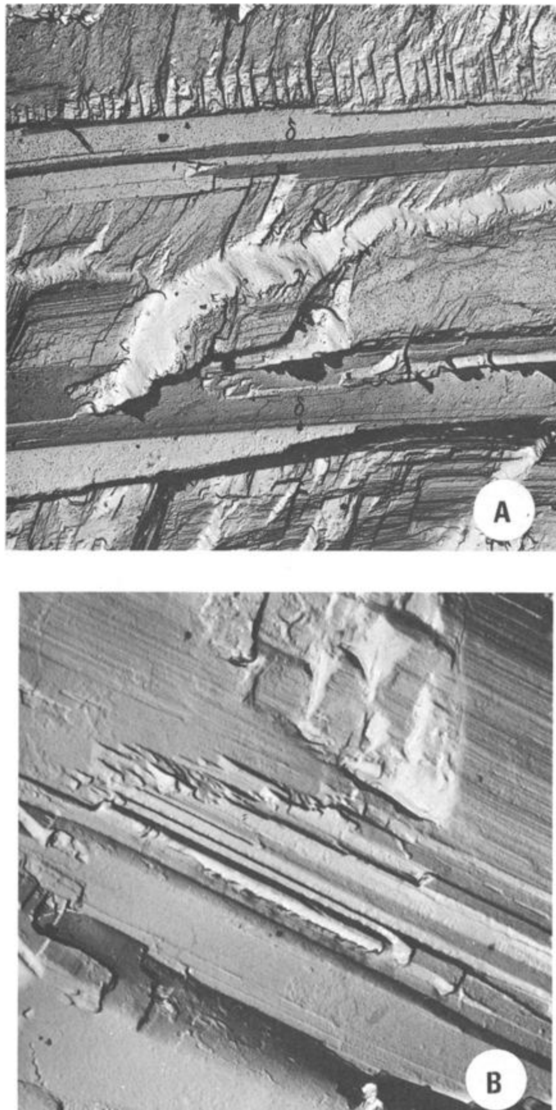

FIG. 11—*Electron fractographs revealing the fracture surface appearance under low* ΔK *conditions.* (a) *Stage I facets on the* γ *fracture surface (X5300).* (b) *Evidence of fine parallel lines superimposed on the* γ *matrix faceted fracture surface (X10 000).*

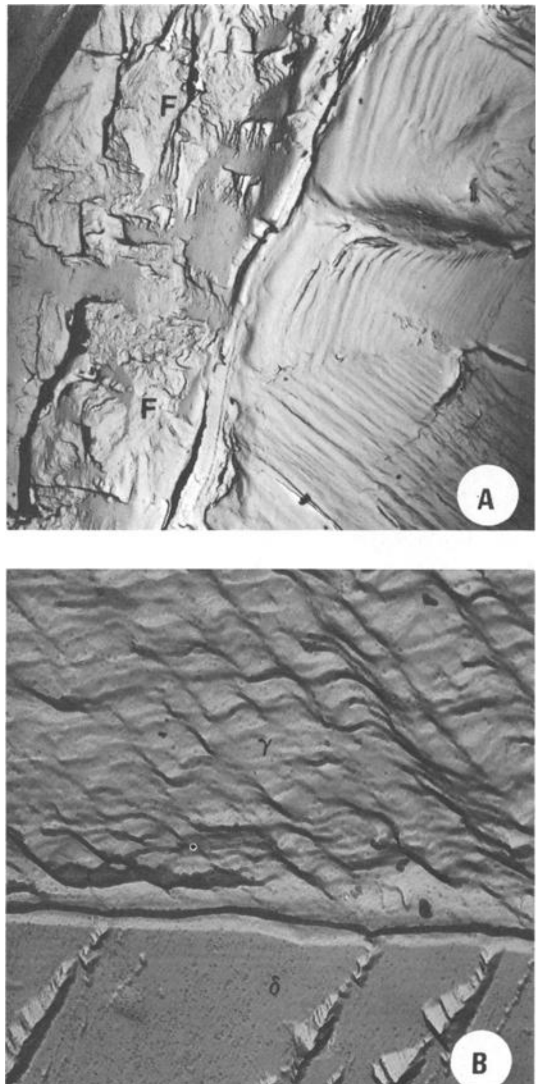

FIG. 12—*Typical electron fractographs of the intermediate growth rate region illustrating:* (a) *poorly defined facets and striations present in the same* γ *phase region* (*X5600*). (b) *evidence of serpentine glide on the* γ *matrix fracture surface* (*X14 000*).

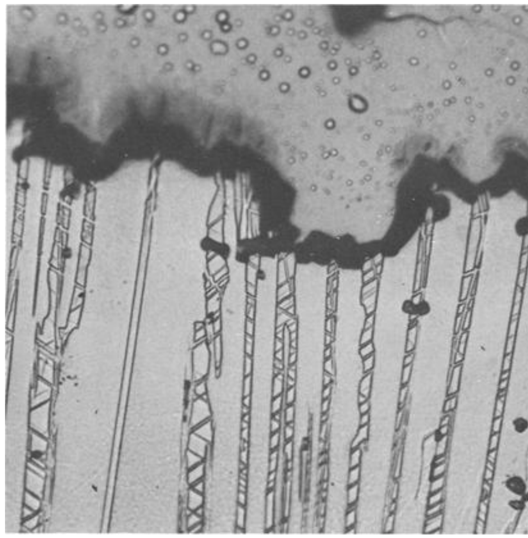

FIG. 13—*Typical metallographic profile of a fatigue fracture at high growth rates revealing* $\{211\}_\delta$ *twinning and associated twin boundary cracking near the fracture surface* (*X533*) (*Etchant B*).

in Fig. 12*a*. It is of significance to note that γ-phase facets were poorly defined when compared to the crisp facets observed under low ΔK conditions (see Fig. 11*a*). The interwoven appearance of the γ-phase fracture surface, as seen in Fig. 12*b*, is evidence of serpentine glide defined by Beachem and Meyn [*31,32*] as partial glide plane decohesion on several slip planes. Evidence of poorly defined facets and serpentine glide suggests that gliding occurred on multiple sets of intersecting planes. Since these intermediate growth rates were associated with higher ΔK levels, more slip systems could operate, thereby increasing the dislocation activity on a number of intersecting slip planes ahead of the crack tip. Such dislocation activity probably weakened the atomic bonds along a number of intersecting slip planes which produced a poorly defined faceted appearance. Finally, the increased local normal stresses under intermediate ΔK conditions associated with the fracture mechanism transition resulted in the formation of striations indicative of a tensile mode fatigue fracture.

Metallographic Observations—Metallographic examination of the fractured specimens has provided important information in determining the fatigue crack growth mechanisms of the Ni-Ni_3Cb eutectic composite.

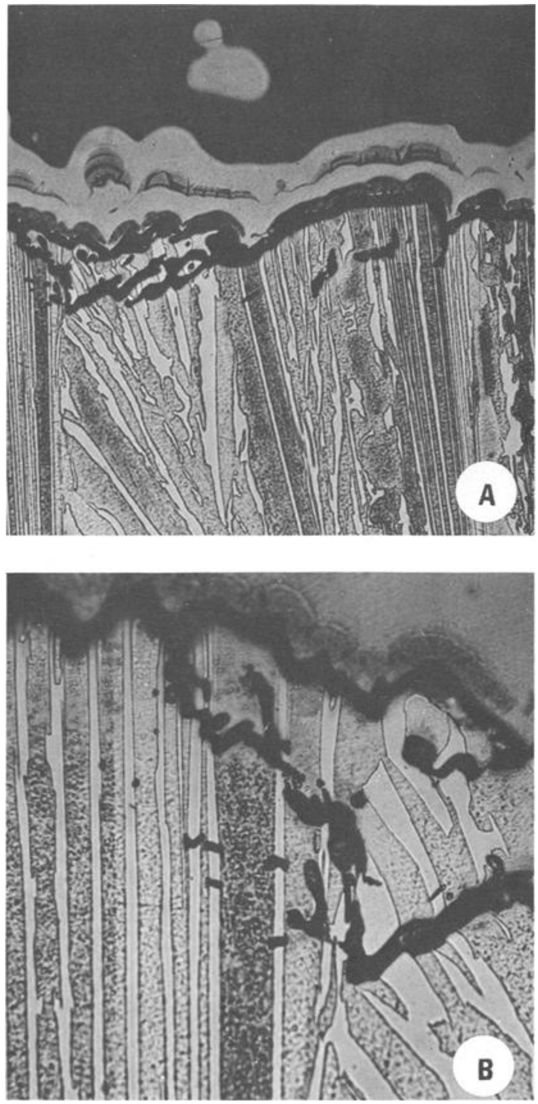

FIG. 14—*Typical metallographic profile of a fatigue fracture at low growth rates. (Etchant A)* (a) *Secondary fatigue cracks that propagated parallel to the primary fatigue crack (X133).* (b) *Increased magnification of the region at the secondary crack tip where a significant number of δ platelets have undergone twin boundary cracking in advance of the crack front (X533).*

Observed in the regions adjacent to the fracture surface was $\{211\}_\delta$ twinning. Figure 13 represents a typical area in the fracture profile which illustrates $\{211\}$ type twinning in the δ lamellae and subsequent twin boundary cracking. Under low stress intensity factor conditions, less than approximately 30 ksi $\sqrt{\text{in.}}$ (33 $\text{mN/M}^{3/2}$), the $\{211\}_\delta$ twinning deformation damage was confined to an area very near the fatigue crack as Hoover [11] had reported. On the other hand, twinning was not restricted to the immediate vicinity of the fracture surface at high ΔK levels. Under both high and low ΔK conditions, however, twin boundary cracking was limited to the region immediately adjacent to the fatigue crack. (Another twin habit, believed to be of the $\{011\}$ type, was observed at high ΔK levels but did not appear to participate in the fracture process.)

At low growth rates, secondary fatigue cracks propagated parallel to the fatigue fracture surface as seen in Fig. 14*a*. Upon closer examination (Fig. 14*b*), it is seen that a number of reinforcing δ plates had undergone twin boundary fracture ahead of the advancing secondary crack front. (Etchant A was employed in order to distinguish the two phases; however, this etch does not reveal δ-phase twins.) The macroscopic FCP rates in this region were less than 1.4×10^{-6} in./cycle and well within the region where the γ matrix failed as a result of Stage I FCP.) The fact that δ platelets fractured ahead of the crack tip indicates that the twin boundary fissures subsequently grew into the γ matrix by Stage I FCP. Thus, Stage I fracture along active slip planes in the γ matrix is believed to control the FCP at low growth rates as well as at high growth rates. This proposed fracture mechanism contradicts the one postulated by Hoover [11] who postulated that for the low growth rate regime, δ platelets fractured only when the crack front reached the γ/δ interface. However, the current investigation has revealed that the δ lamallae fractured ahead of the advancing crack tip.

Conclusions

Based on the experimental results and the subsequent discussion, the following conclusions have been drawn:

1. A power relationship between da/dN and ΔK was found to exist for the aligned Ni-Ni_3Cb composite over a range of growth rates from 10^{-7} to 10^{-4} in./cycle. The FCP behavior of this alloy was analogous to that of steel alloys with comparable elastic moduli.

2. A small shift to higher growth rates was observed as a result of higher mean stress intensity levels, however, the stress intensity factor

range rather than the mean stress intensity level was the major variable controlling the FCP response.

3. The fatigue behavior and toughness of the noncontrolled structure was inferior to that of the aligned composite.

4. The presence of δ phase precipitates of Widmanstätten morphology within the γ matrix as a result of age hardening thermal treatment retarded FCP in the γ-phase, thereby improving the fatigue response of the composite.

5. During Stage II FCP in the γ matrix fracture surface, microscopic growth rates, striation spacings, were in good agreement with macroscopic crack growth rates. At low growth rates, the γ fracture surface exhibited facets indicative of Stage I FCP along active slip planes. Under all ΔK levels, δ lamellae fractured as a result of $\{211\}$ twinning and subsequent twin boundary cracking ahead of the advancing crack tip.

6. The fatigue behavior of the unidirectional solidified Ni-Ni_3Cb eutectic underwent a fracture mechanism transition at intermediate growth rates (5×10^{-6} to 1.5×10^{-5} in./cycle) as evidence of both Stage I and Stage II FCP was observed on the fracture surface.

Acknowledgments

We gratefully acknowledge the financial support of the National Aeronautics and Space Administration under Grant NGR-39-007-007. Appreciation is also extended to the Bell Telephone Laboratories and the Western Electric Company in Allentown, Pa. for machining the fatigue specimens and to R. W. Kraft, M. R. Notis, R. P. Gangloff, and K. A. Hill for many enlightening discussions.

References

[1] Hogan, L. M., Kraft, R. W., and Lemkey, F. D., *Advances in Materials Research*, Vol. 5, Wiley, New York, 1971, p. 83.

[2] Hertzberg, R. W., *Fiber Composite Materials*, American Society for Metals, Metals Park, Ohio, 1965, p. 77.

[3] Salkind, M., Leverant, G., and George, F., *Journal of the Institute of Metals*, Vol. 95, 1967, p. 349.

[4] Graham, L. D. and Kraft, R. W., *Transactions*, American Institute of Mining, Metallurgical, and Petroleum Engineers, Vol. 236, 1966, p. 94.

[5] Kraft, R. W., Albright, D. L., and Ford, J. A., *Transactions*, American Institute of Mining, Metallurgical, and Petroleum Engineers, Vol. 227, 1963, p. 540.

[6] Salkind, M. J., George, F. D., Lemkey, F. D., and Bayles, B. J., "An Investigation of the Creep, Fatigue and Transverse Properties of Al_3Ni Whiskers and $CuAl_2$ Platelet Reinforced Aluminum," Final Report, United Aircraft Research Laboratories, Contract NOw65-0384-d, 1966.

[7] Hoover, W. R. and Hertzberg, R. W., *Transactions*, American Society for Metals, Vol. 61, 1968, p. 769.

[8] Ovens, W. G., Jr. and McEvily, A. J., Jr., *Conference on In Situ Composites*, Vol. 2,

Publication NMAB-308-11, National Academy of Sciences-National Academy of Engineering, Washington, D.C., 1973, p. 273.
[9] Kossowsky, R., Sadananda, K., and Doner, M., *Electron Microscopy and Structure of Materials,* University of California Press, Berkeley, 1972, p. 764.
[10] deSilva, A. R. T. and Chadwick, G. A., *Metal Science Journal,* Vol. 4, 1970, p. 63.
[11] Hoover, W. R. and Hertzberg, R. W., *Metallurgical Transactions,* Vol. 2, 1971, p. 1289.
[12] Thompson, E. R., Kraft, E. H., and George, F. D., "Investigation to Develop a High Strength Eutectic for Aircraft Engine Use," Final Report, Contract N00019-71-C-0096, United Aircraft Research Laboratories, 1971.
[13] Henry, M. F., "Low Cycle Fatigue of the Directionally Solidified Eutectic Ni(Cr)-TaC," presented at the 1973 Spring Meeting of The Metallurgical Society of the American Institute of Mining, Metallurgical, and Petroleum Engineers.
[14] Quinn, R. T., Kraft, R. W., and Hertzberg, R. W., *Transactions,* American Society for Metals, Vol. 62, 1969, p. 38.
[15] Hoover, W. R. and Hertzberg, R. W., *Metallurgical Transactions,* Vol. 2, 1971, p. 1283.
[16] Gangloff, R. P., "Elevated Temperature Tensile and Creep Rupture Behavior of Unidirectionally Solidified Ni-Ni_3Nb Eutectic Composite," Master's thesis, Lehigh University, Bethlehem, Pa., 1972.
[17] Annarumma, P. and Turpin, M., *Metallurgical Transactions,* Vol. 3, 1972, p. 137.
[18] Grossiord, C.; Lesoult, G., and Turpin, M., *Electron Microscopy and Structure of Materials,* University of California Press, Berkeley, 1972, p. 678.
[19] Lemkey, F. D., "Developing Directionally Solidified Eutectics for Use Up to 1235°C," First Quarterly Report, Contract NAS3-15562, United Aircraft Research Laboratories, 1971.
[20] Mills, W. J., "Fatigue Crack Propagation Behavior of the Unidirectionally Solidified Ni-Ni_3Nb Eutectic Composite," Master's thesis, Lehigh University, Bethlehem, Pa., 1973.
[21] Bertorello, H., Hertzberg, R. W., Mills, W. G., Kraft, R. W., and Notis, M. R., "Solubility Limits and Precipitation Phenomena in Ni-Ni_3Nb Aligned Eutectic," submitted for publication.
[22] Parry, M., Nordberg, H., and Hertzberg, R. W., "Fatigue Crack Propagation in A514 Base Plate and Welded Joints," *Welding Journal Research Supplement,* Oct. 1972.
[23] Paris, P. C., *Fatigue—An Interdisciplinary Approach,* Syracuse University Press, Syracuse, N.Y., 1964, p. 107.
[24] Paris, P. and Erdogan, F., *Transactions,* American Society of Mechanical Engineers, Series D, Vol. 85, 1963, p. 528.
[25] Pearson, S., *Nature,* Vol. 211, 1966, p. 1077.
[26] Gell, M. and Leverant, G. R., *Acta Metallurgica,* Vol. 16, 1968, p. 553.
[27] Gell, M. and Leverant, G. R., *Transactions,* American Institute of Mining, Metallurgical, and Petroleum Engineers, Vol. 242, 1968, p. 1869.
[28] Gel, M. and Leverant, G. R., "The Effect of Temperature on Fatigue Fracture in a Directionally-Solidified Nickel-Base Superalloy," *Proceedings,* 2nd International Conference on Fracture, Brighton, 1969.
[29] Gallagher, P. C., *Metallurgical Transactions,* Vol. 1, 1970, p. 2429.
[30] Hill, K. A., "Microstructure and Joining of Ni-Ni_3Nb Unidirectionally Solidified Eutectic Composite," Master's thesis, Lehigh University, Bethlehem, Pa., 1973.
[31] Beachem, C. D. and Meyn, D. A., *Illustrated Glossary of Fractographic Terms,* NRL Memorandum Report 1547, U.S. Naval Research Laboratory, Washington, D.C., 1964.
[32] Beachem, C. D. and Meyn, D. A., in *Electron Fractography, ASTM STP 436,* American Society for Testing and Materials, 1968, p. 59.

J. F. Mandell[1] *and Urs Meier*[2]

Fatigue Crack Propagation in 0° / 90° E-Glass / Epoxy Composites

REFERENCE: Mandell, J. F. and Meier, Urs. "**Fatigue Crack Propagation in 0°/90° E-Glass/Epoxy Composites,**" *Fatigue of Composite Materials, ASTM STP 569*, American Society for Testing and Materials, 1975, pp. 28–44.

ABSTRACT: The mode of fatigue crack growth is described for a 0/90° E-glass/epoxy laminate under cyclic tension-tension loading. Crack growth appears to occur in a stepwise fashion with the crack remaining stationary for many cycles before each step of growth, whereupon a ligament of longitudinal ply at the crack tip is broken. A simple theory is described which assumes that the ligament at the crack tip is fatigued according to the *S-N* curve of the unnotched material. Using an assumed stress field and cumulative damage law, the number of cycles for initial growth from a notch and the rate of crack growth thereafter are predicted, and good agreement is demonstrated with experimental data.

KEY WORDS: composite materials, fatigue (materials), cracking (fracturing), fiber reinforced plastics, crack propagation

The growth of cracks under the influence of cyclic loading is a problem of great engineering importance in structural applications involving relatively brittle materials. The process of fatigue failure in metals has proven difficult to explain in fundamental terms. One significant area of progress has been the description of crack growth under cyclic loading where the rate of crack extension is typically proportional to some power of the stress intensity factor, K_I [*1*].[3] Knowledge of the stress intensity factor-crack growth rate relationship, coupled with an estimate of the critical crack length for unstable crack propagation taken from fracture toughness data, has led to accurate fatigue life predictions for sharply notched metal specimens [*1*].

[1] Research associate, Department of Civil Engineering, Massachusetts Institute of Technology, Cambridge, Mass. 02139.

[2] Head, Plastics Department, Swiss Federal Laboratories for Testing Materials and Research (EMPA), 8600 Dubendorf, Switzerland.

[3] The italic numbers in brackets refer to the list of references appended to this paper.

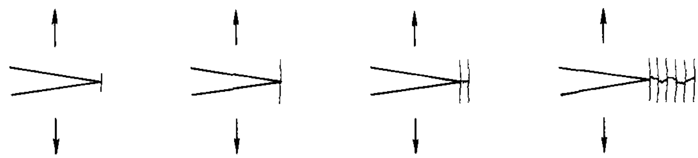

FIG. 1—*Mode of fatigue crack growth in 0° ply of (90°/0°/90°/0°/90°) laminate, fibers perpendicular to main crack.*

Previous work [*2,3*] has indicated that many varieties of fiber reinforced plastic laminates under monotonic loading conditions behave in a crack-sensitive manner that can be described by the fracture mechanics parameters found useful for homogeneous materials. The basic mechanism of crack propagation resistance for several varieties of glass fiber reinforced epoxy and polyester with fibers parallel and perpendicular to the load was found to be crack blunting by the growth of secondary subcritical splits perpendicular to the direction of main crack propagation. The fracture surface work was found to be approximately equivalent to the elastic energy dissipated upon failure of a ligament of longitudinal material, where a ligament is the region of material isolated by successive secondary splits (Fig. 1). The work of fracture was proportional to the length of the splits over a wide range for crossplied laminates; the split length was very sensitive to ply stacking configuration [*3*].

The study reported in this paper extends the understanding and description of the fracture process to include cyclic loading effects. A simple theory is presented which, it appears, may be used to predict the rate of crack propagation for the particular laminate type investigated under sinusoidal tension loading conditions.

Materials and Test Methods

Material

The material investigated was an unwoven, unidirectional-ply laminate of Scotchply Type 1002 E-glass/epoxy,[4] five plies thick, of ply-stacking configuration (90°/0°/90°/0°/90°), where 0° is the direction of loading and 90° is the main crack direction. Each ply of the laminate had a nominal thickness of 0.01 in. and a fiber volume fraction of 0.50. This ply-stacking sequence exhibits a lower fracture toughness in monotonic tests than do

[4] 3M Company.

other possible variations due to the constraint of the 90° ply on each side of each 0° ply [3]. The monotonic fracture behavior under uniaxial loading in the 0° direction can be described by classical fracture mechanics parameters as will be illustrated later.

Test Procedure

Test specimens of the two types shown in Fig. 2 were cut from the laminates; the notches were cut with a 0.011-in.-thick diamond-edged wheel which gives a sufficiently sharp notch for valid fracture toughness testing for this class of materials [3,4]. The specimens were clamped in pin-loaded grips and subjected to either monotonic or pulsating uniaxial tension. The fatigue specimens were cycled between a low tensile stress (≅ 1.0 ksi) and some maximum tension at 5 Hz as shown in Fig. 3. Testing was restricted to this frequency due to significant heat buildup at higher frequencies, particularly at the crack tip. The low stress fatigue tests (>1000 cycles) were run on a dynamic cycler; the higher stress fatigue and monotonic tests were run on a servohydraulic tester. Monotonic fracture and strength tests were conducted at a displacement rate of 20 in./min which coincides with the average displacement rate of the fatigue tests at 5 Hz. The monotonic fracture tests for comparison of

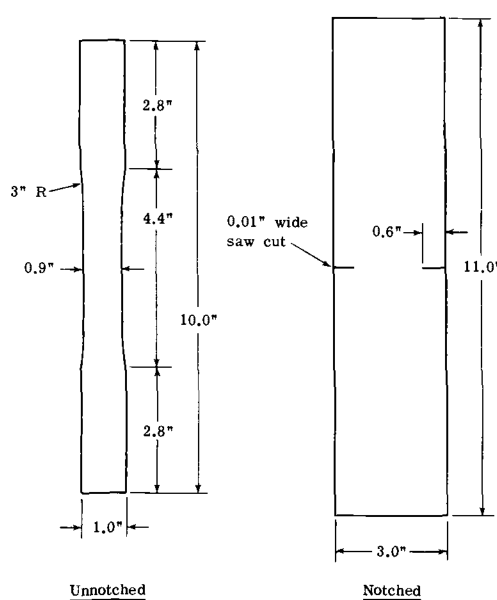

FIG. 2—*Test specimens.*

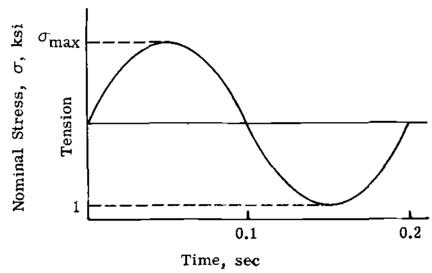

FIG. 3—*Stress versus time for fatigue tests.*

fracture toughness values for various specimen geometries were conducted on a standard tester at a displacement rate of 0.05 in./min.

Mode of Crack Propagation

Fatigue crack propagation for this class of materials appears to occur in the absence of any peculiar mechanism of growth, as is typically observed in metals where the crack extends by a small increment on each cycle [*1*]. As indicated schematically in Fig. 1 and in the micrograph of Fig. 4, the crack in the 0° plies is observed to extend by the following repetitive process:

1. With the crack stationary and terminated by a subcritical split perpendicular to the main crack, the ligament of 0° ply at the crack tip is fatigued by the local stress field.

2. After some number of cycles dependent on the stress intensity, the ligament at the crack tip fails and the main crack extends by a one ligament width.

3. The main crack remains stationary at the new length as steps (1) and (2) are repeated.

Thus, the main crack appears to extend by successively fatiguing small ligaments of the 0° ply at the crack tip to failure, and the ligamented appearance of the fracture region is identical to that observed in monotonic fracture tests [*3*]. The ligament width, *d*, in this case is approximately 0.01 in., encompassing a region containing approximately 700 fibers in each 0° ply. The 90° plies simply crack between fibers as the main crack extends and are not believed to contribute substantially to the fracture resistance except through the effect of their constraint on the deformations of the 0° plies [*3*]. Local delamination between plies at the crack tip is also observed, and the effect of this on the crack growth rate is not clear.

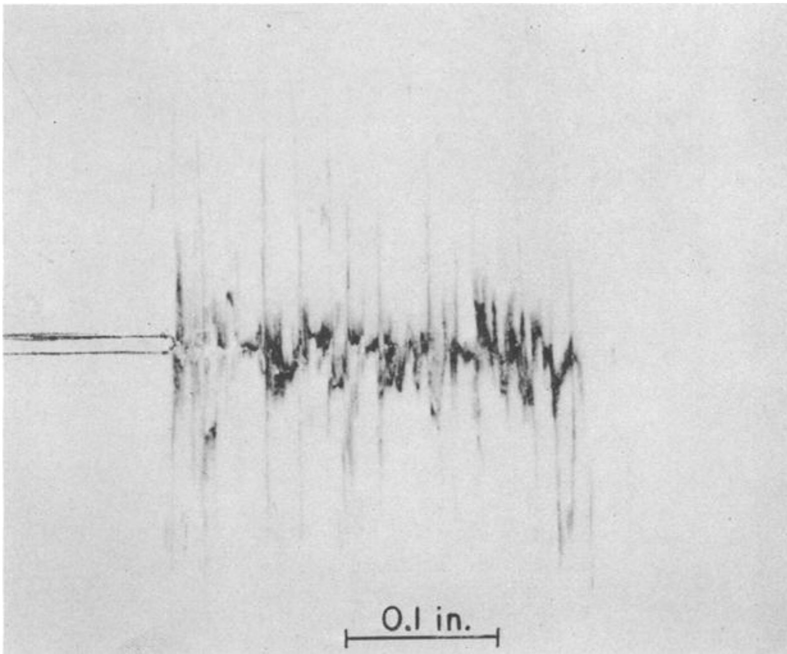

FIG. 4—*Fatigue crack growth from notch (left) in 0° ply of (90°/0°/90°/0°/90°) glass-epoxy laminate. Fibers are perpendicular to notch axis.*

For purposes of this discussion, crack propagation will be defined as extension of the main crack by fracture of fibers in the 0° plies to distinguish it from splitting parallel to the fibers in the 0 or 90° plies or delamination between plies.

Theoretical Prediction of Fatigue Crack Growth Rate

Initial Extension from Precut Notch

The experimentally observed characteristics of fatigue crack growth suggest the following simple theoretical model:

> The material adjacent to the subcritical split in the 0° plies at the crack tip is fatigued to failure according to the fatigue life (S-N) curve of an unnotched strip of material, but at the local stress level.

Thus, by estimating the local stress field acting on the material at the crack tip, initial extension of the main crack colinear with the precut notch can be predicted through the tensile S-N curve of the unnotched material.

The local stress field at the crack tip is simplified by considering only the local stress in the load direction, normal to the axis of the main crack, termed $\sigma(ij)$ for the stress on the i ligament from the original crack tip, with the main crack located at the edge of the j ligament, where the j-1 ligament is broken. For the case of the precut notch with no prior crack extension, the stress at the notch tip, $\sigma(11)$, at a maximum stress intensity factor of K_I, is assumed to be

$$\sigma(11) = \sigma_f \left(\frac{K_I}{K_Q}\right) \tag{1}$$

where σ_f is the ultimate strength of the unnotched material under uniaxial stress, and K_Q is the candidate opening mode critical stress intensity factor for the material, both at the appropriate strain rate. Equation 1 derives from the observation that the material at the crack tip in the 0° ply must reach its local ultimate tensile strength simultaneously as K_I reaches K_Q in a monotonic test and from the assumption that the local stress at the crack tip increases in a linear fashion with the applied stress. The validity of the latter assumption is difficult to establish since the subcritical split in the 0° ply at the crack tip extends gradually under increasing number of cycles beginning at some lesser length than that at fracture in the monotonic test and to a greater length before main crack extension occurs. Since the 0° subcritical split has the effect of blunting the main crack, its extension during cycling should somewhat diminish the local stress $\sigma(11)$. Equation 1 is equivalent to the assumption of a stress concentration at the crack tip of

$$\frac{\sigma(11)}{\sigma} = \frac{\sigma_f Y\sqrt{c}}{K_Q} \tag{2}$$

where σ is the maximum applied stress, and $Y\sqrt{c}$ is from the classical fracture mechanics relationship [5,6]

$$K_I = \sigma Y \sqrt{c} \tag{3}$$

for a crack of length, c.

The number of cycles for initial extension of the main crack can then be determined from the assumed value of $\sigma(11)$ and the S-N curve for the material. If, as in the present case, the S-N curve can be approximated by the linear relationship

$$\log N = \frac{\sigma_f - \sigma}{S} \tag{4}$$

where

N = number of cycles to failure,
σ = maximum applied stress, and
S = absolute value of the slope of the S-N curve,

then the number of cycles to initial crack extension will be given by substituting $\sigma(11)$ from Eq 1 for σ in Eq 4

$$\log N_i = \frac{\sigma_f}{S}\left(1 - \frac{K_I}{K_Q}\right) \tag{5}$$

where N_i is the number of cycles for initial extension of the main crack.

Fatigue Crack Growth Rate

The rate of fatigue crack growth can be predicted by the same model if additional assumptions are made as to the distribution of stress ahead of the main crack and the cumulative damage law for failure of the ligaments under several cyclic stress levels. Figure 5 gives the assumed variation in local stress in load direction ahead of the main crack. The stress at the crack tip is assumed to be given by Eq 1, and the variation along a line colinear with the main crack is assumed to follow an inverse relationship with $\sqrt{r}$, where r is the distance from the crack tip. This distribution is essentially that of the sharp crack problem for orthotropic materials [*5*] and isotropic materials [*6*] which reduce to the same relationship directly ahead of the crack tip. Ignoring higher order terms

$$\sigma_{yy} = \frac{K_I}{(2\pi r)^{1/2}} \tag{6}$$

where σ_{yy} is the local stress in the load direction. Near the crack tip, the stress field is truncated by Eq 1 since the local stress clearly cannot exceed this value. A more accurate description of the stress field awaits solution of the problem of a crack terminated by splits in the 0° plies which may soon be available [*4*].

An additional assumption is Miner's cumulative damage relationship which predicts failure when [*7*]

$$\sum \frac{n_k}{N_k} = 1 \tag{7}$$

where n_k is the number of cycles experienced at the k stress level, and N_k is the number of cycles which could be withstood for cycling at the k stress only. Although Miner's equation is not in good agreement with data

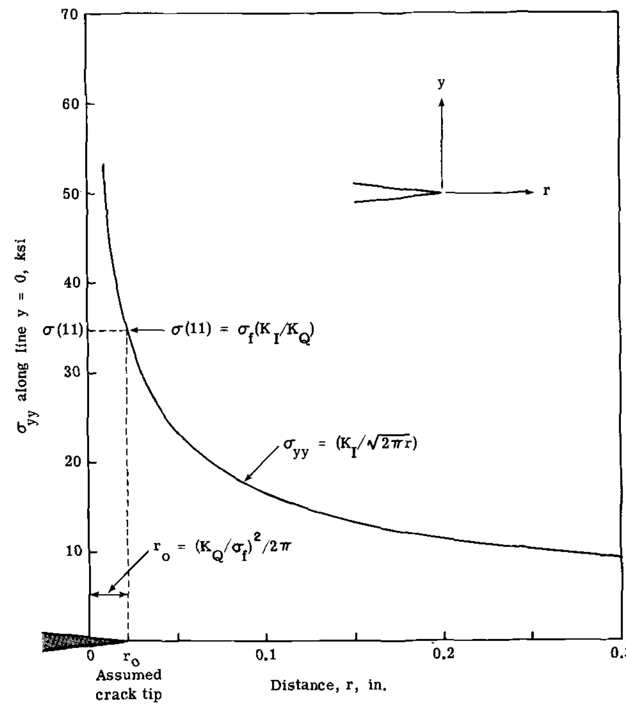

FIG. 5—*Assumed stress distribution ahead of crack for* $K_I = 13.0$ *ksi* $\sqrt{in.}$, $\sigma = 8.32$ *ksi.*

for composites of this type [*8*], no better theory is known to the authors at this time.

The number of cycles for the first several ligaments of crack extension is given by Eq 7 as

$$
\begin{aligned}
n_{11} &= N_{11} \\
n_{22} &= \left(1 - \frac{n_{11}}{N_{21}}\right) N_{22} \\
n_{33} &= \left(1 - \frac{n_{11}}{N_{31}} - \frac{n_{22}}{N_{32}}\right) N_{33}
\end{aligned}
\tag{8}
$$

where the first subscript gives the number of the ligament from the original crack tip, and the second subscript gives the location of the crack. Thus, N_{32} is the number of cycles for the third ligament with the crack at the edge of the second ligament, the first ligament having been broken.

Following the previous section, the number of cycles to first crack extension will be given by Eq 5, and

$$n_{11} = \exp \frac{[2.3\sigma_f(1 - K_1/K_Q)]}{S} \tag{9}$$

so the crack growth rate for the first ligament will be

$$\frac{dc}{dN} = d/\exp \frac{[2.3\sigma_f(1 - K_1/K_Q)]}{S} \tag{10}$$

The stress on the second ligament for the unextended crack is given by Eqs 3 and 6 as discussed previously as

$$\sigma(21) = \frac{K_I}{[2\pi(r_0 + d)]^{1/2}} \tag{11}$$

where r_0 is defined in Fig. 5. Substitution of $\sigma(21)$ into Eq 4 gives

$$N_{21} = \exp\left[2.3\,\frac{\sigma_f}{S}\left(1 - \frac{K_I}{\sigma_f\sqrt{2\pi(r_0 + d)}}\right)\right] \tag{12}$$

Since $N_{22} = N_{11}$, n_{22} reduces to

$$n_{22} = \exp\left[2.3\,\frac{\sigma_f}{S}\left(1 - \frac{K_I}{K_Q}\right)\right] - \exp\left[2.3\,\frac{\sigma_f}{S}\left(1 - \frac{2K_I}{K_Q} + \frac{K_I}{\sigma_f\sqrt{2\pi(r_0 + d)}}\right)\right] \tag{13}$$

and $dc/dn = d/n_{22}$ for the crack growth rate of the second ligament.

The same procedure can be used to obtain the crack growth rate for succeeding ligaments with the calculations most conveniently carried out by computer. Although the ligament width, d, is experimentally determined to be approximately 0.01 in. for the laminate considered here, this dimension may vary for other laminate constructions. Figure 6 gives the crack length as a function of the number of cycles under constant K_I conditions for three ligament widths. These crack growth curves indicate the stepwise growth of the crack at an approximately constant rate after the first, slower step. The difference in the number of cycles to fail the first ligament and some later ligament is a measure of the importance of the cumulative damage law. Cumulative damage has a significant effect on the 0.001-in.-wide ligaments, but on wider ligaments the local stress so diminishes from the crack tip to the far side of the first ligament that damage to the second and succeeding ligaments away from the crack tip is not significant. The differences between the ligament widths, although

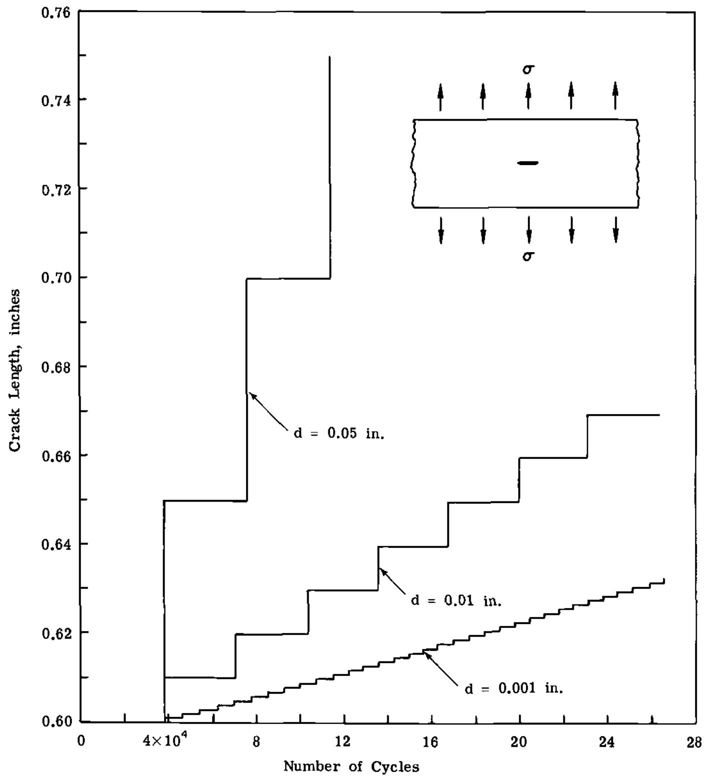

FIG. 6—*Predicted crack growth in infinite plate for several ligament sizes* ($K_I = 13.0$ *ksi* $\sqrt{in.}$, *initial crack length* = *0.60 in.*).

strongly evident in Fig. 6, fade in importance on typical crack growth rate plots which cover many orders of magnitude of rate. For finite width specimens under constant load amplitude, the value of K_I will vary as the crack extends. Figure 7 indicates the predicted crack length as a function of the number of cycles for the 3-in.-wide specimen with 0.60-in. notches used in this study, with a ligament width of 0.01 in. as experimentally observed.

Experimental Results and Discussion

Experimental Results

The purpose of the experimental program, in addition to describing the proposed mode of crack propagation, was to measure the rate of fatigue

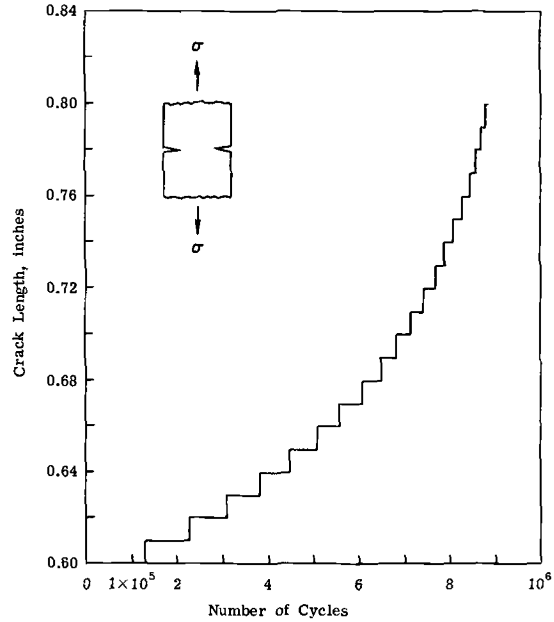

FIG. 7—*Predicted crack growth for 3-in.-wide specimen with initial crack length of 0.60 in.* (σ_{max} = *7.57 ksi,* d = *0.01 in.*).

crack growth and to establish the necessary material properties for prediction of the rate of growth by the proposed theory. As a preliminary step, it was also necessary to establish the constancy of K_Q for a range of specimen sizes and crack lengths.

The validity of classical fracture mechanics for this class of composite materials has been discussed elsewhere [*3,4*]. Additional evidence for the particular ply configuration under consideration is given in Fig. 8, where the fracture toughness, K_Q, calculated from Eq 3 using the K calibration for isotropic materials [*9*], is plotted against crack length to specimen width ratio for several specimen sizes. The data confirm an approximately constant value of K_Q for all specimen sizes and crack lengths tested, indicating that K_Q is a valid material property. The use of K_Q in predicting the rate of fatigue crack growth also requires that the tests be conducted at the rate of deflection experienced in the fatigue test. The frequency of 5 Hz used for the fatigue tests translates to a deflection rate of approximately 20 in./min for the monotonic fracture test. As Table 1 indicates, K_Q at this rate is significantly higher than that for the 0.05-in./min tests represented in Fig. 8, an increase from 16.3 to 24.0 ksi $\sqrt{\text{in.}}$ for the notched specimen configuration shown in Fig. 2.

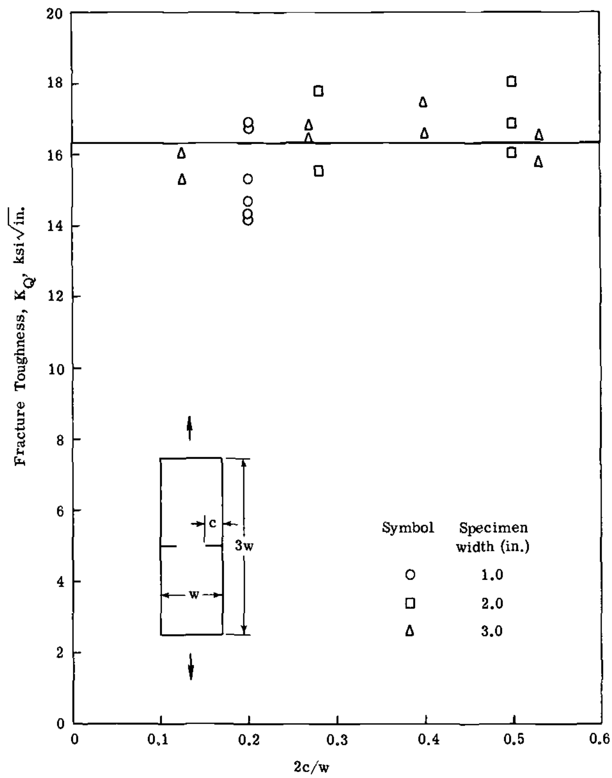

FIG. 8—*Fracture toughness for various specimen sizes and crack lengths, 90°/0°/90°/0°/90° scotchply, deflection rate = 0.05 in./min.*

Figure 9 gives the fatigue life data for the unnotched specimen shown in Fig. 2. The data are approximated by a line having a slope of 6.16 ksi per decade of cycles, and monotonic strength of 60.7 ksi, as determined by a least-squares curve fit. These data, along with the data previously described for K_Q and the observed ligament size at the crack tip, are sufficient to allow prediction of initial crack growth from the notch and the

TABLE 1—*Mechanical properties assumed in fatigue crack growth theory.*

Fracture toughness, $K_Q = 24.0$ ksi $\sqrt{\text{in.}}$
Ultimate strength, $\sigma_f = 60.7$ ksi
Slope of S-N curve, $S = 6.16$ ksi/decade
Ligament width, $d = 0.01$ in.

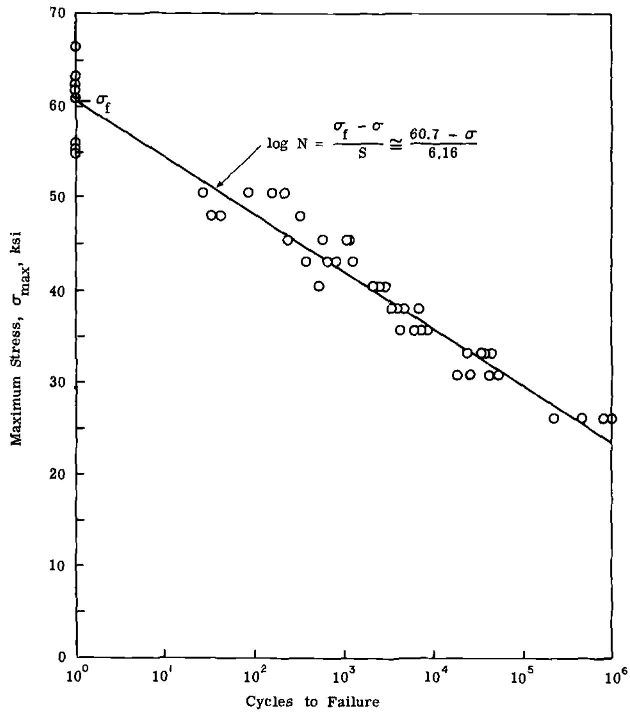

FIG. 9—*Fatigue life* (S-N) *curve for unnotched E-glass/epoxy, ply configuration* (*90°/0°/90°/0°/90°*).

rate of crack growth by the theory presented in the previous section. Table 1 summarizes these properties.

Figure 10 gives the number of cycles to produce first crack extension from the precut notch as a function of the stress intensity factor. The data show good agreement with the theoretical prediction of Eq 5 over the complete range.

The rate of fatigue crack growth was measured for the first 0.05 in. of crack extension by observing the location of the terminal subcritical split at the crack tip in the 0° ply at low magnification. Data were taken only when the length of both cracks in the specimen were within 0.02 in. of each other and the crack length was measured for the 0° ply with the largest crack for the uncommon cases where the two 0° plies showed unequal crack growth.

Figure 11 indicates good agreement between the experimental data and theoretical predictions based on Eqs 10 and 13 and an average of the

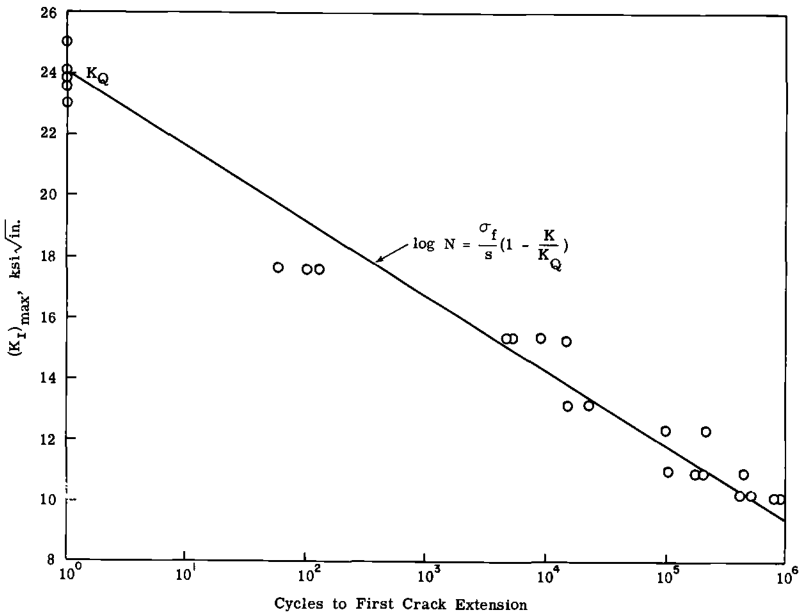

FIG. 10—*Theoretical versus experimental number of cycles for first crack growth from notch.*

predicted growth rate for the first five ligaments over several decades of crack growth rate. Even the simple relationship of Eq 10 which ignores cumulative damage effects accurately predicts both the trend of dc/dN versus K_I and the absolute value of the data.

Discussion

The geometry of the test specimen used to measure the crack growth rate is not convenient, as the crack rapidly becomes unstable after a relatively short length in which growth rates can be measured. The specimen is well suited to thin laminates, however, and provides two propagating cracks for growth measurements. It is thought that the measurement of only small amounts of crack extension from the precut notch does not severely restrict the data because the stress field, very local to the crack tip, dominates the crack growth characteristics, so that the failure of each ligament is almost independent of the stress history before the crack tip reaches the ligament. Thus, the predicted growth rate for the first few ligaments of growth in Fig. 6 is almost identical to that for subsequent ligaments which have a longer stress history. For ligaments

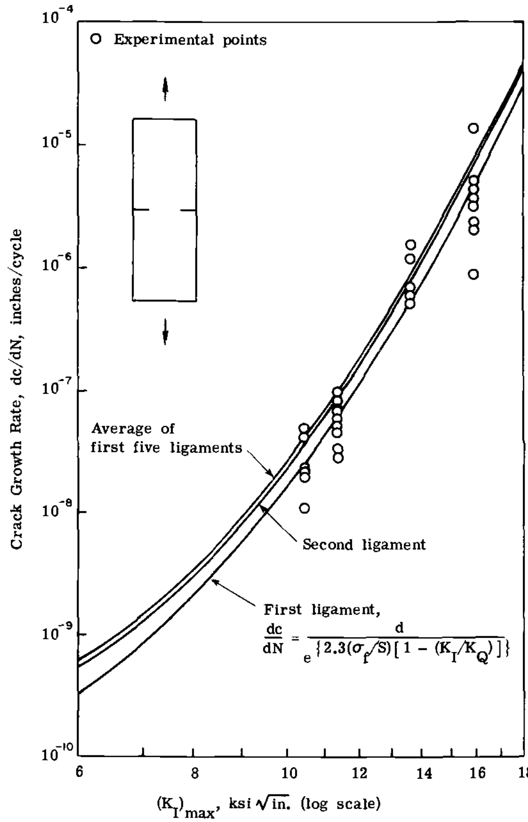

FIG. 11—*Theoretical versus experimental fatigue crack growth rate, E-glass/epoxy ply configuration (90°/0°/90°/0°/90°), tension-tension fatigue.*

0.01 in. wide or greater, a sufficiently accurate prediction of crack growth rate can be obtained without consideration of the cumulative damage law or the stress distribution away from the immediate crack tip. Recent unpublished results using thicker specimens confirm this approach for more standard cleavage type specimens where crack growth can be observed over greater length.

The exponential relationship between K and dc/dN results in a rapid variation in crack growth rate with increasing load equivalent to a high exponent if the relationship were linear on a logarithm-logarithm plot as is commonly the case in metals. A linear approximation to the data in Fig. 11 gives approximately

$$\frac{dc}{dN} \alpha(K_I)^{11} \tag{14}$$

which is a considerably higher exponent than is commonly observed for metals [*1*]. This exponent is not necessarily typical of composites in general, as an exponent of approximately 5.0 has been reported for chopped E-glass mat/polyester laminates [*10*].

Although the data given in Fig. 8 are consistent with the assumptions of linear elastic fracture mechanics, they prove no more than an inverse relationship between applied stress at fracture and the square root of the notch depth. The data are equally consistent with a stress concentration factor approach which may be more appropriate in view of the apparent bluntness of a natural crack, particularly a fatigue crack, in these materials. As noted previously, the local stresses assumed in the theoretical treatment would also apply to a stress concentration factor approach without significant alteration; and, the initial crack extension and crack growth rate predictions would remain essentially unchanged.

The application of the theory presented in this paper to other composite materials should depend on whether the local mode of crack propagation is similar. The mode of crack propagation for monotonic fracture tests is known to be of this type for woven fabric and unwoven 0°/90° crossplied laminates of other ply stacking arrangements [*3*]. Recent work indicates a similar mode for some angle-ply composites, although Mode II and interlaminar mode failures may also occur in angle-ply composites in monotonic [*4*] and fatigue loading [*11*]. The approach taken here could not be expected to apply to such cases. Laminates which show a tendency to form longer splits in the 0° plies [*3*] may also shift to notch-insensitive behavior if the splits extend sufficiently in fatigue.

The work at this stage is clearly restricted to uniaxial tension-tension fatigue. The uniaxial *S-N* curve has been used as a basic material property to predict behavior under multiaxial stress conditions at the crack tip, and this approach needs further investigation. The applicability of the theory to tension-compression fatigue or other load conditions is not clear at this time.

Conclusions

Fatigue crack propagation appears to occur by the successive failure of ligaments at the crack tip. The rate of crack growth can be predicted by a model based on the assumption that the ligaments follow the *S-N* curve of the unnotched material. The predicted growth rate is sensitive to the assumed stress at the crack tip, but relatively insensitive to the assumed distribution of stress ahead of the crack tip or to the cumulative damage law used.

Acknowledgments

This work was sponsored by the Advanced Research Projects Agency through the Center for Materials Science and Engineering and the Dow Chemical Company. Mr. Meier was supported by the Swiss Federal Laboratories for Testing Materials and Research while at Massachusetts Institute of Technology.

References

[1] Tetelman, A. S. and McEvily, A. J., Jr., *Fracture of Structural Materials*, Wiley, 1967.
[2] McGarry, F. J. and Mandell, J. F., "Fracture Toughness of Fibrous Glass Reinforced Plastic Composites," *Proceedings*, Society of the Plastics Institute, Section 9-A, 1972.
[3] McGarry, F. J. and Mandell, J. F., "Fracture Toughness Studies of Fiber Reinforced Plastic Laminates," *Proceedings*, Special Discussion of Solid-Solid Interfaces, Faraday Division, The Chemical Society, Nottingham, England, 1972.
[4] Mandell, J. F., Wang, S. S., and McGarry, F. J., "Fracture of Graphite Fiber Reinforced Composites," Technical Report AFML-TR-73-142, Air Force Materials Laboratory, Dayton, Ohio, 1973.
[5] Sih, G. C. and Liebowitz, H., *Fracture*, Vol. 2, H. Liebowitz, Ed., Academic Press, 1968.
[6] Irwin, G. R., *Transactions*, American Society of Mechanical Engineers, *Journal of Applied Mechanics*, 1957, p. 361.
[7] Miner, M. A., *Journal of Applied Mechanics*, American Society of Mechanical Engineers, 1945, p. A159.
[8] Broutman, L. J. and Sahu, S., "A New Theory to Predict Cumulative Fatigue Damage in Fiberglass Reinforced Plastics," 24th Annual Technical Conference, Reinforced Plastics/Composites Division, Society of the Plastics Institute, Paper 11D, 1969.
[9] Bowie D. L., "Rectangular Tensile Sheet with Symmetric Edge Cracks," American Society of Mechanical Engineers, Paper 64-APM-3, 1964.
[10] Owen, M. J. and Rose, R. G., *Plastics and Polymers*, 1972, p. 325.
[11] Hachler, A., M.S. thesis, Eidgenossische Technische Hochschule, Zurich, Switzerland, 1972.

J. V. Gauchel,[1] I. Steg,[1] and J. E. Cowling[1]

Reducing the Effect of Water on the Fatigue Properties of S-Glass Epoxy Composites

REFERENCE: Gauchel, J. V., Steg, I., and Cowling, J. E., **"Reducing the Effect of Water on the Fatigue Properties of S-Glass Epoxy Composites,"** *Fatigue of Composite Materials, ASTM STP 569,* American Society for Testing and Materials, 1975, pp. 45–52.

ABSTRACT: An epoxy resin composed of N,N-diglycidyl tribromoaniline (DGTBA) crosslinked with metaphenyline diamine (MPDA) has proven to be far superior to standard epoxy systems in reducing the effect of long-term water immersion on the fatigue life of epoxy-S glass composites. The results of experiments indicate up to a 20 to 30 percent improvement in fatigue life retention for the DGTBA/MPDA-S glass system over conventional bisphenol-A based epoxy-S glass systems. Copolymers of DGTBA and diglycidyl ether of bisphenol-A (DGEBA) containing over 50 percent DGTBA have essentially the same fatigue properties as those with pure DGTBA matrices. Copolymer results are explained in terms of a simple relationship between matrix water absorption and composite fatigue life.

KEY WORDS: composite materials, fatigue (materials), mechanical properties, epoxy resins, environmental tests

With the advent of naval crafts such as the patrol craft hydrofoil and the surface effect ship, there has been an increased interest in the development of light-weight materials that have long-term reliability under a combination of high-level dynamic stress and a marine environment. Since organic matrix composites have been frequently mentioned as candidates for use in these high-performance vessels, the underwater fatigue characteristics of these materials are critical in determining their acceptability as structural components.

[1] Chemical engineer; visiting scientist; and head, Organic Coatings Section; respectively, Chemistry Division, Naval Research Laboratory, Washington, D. C. 20375. Dr. Steg is from the Israel Department of Defense.

The full potential of organic matrix composites as engineering materials is not being realized because designers and users lack confidence in their reliability. The recent recognition of fiber-reinforced plastics as a new and valuable class of structural materials is not yet supported by a broad base of engineering design data such as has been accumulated on wood, steel, etc. over a period of many years. For the most part, the data which do exist have been derived from short-term laboratory tests and shed more light on the qualitative response of composite materials to stress and environment than on a quantitative indication of their long-term serviceability.

The underwater fatigue life of an organic matrix composite is strongly influenced by the hydrolytic stability of its three components: the fiber, the fiber-matrix interface, and the matrix. In S-glass fiber composites, the innate sensitivity of the fiber to water degradation has been shown previously by Kies [*1*],[2] Irwin [*2*], and Dietz [*3*], while Zisman [*4*], Bascom [*5*], Schmitz and Metcalf [*6*], and Schmitz et al [*7*] have firmly established the vulnerability of the glass fiber-matrix bond. Romans et al [*8*] have shed much light on the significance of matrix composition in determining the fatigue characteristics of S-glass reinforced epoxy plastics. It was shown that epoxy resins suffer accelerated degradation by water when they are subjected to high static stresses, and dynamic stresses in combination with water usually are 10 to 100 times as damaging as static stresses. The susceptibility of different epoxies to hydrolytic attack was shown to vary widely depending upon molecular composition. When the entry of water into epoxy resins was held to a very low value, the performance of the structural composites resulting from the use of these resins was vastly improved.

The objective of this study was to expand Romans' work to include the effect of long-term static exposure on the fatigue life of the epoxy S-glass system, and to establish a quantitative relationship between matrix water absorption and underwater fatigue life.

Materials

The five epoxy resin systems examined in this study are described in Table 1. Systems 1 to 4 represent state-of-the-art epoxies currently in use in Navy programs. System 5 consists of an experimental brominated epoxy resin that has been shown to have high fatigue life and low water absorption [*8*]. The fiberglass used throughout has been the Ferro Corporation's Type S 1014 with S-24 "non-aging" finish.

[2] The italic numbers in brackets refer to the list of references appended to this paper.

TABLE 1—*Epoxy resin systems studied for underwater fatigue life characteristics.*

System	Mixture [a]	Chemical Designation	Source
1. Epon 826	100	diglycidyl ether of bisphenol-A (DGEBA)	Shell Chemical Co.
NMA	85	nadic methyl anhydride	Allied Chemical Co.
BDMA	1	benzyldimethylamine	Eastman Organic Division of Eastman Kodak Co.
2. Epon 826	100	diglycidyl ether of bisphenol-A (DGEBA)	Shell Chemical Co.
MPDA	14.5	meta-phenylenediamine	Miller-Stephenson Chemical Co., Inc.
3. ERL 2256	100	diglycidyl ether of bisphenol-A (62.5%) 2,3-epoxycyclopentyl ether (37.5%)	Union Carbide Co.
Bakelite ZZL-0820	27	eutectic blend of aromatic amines	
4. ERL 2256	100	diglycidyl ether of bisphenol-A (62.5%) 2,3-epoxycyclopentyl ether (37.5%)	Union Carbide Co.
Bakelite ZZL-0820	27	eutectic blend of aromatic amines	
Aroclor 1254	10	chlorinated biphenyl	Monsanto Co.
5. ERX-67	10	N,N-diglycidyl tribromoaniline (DGTBA)	Shell Chemical Co.
MPDA	1	meta-phenylenediamine	Miller-Stephenson Chemical Co., Inc.

[a] Parts by weight.

Test Procedure

Specimens

Glass filament-wound Naval Ordnance Laboratory (NOL) rings fabricated according to ASTM Recommended Practice for Fabrication of Ring Test Specimens for Reinforced Plastics (D 2291-67) were used throughout this investigation. Curing was in accordance with manufacturers recommended procedures for each resin.

Test Method

Fatigue studies were performed by diametrically compressing each Naval Ordnance Laboratory (NOL) ring to a standard deflection (2.53

in.) over a 24-s period, holding the deflection constant for 1 min; returning to zero deflection over a 3-s interval, holding at zero for 3 s; and, then repeating this cycle. The test was conducted in water and was concluded when the load required to compress the ring to the standard deflection decreased 20 percent from the initial load required. Distilled water was used throughout the test because it has been shown to be at least as severe as salt water in degrading polymer composites [*9,10,11*].

Water Absorption

Disks, 2.54 cm in diameter and 0.32 cm thick, were cast for each resin composition. These disks were soaked in distilled water and weighed at various time intervals to determine the rate of water absorption. The water absorption of sample NOL rings was also monitored in a similar fashion. A more detailed description of the test procedure is given by Romans et al [*8*].

Results

In order for a composite system to be useful for naval applications, it must be able to endure long-term exposure to a marine environment with little or no degradation of its physical properties. The results of Romans et al [*8*] (Table 2) have shown, for short-term experiments, that the underwater fatigue life of S-glass composites with a matrix of N,N-diglycidyl tribromoaniline (DGTBA) crosslinked with metaphenylene diamine (MPDA) is far superior to that of any other epoxy resin tested. In the current experiment, NOL rings of the five systems reported by Romans were immersed in distilled water at room temperature for 400 days prior to fatigue testing. The results of this second experiment are shown in Table 3. Again, composites with DGTBA-MPDA matrices prove far superior in residual fatigue life. The results are also in agreement with previously reported data [*12*] on the interlaminar shear stability for these systems. Because the DGTBA-MPDA system showed so well in the

TABLE 2—*Underwater fatigue life of various epoxy resin S-glass composites* [*8*].

System	Underwater Fatigue Life, cycles to failure
1. ERX-67/MPDA	15 000
2. Epon 826/NMA/BDMA	5 600
3. ERL 2256/ZZL-0820/Aroclor 1254	8 200
4. ERL 2256/ZZL-0820	6 200
5. Epon 826/MPDA	4 000

TABLE 3—*Percent retention*[a] *of unsoaked underwater fatigue life for epoxy resin S-glass composite soaked 400 days in room temperature water.*

System	Retention, %
1. ERX-67/MPDA	100
2. Epon 826/NMA/BDMA	91
3. ERL 2256/ZZL-0820/Aroclor 1254	62.5
4. ERL 2256/ZZL-0820	56.25
5. Epon 826/MPDA	37.2

[a] Percent retention $= \dfrac{\text{fatigue life after soak}}{\text{fatigue life with no soak}} \times 100.$

previous experiments, further studies on the system were indicated. These studies included copolymerizing DGTBA with diglycidyl ether of bisphenol-A (DGEBA). The resulting copolymers all had increased fatigue life over the standard DGEBA system. In fact, copolymers with over 50 percent DGTBA had essentially the same short-term fatigue properties as the pure DGTBA system (Table 4).

Romans had qualitatively related his results to the very low water absorption of the DGTBA-MPDA matrices but, because of variance in such parameters as void content and matrix content, no quantitative correlation between absolute fatigue life and resin water absorption was made. In the current copolymer experiments all physical and structural parameters were essentially constant. Void content, resin content, and the epoxy-epoxy distance of the resins were similar. By using the results of Table 4 and the initial water absorption of the various resin systems,

TABLE 4—*Underwater fatigue life of S-glass composites with matrices of copolymers of DGTBA and DGEBA.*

System	DGTBA in Matrix, %	Relative Underwater Fatigue Life[a]
1	0	0.33
2	33.3	0.62
3	50	0.94
4	67.7	1.0
5	75	1.0
6	100	1.0

[a] Relative fatigue life $= \dfrac{\text{fatigue life of modified DGTBA}}{\text{fatigue life of pure DGTBA}}.$

it was found that the underwater fatigue life of these systems could be predicted accurately by using

$$Y_{cp} = Y_E \frac{a_E}{a_{c_d}} \tag{1}$$

where

Y_{cp} = fatigue life of the copolymer matrix composition,
Y_E = fatigue life of the DGTBA,
a_{c_d} = initial water absorption of the copolymer, and
a_E = initial water absorption of the DGTBA

as shown in Table 5.

TABLE 5—*Comparison of predicted and experimental relative fatigue lives for S-glass composites with DGTBA/DGEBA copolymer matrices.*

System	Predicted Relative Fatigue Life	Experimental Relative Fatigue Life
1	0.31	0.33
2	0.55	0.62
3	0.92	0.94
4	0.99	1.0
5	0.99	1.0
6	1.0	1.0

Equation 1 implies that the ratio of the fatigue lives of two series of NOL rings fabricated with the same volume-fraction glass and volume-fraction voids but with different resin matrices will be inversely proportional to the ratio of the initial water absorptions of the matrix materials. Thus, one could predict the expected fatigue life in the NOL ring underwater fatigue test of an experimental resin from its short-term water absorption. This is an extremely useful tool to the polymer chemist for quickly evaluating the potential of new resin systems for naval applications.

Discussion

The relationship between matrix water absorption and fatigue life depicted previously was based on the observed mode of failure of the NOL rings in the underwater fatigue test. As the test progressed, the glass fibers at the points of maximum stress began failing in layers forming a "broom." This failure continued until the total load bearing area was decreased to such extent that overall ring failure occurred.

From the foregoing observation one can postulate a plausible description of the failure process. Initially, water is absorbed at the outer surface of the ring. This water diffuses through the resin (and through any available voids) to the fiber-matrix interface. At the interface, the water degrades the fiber-matrix interfacial bonds and is absorbed on the fiber. The combined action of dynamic loading and the presence of water degrades the glass to a point where it no longer can support the applied stress and fails. If one considers a NOL ring to be a series of concentric lamina, this failure would open the outermost layer and expose the next layer directly to the water. The failure process would then repeat itself until total failure of the ring structure occurred. Equation 1 postulates that the initial absorption and diffusion steps in the above mechanism are rate controlling and, therefore, that the relative fatigue life of the various resins will depend on their relative water uptake. Because of the dominance of the fibers in determining the strength characteristics of the NOL ring composites, the effect of matrix plasticization is of minor importance. The relative water absorption of all resins used in this study is small, which also contributes to the minimization of the plasticization mechanism. The time frame of the NOL underwater fatigue test and the proposed stepwise failure mechanism explain why the initial matrix water absorption is used instead of the long-term values. In cases where long static soak is applied prior to dynamic oscillation, Eq 1 would probably not be valid without modification.

Summary

The reliability of an organic-matrix composite for use in a marine environment is dependent on the matrix ability to withstand a combination of long-term exposure to water and dynamic stress. It has been shown that slowing the migration rate of water into the composite by using matrix resins of low water absorption increases the fatigue life of composite materials. In certain situations, this increase in fatigue life is quantitatively related to the initial water absorption of the resin. This relationship is useful in estimating relative fatigue resistance of experimental epoxy resin composites from limited quantities of the matrix material.

References

[1] Kies, J. A., "The Strength of Glass Fibers and the Failure of Filament Wound Pressure Vessels," Report 6034, Naval Research Laboratory, Feb. 1964.

[2] Irwin, G. R., "Moisture Assisted Slow Crack Extension in Glass Plates," Memorandum Report 1678, Naval Research Laboratory, Jan. 1966.

[3] Dietz, Victor R., "Interaction of Water Vapor With Pristine E-Glass Fiber," Report 6812, Naval Research Laboratory, Dec. 1968.
[4] Zisman, W. A., *Industrial and Engineering Chemistry Product Research and Development*, Vol. 8, 1969, p. 98.
[5] Bascom, W. D., *Journal of Adhesives*, Vol. 2, 1970, p. 161.
[6] Schmitz, C. K. and Metcalfe, A. G., *Industrial and Engineering Chemistry Product Research and Development*, Vol. 5, 1966, p. 1.
[7] Schmitz, G. K., Gulden, M. E., and Metcalfe, A. G., "A Study of Stress Corrosion of Glass Fibers; Part II – Effect of Glass Composition," Final Report, Naval Air Systems Command Contract N00019-69-C-0145, Feb. 1970.
[8] Romans, J. B., Sands, A. G. and Cowling, J. E., *Industrial and Engineering Chemistry Product Research and Development*, Vol. 11, 1972, p. 3.
[9] Battelle Memorial Institute, "Mechanism of Water Absorption in Glass-Reinforced Plastics," Contract NObs-86871, Navy Bureau of Ships 98-1008-10, 1962–63.
[10] Glowacki, A. S. and MacDonald, D. C., "Protective Coatings for Filament-Wound Deep Submergence Vessels," Final Report, Navy Bureau of Ships Contract NObs-90246, March 1965.
[11] Herrick, J. W., "The Permeability of Plastic Films Exposed to Pressurized Fresh and Salt Water," Technical Memorandum RAD-TM-64-8, AVCO Corp., Feb. 1964.
[12] Gauchel, J. V., Griffith, J. R., Steg, I., and Cowling, J. E., American Chemical Society Polymer Preprint, Vol. 14, Aug. 1973, p. 1148.

E. B. Kula,[1] *A. A. Anctil,*[1] *and H. H. Johnson*[2]

Fatigue Crack Growth in Dual Hardness Steel Armor

REFERENCE: Kula, E. B., Anctil, A. A., and Johnson, H. H., "**Fatigue Crack Growth in Dual Hardness Steel Armor,**" *Fatigue of Composite Materials, ASTM STP 569,* American Society for Testing and Materials, 1975, pp. 53–70.

ABSTRACT: Crack growth tests under cyclic loading conditions were conducted on samples from different lots of dual hardness steel (DHS) armor. The results showed that the growth rate increased with stress level, and the cracks grew at a different rate in the frontal and backup layers of the armor. This difference in growth rate became progressively greater with increases in the stress level. The crack growth rate also increased with reductions in the frequency of loading and temperature increases over the range of −60 to +200°F.

Attempts are made to explain the crack growth behavior of the composite in terms of the behavior of each component. The growth rates in the composite are related to the stress intensity factor, ΔK, calculated from the surface crack length assuming that there was no interaction between the layers and the displacement in each layer was the same on the crack line. The latter procedure yielded better results and suggested that the interface plays an important role in retarding crack growth in the frontal layer of DHS.

KEY WORDS: composite materials, fatigue (materials), crack propagation, steels, armor, laminates

Dual hardness steel (DHS) is a roll-bonded composite that has particularly attractive properties as an armor material [*1*].[3] Produced from steel plates of two different chemical compositions, the front layer with the higher carbon content is heat-treated to a hardness of about HRC 60; the backup layer, with a lower carbon content, has a hardness value of about HRC 50. A further advantage of DHS is that it has structural properties adequate for certain applications. In helicopters, the use of

[1] Chief and mechanical engineer, respectively, Metals Research Division, Army Materials and Mechanics Research Center, Watertown, Mass. 02172.

[2] Professor, Department of Materials Science and Engineering, Cornell University, Ithaca, N. Y. 14850.

[3] The italic numbers in brackets refer to the list of references appended to this paper.

DHS armor in a structural capacity may provide a lighter weight structure than conventional construction utilizing ceramic composite armor in a parasitic fashion.

Several reports have been published on the structural properties and fabricability of DHS [*2–5*]. This paper is restricted to the specific problem of the behavior of through cracks in DHS under fatigue-type loading conditions. These are cracks that might appear near welds or at stress concentrations such as bolt holes as a result of manufacturing defects or projectile damage during ballistic impact.

A fracture mechanics approach can be taken to fatigue crack growth. It is assumed that the crack growth rate per cycle, $d2a/dn$, is controlled by the stress intensity factor range, ΔK, at the crack tip, where ΔK is determined by the gross stress range, σ; the crack length, $2a$; and the geometry of the system. An empirical relationship between the crack growth rate and ΔK was proposed by Paris [*6*]

$$\frac{d2a}{dn} = C(\Delta K)^m \tag{1}$$

where C and m are constants. This equation has been found to adequately describe crack growth for many metals. A preexisting crack or flaw would grow under cyclic loading conditions until it reached a certain length; then, the entire specimen would fail by tensile overload under fast fracture conditions.

Although this equation is satisfactory for monolithic materials, it is not clear how it applies to a layered composite such as DHS where the behavior of the composite depends complexly on the size and properties of each component as well as the integrity of the interfacial bond.

Crack growth behavior of several lots of DHS is described in terms of several variables including stress level, test temperature, and frequency; and, attempts are made to analyze the crack growth behavior in terms of the properties of the two elements of which the composite is comprised.

Materials and Procedure

Evaluations of three separate lots of DHS were made, one of which was produced by ausforming and the other two by roll bonding followed by heat treating. One of the latter was air melted (AM), while the other was a vacuum-induction melt (VIM). Nominal compositions and processing histories are listed in Table 1. In all materials investigated, frontal and backup elements were approximately the same in thickness.

The front and rear surfaces of each plate were measured for HRC hardnesses. Tensile properties for the ausformed and air-melted steels

TABLE 1—*Summary of DHS.*

	Ausformed Steel	Heat-Treatable Steel AM	Heat-Treatable Steel VIM
Composition			
Frontal	0.41C-5Cr-1.3Mo -0.4V	0.57C-1Ni-0.8Cr -0.5Mo	0.54C-1Ni-0.75Cr -0.5Mo
Backup	0.31C-7.5Ni-1Cr-1Mo-4.3Co	0.31C-1Ni-0.8Cr -0.5Mo	0.31C-1Ni-0.75Cr -0.5Mo
Processing	roll bond at 1900°F quench to 1500°F, roll 54% quench temper at 400°F	roll bond at 2275°F oil quench from 1500°F double temper at 250°F	roll bond at 2100°F oil quench from 1500°F temper at 275°F
Plate thickness	0.20 in.	0.20 in.	0.22 in.

were supplied by the producer on the specimens of the backup, and frontal material processed separately. For the two heat-treatable steels, tension tests were conducted on specimens machined from the composite armor. Standard gage length (½ by 2 in.) flat tension specimens were used.

The target hardness was HRC 60 for the frontal material. For the backup material, a target hardness of HRC 50 was suggested. The AM steel came close to these values, while the hardness of the others was slightly low. The tensile strengths, 350 to 360 ksi for the frontal material, are extremely high for a structural material but consistent with the high hardness. The hardness and tensile properties for the various lots of DHS are listed in Table 2.

TABLE 2—*Typical mechanical properties of DHS.*

DHS Armor		0.1% Yield Strength, ksi	0.2% Yield Strength, ksi	Ultimate Tensile Strength, ksi	Elongation, %	Reduction of Area, %	HRC
Ausformed	frontal	233	258	349	7	...	57
	backup	200	220	289	9	...	50
AM	frontal	...	219	361	6	15	61
	backup	...	183	262	9	45	51
	composite	...	185	319	9	12	...
VIM	composite	155	184	285	5	7	58 [a] 48 [b]

[a] Frontal hardness.
[b] Backup hardness.
Properties of ausformed and air-melted steels supplied by producers.

Fatigue crack propagation data were generally obtained from center-notched specimens 3.0 in. wide and 12.0 in. long. Approximately 0.020 in. was ground off each surface. The 0.5 or 1.0-in. center notch was electric-discharge machined perpendicular to the plate rolling direction. The specimens were subjected to sinusoidal loading with a constant mean load at 4 or 15 Hz by an axial-fatigue, hydraulic, closed-loop testing machine. The specimens are identified by the applied maximum gross section stress. The minimum gross section stress was either 3.0 or 5.0 ksi. Crack growth was measured simultaneously on the frontal and backup material from the specimen center line to one edge. Measurements were made using a traveling microscope with ×30 magnification and stroboscopic illumination. The crack growth curves included the number of cycles necessary to initiate the fatigue crack from the 0.002-in. machined-notch radius. Testing temperatures below room temperature were obtained by varying the flow of gas from a liquid nitrogen reservoir through a plexiglas cell. The variation in temperature was ±3°F.

For measurement of the crack growth behavior of the separate frontal and backup components of the AM steel, center notched specimens were used; but, the total crack length was determined with an electric potential technique [*7*]. In the case of the ausformed steel, single edge notch, compact tension type specimens, 2.5 by 3.2 in., of each component were prepared by grinding the DHS from either face. On these specimens, crack lengths were measured visually.

In several cases fractographic examination was carried out on the fatigue cracked surfaces using light and electron fractography. Two-stage plastic-carbon replicas shadowed with chromium were used for the electron fractography.

Results

Monolithic Components

Fatigue crack growth curves, crack length as a function of the number of cycles, are shown in Fig. 1 for the frontal and backup components of the AM steel. The tests were conducted at a gross stress range, $\Delta\sigma_g$, of 15 ksi and stress ratio, R, of 0.25. The general behavior of an accelerating rate of crack growth with crack length is clearly visible.

The frontal material fails at about 18 000 cycles, after the crack has grown to a length of 1.8 in. The final separation took place by rapid, tensile failure. The backup material failed in about 220 000 cycles, and the crack grew almost across the whole width of the 3-in.-wide specimen by fatigue. This is indicative of the superior toughness and crack growth resistance of the lower hardness backup steel.

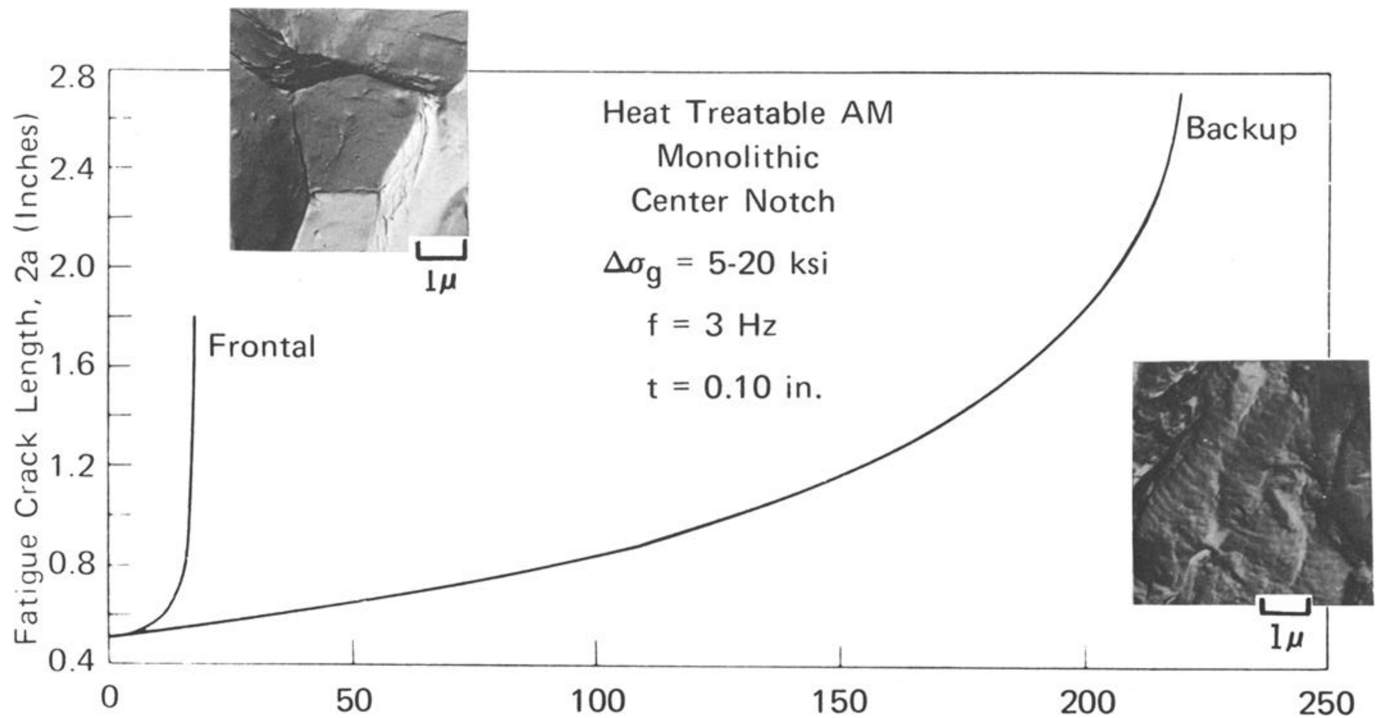

FIG. 1—*Fatigue crack length as a function of the number of load cycles for monolithic components of AM DHS tested at* $\Delta\sigma_g = 15$ *ksi,* R = *0.25. Fractographs show intergranular fracture and fatigue striations in frontal and backup steel, respectively.*

Electron fractographs typical of the fatigue portion of the test are included in Fig. 1. In the frontal steel, the fatigue fracture is predominantly intergranular, and no striations usually associated with fatigue are found. In the backup steel, typical well-defined striations are visible. The fast fracture region of both specimens (not illustrated) showed dimpled rupture, typical of tensile overload failure.

Crack growth tests were also conducted on the two components of the ausformed DHS. In this case, single-edge notch, compact tension specimens, produced by grinding the DHS plate were used. The crack growth curves for a stress range of 1.3 ksi from 0.4 to 1.7 ksi are plotted in Fig. 2. This is approximately the same range in ΔK as was used for the center notch specimens. While these curves cannot be compared to those for the AM steel shown in Fig. 1 because of the difference in the type of specimen, they do show that the frontal material has a higher crack growth rate and a shorter crack length at fracture than the backup material. The differences between the two components, however, appear to be less than in the case of the components of the AM steel in Fig. 1.

Dual Hardness Steel Composites

A typical fatigue crack growth curve for the AM DHS is shown in Fig. 3, tested at the same stress range used for the separate components shown in Fig. 1. Figure 3 shows that the crack grows at a faster rate in the frontal than in the backup steel. The crack grows completely across the front by fatigue in about 29 000 cycles, followed by tensile overload failure of the backup about 1000 cycles later. This should be contrasted with the behavior shown in Fig. 1 where the frontal steel, alone, fails by tensile overload failure after 18 000 cycles.

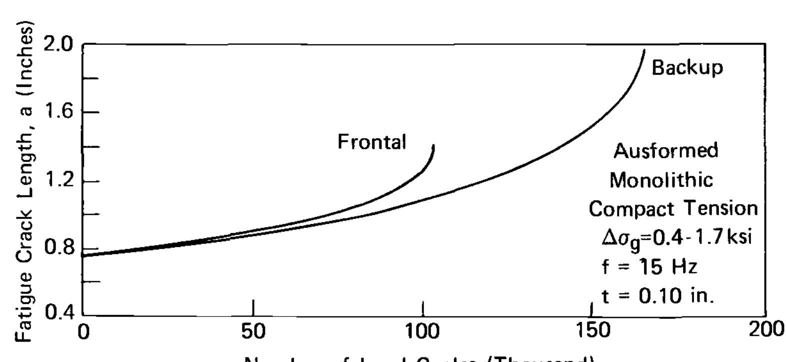

FIG. 2—*Fatigue crack length as a function of the number of load cycles for monolithic components of ausformed DHS tested at $\Delta\sigma_g = 1.3$ ksi, R = 0.235.*

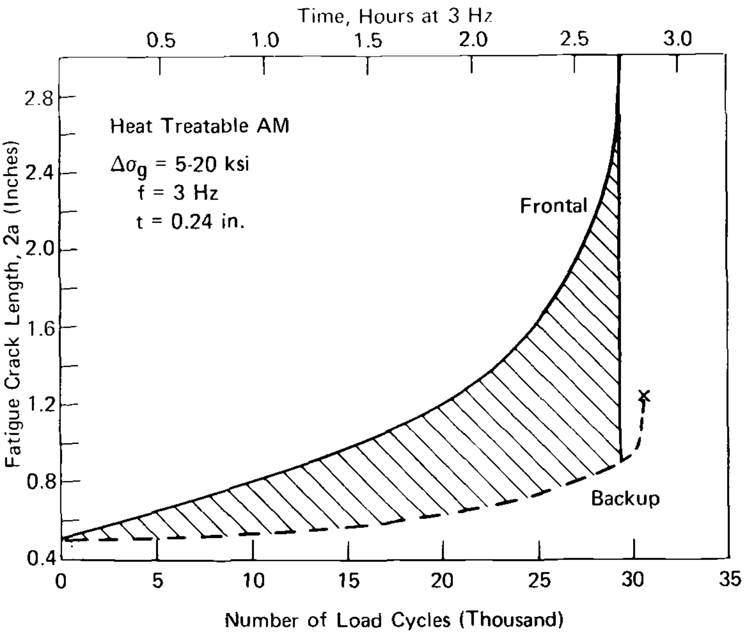

FIG. 3—*Fatigue crack length as a function of the number of load cycles for AM DHS tested at* $\Delta\sigma_g = 15$ *ksi,* R = *0.25.*

Fatigue crack growth data at several different maximum stresses are presented in Fig. 4 for the ausformed steel. The cracks grow at an increasing rate as the number of cycles increases. In general, the cracks grow at a faster rate in the hard, frontal material, and lag behind in the softer, backup material. On these 3-in.-wide specimens, in typical circumstances, the cracks in the hard face will grow by fatigue completely across the width of the specimen, followed by fast fracture of the remaining backup material.

As the gross stress level is increased, the number of cycles to failure decreases in customary fashion. Of particular interest in these DHS specimens is the observation that the lag in crack growth in the backup material increases as the maximum gross stress increases, for example, at the onset of fast fracture in the backup the fatigue crack length is smaller the higher the stress. This is in general agreement with the observation that the crack growth rate is faster in the frontal material than in the backup.

The frequency of loading can have an important effect on crack propagation. Crack growth curves for the AM steel at three different stress

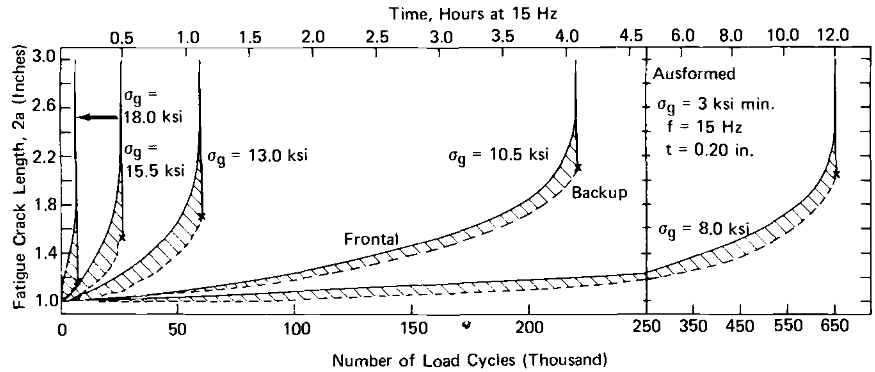

FIG. 4—*Fatigue crack length as a function of the number of load cycles and maximum stress for ausformed DHS tested over range* $\Delta\sigma_g = 5$ *ksi*, R = *0.375 to* $\Delta\sigma_g = 15$ *ksi*, R = *0.167.*

levels and frequencies, 4 and 15 Hz, are shown in Fig. 5. These frequencies are typical of those that would be encountered by DHS in a helicopter, where the frequency of loading is determined by the product of the number of rotor blades and the revolutions per minute of the rotor. It can be seen that at the lowest maximum stress used, 8 ksi, there is little difference between the two frequencies; but at gross maximum stress levels of 10.5 and 13 ksi, the crack growth rates and the fatigue lives are markedly affected, with the lower frequency giving rise to the poorer properties.

Frequency effects can be caused by inherent effects of strain rate on the materials' properties or by adiabatic heating. Neither of these factors are considered to be significant here. It is well known that the environ-

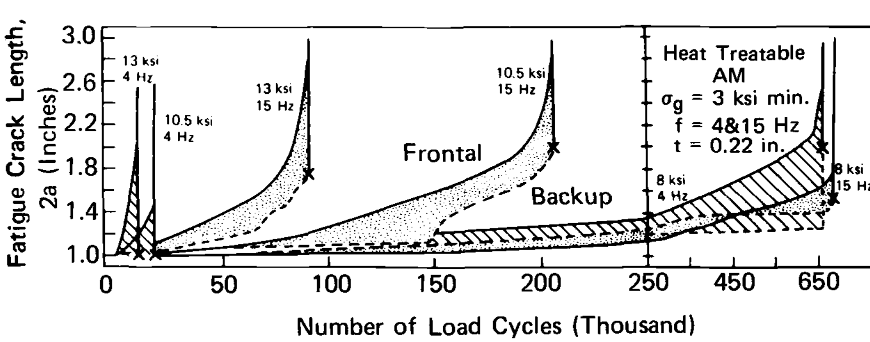

FIG. 5—*Fatigue crack length as a function of the number of load cycles and frequency for AM DHS, tested at* $\Delta\sigma_g = 5$ *ksi*, R = *0.375;* $\Delta\sigma_g = 7.5$ *ksi*, R = *0.286; and* $\Delta\sigma_g = 10$ *ksi*, R = *0.231.*

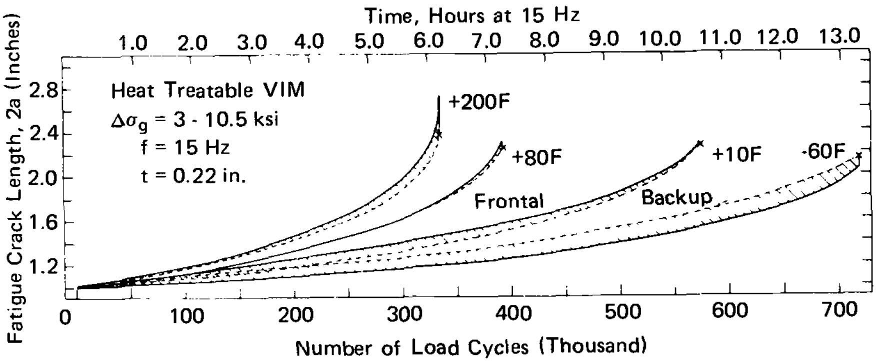

FIG. 6—*Fatigue crack length as a function of the number of load cycles and temperature for VIM DHS tested at* $\Delta\sigma_g = 7.5$ *ksi*, R = *0.285.*

ment (air, water vapor, etc.) can have an accelerating influence on crack growth. For a given number of cycles, specimens tested at a lower frequency are exposed to the environment for a longer time and, hence, suffer more degradation. It is believed that such environmental factors are active in DHS.

Another major variable influencing crack growth is temperature. Figure 6 shows the effect of temperature variations from −60 to +200°F on crack growth in the VIM steel. As the temperature decreases, the rate of crack growth decreases, and the fatigue life increases. However, the crack length at failure decreases. Note for this VIM steel that the rates of crack growth for the frontal and backup materials are quite similar, in contrast to the ausformed and AM steels shown in Figs. 3–5.

It should be emphasized that the various dual hardness steels have varying chemistries and processing histories and, hence, varying properties. Note that the AM and VIM steels have similar compositions, although they have been tempered to different hardness levels. A comparison of the fatigue lives for notched specimens over a range of gross stresses is shown in Fig. 7. The ausformed and AM steels have the shortest lives, while the limited data for the VIM steel show it to have markedly superior fatigue properties. Whether this difference is due to the vacuum melting or to the difference in hardness level is not known.

Discussion

Monolithic Components

Crack growth data are often analyzed by the empirical Eq 1 presented earlier. The crack growth rate, $d2a/dn$, can be determined directly from

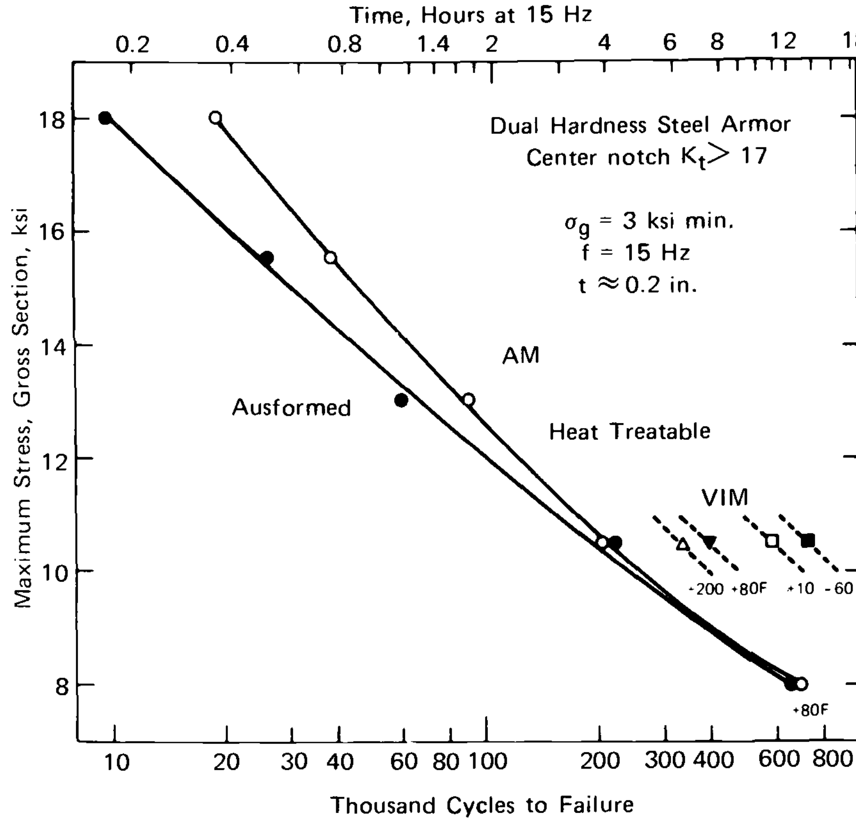

FIG. 7—*Maximum gross section stress versus the number of load cycles to failure for notched specimens of DHS. Specimens 3.0 in. wide with 1.0-in.-center notch.*

experimental curves such as those in Fig. 1 or 2, while ΔK is calculated from

$$\Delta K = \Delta\sigma \; a^{1/2} Y \tag{2}$$

The term Y is a finite width correction which increases as the ratio of crack length to specimen width, $2a/w$, increases. The analysis of Isida for center-notched specimens and Gross for compact tension specimens was used to determine Y [*8*].

Figure 8 is a plot of $d2a/dn$ versus ΔK for the frontal and backup monolithic components of the AM steel determined from the data in Fig. 1. Figure 9 shows similar data for the components of the ausformed DHS taken from Fig. 2. In this case, using the compact tension specimen, the crack growth rates have been doubled to provide values of $d2a/dn$ that

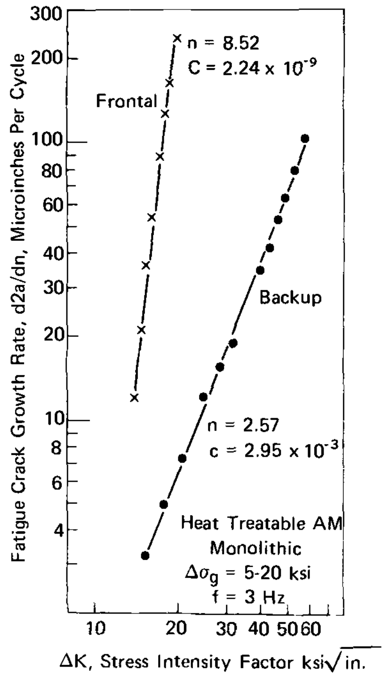

FIG. 8—*Fatigue crack growth rate as a function of stress intensity factor range for monolithic components of AM DHS tested at* $\Delta\sigma_g = 15$ *ksi,* R = *0.25.*

would be compatible with the data from the center-notched specimen used in the other crack growth tests. For all materials, a straight line has been drawn through the data, the slope of which is the growth rate exponent m and the intercept at $\Delta K = 1$ ksi in.$^{1/2}$ the preexponential term C. The constants are listed in Table 3.

TABLE 3—*Crack propagation rate constants and exponents from* $d2a/dn = C(\Delta K)^m$ *for components of ausformed and AM DHS.*

Material	C^a	m
Heat treatable AM		
frontal	2.24×10^{-9}	8.52
backup	2.95×10^{-3}	2.57
Ausformed		
frontal	7.90×10^{-6}	5.07
backup	4.84×10^{-3}	2.68

[a] $d2a/dn$ in μin./cycle, K in *ksi* $\sqrt{\text{in.}}$

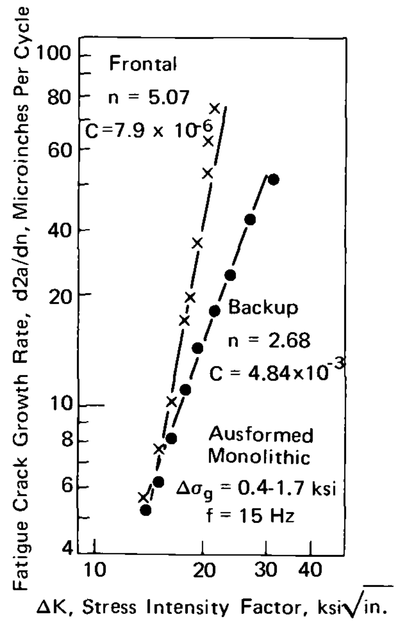

FIG. 9—*Fatigue crack growth rate as a function of stress intensity factor range for monolithic components of ausformed DHS tested at* $\Delta\sigma_g = 1.3$ *ksi,* R = *0.235.*

In each case, the growth rate exponent m of the frontal component is higher than that of the backup. This is also true of the crack growth rate itself except at the very lowest values of ΔK. The difference is especially great in the case of the AM steel. The very high crack growth rates of the frontal component of the AM steel are undoubtedly related to the intergranular mode of fracture during fatigue and the absence of striations usually associated with crack growth in structural metals.

Qualitatively, one can understand the crack growth behavior of the DHS composites from these results on the component materials. Because the growth rate of the frontal material is higher than that of the backup, growth will lag in the backup in the composite. This is shown in Figs. 3 and 4. Moreover, since the curves in Figs. 8 and 9 diverge (for example, the growth rate exponent is higher for the frontal than the backup), the difference in growth rate will be greater the higher the initial stress level during fatiguing. Again, this is the behavior depicted in Figs. 4 and 5. Although data on the individual components of the VIM steel are not available, it is possible to conclude from Fig. 6 that the crack growth behavior of the components is almost the same.

Dual Hardness Steel Composites

The question of how to relate the crack growth behavior of a bonded composite, such as DHS, to the behavior of the component steels is not a simple one. The shape of the crack front can be seen in Fig. 10. This is a fractograph of a broken specimen of DHS and the crack front at the onset of rapid fracture is indicated.

In each case investigated, there was no evidence of delamination at the bonded interface. Accordingly, the crack front was continuous through the interface. This was further supported by metallographic examination which showed a good bond with no oxides or other foreign particles at the interface. The complex shape of the crack front poses a problem in calculating ΔK since an expression for ΔK should be used taking into consideration the curvature of the crack front at each point. No such expression for ΔK has been developed. Furthermore, convenience dictates that the crack length as seen on each surface be used as a single parameter to describe the crack length in that layer which introduces another error.

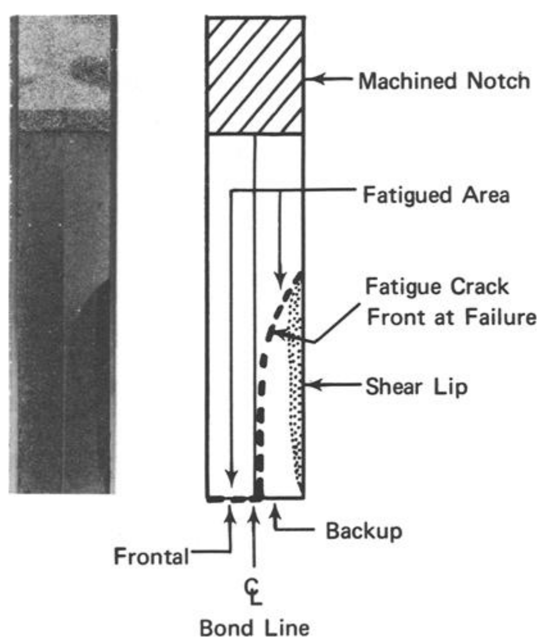

FIG. 10—*Fatigue crack front at failure typical of ausformed and AM DHS.*

As a first approximation, no interaction between the layers can be assumed, and the expressions for ΔK developed for through-cracks can be employed, using the gross stress and the crack size as seen on the surface as a crack length. Thus for two components, 1 and 2, the growth rates are

$$\begin{aligned} d2a_1/dn &= C_1(\Delta\sigma\ a_1^{1/2}Y_1)^{m_1} \\ d2a_2/dn &= C_2(\Delta\sigma\ a_2^{1/2}Y_2)^{m_2} \end{aligned} \tag{3}$$

However, this procedure leads to unrealistically high values of ΔK for the frontal material when the uncracked area of the frontal material is very low. This can be seen by the fact that the frontal material fails completely by fatigue rather than by tensile overload, provided the uncracked area in the backup is large enough. Clearly there must be some readjustment of the load with a greater portion of the load carried by the component with the shorter crack length, the backup steel. Effectively, σ would be different in the two components.

Equation 3 implies different section compliances in the frontal and backup layers. This assumption would lead to different displacements, which is not compatible with the continuous bond across the interface. A more rigorous method is to allow the load to be redistributed to make the displacement in the two components the same. Tada [9] has derived an expression for the displacement of a center cracked specimen on the crack line. This displacement, δ, at the center on the crack line is

$$\delta = \frac{4\sigma a(1-\nu^2)}{E} V'\left(\frac{2a}{w}\right) \tag{4}$$

where

$$\begin{aligned} V'(2a/w) = &-0.071 - 0.535(2a/w) + 0.169(2a/w)^2 + 0.020(2a/w)^3 \\ &-1.071[1/(2a/w)] \ln [1-(2a/w)] \end{aligned} \tag{5}$$

If the displacement on the crack line in the two components is the same

$$\sigma_1 a_1 V'(2a_1/w) = \sigma_2 a_2 V'(2a_2/w) \tag{6}$$

Furthermore, the total load is the sum of the loads on each component

$$\sigma_1 t_1 + \sigma_2 t_2 = \sigma(t_1 + t_2) \tag{7}$$

where w is the specimen width, and t, the thickness of the layer. Simultaneous solution of Eqs 6 and 7 allows the gross stress in either component to be expressed as a function of the overall gross stress. Assuming equal thickness components, the growth rates are

$$\frac{d2a_1}{dn} = C_1 \left\{\frac{2}{1 + [a_1V'(2a_1/w)/a_2V'(2a_2/w)]} \Delta\sigma a_1^{1/2} Y_1\right\}^{m1}$$
$$\frac{d2a_2}{dn} = C_2 \left\{\frac{2}{1 + [a_2V'(2a_2/w)/a_1V'(2a_1/w)]} \Delta\sigma a_2^{1/2} Y_2\right\}^{m_2} \quad (8)$$

Similar expressions to Eqs 4 and 5 were developed by Tada for the displacement at points remote from the crack ($>1.5w$) [*9*]. For the case of DHS where there is no delamination, it is felt that the assumption of equal displacement on the crack line is more valid.

The foregoing procedures assume that the cracks grow independently at a rate determined by the power law and the value of ΔK for a center cracked specimen. Effects of the interface and specimen thickness are necessarily neglected. The two procedures, assuming that there is no interaction between the layers and that there is equal displacement on the crack line, have been checked for the AM and the ausformed steels. The experimental crack growth data are shown in Figs. 3 and 4.

Figure 11 shows the crack growth rate for the AM and ausformed

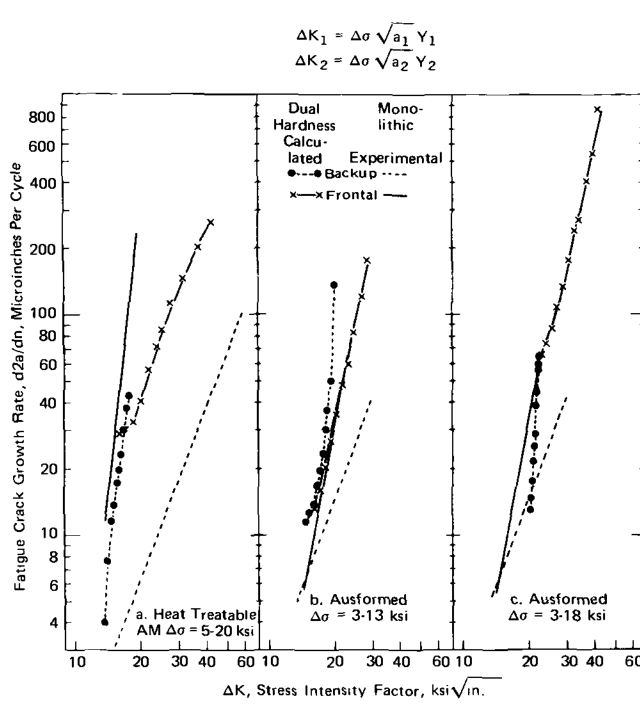

FIG. 11—*Fatigue crack growth rate of DHS as a function of stress intensity factor range calculated assuming no interaction:* (a) $\Delta\sigma_g = 15$ *ksi*, R $= 0.25$; (b) $\Delta\sigma_g = 10$ *ksi*, R $= 0.231$; *and,* (c) $\Delta\sigma_g = 15$ *ksi*, R $= 0.167$.

steels plotted versus ΔK, where ΔK was calculated from the gross stress and crack lengths on each surface (Eq 3), that is, no interaction between the layers. Two gross stress ranges are shown for the ausformed steel, 10 and 15 ksi. For comparison purposes, the growth data for the monolithic components are also shown. In each case, the crack growth rate exponent or slope for the backup portion is higher than that for the frontal material. At the higher values of ΔK, it appears that the backup grows at a faster rate than the frontal. This is an anomaly, however. The data points shown in Fig. 11 for the front and back are taken in pairs at the same cycle count. At any one time the growth rate and ΔK for the frontal material are, in reality, higher than for the backup.

Compared to the data for the monolithic components, the frontal material shows too low a slope and generally low values of growth rate, while the behavior of the backup is the opposite. This method of data analysis yields unsatisfactory results.

The results for the correction based on equal displacement on the crack line (Eq 8) are shown in Fig. 12. In terms of similarity of the slopes to the monolithic data and relative position of the curves, this procedure gives better results than that assuming no interaction between the layers (Fig. 11).

A similar calculation was performed, using the assumption of equal displacement in the two layers remote from the crack. These results were markedly poorer than those shown in Fig. 12.

While the simple assumption of load transfer to allow equal displacement in each layer on the crack line yielded markedly better results than the assumption of no interaction at all, the results are not completely satisfactory. A more rigorous approach awaits the development of equations that will take into account the complete three-dimensional nature of the crack front.

Summary and Conclusions

Crack growth behavior has been studied in dual hardness steel. Three lots have been investigated, including ausformed DHS, a heat treatable AM DHS, and a heat treatable VIM DHS. Individual components of the frontal and backup components of the ausformed and AM steels were also investigated.

1. For the separate components of the AM and ausformed steels, the crack growth resistance of the hard frontal steel is poorer than that of the backup steel. In the AM frontal steel, fatigue crack growth is accompanied by intergranular fracture rather than fatigue striations and transgranular fracture.

$$\Delta K_1 = \left[2/1 + \frac{a_1 V(2a_1/w)}{a_2 V(2a_2/w)}\right] \Delta\sigma \sqrt{a_1} Y_1$$

$$\Delta K_2 = \left[2/1 + \frac{a_2 V(2a_2/w)}{a_1 V(2a_1/w)}\right] \Delta\sigma \sqrt{a_2} Y_2$$

$$V(2a/w) = -0.071 - 0.535\,(2a/w) + 0.169\,(2a/w)^2 + 0.020\,(2a/w)^3 - 1.071\,1/(2a/w)\ \ln\,(1 - 2a/w)$$

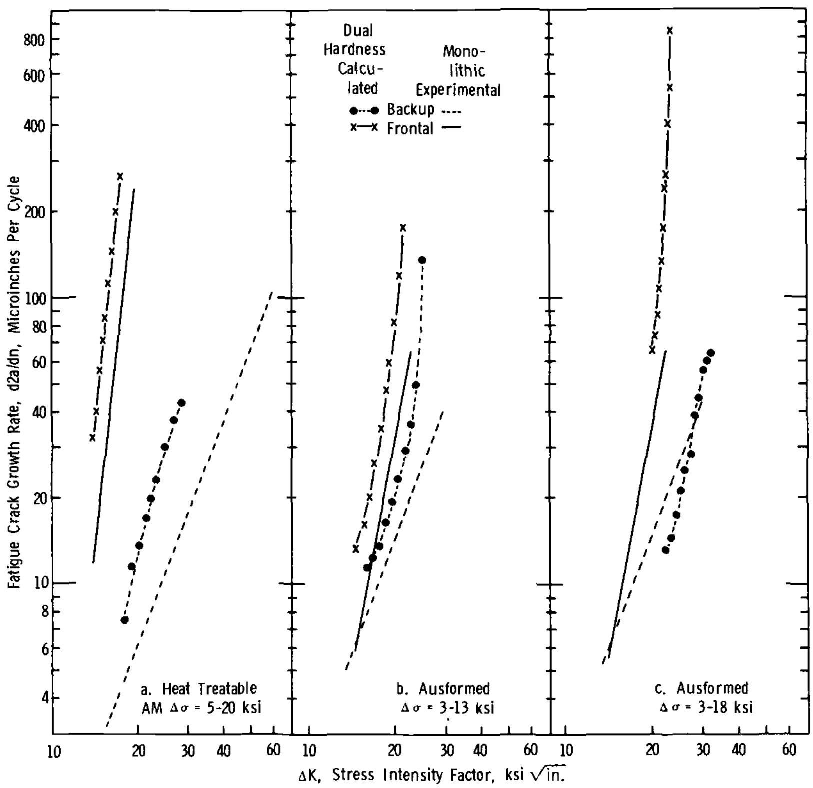

FIG. 12—*Fatigue crack growth rate of DHS as a function of stress intensity factor range based upon the stress distributed so as to result in equal displacement at the crack line:* (a) $\Delta\sigma_g = 15$ *ksi,* $R = 0.25$; (b) $\Delta\sigma_g = 10$ *ksi,* $R = 0.231$; *and,* (c) $\Delta\sigma_g = 15$ *ksi,* $R = 0.167$.

2. In the DHS laminated composite, the crack grows at a different rate in the frontal and backup components. This difference in growth rate increases with increasing stress level and is a function of the type of steels used. The crack growth resistance of the frontal steel is improved by being bonded to the backup steel in the DHS.

3. The reduction of the frequency of loading from 15 to 4 Hz increases the rate of crack growth. Temperature of testing is also an important

variable with the crack growth rate decreasing and fatigue life increasing as the test temperature decreases from +200 to −60°F.

4. Of the three DHS composites tested, the VIM steel had the best crack growth resistance.

5. The results were analyzed in terms of the power law for fatigue crack growth, Eq 1. The results for the monolithic materials conformed to this expression, yielding values for C and m of 2.24×10^{-9} and 8.52, and 2.95×10^{-3} and 2.57, respectively, for the frontal and backup components of the AM steels. The corresponding results for the ausformed steels were 7.90×10^{-6} and 5.07, and 4.84×10^{-3} and 2.68, respectively, with the crack growth rates expressed in μin./cycle and ΔK in ksi in.$^{1/2}$.

6. The crack growth data for the DHS composites were analyzed in terms of the growth characteristics of each individual component. It was assumed that crack growth proceeded independently in each layer at a rate governed by the ΔK in that layer. Two cases were considered: no interaction or the same stress in each layer; and, the gross stress distributed so that there was equal displacement at the crack line. Closer agreement with the experimental results for the individual layers was obtained by allowing the stress to be distributed so that there was equal displacement at the crack line. The fact that better agreement was not obtained with these models suggests that the interface plays an important role in inhibiting crack growth in the frontal layer of dual hardness steel.

References

[1] Manganello, S. J. and Abbott, K. H., *Journal of Materials*, Vol. 7, No. 2, June 1972, p. 231.

[2] Anctil, A. A. and Kula, E. B, "Fatigue Crack Propagation in Armor Steels," Army Materials and Mechanics Research Center, AMMRC TR 69-25, Nov. 1969.

[3] Anctil, A. A., Chait, R., Curll, C. H., and Kula, E. B., "Structural Properties of Dual Hardness Steel Armor," Army Materials and Mechanics Research Center, AMMRC TR 73-6, Feb. 1973.

[4] Swanson, R. A. and Anctil, A. A., "Dual Hardness Steel Armor-Observations on Material Characteristics and Specimen Preparation," Army Materials and Mechanics Research Center, AMMRC TN 71-2, Aug. 1971.

[5] Burr, C. W., Degnan, W. G., Grumm, A. W., and McCaul, C. O., "Aerial Armored Fuselage Engineering and Manufacturing Report, Part I (U)," Sikorsky Aircraft, AMMRC CR 70-2/1, Feb. 1970.

[6] Paris, P. C., in *Fatigue, An Interdisciplinary Approach,* Syracuse University Press, New York, 1964, p. 107.

[7] Anctil, A. A., Kula, E. B., and DiCesare, E., *Proceedings,* American Society for Testing and Materials, Vol. 63, 1963, p. 799.

[8] *Plane Strain Crack Toughness Testing of High-Strength Metallic Materials, ASTM STP 410,* American Society for Testing and Materials, 1967, p. 8.

[9] Tada, H., Paris, P. C., and Irwin, G. R., in *The Stress Analysis of Cracks Handbook,"* Del Research Corp., Hellertown, Pa., 1973, pp. 2–4.

S. C. Kunz[1] *and P. W. R. Beaumont*[1]

Microcrack Growth in Graphite Fiber-Epoxy Resin Systems During Compressive Fatigue

REFERENCE: Kunz, S. C. and Beaumont, P. W. R., "**Microcrack Growth in Graphite Fiber-Epoxy Resin Systems During Compressive Fatigue,**" *Fatigue of Composite Materials, ASTM STP 569,* American Society for Testing and Materials, 1975, pp. 71–91.

ABSTRACT: Transfibrile crack extension in graphite fiber-epoxy resin composites was investigated in notched beams under cyclic compressive loading. Compressive fatigue crack growth was evaluated using selected linear elastic fracture mechanics parameters. A model was used to correlate observed micro-fracture processes with compressive crack extension behavior. Crack propagation underwent periods of deceleration and acceleration, and the crack growth rate dependence on material and environmental variables was determined. Transfibrile fatigue crack extension in unidirectional composites is a result of axial cracking and frequently resulted in crack arrest. Comparison of unidirectional composites with different epoxy resins showed the composite with the higher bond strength to be less susceptible to axial cracking along the fiber-matrix interface than the one with the lower bond strength. Crossplied (0°/90°) composites had lower compressive strengths, and through-specimen fractures resulted from axial cracking in the 0° plies, splitting in the 90° transverse plies, and splitting between plies. Exposure to a saline solution greatly increased axial cracking in all the composites and enhanced transverse ply splitting in the cross-plied material. Crack tip blunting and crack arrest due to solution-induced interfacial degradation was frequent.

KEY WORDS: composite materials, graphite fibers, epoxy resins, failure mechanisms, environment, fatigue (materials)

The lifetime of a structural material that is subjected to changing stresses and environments may be determined by the rate at which an existing crack or flaw can grow to a critical size and cause catastrophic failure. The toughness of a material is a measure of its resistance to crack

[1] Postgraduate research student and lecturer, respectively, University Engineering Department, Cambridge University, Cambridge, England; formerly with the School of Engineering and Applied Science, University of California, Los Angeles, Calif. 90024.

propagation. In conventional metal alloys, notch sensitivity usually increases as the unnotched strength increases. It has been shown [*1*][2] that carbon fiber reinforced epoxy (CFRE) composites exhibit an increase in notch toughness with increasing unnotched strength. The high strength carbon fibers raise the longitudinal strength of the composite, and the fiber-matrix interface acts as a crack arrestor by splitting or debonding.

A critical condition in a unidirectional composite is crack propagation in a direction transverse to the fibers. The inherent crack-blunting ability of aligned fibers in a solid is no longer realized when a crack propagates through the composite instead of being deflected along the fibers at the fiber-matrix interface. Transfibrile fracture has been observed [*2*] in unidirectional CFRE composites subjected to cyclic compressive loads applied in the fiber direction. Determination of the crack growth rate dependence on material and environmental variables will provide insight into the design of a composite material resistant to compressive fatigue.

Compressive fatigue crack propagation may be evaluated in terms of selected linear elastic fracture mechanics (LEFM) parameters [*3*]. According to LEFM, stable crack propagation and subsequent catastrophic failure are governed by the stress intensity factor, K [*4*]. The relation between K, the crack length, a, and the applied stress, σ, is expressed as [*5*]

$$K = \sigma\sqrt{\alpha\pi a} \tag{1}$$

where α is a parameter depending on specimen and crack geometries.

A number of empirical laws have been proposed to describe the crack growth rate in fatigue as a function of the stress intensity factor. The most general one is given by [*6*]

$$\frac{da}{dN} = B(\Delta K)^n \tag{2}$$

where B and n are material constants, N is the number of cycles, and ΔK is the stress intensity factor range ($\Delta K = \Delta\sigma\sqrt{\alpha\pi a}$). Crack growth will be stable (slow) if K is below the critical value for fast fracture. The rate controlling exponent, n, reflects the material properties (namely, fiber, matrix, fiber-matrix interface) and environmental conditions; thus, the time-dependent compressive failure of composite materials with varying microstructures may be related to their microfracture processes.

[2] The italic numbers in brackets refer to the list of references appended to this paper.

Experimental Procedures

Material Characterization and Testing Techniques

The specimens used in the fatigue tests were machined from plates of three different types of composite materials containing the same type of continuous, surface-treated graphite fiber, Hitron 401: a U.S. Polymeric 702 epoxy resin with 60 percent unidirectional fibers, an ERLA 4617 epoxy resin with 60 percent unidirectional fibers, and an ERLA 4617 resin with 65 percent crossplied fibers, half in the 0° direction and half in the 90° direction. A single-edge notched specimen was used in the four-point (pure) bend tests. The specimen configuration was 5 in. by 0.5 in. by 0.25 in. with a sharpened 0.05-in. notch.

Fatigue testing was performed on an MTS machine programmed to cycle sinusoidally in zero-compression, constant load control, at a frequency between 1 and 3 Hz. The notched bars were mounted on ¼-in.-diameter rollers positioned to give a major span of 4 in. and a minor span of 1 in. such that roller crushing damage was eliminated and shear stresses in the outer portions of the bar were reduced. Under this loading configuration, the notched half of the specimen was subjected to pure compressive stresses in the axial direction.

Crack growth rates were measured using a traveling microscope positioned in front of the specimen. Environmental testing was done using a dilute saline solution as a wetting or corrosive agent. A lucite-walled chamber was installed around the testing apparatus through which measurements on the immersed specimens could be made. Fracture surface evaluations were made using both an optical and a scanning electron microscope (SEM).

Method of Data Analysis

Upon crack initiation at the machined notch, the testing machine was stopped at regular time intervals to record the crack length, a, and the corresponding number of cycles completed, N. The values of a were then plotted versus N and a best-fit curve was drawn. From such a graph, typified by Fig. 1, the crack growth rate, da/dN, was obtained by measuring the slope of the curve at various values of a.

Equation 2 can be expressed in logarithmic form

$$\log da/dN = \log B + n \log \Delta K \tag{3}$$

Assuming that the compressional crack tip stress singularity ΔK is proportional to a^m rather than $a^{1/2}$ [3], Eq 1 can be written as

$$K = C\ \Delta\sigma\ a^m \tag{4}$$

where $C \equiv f(\alpha,\pi)$.

Combining Eqs 3 and 4,

$$\log da/dN = \log B + n \log (C\ \Delta\sigma) + nm \log a \tag{5}$$

Simplifying Eq 5

$$\log da/dN = A + n' \log a \tag{6}$$

where A is a constant that includes the constant stress range $\Delta\sigma$ and the constants B and C, and n' is the product of the rate exponents n and m. The constant n' is the parameter reflecting the compositional and environmental variables of each material that determines the exponential variation of crack growth rate with crack length. Values of n' are obtained by taking the slopes of log da/dN versus log a.

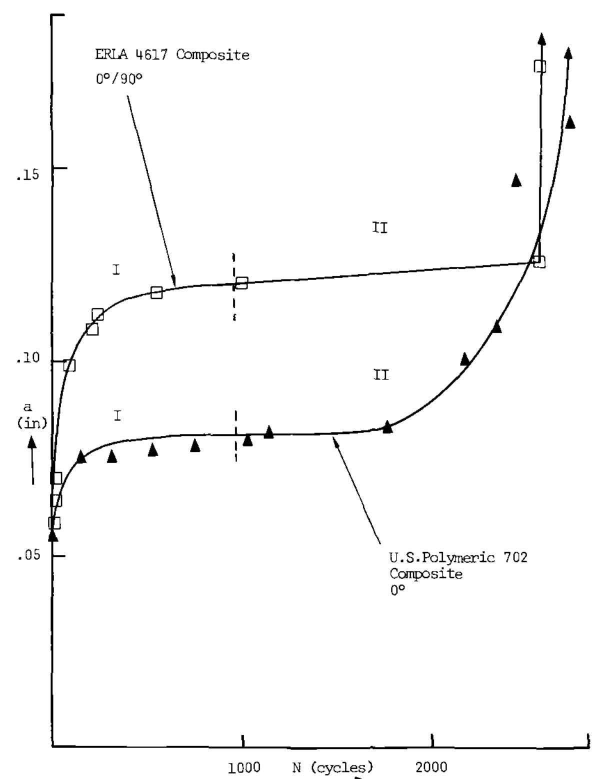

FIG. 1—*Crack length versus number of cycles for crossply and unidirectional composites that underwent complete failure.*

Experimental Results

Crack growth measurements were obtained from compressive fatigue tests to determine the effects of matrix properties, fiber orientation, and saline environment on stable crack propagation. Figure 1 gives typical plots of crack length, a, versus number of cycles, N, for unidirectional and crossplied specimens. An example of the effect of specimen exposure to a saline solution during fatigue testing on the a-N curves is shown in Fig. 2. The curves can be divided into three regions: Region I indicates crack deceleration; Region II represents crack reacceleration; and, Region III is a deceleration stage leading to crack arrest.

The da/dN versus a plots were converted to log da/dN versus log a plots from which the slope, n', was obtained in accordance with Eq 6. Figures 3–7 show the results of cross-plotting log da/dN versus log a values to compare the relative shifts in n' that occur when fiber orienta-

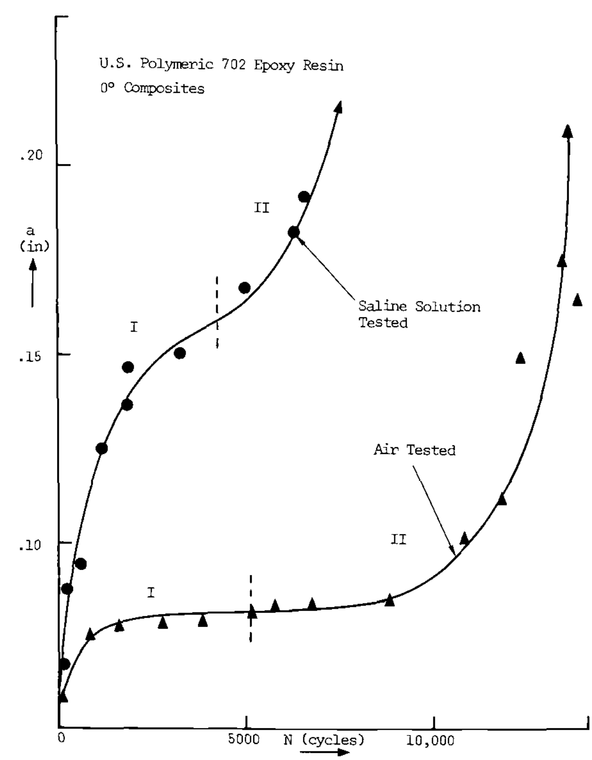

FIG. 2—*Crack length versus number of cycles for unidirectionally reinforced U.S. Polymeric 702 epoxy resin.*

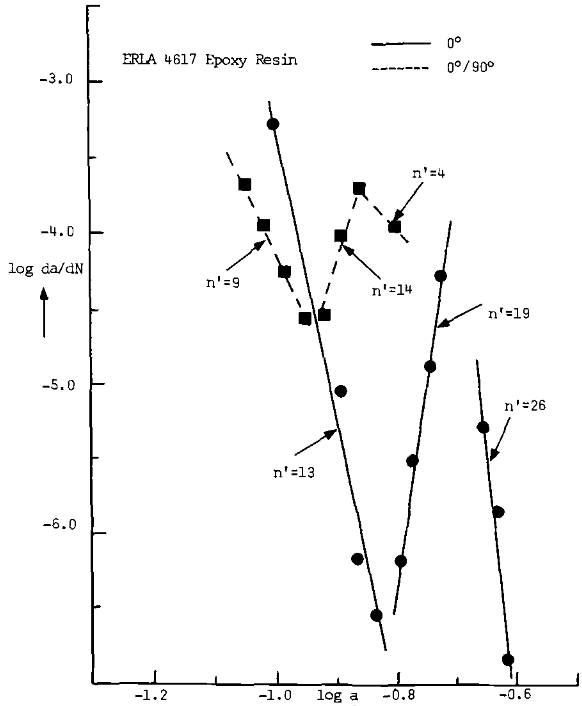

FIG. 3—*Crack growth rate comparison of crossplied and unidirectional reinforcement of ERLA 4617 epoxy resin.*

tion, matrix resin, or environment are varied. Figure 3 demonstrates that crack propagation behavior in a crossplied material differs from that in a unidirectional material due to the transverse plies. The effect of variable microstructure on the rate exponent, n', is seen in Fig. 4 for two unidirectional composites with different resins. Figures 5–7 show that the degree to which a saline solution affects cracking behavior depends on the fiber orientation and the composite microstructure.

The da/dN versus a curve comparisons are made for specimens that were subjected to equal cyclic stresses during testing or for data that were appropriately normalized. According to Eq 6 the stress levels at which the specimens were cycled determines only the relative vertical positions (vertical axis intercepts) of the da/dN versus a graphs and not their slopes. Values of the latter should, therefore, be constant over the stress ranges considered and reflect only the changes in intrinsic and en-

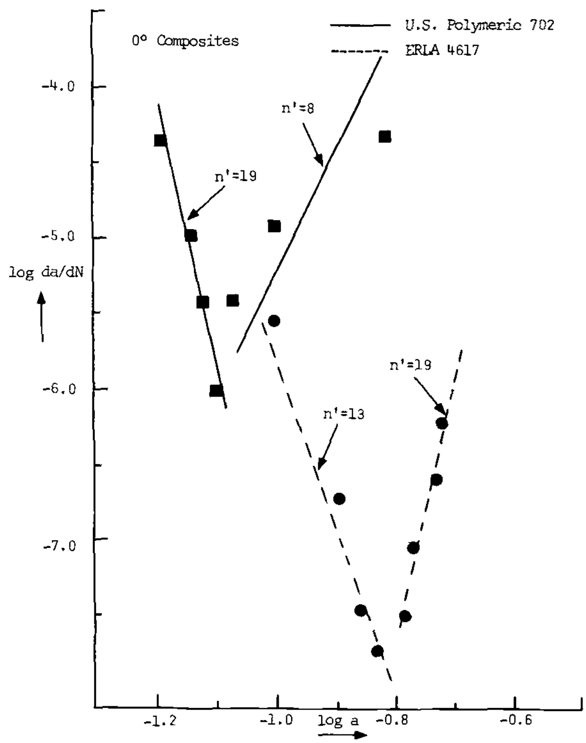

FIG. 4—*Crack growth rate comparison of unidirectionally reinforced U.S. Polymeric 702 and ERLA 4617 epoxy resins.*

vironmental variables. The n' values designated in the figures and summarized in Table 1 are averaged from several specimens and should be used for magnitude comparison purposes and not regarded as absolute.

Discussion

The characteristic shape of the a versus N curves in Figs. 1 and 2 indicates the existence of regions through which the crack alternately decelerates and accelerates. From experimental observations it was noted that during the cycling period corresponding to Region I, the crack that had initiated at the machined notch grew rapidly under the applied stress and then visibly slowed down. Continued cycling produced cracks that originated at the newly created fracture surface behind the crack tip and grew parallel to the fibers in the axial direction. This axial cracking pro-

TABLE 1—*Values of the rate exponent,* n'.

Composite system	Region I		Region II		Region III	
	air	saline	air	saline	air	saline
ERLA 4617, 0°	13	...	19	8	26	20
ERLA 4617, 0°/90°	9	16	14	25	4	26
U.S. Polymeric 702, 0°	19	6	8	5	...	...

cess is shown schematically in Fig. 8. After a given number of cycles, the crack proceeded again across the fibers with a visible increase in velocity. This reacceleration period corresponds to Region II. It was found that the crack either propagated through the specimen until tensile failure occurred or decelerated again and remained arrested, depending upon whether further axial cracking developed during the latter cycling

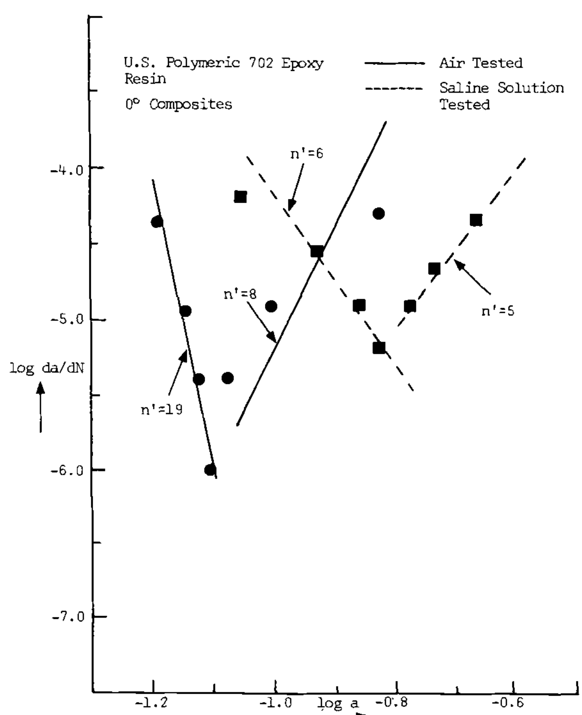

FIG. 5—*Crack growth rate comparison for solution and air tested U.S. Polymeric 702 resin with unidirectional fibers.*

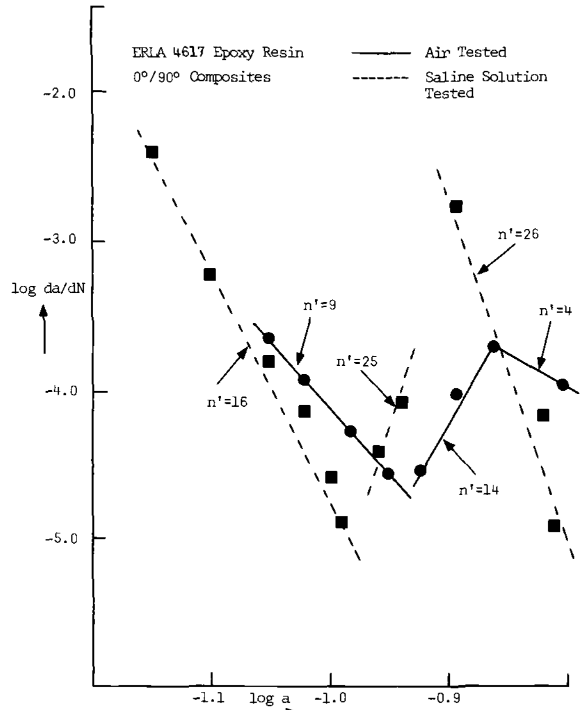

FIG. 6—*Crack growth rate comparison for solution and air tested ERLA 4617 resin with crossplied fibers.*

period. This succession of varying crack growth rates suggests that crack extension during continuous cycling is controlled by microfracture processes occurring at and behind the crack tip.

The basis of the model [2] adopted in this work is the assumption that the cracking rate, da/dN, is a monotonically increasing function of the strength of the stress singularity at the crack tip, which in turn is assumed to increase with crack length for constant $\Delta\sigma$. As the crack grows under an applied bending moment, M, and if the flanks of the newly formed crack were to remain free of traction, the stress singularity at the crack tip would become more severe and cause acceleration of cracking. The observed initial deceleration of the crack is attributed to the load-bearing capability of the newly created flanks, Δa, as shown in Fig. 9. As the flanks are compressed during loading, they can support and transmit a uniform stress, σ_0, which reduces the magnitude of the stress field at the crack tip

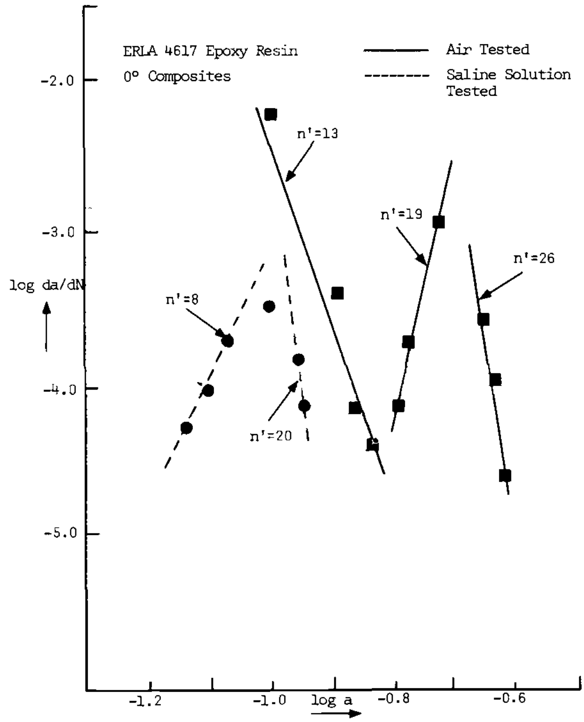

FIG. 7—*Crack growth rate comparison for solution and air tested ERLA 4617 resin with unidirectional fibers.*

and causes decleration of the advancing crack. Subsequent crack acceleration results from progressive destruction of the compressive load-bearing capacity of the crack flanks caused by axial cracking. As a result, the stress singularity at the crack tip intensifies and the crack growth rate increases.

The failure of a unidirectionally reinforced composite under compressive load applied along the fiber axis is attributed to elastic buckling of the fibers [7]. At large fiber volume fractions (for example, 60 percent) in-phase fiber buckling occurs, and the matrix between fibers deforms in shear as shown in Figs. 10*a*, *b*, and *c*. Crack extension across a band of fibers takes place by fiber buckling followed by fiber fracture and matrix shearing. Figure 10*d* demonstrates how axial cracks along the fiber direction permit the linking up of two microbuckling planes that allows the compressive fracture to proceed across the specimen.

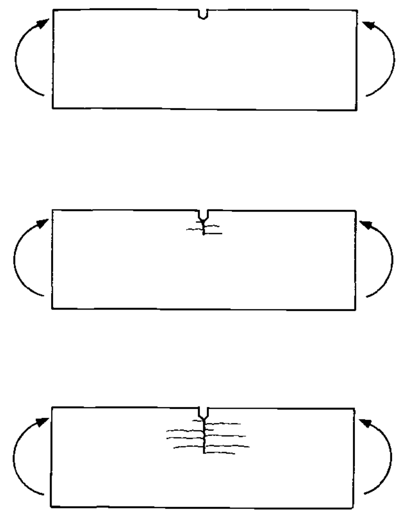

FIG. 8—*Model for axial cracking at and behind the crack tip.*

Analysis of Material and Environmental Variables on the Rate of Compressive Crack Propagation

Effect of Fiber Orientation—Typical crack propagation behavior of air-tested unidirectional and crossplied composite specimens with the same matrix resin (ERLA 4617 epoxy) is shown in Fig. 3. The Region I deceleration rate is lower for the crossplied than for the unidirectional material. Subsequent Region II crack acceleration occurs at a higher rate in the unidirectional than in the crossplied material. In the event of crack arrest, Region III deceleration was faster in the unidirectional specimens than in the crossplied ones. Crack arrest frequently occurred in the unidirectional material, whereas the crossplied material generally suffered from through-specimen failures.

The crossplied material has 50 percent fewer fibers lying in the loading direction than the unidirectional material. This reduction in the number of load-carrying fibers results in a decrease in the compressive strength of the crossplied material [*3*] and provides less resistance to crack extension by way of a fiber buckling process. Axial cracking along the fiber-matrix interface (Fig. 11) took place extensively in both the unidirectional and crossplied materials. The latter has a 50 percent lower 0° fiber-matrix interface area and, consequently, has a lower susceptibility than the unidirectional material to axial cracking. In addition, the alternating orienta-

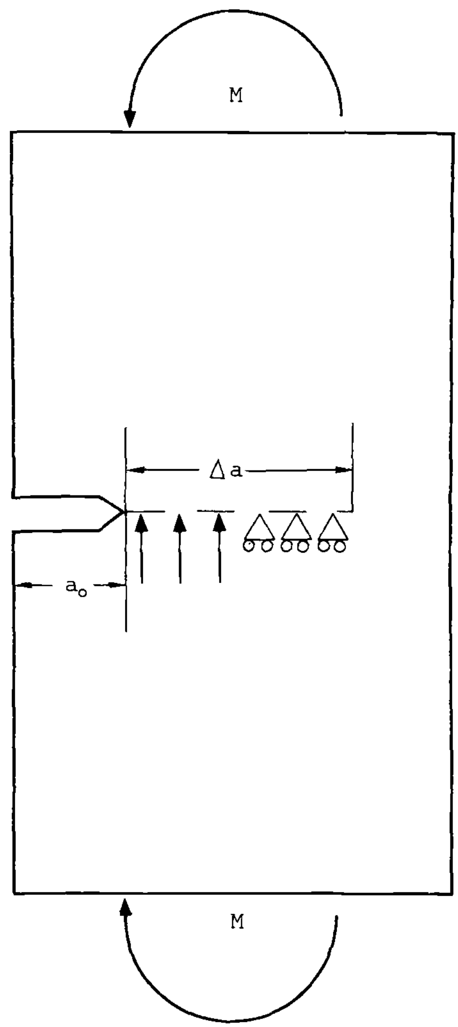

FIG. 9—*Berg model for compressive fatigue crack extension* [2].

tion of plies causes discontinuities across the specimen, that is, a 0° ply is adjacent on either side to a 90° ply. Thus, the linking up of microbuckling paths across an entire specimen by means of axial cracks, that results in through-specimen failure in a 0° material (Fig. 10*d*), is prevented. Figure 12 shows axial cracking across a 0° ply protruding from a fracture surface; cracking is effectively limited to that ply and becomes blunted out at the ply interface.

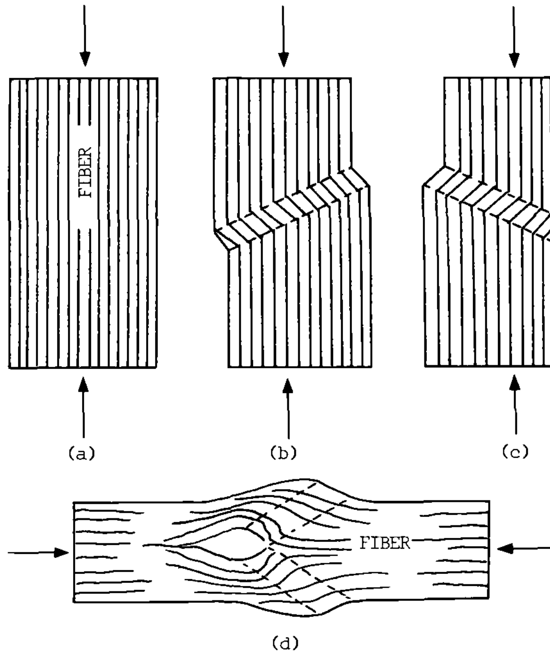

FIG. 10—(a) *Fiber reinforced material under compression.* (b *and* c) *Possible planes for microbuckling; shearing displacement is permissible across these planes.* (d) *Microbuckling may occur on two different planes if axial cracking occurs* [2].

Investigations on graphite-epoxy crossplied systems [*8,9*] have revealed a susceptibility to cracking in the transverse (90°) plies. Figure 13 shows splitting within a 90° ply where the crack alternately follows interfibrile and transfibrile paths. In addition, extensive splitting occurs between the 0° and 90° plies.

The fractography results indicate different microfracture processes in the crossplied and unidirectional materials. The inherent reduced axial load-carrying ability of the crossplied material limits its resistance to crack propagation which is reflected by a lower Region I deceleration rate than in the unidirectional material. Axial cracks effectively decrease the already reduced axial load-bearing capability and enhance subsequent crack extension. Alternatively, limitation on transply crack extension in the 0°/90° material accounts for its greater resistance to crack acceleration in Region II over that of a unidirectional material. The marked rapid deceleration rate and frequent crack arrest behavior of the unidirectional composite, on the other hand, reveal a critical dependence of crack propagation on axial cracking. While the latter is essential to crack extension

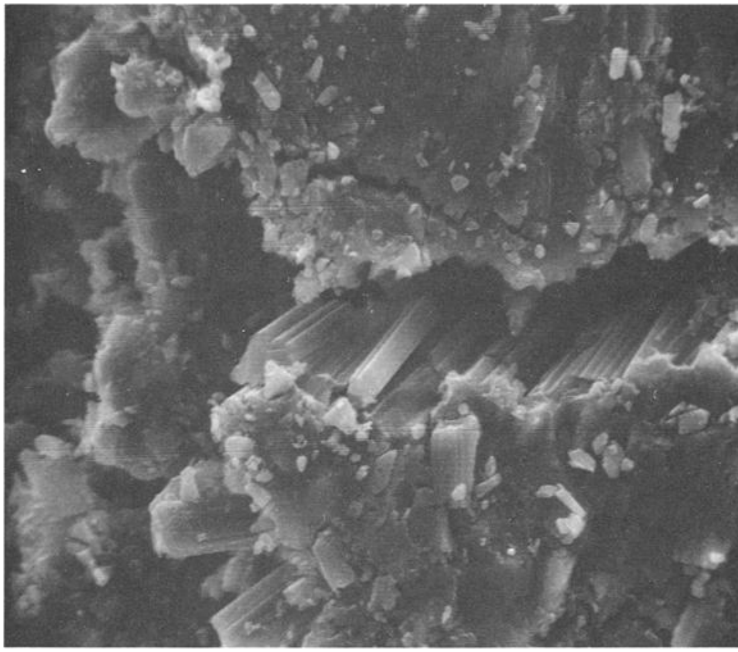

FIG. 11—*Axial cracking along the fiber-matrix interface in a 0° ERLA 4617 composite (X460).*

FIG. 12—*Axial cracking in 0° ply of 0°/90° composite. Note separation between plies (X43).*

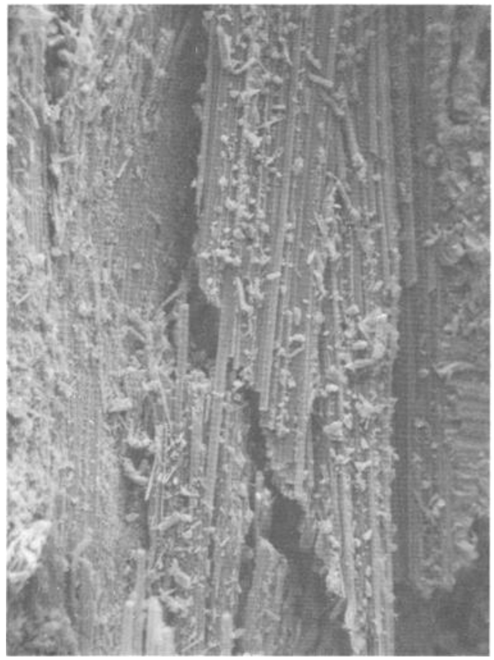

FIG. 13—*Splitting within transverse (90°) ply (X88).*

according to the present model, large scale axial cracking can also cause complete blunting out of the primary crack. The geometry of the crossplied material is such that the failure process need not rely solely on axial cracking; a crack can alternatively propagate by way of transply or interply splitting. Figure 14 shows schematically the possible crack extension paths in crossplied material.

Effect of Matrix—The crack growth rate behavior of the two types of unidirectional composites is compared in Fig. 4. The U.S. Polymeric composite shows a greater resistance to crack propagation in Region I where its deceleration rate is higher than that of the ERLA epoxy composite. Alternatively, the crack acceleration rate in Region II is lower for the U.S. Polymeric composites than for the ERLA type. Region II crack acceleration invariably led to complete failure in the U.S. Polymeric composites, whereas the ERLA composites typically underwent crack arrest. The brittle nature of epoxies severely limits their capacity for slow crack growth [*10*], and compressive fatigue is, therefore, examined in terms of fiber-matrix microfracture processes.

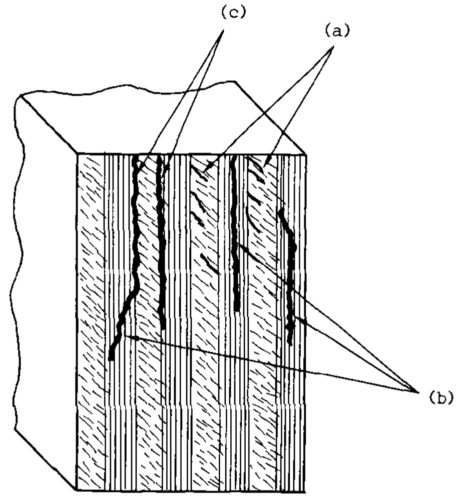

FIG. 14—*Schematic of possible paths for crack extension in crossplied material.* (a) *Along fiber-matrix interface.* (b) *Splitting within 90° ply.* (c) *Splitting between 0° ply and 90° ply.*

The relative fiber-matrix bond strengths of the two unidirectional composites can be qualitatively evaluated from the fractographs in Figs. 15*a* and *b*. Comparison of the tensile fracture regions indicates that greater fiber pull-out occurred in the ERLA composite than in the U.S. Polymeric composite. The average fracture surface pull-out length of fibers is inversely proportional to the shear strength of the fiber-matrix interface which, itself, is a measure of the fiber-matrix bond strength [*11*]. Fibers in U.S. Polymeric epoxy form a stronger mechanical interfacial bond than when combined with ERLA epoxy.

Strong fiber-matrix bonding decreases susceptibility to degradation of the interface under compressive stress because of the reduced possibility of axial cracking along the fiber-matrix interface. Both composites showed extensive crack networks on the compressive fracture surfaces (Fig. 16). The large scale axial cracks that were observed on the specimen surface during testing extend through the thickness of the specimen (Fig. 17). Cracks in the ERLA material arose from splitting between the fiber and resin (Fig. 11), whereas fiber-matrix interfacial splitting was rarely observed in the U.S. Polymeric composite, and cracking within the resin predominated.

Fractography results of the two composite systems indicate different microfracture processes which result in differing crack growth behavior.

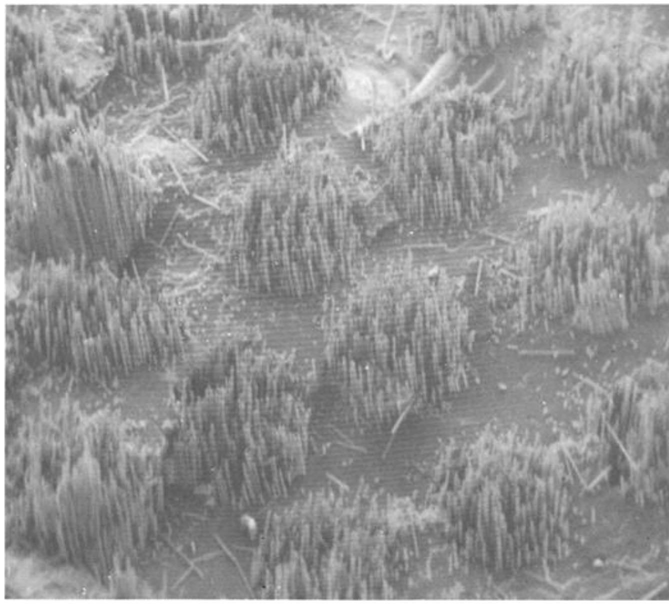

FIG. 15a—*Fiber pull-out on tensile fracture surface of 0° U.S. Polymeric composite (X48).*

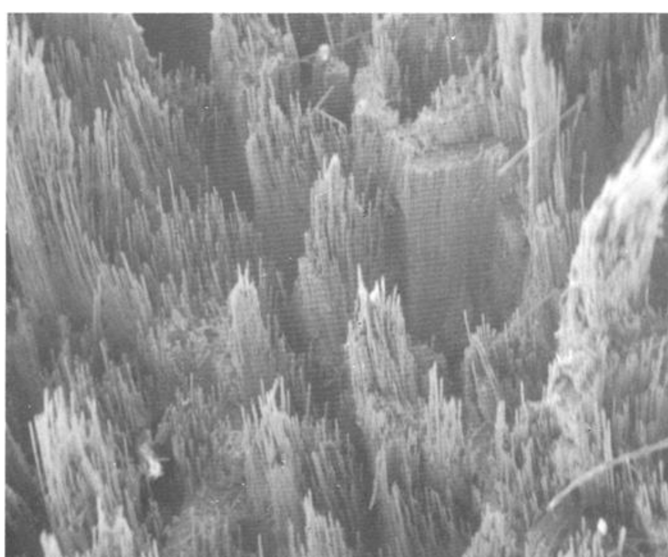

FIG. 15b—*Fiber pull-out on tensile fracture surface of 0° ERLA 4617 composite (X45)*

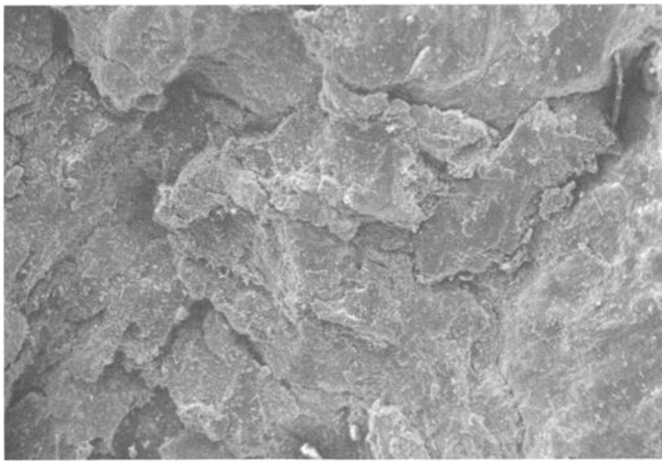

FIG. 16—*Axial cracking networks in 0° U.S. Polymeric composite which occur in resin-rich regions (X18).*

The relatively weak fiber-matrix shear strength in the ERLA material enhances interfacial cracking and, hence, Regions I and II crack extension. Extensive interfacial debonding causes crack tip blunting and results in the frequently observed crack arrest behavior. Alternatively, the lack of substantial fiber-matrix cracking in the U.S. Polymeric composites causes rapid crack deceleration and retards crack extension.

Effect of Environment—The fiber-matrix interface is instrumental in compressive fatigue crack extension, and degradation of the interface in carbon-epoxy composites due to humidity has previously been observed [*12*]. The contribution of stress corrosion cracking of the matrix to the crack growth rate is considered negligible compared to the solution's effect on fiber-matrix debonding [*3*].

Figures 2 and 5 show the effect of a saline solution on crack deceleration and acceleration rates of the unidirectional U.S. Polymeric composite. Regions I and II have lower deceleration and acceleration rates, respectively. The unidirectional ERLA composites underwent immediate crack deceleration which yielded inconclusive Region I n' values. The Region II acceleration rate decreased twofold with the solution (Fig. 7), and very little crack growth occurred before crack arrest. No through-specimen failures were observed in this material.

More extensive axial cracking was observed in the solution-exposed specimens than in the air-tested ones. Weakening of the fiber-matrix interfacial bond by the solution induces axial cracking and initially ac-

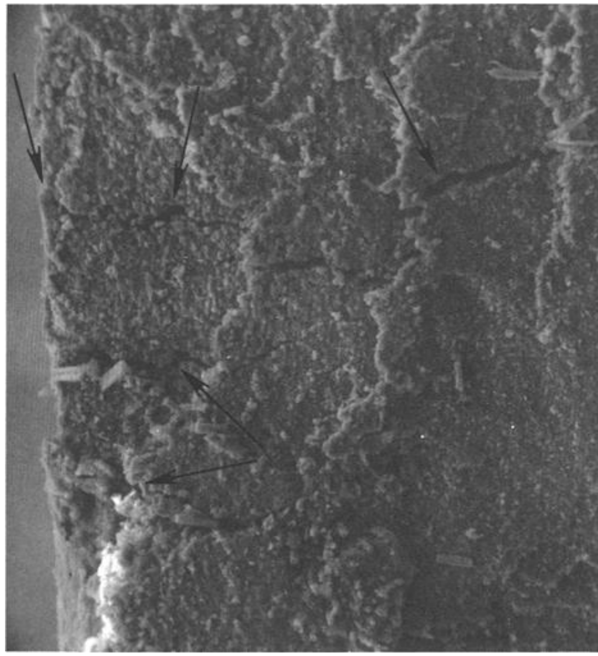

FIG. 17—*Extension of axial cracking from specimen surface across specimen width (X92).*

celerates crack extension. Repeated cycling and solution diffusion to the crack tip, however, cause larger scale interfacial degradation. Crack tip blunting results in complete crack arrest if extensive interface debonding prevents crack reinitiation. The crack extension process in a wet environment depends on the extent of axial cracking and interfacial damage induced by the solution.

The susceptibility of the interface to solution weakening is largely determined by its bond strength. The U.S. Polymeric material exhibits little fiber-matrix debonding in air. The increase in axial cracking with a wet environment results in lower Region I deceleration rates. Crack tip blunting retards subsequent crack acceleration, but interfacial damage is not extensive enough to prevent through-specimen failures. The poorer bond strength of the ERLA material, however, dramatically enhances solution weakening of the interface which results in rapid crack blunting and arrest.

The crossplied ERLA material (Fig. 6) showed more rapid crack deceleration and acceleration when solution tested. Fracture in 0°/90° material occurs in part via transply and interply splitting (Figs. 13, 14), and solution flow along these paths results in ply weakening and separation. The solution thus promotes the transverse ply failure process and accelerates cracking. As in the unidirectional ERLA material, axial cracking in the 0° plies is promoted by the solution. The resulting crack blunting tendencies in the 0° plies and at the ply interfaces simultaneously impede crack extension which is reflected in the more rapid crack deceleration behavior.

Conclusions

This study has shown that transfibrile compressive fatigue crack growth may be retarded or arrested with the proper combination of material variables. Axial cracking is the primary fracture mechanism in unidirectional composites; splitting within and between transverse plies is instrumental in promoting crack extension in crossplied composites. Prevention of these microfracture processes and, hence, compressive fatigue may be achieved by consideration of the following.

1. Composites with high interfacial shear strength are less susceptible to axial cracking along the fiber-matrix interface.
2. High interlaminar shear strength minimizes splitting between and within the transverse plies in a crossplied composite. This is important in preventing solution-induced splitting along the ply interfaces.
3. There is an optimum bond strength for which axial cracking is minimized and transfibrile crack extension prevented. Lower strengths may lead, particularly in a wet environment, to extensive interfacial splitting resulting in crack tip blunting and arrest.

Acknowledgments

We wish to express our gratitude to the U.S. Public Health Service for financial support. We also wish to thank A. S. Tetelman for his valuable advice and HITCO Corporation for providing the material.

References

[1] Beaumont, P. W. R. and Tetelman, A. S., "The Fracture Strength and Toughness of Fibrous Composites," UCLA-ENG-7269, School of Engineering and Applied Science, University of California, Los Angeles, Aug. 1972.
[2] Berg, C. A. and Salama, M., *Journal of Materials*, Vol. 7, No. 2, pp. 216–230.
[3] Kunz, S. C., "Microcrack Growth During Compressive Fatigue in Graphite Fiber-Epoxy Resin Systems," M.S. thesis in Engineering, Materials Department, University of California, Los Angeles, March 1974.
[4] Irwin, G. R., *Encyclopedia of Physics*, Vol. 6, Springer, Heidelberg, Germany, 1958.
[5] Paris, P. C. and Sih, G. C. M., in *Symposium on Fracture Toughness Testing and Its*

Applications, ASTM STP 381, American Society for Testing and Materials, Philadelphia, 1965.
[6] Paris, P. C., *Proceedings,* Tenth Sagamore Army Materials Research Conference, Syracuse University Press, Syracuse, N.Y., 1964.
[7] Dow, N. F. et al, GE-TIS 60SD389, General Electric Space Sciences Laboratory, King of Prussia, Pa., June 1960.
[8] Michno, M. J. and Lavengood, R. E., "The Effect of Prestrain and Water Soak on the Mechanical Performance of Cross-Plied Composites," Monsanto/Washington University, Office of Naval Research/Advanced Research Projects Agency Association, HPC73-154, Oct. 1973.
[9] Waddoups, M. E., "Characterization and Design of Composite Materials," *Composite Materials Workshop,* S. W. Tsai, Ed., Technomic, Stamford, Conn., 1968.
[10] Hertzberg, R. W., Manson, J. A., and Nordberg, H., *Journal of Materials Science,* Vol. 5, 1970, pp. 521–526.
[11] Cooper, G. A., "Micromechanics of Fracture and Fracture Toughness of a Composite Material," Paper ISMET 4108/JCM 41, United Kingdom Inter-Service Metallurgical Research Council, 1969.
[12] Beaumont, P. W. R. and Harris, B., "The Effect of Environment on Fatigue and Crack Propagation in Carbon Fiber-Reinforced Epoxy Resin," *Proceedings,* First International Conference on Carbon Fibers, Institute of Plastics, London, 1971.

Fatigue Deformation and Damage

C. C. Chamis [1] *and T. L. Sullivan* [1]

Nonlinear Response of Boron/Aluminum Angleplied Laminates Under Cyclic Tensile Loading: Contributing Mechanisms and Their Effects

REFERENCE: Chamis, C. C. and Sullivan, T. L., "**Nonlinear Response of Boron/Aluminum Angleplied Laminates Under Cyclic Tensile Loading: Contributing Mechanisms and Their Effects,**" *Fatigue of Composite Materials, ASTM STP 569*, American Society for Testing and Materials, 1975, pp. 95–114.

ABSTRACT: The nonlinear response of boron/aluminum angleplied laminates subjected to cyclic loads was investigated. A procedure is outlined and criteria are proposed which can be used to assess the nonlinear response. The procedure consists of testing strategically selected laminate configurations and analyzing the results using composite mechanics. Results from the investigation show that the contributions to nonlinear behavior are due to: premature random fiber breaks where the ply orientation angle (POA) is small relative to the load direction, ply relative rotation (PRR) at intermediate values of the POA, and nonlinear aluminum matrix behavior at large values of the orientation angle. Premature fiber breaks result in progressively more complaint material; large PRR result in progressively stiffer material; and, pronounced matrix nonlinear behavior results in no significant change in the modulus of the initial portion of the stress-strain curve.

KEY WORDS: composite materials, boron, aluminum, laminates, responses, cyclic loads, fibers, fracturing, rotation, experimentation, stress analysis

Boron/aluminum angleplied laminates exhibit nonlinear stress-strain relationships at relatively low loads [*1*] [2] as compared with their fracture load. The primary factors that may contribute to this nonlinearity are: early aluminum matrix nonlinear response; premature random fiber fractures; and, ply relative rotations (PRR). The amount each factor con-

[1] Aerospace engineers, Composites and Structures Branch, NASA-Lewis Research Center, Cleveland, Ohio 44135

[2] The italic numbers in brackets refer to the list of references appended to this paper.

tributes depends on the ply orientation. This paper assesses the effects of the aforementioned factors on the nonlinear response of boron/aluminum angleplied laminates under monotonic and cyclic tensile load.

The procedure followed for the assessment consisted of both experimental and approximate theoretical investigations. The experimental investigation consisted of testing selected boron/aluminum angleplied laminates in cyclic tension. The laminates selected had low, intermediate, and high ply orientation angles (POA) relative to the load direction. Specimens with some low POA were selected to assess the influence of premature fiber fractures on nonlinear response. Those of intermediate angles were selected to assess the PRR (scissoring effect), and those of high angles, for the influence of the matrix. Since the focus of the investigation was on nonlinear response, the specimens were loaded well into the nonlinear stress-strain regime and, therefore, failed in a few cycles.

In the theoretical investigation, well known strain transformations were used in conjunction with the strain-magnification-factor (SMF) concept [*2,3*] to determine the strains in the plies, the maximum strains in the matrix, and the changes in the fiber direction. The emphasis of this investigation is on how an assessment can be obtained of the factors contributing to composite nonlinear response using measured strains from a few strategically selected test specimens and available, approximate, theoretical methods. In this sense, the approach can be used as a procedure for obtaining such an assessment. A more detailed stress analysis may be obtained by using nonlinear finite element methods.

In this paper, the term "yield" is used to denote the onset of nonlinear stress-strain behavior in the matrix rather than its classical plasticity meaning.

Experimental Investigation

Material, Test Apparatus, and Procedure

The composite material for this investigation was 4-mil-boron fiber and 6061-O aluminum foil which was fabricated into 12-in.-square plates by a supplier using a conventional diffusion bonding process. Fiber volume was approximately 50 percent. The laminate configurations were of the form $(0_2°, \pm\theta°)_s$ where θ was 15, 30, 45 and 90 deg and are identified as plates C, D, E, and F, respectively, see Ref *1*. Coupons were cut at specified angles from the plates by shearing. The background for specimen selection is given in the theoretical investigation. The sheared edges of the specimens were ground with a diamond wheel to produce a coupon with smooth edges and a 0.500 in. width. The specimen configuration, notation, ply orientation and specimen length are depicted in Fig. 1. The

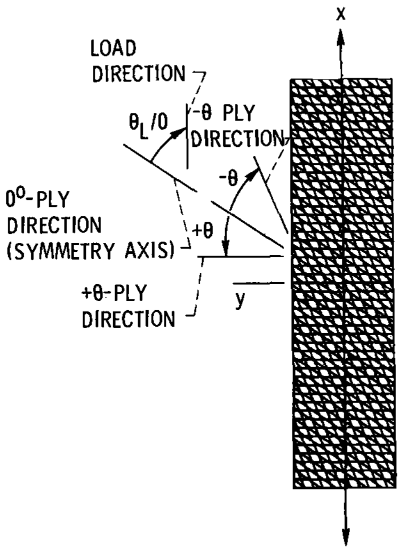

PLY ORIENTATION, LOAD DIRECTION & LENGTH

SPECIMEN, DEG	θ, DEG	$\theta_L/0$, DEG	LENGTH, IN.
C-80	15	-80	10.0
D-22.5	30	-22.5	10.0
D-80	30	-80	10.0
E-37.5	45	-37.5	9.60
F-37.5	90	-37.5	9.60

FIG. 1—*Schematic of specimen geometry 8(0,0,+θ,−θ,−θ,+θ,0,0) boron/aluminum angleplied laminate.*

fiber directions relative to the load direction are shown schematically in Fig. 2. Photomicrographs of specimen cross sections are shown in Fig. 3. Each coupon was instrumented with strain gage rosettes. The coupons were clamped in serrated, bolted grips (Fig. 4) and cyclicly loaded to failure in a hydraulic universal testing machine. The maximum load of each successive cycle was increased to ensure failure in relatively few cycles. Loading was halted at intervals for acquiring strain gage data on a digital strain recorder.

The strain gage data were reduced using a computer program [*4*]. This program calculated the strains along the load direction and normal to it, taking into account strain gage transverse sensitivity. It also provided instantaneous tangent modulus of elasticity, Poisson's ratio, the extension-shear coupling ratio, and the angular change of the principal strain axes.

Theoretical Investigation

Theoretical Background

In order to identify and assess the factors contributing to composite nonlinear response the strain states in the composite, plies, and matrix are required as a minimum. In this investigation, the strain state in the

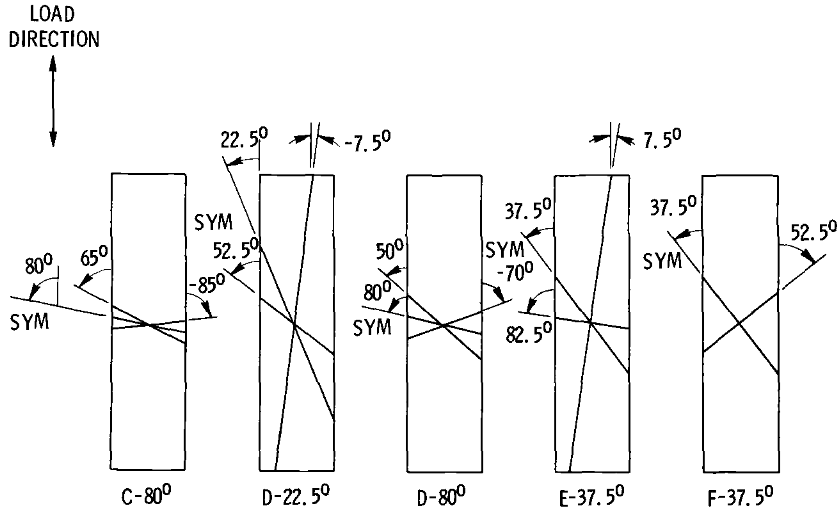

FIG. 2—*Schematic depicting the fiber directions in the various specimens.*

composite was measured using delta rosette strain gages.[3] When the composite strain state is known, the other strain states can be determined using available theoretical methods. The underlying theoretical concepts and the equations to be used in the computations are briefly described herein.

Since the strains are kinematic quantities and since three strains are known at a point from the strain gage readings, strains along any ply orientation are determined by well known transformations. The implicit assumption in this transformation is that the strain is constant through the specimen thickness. This assumption is valid so long as no delamination takes place. No delamination was observed in the specimens tested in this program.

Once the ply strains are known, the maximum strains in the matrix are obtained as follows

$$\epsilon_{m11} = \epsilon_{l11} \tag{1}$$

$$\epsilon_{m22\max} = \text{SMF}_{22}\epsilon_{l22} \tag{2}$$

$$\epsilon_{m12\max} = \text{SMF}_{12}\epsilon_{l12} \tag{3}$$

where ϵ_l is the strain in the ply and ϵ_m is the strain in the matrix. The subscript l denotes a measurement along the fiber direction and 2, normal to it.

The SMF used are given by the following approximate equations

[3] Micro-measurements gage type EA-13-030YB-120.

$$\mathrm{SMF}_{22} = \frac{1}{1 - p\left(1 - \dfrac{E_m}{E_f}\right)} \tag{4}$$

$$\mathrm{SMF}_{12} = \frac{1}{1 - p\left(1 - \dfrac{G_m}{G_f}\right)} \tag{5}$$

$$p = \left(\frac{4k_f}{\pi}\right)^{1/2} \tag{6}$$

G_m, $E_m \rightarrow 0$ as the matrix becomes highly nonlinear.

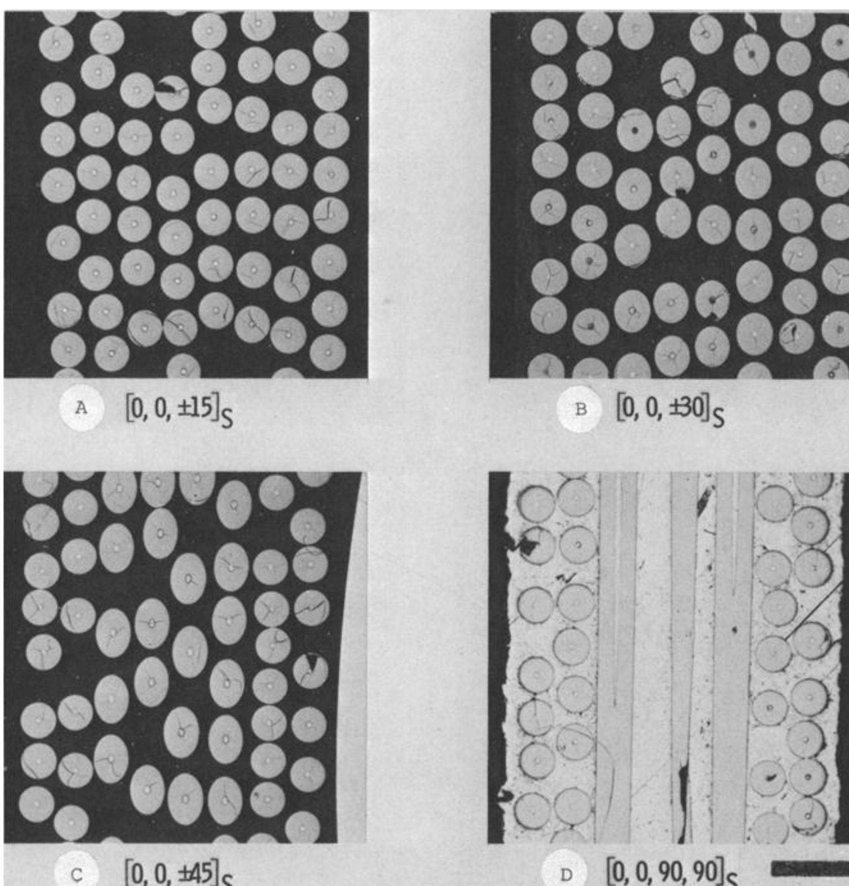

FIG. 3—*Photomicrographs of cross section of boron/aluminum angleplied laminates (×75).*

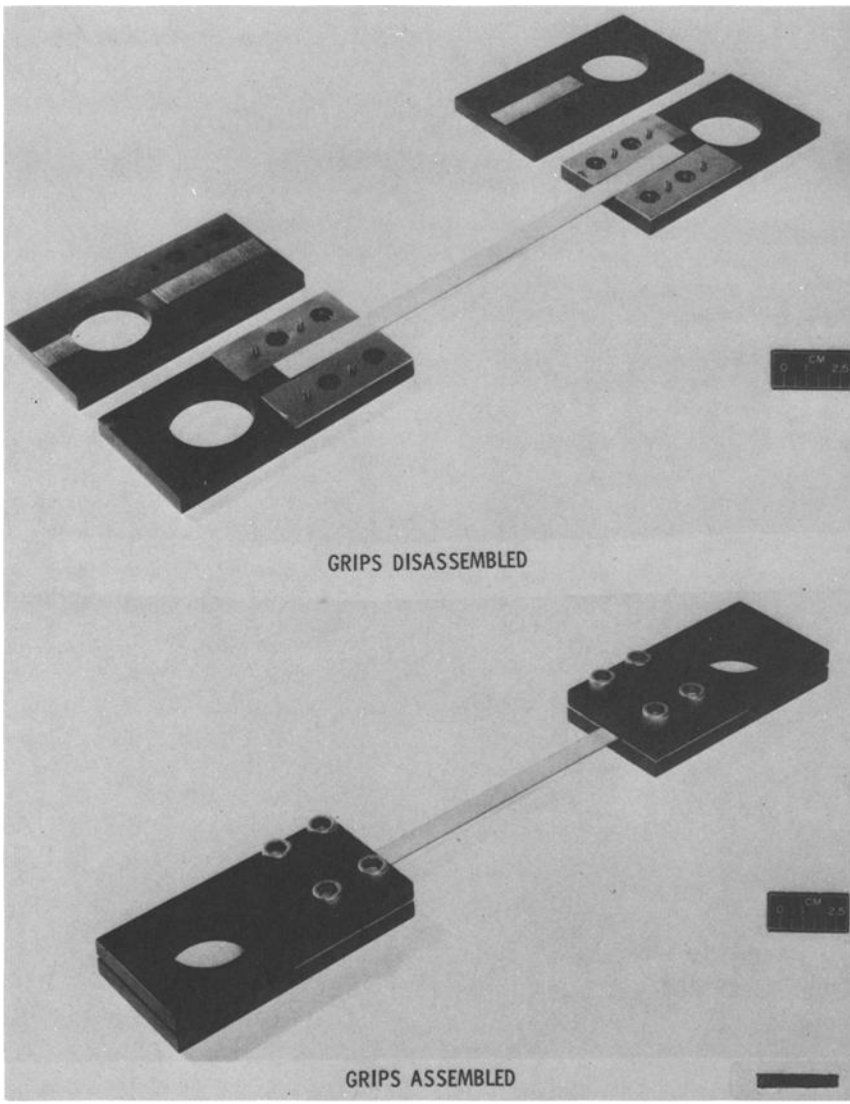

FIG. 4—*Boron/aluminum angleplied laminate test specimen and grips.*

The undefined notation in Eqs 4, 5, and 6 is as follows: E is the modulus of elasticity, G is the shear modulus; the subscripts f and m denote fiber and matrix, respectively; and, k_f is the fiber volume ratio.

The values for the moduli used in this calculation were: $E_f = 60 \times 10^6$ psi; $E_m = 10 \times 10^6$ psi if $\epsilon_{m22} < 0.001$ and $E_m = 0$ if $\epsilon_{m22} \geqslant 0.001$; the ratio of $G_m/G_f = 1/6$ if $\epsilon_{m12} \leqslant 0.002$; and, $G_m/G_f = 0$ if $\epsilon_{m12} > 0.002$. The strain limits of 0.001 and 0.002 were determined from normal and shear stress-strain curves, respectively.

The ply strains were computed from the measured strains by the following well known transformation equation

$$\begin{Bmatrix} \epsilon_{l11} \\ \epsilon_{l22} \\ \epsilon_{l12} \end{Bmatrix} = \begin{bmatrix} \cos^2\theta_l & \sin^2\theta_l & \frac{1}{2}\sin 2\theta_l \\ \sin^2\theta_l & \cos^2\theta_l & -\frac{1}{2}\sin 2\theta_l \\ -\sin 2\theta_l & \sin 2\theta_l & \cos 2\theta_l \end{bmatrix} \begin{Bmatrix} \epsilon_{cxx} \\ \epsilon_{cyy} \\ \epsilon_{cxy} \end{Bmatrix} \tag{7}$$

where θ_l is the angle between the load and the direction of the fibers in the ply under consideration and is given by $\theta_l = \theta_{L/O} + \theta$ (see Fig. 1); ϵ_{cxx} is the measured strain in the laminate along the load direction; ϵ_{cyy} is the measured strain normal to the load direction, and, ϵ_{cxy} is the corresponding shear strain.

The change in the fiber direction can be determined from the last equation of Eq 7 (see Ref *3* or *5*).

The instantaneous change of the principal-strain axes as a function of load is another measure of nonlinear response especially for nonsymmetrically loaded specimens. By definition, the principal-strain axes comprise a set of axes on which the shear strains are equal to zero. The equation for the principal-strain axes is given by

$$\theta = \frac{1}{2}\tan^{-1}\left(\frac{\epsilon_{cxy}}{\epsilon_{cxx} - \epsilon_{cyy}}\right) \tag{8}$$

where θ is the angle between the load direction and the ϵ_{11} axis of the principal-strain axes. The composite strains, ϵ_c, have been already defined. Equation 8 is derived from the last equation of Eq 7 by letting $\theta_l = \theta$ and requiring ϵ_{l12} to equal zero.

In addition to the above mentioned calculations, the equivalent modified-total strain (or equivalent strain for convenience) in the matrix was calculated. The general equation for calculating this strain is given by [6]

$$\epsilon_e = \frac{\sqrt{2}}{3}\left[(\epsilon_x - \epsilon_y)^2 + (\epsilon_y - \epsilon_z)^2 + (\epsilon_z - \epsilon_x)^2 + 6(\epsilon_{xy}^2 + \epsilon_{yx}^2 + \epsilon_{zx}^2)\right]^{1/2} \quad (9)$$

where ϵ_x, etc. are the normal strains along a mutually orthogonal coordinate axes and ϵ_{xy}, etc. are the shear strains associated with these normal strains. For the present case, the strains ϵ_z, ϵ_{xz} and ϵ_{yz} represent strains in the matrix through the specimen thickness and were assumed to be negligible compared to the other strains. With this assumption and using the previous notation, Eq 9 reduces to

$$\epsilon_{me} = \frac{\sqrt{2}}{3}\left[2(\epsilon_{m11}^2 + \epsilon_{m22}^2 - \epsilon_{m11}\epsilon_{m22}) + 6\epsilon_{m12}^2\right]^{1/2} \quad (10)$$

where ϵ_{me} is the equivalent strain in the matrix, and the other strains have been defined previously.

The equivalent strain concept is useful in performing approximate stress analyses in the presence of material nonlinearities. Our interest is to obtain some indication as to whether this approach may be applicable to the present problem.

The foregoing approach for determining the maximum strains in the matrix has several advantages over more refined analyses. These advantages include simplicity, amenable to quick hand computations, no required detailed knowledge of the nonlinear material properties, no required calculation of the stresses in the ply. Its main disadvantage is that it only yields a good approximation of the maximum strains in the matrix. It provides no direct means for determining the strain variation in the matrix or the stresses in the plies. However, this approach can be used in conjunction with an incremental nonlinear analysis to facilitate estimation of material properties for the current increment.

It should be noted that the measured strains do not include residual strains. In the following discussion, the influence of the residual stress is not considered separately. Its presence produces nonlinear behavior in the matrix at relatively low loads [1] which is picked up by the strain gage as a mechanical load effect.

Specimen Selection Background

Some remarks with regard to the anticipated results will help set the stage for the discussion that follows. The ply orientations (fiber directions) in the specimens selected are shown in Fig. 2. These configurations were selected because when the specimens were loaded, as noted in Fig.

2, one of the factors mentioned earlier contributes a significant part to nonlinear response with some interaction from the other factors. For example, the matrix will contribute the major portion to the nonlinear response in specimens C-80° and D-80°. Premature fiber fracture will contribute to the nonlinear response of specimens D-22.5° and E-37.5°. Ply relative rotation will contribute to the nonlinear response of specimen F-37.5°.

Specimens D-22.5° and E-37.5° are loaded more unsymmetrically than the other specimens. These specimens will exhibit considerable change in the principal-strain-axes direction during each loading cycle and from loading cycle to loading cycle. The other specimens will exhibit only small changes in the principal-strain-axes direction. Specimens D-22.5° and E-37.5° will exhibit some PRR.

The foregoing remarks lead to specific criteria for identifying and assessing factors contributing to the nonlinear response of boron/aluminum angleplied laminates as will be described.

Criteria for Assessing Factors Contributing to Nonlinear Response

Two criteria will be used for identifying and assessing the importance of the factors contributing to the nonlinear response. The primary criterion is the change of the specimen instantaneous (tangent) modulus during the *initial portion* of the *loading* with successive cycles. Specifically:

(*a*) Negligible changes in modulus with successive loading cycles indicate that the matrix is the major contributor.

(*b*) Decreases in modulus with successive loading cycles indicate that premature fiber fracture is the major contributor.

(*c*) Increases in modulus with successive loading cycles indicate that PRR is the major contributor.

The secondary criterion to be used is the shape of the load versus strain curve. Specifically:

(*a*) When the matrix is the major contributor, the curve will be analogous to that of a material showing strain hardening, that is, linear unloading response and little or no hysteresis.

(*b*) When premature fiber fracture is a significant contributor, the unloading portion of the curve will be linear initially, with a smaller slope than the corresponding loading part, followed by a nonlinear portion analogous to Bauschinger effect. The reason for this is that fiber fractures cause excessive localized matrix nonlinearities. Upon unloading, these local nonlinearities go into compression and yield in compression long before the specimen is completely unloaded. The curve for this case will show considerable hysteresis.

Also, during unloading, it is possible for the matrix to go into nonlinear compression without premature fiber fractures. This will be the case when the longitudinal tensile strain in some plies is greater than the yield strain of the matrix. However, for this case the modulus of elasticity of the initial portion of both unloading and next-cycle-loading curves will be approximately equal to the corresponding portion of the previous cycle.

(*c*) When PRR is a significant contributor, the unloading curve will be linear with no or little hysteresis, so long as *no* severe matrix shear "yielding" takes place [7]. The curve will show a higher strain hardening rate than the curve for case (*a*). The reason for this is that the PRR is caused by fiber direction changes which tend to decrease the angle between fiber and load directions for the tensile load case. This results in a stiffer material and, therefore, a steeper strain hardening slope.

Results and Discussion

Nonlinear Response of the Specimens Tested and Assessment of Contributing Factors

In view of the secondary criterion, a convenient way for assessing factors contributing to nonlinear response is to plot tensile load in the specimen versus composite strain along the load direction (axial strain). This is a stiffness curve and reflects the effects of any cross-section changes.

Tensile cyclic load versus axial strain plots were made for all the

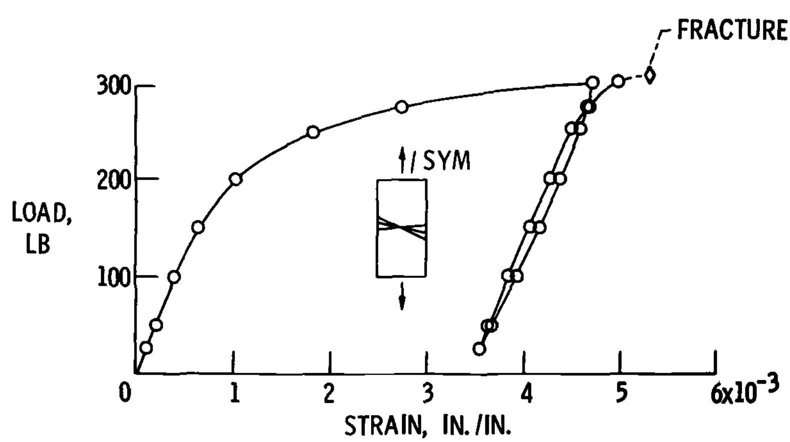

FIG. 5—*Experimental nonlinear cyclic load response of boron/aluminum angleplied laminate C-80° 8(0,0, ± 15, ∓ 15,0,0) loaded in tension at −80° to the 0°-ply direction. (4-mil-diameter fiber; fiber volume ratio ≈ 0.5; 6061-O aluminum alloy.)*

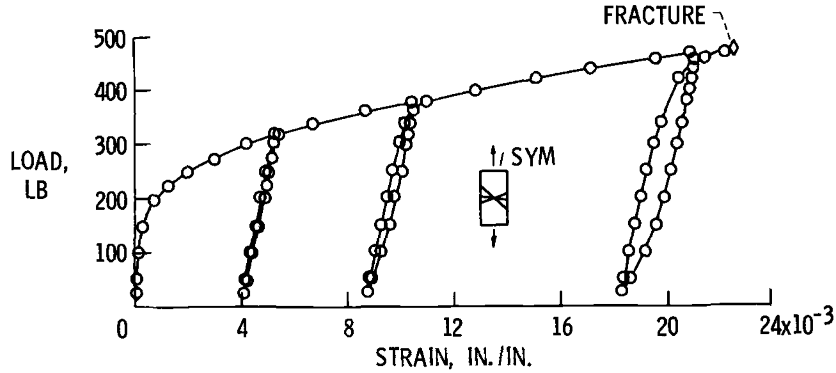

FIG. 6—*Experimental nonlinear cyclic load response of boron/aluminum angleplied laminate D-80° 8(0,0,±30,∓30,0,0,) loaded in tension at —80° to the 0°-ply direction. (4-mil-diameter fiber; fiber volume ratio ≈ 0.5; 6061-O aluminum alloy.)*

specimens tested. The results are shown in Figs. 5–9. Applying the secondary criterion to these curves leads to the following observations:

(*a*) The matrix was the major contributor to the nonlinear response of specimens C-80° (Fig. 5) and D-80° (Fig. 6).

(*b*) Premature fiber fracture was a significant contributor to the nonlinear response of specimens D-22.5° (Fig. 7) and E-37.5° (Fig. 8).

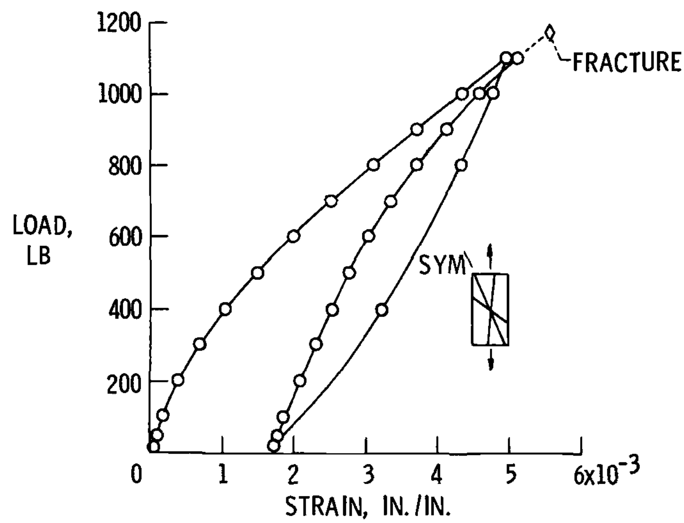

FIG. 7—*Experimental nonlinear cyclic load response of boron/aluminum angleplied laminate D-22.5° 8(0,0, ± 30, ∓ 30,0,0) loaded in tension at —22.5° to the 0°-ply direction. (4-mil-diameter fiber; fiber volume ratio ≈ 0.50; 6061-O aluminum alloy.)*

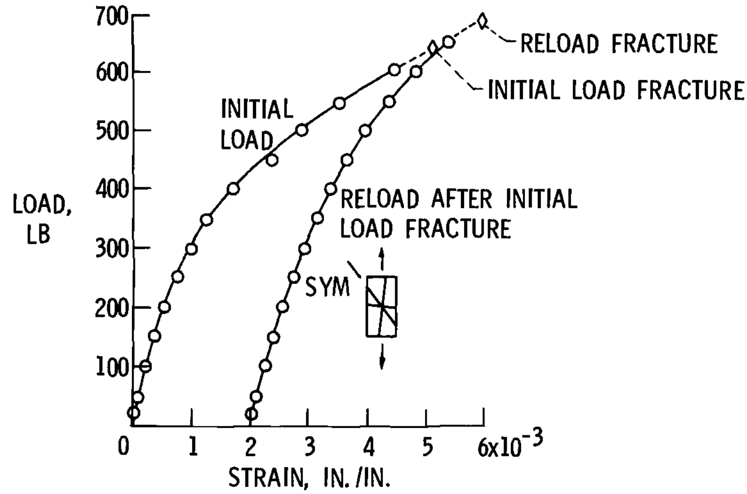

FIG. 8—*Experimental nonlinear cyclic load response of boron/aluminum angleplied laminate E-37.5° 8(0,0,±45,∓45,0,0) loaded in tension at −37.5° to the 0°-ply direction. (4-mil-diameter fiber; fiber volume ratio ≈ 0.5; 6061-O aluminum alloy.)*

Note, the nonlinear portion of the unloading curve and the relatively large hysteresis loop in Fig. 7.

(*c*) The PRR was a significant contributor to the nonlinear response of specimen F-37.5° (Fig. 9). Note, the unloading curve is linear in its entirety and the lack of hysteresis.

All of the foregoing observations are consistent with the anticipated results from the specimen selection background section. An important conclusion from the above observations is that the secondary criterion may be a sufficient condition for assessing the contribution to the composite nonlinear response of the three major factors.

The changes in the tangent modulus with successive loading cycles may be illustrated by plotting the tangent modulus versus relative axial strain. By relative strain it is meant that the residual strain from previous cycles has been subtracted. Tangent modulus versus relative axial strain was plotted for some of the specimens tested. The results are shown in Figs. 10–12. Applying the primary criterion and restricting our attention to the initial portion of the loading curve it is observed that:

(*a*) The matrix was the major contributor to the nonlinear response of specimen C-80° (Fig. 10) with some contribution from PRR.

(*b*) Premature fiber fracture was the predominant contributor to the nonlinear response of specimen D-22.5° (Fig. 11).

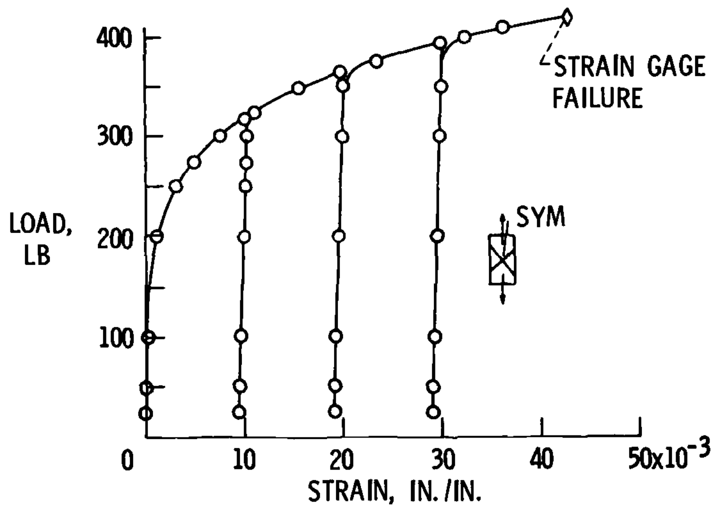

FIG. 9—*Experimental nonlinear cyclic load response of boron/aluminum angleplied laminate F-37.5° 8(0,0,4(90),0,0) loaded in tension at —37.5° to the 0°-ply direction. (4-mil-diameter fiber; fiber volume ratio ≈ 0.5; 6061-O aluminum alloy.)*

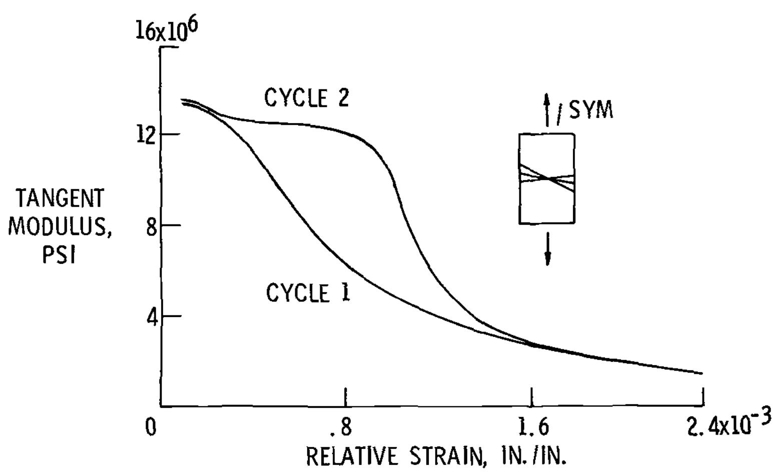

FIG. 10—*Nonlinear matrix behavior influence on modulus. Boron/aluminum angleplied laminate C-80° 8(0,0,±15,∓15,0,0) loaded —80° in tension to the 0°-ply direction. (4-mil-diameter fiber; fiber volume ratio ≈ 0.50; 6061-O aluminum alloy.)*

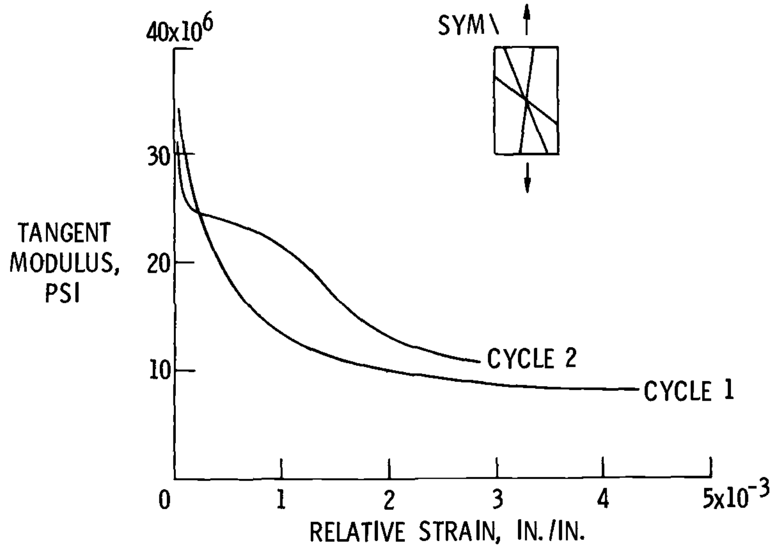

FIG. 11—*Premature fiber fracture influence on modulus. Boron/aluminum angleplied laminate D-22.5° 8(0,0,±30,∓30,0,0) loaded −22.5° in tension to the 0°-ply direction. (4-mil-diameter fiber; fiber volume ratio ≈ 0.50; 6061-O aluminum alloy.)*

(*c*) Ply relative rotation was the predominant contributor to the nonlinear response of specimen F-37.5° (Fig. 12).

These observations are in agreement with those made using the secondary criterion and are consistent with the anticipated results discussed previously.

An additional observation from the results in Fig. 12 is that the matrix strain-hardening effect on the yield strain is maximum on the second load cycle and decreases rapidly with additional cycles.

The results discussed thus far show that the significant contribution to the nonlinear response of B/Al angleplied laminates when subjected to a few cycles of tensile load was from premature random fiber breaks when the POA was small (less than 10 deg) relative to the load direction; PRR at intermediate values (35 to 55 deg) of the ply orientation angle, and, aluminum matrix nonlinear behavior at large values (greater than 70 deg) of the POA.

Principal-Strain Axes Change

The change of the principal-strain axes (θ) is a good measure of obtaining a combined measure of nonlinear response. A graphical repre-

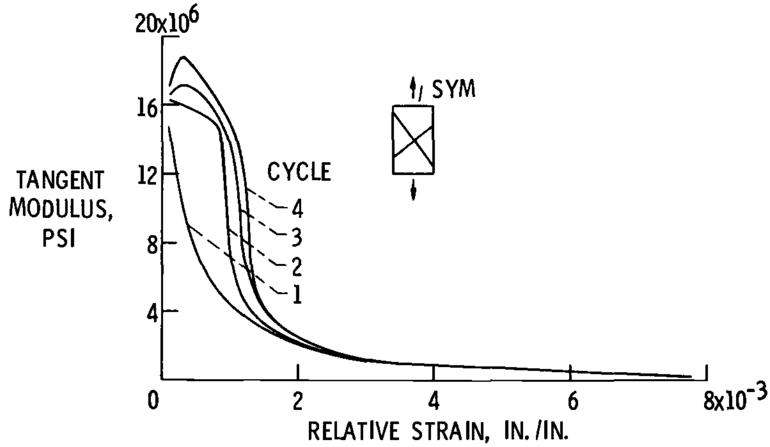

FIG. 12—*Ply relative rotation influence on modulus. Boron/aluminum angleplied laminate F-37.5° 8(2(0),4(90),2(0)) loaded at —37.5° in tension to the 0°-ply direction. (4-mil-diameter fiber; fiber volume ratio ≈ 0.50; 6061-O aluminum alloy.)*

sentation of this change may be obtained by plotting θ versus initial-area stress or relative axial strain.

A plot of θ versus relative axial strain is shown in Fig. 13 for all the specimens tested. As can be readily observed in Fig. 13, the instantaneous values of θ increase with increasing relative strain. The maximum

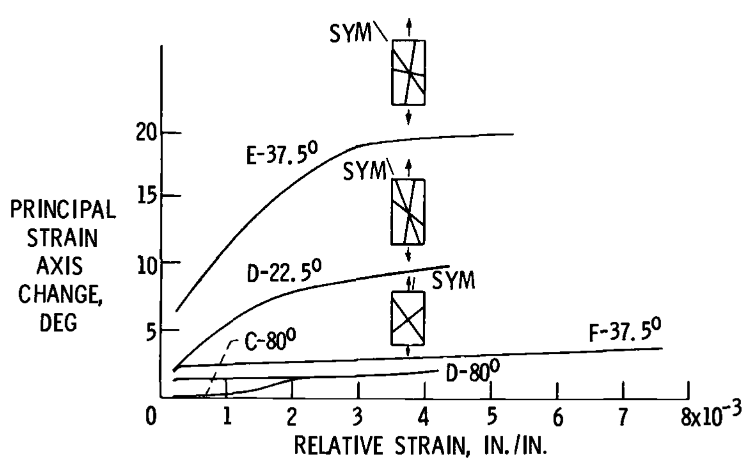

FIG. 13—*First cycle principal-strain axis change with strain. Boron/aluminum angleplied laminates loaded in tension as noted in the figure. (4-mil-diameter fiber; fiber volume ratio ≈ 0.50; 6061-O aluminum alloy.)*

values of θ are less than 4 deg for specimens C-22.5°, D-80°, and F-37.5°; about 10 deg for specimen D-22.5°; and about 20 deg for specimen E-37.5°. As can be seen from the schematics in Figs. 13 or 2, low values of θ correspond with specimens whose axis of symmetry is nearly coincident with the load direction. The converse is true for the larger θ values.

Two points need be made in connection with the above discussion: (*a*) upon unloading, the major portion of the θ value remains as residual angle; and, (*b*) fiber direction shifts are possible with large or progressively larger values of θ.

Maximum Matrix Strains

The maximum strains in the matrix were computed using Eqs 1–6. The variation of the maximum transverse matrix strain with composite stress is shown in Fig. 14 for all the specimens tested. Note that the transverse strain increases very rapidly at about the same value of composite stress in specimens (C-80° and D-80°) where the matrix carried the major portion of the load. In the specimens where the fibers carried the major portion of the load (D-22.5° and E-37.5°), the maximum transverse strain was significantly less. This indicates that once the matrix becomes nonlinear its load-carrying ability is small.

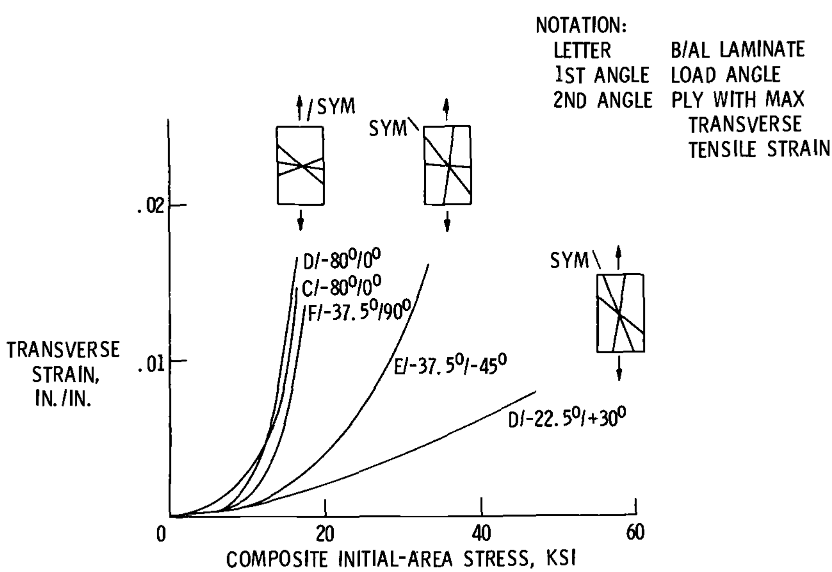

FIG. 14—*The effect of composite stress on the maximum transverse matrix strain. Boron/aluminum angleplied laminates loaded in tension at various angles to the 0°-ply direction. (4-mil-diameter fiber; fiber volume ratio ≈ 0.50; 6061-O aluminum alloy.)*

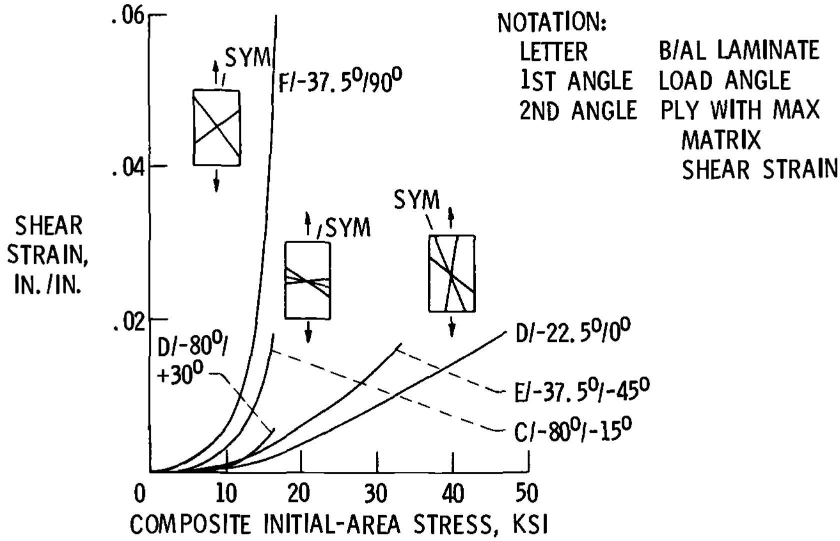

FIG. 15—*The effect of composite stress on the maximum shear matrix strain. Boron/aluminum angleplied laminates loaded in tension at various angles to 0°-ply direction. (4-mil-diameter fiber; fiber volume ratio ≈0.50; 6061-O aluminum alloy.)*

The previous discussion leads to the following conclusion. The maximum transverse tensile strain in the matrix may be used as a criterion to identify plies or composites or both in which the matrix carries the major portion of the load. This strain increases very rapidly at some composite stress value indicating onset of pronounced matrix nonlinearity.

The maximum shear strain in the matrix is plotted versus composite initial-area stress in Fig. 15 for all the specimens tested. The important point to be observed in Fig. 15 is the very large shear strain for the specimen F-37.5° as compared with the other specimens. It is this large shear strain that causes PRR (scissoring effect). The conclusion is, then, that very large shear strains in the matrix may be used as a criterion to identify plies undergoing PRR. Advantage may be taken of this observation in practical designs where the need for the structural part is to become stiffer with successive loading cycles.

The equivalent strain in the matrix may also be used as a combined index to assess composite nonlinear response. The equivalent strain is plotted versus composite initial-area stress in Fig. 16 for all the specimens tested. Comparing the curves in Fig. 16 with the corresponding ones in Fig. 15, it is seen that the equivalent strains are similar to the maximum shear strains. This is anticipated from Eq 1 where it is seen that the shear

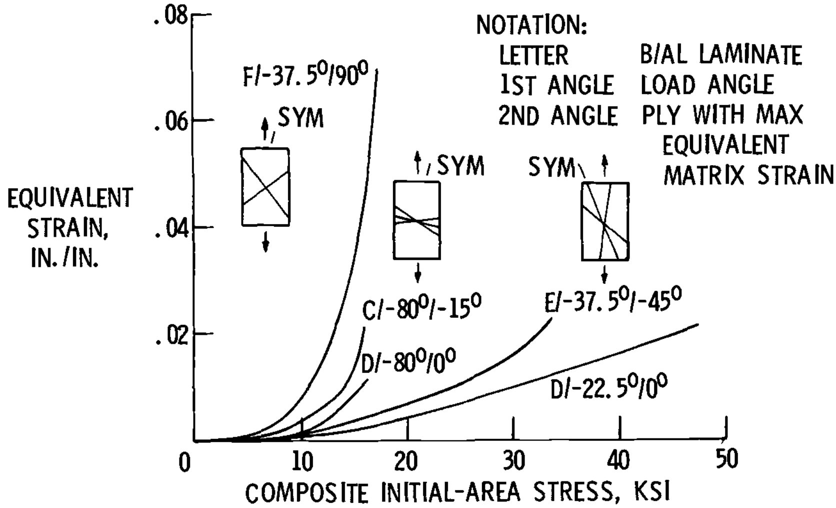

FIG. 16—*The effect of composite stress on equivalent matrix strain. Boron/aluminum angleplied laminates loaded in tension at various angles to 0°-ply direction. (4-mil-diameter fiber; fiber volume ratio ≈ 0.50; 6061-O aluminum alloy.)*

strain terms ϵ_{m12} has the largest multiplier. We conclude, therefore, that the equivalent strain in the matrix does not provide any more information than the maximum shear strain in the matrix.

As a side note, the equivalent strain in the matrix is used to carry out nonlinear stress analysis of fiber composites based at the constituents level. The equivalent strain approach presupposes isotropic yielding or deviations from linearity. In view of the yielding directionality forced on the matrix by the restraining fibers, the isotropic yielding assumption might be premature.

Changes in Fiber Direction

It was mentioned in the theoretical background section that the change in the fiber direction may be computed from the last equation of Eq 7. An assessment on the fiber direction change may be obtained by plotting the fiber direction change versus composite initial-area stress or relative axial strain.

The fiber direction change versus composite initial-area stress is plotted in Fig. 17 for the specimens tested. Note that the curves in Fig. 17 are similar to those in Fig. 15 for maximum shear stress in the matrix. This should be so since they both were computed using the same equation but with different multipliers. The conclusion, therefore, is that excessively

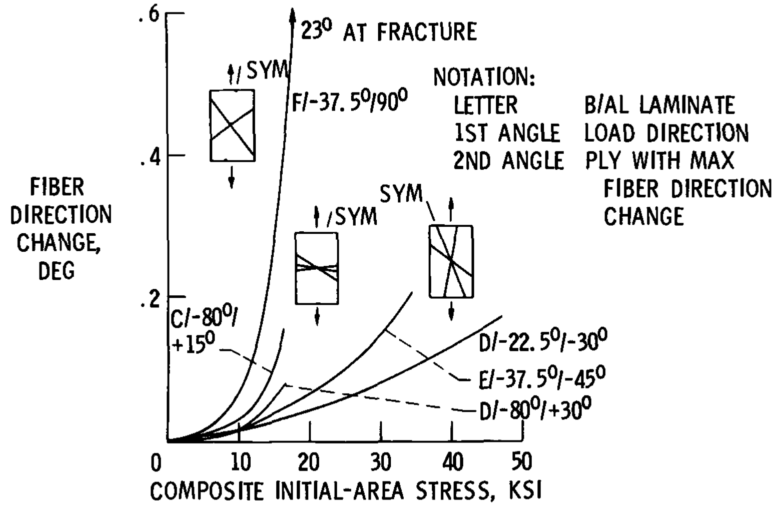

FIG. 17—*The effect of composite stress on fiber direction change. Boron/aluminum angleplied laminates loaded in tension at various angles to the 0°-ply direction. (4-mil-diameter fiber; fiber volume ratio ≈ 0.50; 6061-O aluminum alloy.)*

large shear strains in the matrix produce corresponding changes in the fiber direction. As is seen in Fig. 17, the maximum change in fiber direction was in the F-37.5° as was expected.

As a side note, the computed change in angle between the 0 and 90 deg plies in the F-37.5° laminate was about 3.2 deg at the end of the third loading cycle. The measured change in angle when the specimen broke was about 23 deg corresponding to a 20 percent width reduction.

Summary of Results

The following are the important results obtained from an investigation of boron/aluminum angleplied laminates subjected to cyclic tensile loading.

A procedure has been described and criteria have been proposed which can be used to assess the factors contributing to nonlinear response of fiber composite angleplied laminates when subjected to tensile cyclic loading.

The results of the specimens tested and analyzed showed that the significant contribution to the nonlinear response of B/Al angleplied laminates when subjected to a few cycles of tensile load was from: premature random fiber breaks when the POA is small (less than 10 deg) relative to the load direction; PRR at intermediate values (35 to 55 deg) of the POA;

and, aluminum matrix nonlinear behavior at large values (greater than 70 deg) of POA.

Premature fiber breaks result in a progressively more compliant material with considerable nonlinearity in the unloading curve and a significant amount of hysteresis.

Ply relative rotation results in a progressively stiffer material with linear unloading and little or no hysteresis.

Pronounced matrix nonlinear behavior results in: no significant changes in stiffness with successive load cycles; linear unloading; and, little hysteresis which seems to grow larger with successive cycles. The strain hardening effects on the yield strain are significant from the first to the second cycle and appear to diminish thereafter.

Nonsymmetrically loaded B/Al angleplied laminates exhibit significant changes in the direction of the principal strain axes which becomes progressively larger. The major portion of this change remains as residual.

Pronounced matrix nonlinear behavior is the result of large transverse strain in the matrix. This strain increases very rapidly at about the 0.1 percent value of the relative axial strain for the specimens tested.

Ply relative rotation (fiber direction change) is caused by large shear strains in the matrix. The specimen used to test this condition accumulated a PRR of about 23 deg when it fractured.

References

[1] Chamis, C. C. and Sullivan, T. L., "Theoretical and Experimental Investigation of the Nonlinear Behavior of Angleplied Boron/Aluminum Composites," NASA TM X-68205, National Aeronautics and Space Administration, Washington, D. C., 1973.

[2] Chamis, C. C., in *Composite Materials: Testing and Design, ASTM STP 460*, American Society for Testing and Materials, 1969, pp. 336–351.

[3] Chamis, C. C., "Computer Code for the Analysis of Multilayered Fiber Composites-User's Manual," NASA TN D-7013, National Aeronautics and Space Administration, Washington, D.C., 1971.

[4] Chamis, C. C., Kring, J. F., and Sullivan, T. L., "Automated Testing Data Reduction Computer Program," NASA TM X-68050, National Aeronautics and Space Administration, Washington, D. C., 1972.

[5] Chamis, C. C., "Important Factors in Fiber Composite Design," Part 1, *Modern Plastics*, Sept. 1969.

[6] Mendelson, A., *Plasticity Theory and Application*, Macmillan, N. Y., 1968, pp. 123–125.

[7] Dieter, G. E.. *Mechanical Metallurgy*, McGraw-Hill, N. Y., 1961, pp. 112.

W. W. Stinchcomb,[1] *K. L. Reifsnider,*[1] *L. A. Marcus,*[1] *and R. S. Williams*[1]

Effects of Frequency on the Mechanical Response of Two Composite Materials to Fatigue Loads

REFERENCE: Stinchcomb, W. W., Reifsnider, K. L., Marcus, L. A., and Williams, R. S., **"Effects of Frequency on the Mechanical Response of Two Composite Materials to Fatigue Loads,"** *Fatigue of Composite Materials, ASTM STP 569,* American Society for Testing and Materials, 1975, pp. 115–129.

ABSTRACT: A new class of mechanical response characteristics in composite materials is reported. These characteristics were found to come about because of a nonlinear dependence of the fatigue response of biasply boron-aluminum and boron-epoxy flawed plate specimens on the frequency of load (or strain) oscillation. This nonlinear frequency effect was found to alter such properties as fatigue strength, stiffness, residual strength, and energy dissipation by as much as an order of magnitude. Several conceptual interpretations are developed and compared with data correlations.

KEY WORDS: composite materials, fatigue tests, frequencies, damage, mechanical properties, heat, temperature, energy dissipation

Under many common circumstances, it would appear that composite materials are superior to metals in their fatigue resistance. However, our present understanding of fatigue and fatigue damage in these inhomogeneous materials is quite incompletely developed. This is due, in part, to the fact that there are at least three basic differences between the fatigue phenomenon in composite materials and the fatigue response of more common structural materials such as steel, aluminum, and titanium. The first of these comes about because a single fatigue crack which propagates through a (composite) component to cause failure

[1] Assistant professor, associate professor, graduate research assistant, and instructor, respectively, Department of Engineering Science and Mechanics, Virginia Polytechnic Institute and State University, Blacksburg, Va. 24061.

rarely occurs in the singular manner identified with homogeneous materials. Instead, fatigue damage consists of various combinations of matrix cracking, debonding, delamination, void growth, and fiber breakage. As a result, fatigue cannot be defined in terms of a single failure mode and, indeed, a single criterion for fatigue failure is difficult to choose.

A second difference stems from the fact that a common consequence of fatigue in composites is a reduction in stiffness which begins very early in the fatigue life and reaches significant magnitudes long before the component actually breaks [*1*].[2] Consequently, it is possible that fatigue "failure" should be defined in terms of stiffness reduction for certain applications.

A third basic difference has recently been discovered by the authors and is the subject of the present discussion. It has been determined that the eightply boron-aluminum (B/Al) and boron-epoxy (B/Ep) specimens investigated exhibit a nonlinear dependence on the frequency of load (or strain) oscillation which may alter such properties as residual stiffness, residual strength, and dissipated energy rate by as much as an order of magnitude. The dissipated energy rate controls the amount of heat generated during fatigue testing. In previous reports, the authors found that the resulting temperature rise in these materials could be the order of 70°F for B/Ep and 35°F for B/Al [*2,3*]. Using a video-thermography device, it was found that the real-time surface temperature patterns showed great similarity to known stress distributions during early testing and subsequently changed, indicating the positions and amount of damage development. It was found that the heat emission was very sensitive to frequency, but that the dependence appeared to have maxima and minima, that is, was nonlinear in some cases. This fact and other related ones [*4*] precluded the exclusive explanation of these effects on the basis of rate-dependent (viscoelastic) models, and obviated the contribution of cycle-dependent (mechanical hysteresis) behavior. The latter is intimately associated with damage development and dominates near the end of the fatigue life. Marcus and Stinchcomb have shown that the rate-dependent heat emission is closely related to stress and distortional energy distributions before damage develops by solving the three dimensional boundary value problem using a finite element scheme [*5,6*].

It now appears that the other two basic differences in fatigue response (stiffness change and fracture mode complexity) are also very dependent on frequency of load (or strain) oscillation, even when *all* other param-

[2] The italic numbers in brackets refer to the list of references appended to this paper.

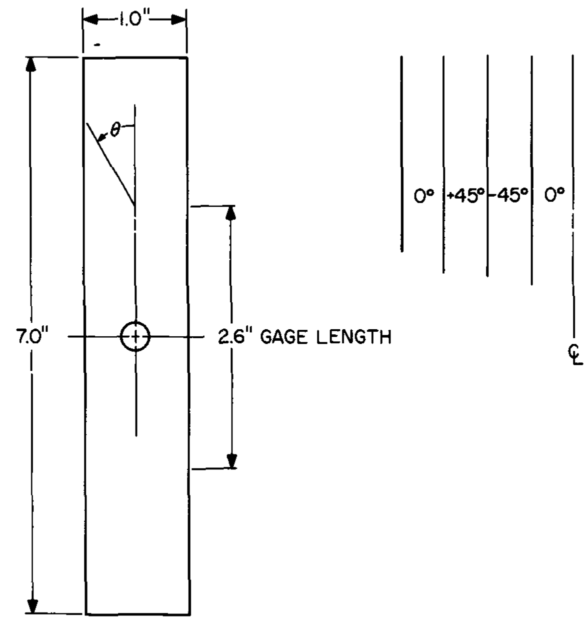

FIG. 1—*Geometry of the boron-aluminum fatigue specimens.*

eters are held constant. First evidence of this appeared in an earlier report [*7*]. In fact, the nonlinear frequency dependence has been more firmly established by our recent investigations [*8*] including the work reported herein. Quite recently the frequency dependent fatigue response of B/Ep was confirmed by an independent investigator.[3] The present paper deals with the effects of this newly discovered frequency dependence on the mechanical properties of B/Al and B/Ep. Failure modes will be discussed in a later report.

Experimental Procedure

The B/Al specimens (Fig. 1) were eightply $[0, \pm 45, 0]_s$ laminates while the eightply B/Ep specimens had a [0, ±45, 0, 0, ±45, 0] fiber orientation. The B/Ep specimens were layed up with Avco 5505 boron tape and had a fiber content of 55 to 60 percent with a maximum void content of five percent. The B/Al specimens had a 50 volume percent of a 5.6-mil-uncoated boron filament embedded in a 6061 aluminum matrix. Each specimen had an 0.25-in.-diameter center hole which was ultrasonically cut in the B/Ep and punched in the B/Al.

[3] Heller, R. A., private communication.

The fatigue tests were conducted using an MTS servo-hydraulic testing system using standard wedge grips with very fine serrations. It was found that wrapping the ends of the specimen with one thickness of emory paper prevented grip failures even in non-flawed specimens.

Strain controlled cyclic tests of two types were conducted on specimens of both materials for the frequency range 0.5 to 45 Hz. In what will be referred to as cyclic stress-strain tests [7,9], specimens were subjected to incremental steps of controlled cyclic strain amplitude until failure such that, for each strain level, the specimen was cycled through six modulations (triangular form) of linearly increasing, then decreasing, programmed tensile strain amplitude. Such tests were performed on specimens of both materials at selected cyclic frequencies to establish the cyclic stress-strain behavior, as a function of frequency, of the two materials.

The second type of test was a strain controlled tension-tension fatigue test with a nominal maximum strain of 60 percent of the average fracture strain as determined from the cyclic stress-strain data. For the B/Ep specimens, the ratio of minimum strain to maximum strain was 0.20; and for the B/Al, the ratio was 0.32 (several B/Al tests were conducted at a ratio of 0.36). The tests were conducted at selected frequencies of 1, 15, 30 and 45 Hz and were terminated following a significant decrease in load stiffness which, in most cases, occurred before 2.5 million cycles for the strain amplitudes used. Following the fatigue tests, "post-mortem" cyclic stress-strain tests (similar to those described previously) were conducted on the damaged specimens to provide data on residual behavior for comparative purposes.

Cyclic load and strain data were recorded on magnetic tape and played back at reduced speed for analysis of changes in hysteresis characteristics as a function of frequency and applied strain cycles. Heat generation was monitored using a thermographic camera with ten color isotherm display unit for field measurements and thermocouples for point-wise measurements.

Results

Figure 2 shows the change in load (or remote stress) and variation of local temperature at a point on the specimen horizontal axis near the edge of the hole during strain controlled 30-Hz fatigue tests of B/Ep and B/Al. In comparison, the two materials exhibit similar trends for both stress and surface temperature although there is, in B/Ep, an initial sharp temperature rise and generally higher local temperature throughout the test. A definite correlation is seen between the decreasing load

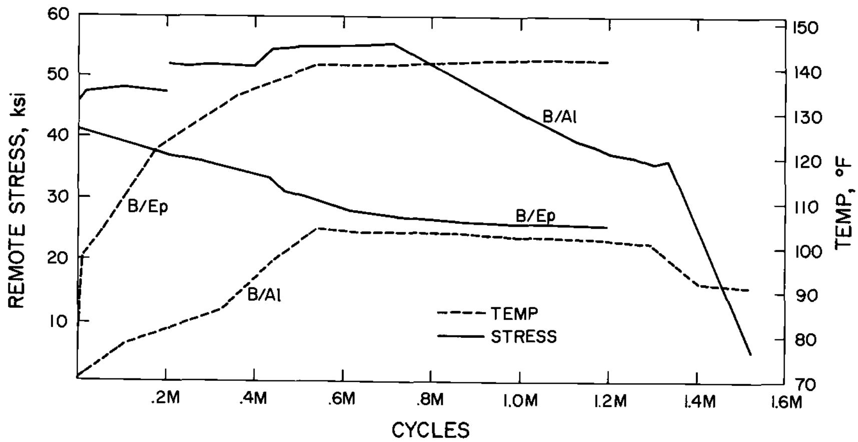

FIG. 2—*Remote stress and temperature behavior for B/Ep and B/Al 30-Hz fatigue tests.*

due to stiffness reduction as damage develops and increasing temperature for B/Ep, that is, the rate of temperature increase closely follows the rate of load (remote stress) decrease. In the B/Al specimen, an early correlation of load-temperature data is obscured by strain hardening of the aluminum matrix (rising, broken curve) although a very significant increase in temperature is observed during this period. A load reduction is accompanied by a gradual decrease in temperature during the middle cycles followed by a very sharp drop in load and local specimen temperature at the end of the test.

The cyclic stress-strain response of B/Ep, as a function of frequency, is shown in Fig. 3. Although the increase in cyclic fracture strain with frequency is very slight for the lower three frequencies, there is a very pronounced difference in response for the 45 Hz case; an effect attributed to, in part, a frequency dependent fracture mode which changes from predominantly transverse at lower frequencies to predominantly longitudinal at the higher frequency. The decrease in remote stress at the 0.6 percent strain level in the 45-Hz test was marked by a sharp increase in the rate of acoustic emission due to specimen damage and by changes in shape and size of the recorded hysteresis loops, all of which denote the incipience of failure. The fracture strains measured from cyclic stress-strain data were used as a basis for determining the strain amplitudes for the fatigue tests.

A decrease in remote stress (load) during a strain controlled fatigue (or cyclic stress-strain) test implies a corresponding decrease in specimen stiffness and, thus, an increase in specimen damage. Figure 4 shows

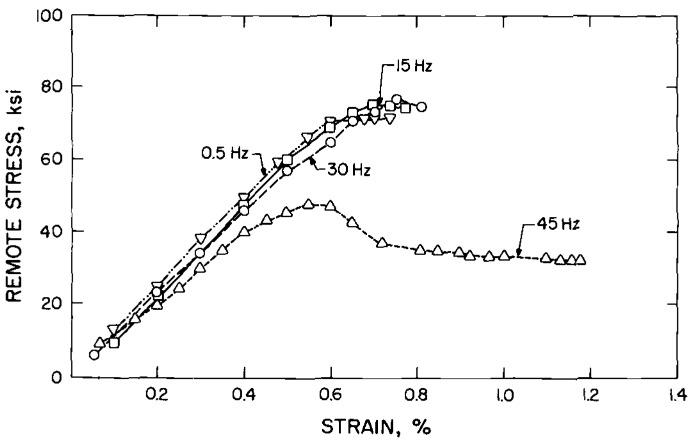

FIG. 3—*Virgin cyclic stress-strain curve for B/Ep.*

the effect of frequency on the change in stiffness for the selected test frequencies. Of interest to note is the large change measured for the 30-Hz case followed, in decreasing order, by 1, 45, and 15-Hz tests, that is, a nonlinear frequency dependent response. The very sharp stiffness changes early in the B/Ep tests correspond to the period of initial load reduction (Fig. 2, for example) and large temperature rise.

Reduction in remote stress and stiffness accompanied by increasing specimen temperature during constant strain amplitude fatigue testing can be accounted for only by rate independent (damage dependent) energy dissipative mechanisms. In Fig. 5, the variation of specific damping, compared to the first stable values of 0.018, 0.075, 0.056, and 0.196 (in order of increasing frequency), is shown for the B/Ep fatigue tests. For constant strain amplitude testing, the variation in specific damping (ratio of hysteresis loop area to the area under the loading part of the stress-strain curve) reflects changes in both dissipated energy and supplied energy. Therefore, the very significant change in damping characteristics during a 30-Hz test is due not only to an input energy decrease (reduction in stiffness) but to an increasing amount of dissipated energy (much of it as heat) as evidenced by the opening up of the hysteresis loops as damage develops. In sharp contrast, then, the 15-Hz data show much less cycle dependent response and, correspondingly, a relatively small initial increase in temperature which remains stable throughout the test. In addition to the continued extreme behavior of the 15 and 30-Hz data, the 1 and 45-Hz data follow the same frequency ordering in the stiffness plots as in the damping plots.

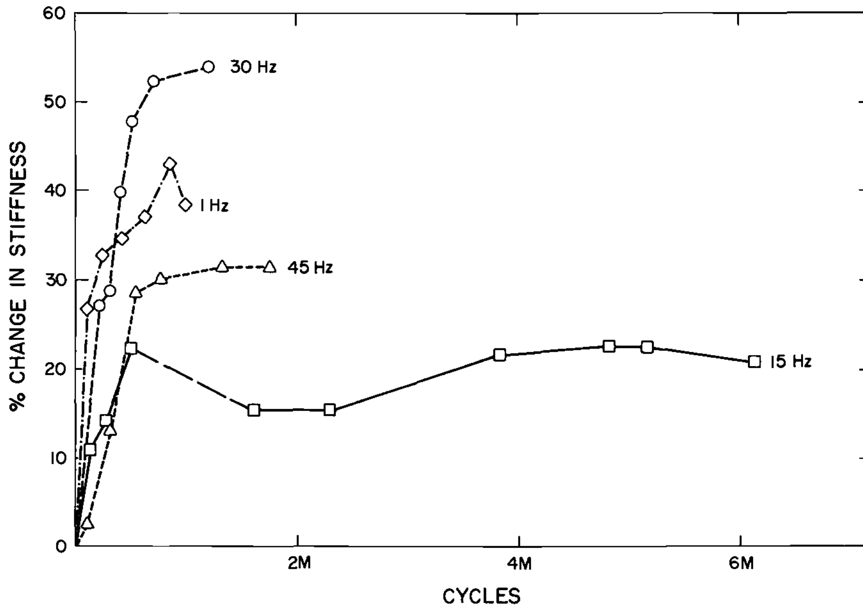

FIG. 4—*Change in stiffness of B/Ep at four test frequencies.*

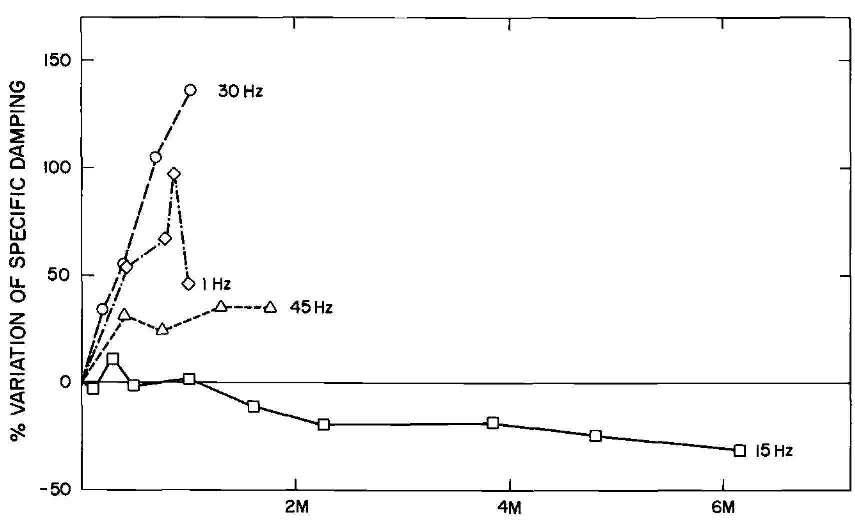

FIG. 5—*Change in specific damping of B/Ep at four test frequencies.*

Following the termination of the B/Ep fatigue tests, cyclic stress-strain tests (similar to those performed on virgin specimens) were conducted at the corresponding cyclic strain frequency to obtain residual strength, stiffness and ductility data as shown in Fig. 6. Several observations are of interest. First, the 15 and 30-Hz data continue to exhibit the same extreme behavior as noted above. Perhaps even more important is that this behavior is so readily apparent even though the 30-Hz test reported here continued for 1.2 million cycles as compared to over 6 million cycles for the 15-Hz test. The second observation, which then follows from the first, is that the post-mortem response of B/Ep exhibits a nonlinear frequency dependence in residual strength, stiffness, and ductility. As mentioned previously, a frequency dependent fracture mode was noted during the virgin cyclic stress-strain tests. The damage that developed during the strain controlled fatigue tests again gave an indication of such a frequency dependent transition, an impression that was confirmed during the post-mortem tests.

The results of tests conducted on B/Al specimens in the same fashion as those reported above for B/Ep specimens of similar geometry are presented in Figs. 7 to 11. The cyclic stress-strain data (Fig. 7) shows a decreasing cyclic fracture strain with increasing frequency and a lower cyclic fracture stress for the 45-Hz case.

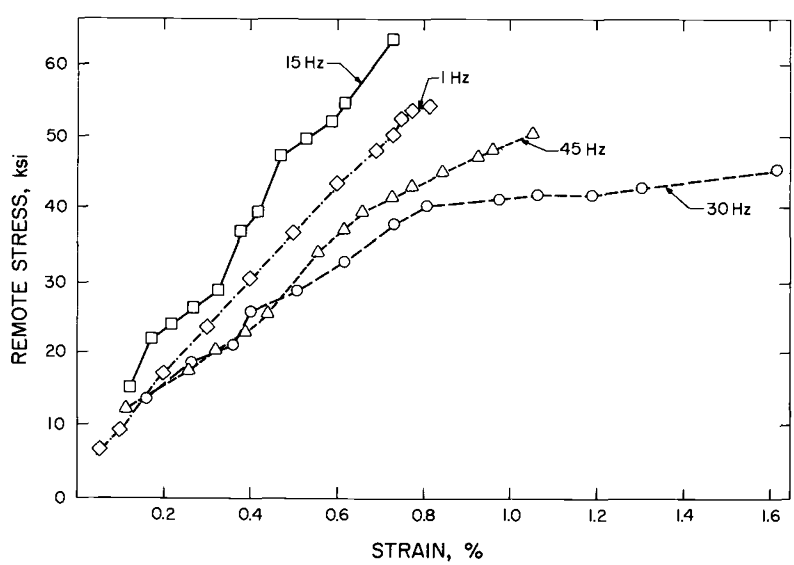

FIG. 6—*Post-mortem cyclic stress-strain curves for B/Ep.*

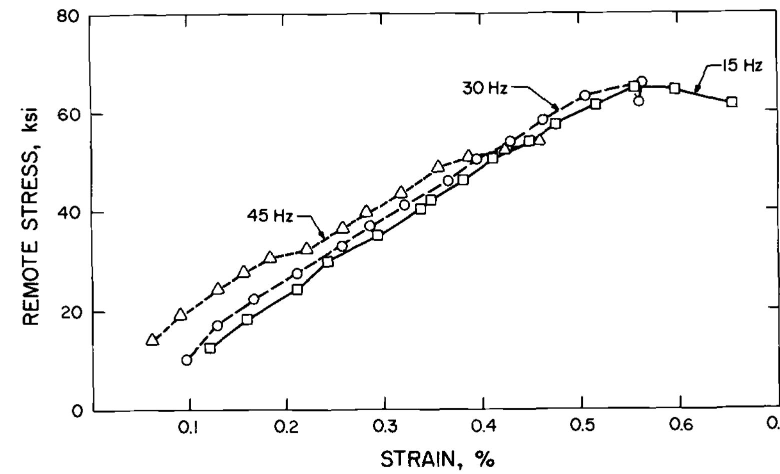

FIG. 7—*Virgin cyclic stress-strain curves for B/Al.*

The 30-Hz cyclic-strain frequency produces maximum changes in the response of B/Al just as it did in B/Ep. Figure 8 shows the frequency and cycle dependence of stiffness with 30 Hz again being the most sensitive case of the three selected frequencies. The nonlinear frequency effect is just as apparent in B/Al as it is in B/Ep; however, the 15 and

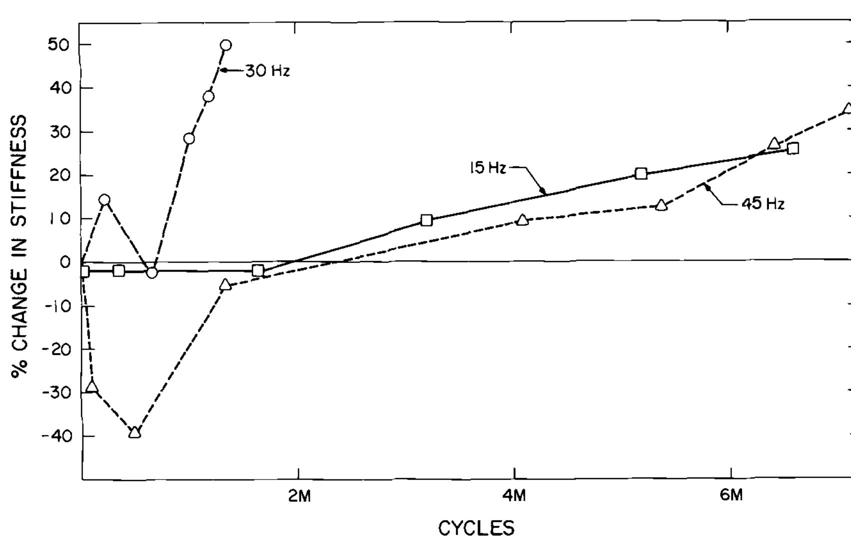

FIG. 8—*Change in stiffness of B/Al at three test frequencies.*

45-Hz curves are quite similar (except for some early strain hardening at 45 Hz) in this case.

Post-mortem cyclic stress-strain curves for B/Al are shown in Fig. 9. The 15 and 30-Hz curves denoted by the solid symbols represent the response of the specimens whose stiffness changes are plotted in Fig. 8. As was the case for B/Ep, the 30-Hz curve shows a much more severe effect on residual properties even though more than three times as many strain cycles were imposed during the 15-Hz test.

Although most of the fatigue tests were terminated based on observed reduction in load, several B/Al tests were terminated after 1.5 million cycles to run cyclic stress strain tests for comparative purposes. The 45-Hz and two 15-Hz curves (open symbols) in the middle of Fig. 9 represent such data. Not only was the post-mortem behavior of these specimens similar, but the behavior during the fatigue tests (Figs. 10 and 11) was virtually identical even though the data represents two different frequencies. These correlations, along with the work of Reifsnider and Henneke [*8*], point out the potential importance of in-service nondestructive testing to measure fatigue damage in composites. Figure 12 shows results obtained by the authors using a thermographic camera with a ten color isotherm display unit to nondestructively monitor changes in material response from stress field dependent behavior (Fig. 12*a*) to damage-dependent behavior (Fig. 12*d*). This technique, based on heat emission, is described more fully in Refs *3*, *5*, and *6*.

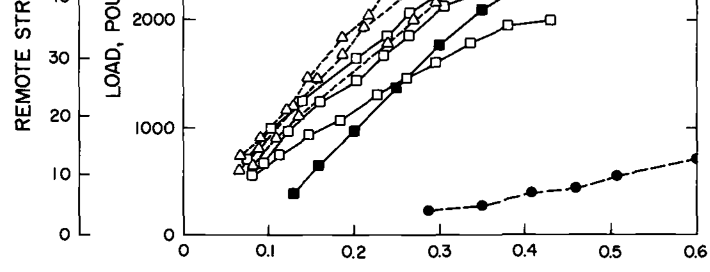

FIG. 9—*Post-mortem cyclic stress-strain curves for B/A.*

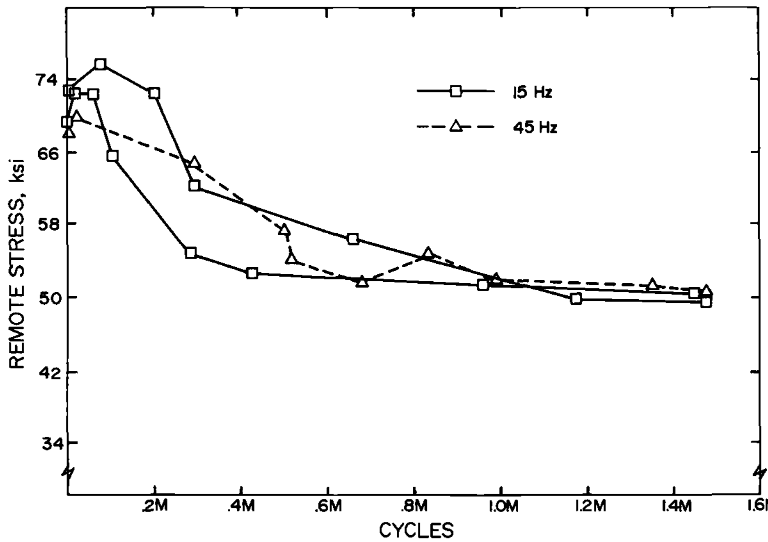

FIG. 10—*Comparison of change in remote stress for selected 15 and 45-Hz tests from Fig. 9.*

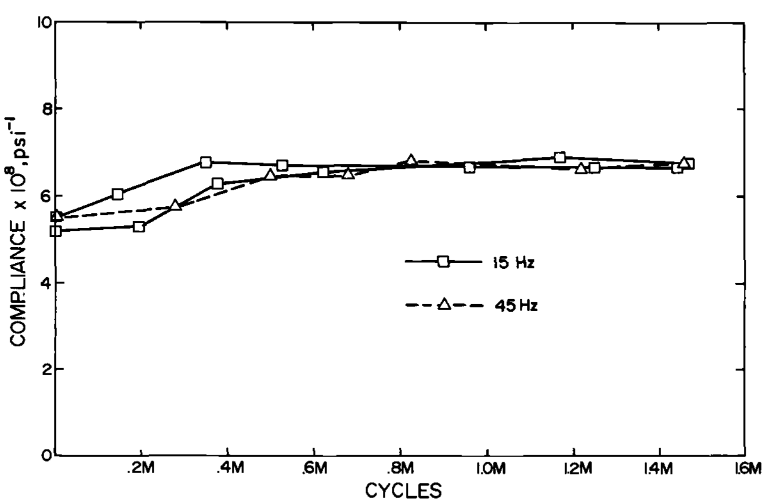

FIG. 11—*Comparison of change in compliance for selected 15 and 45-Hz tests from Fig. 9.*

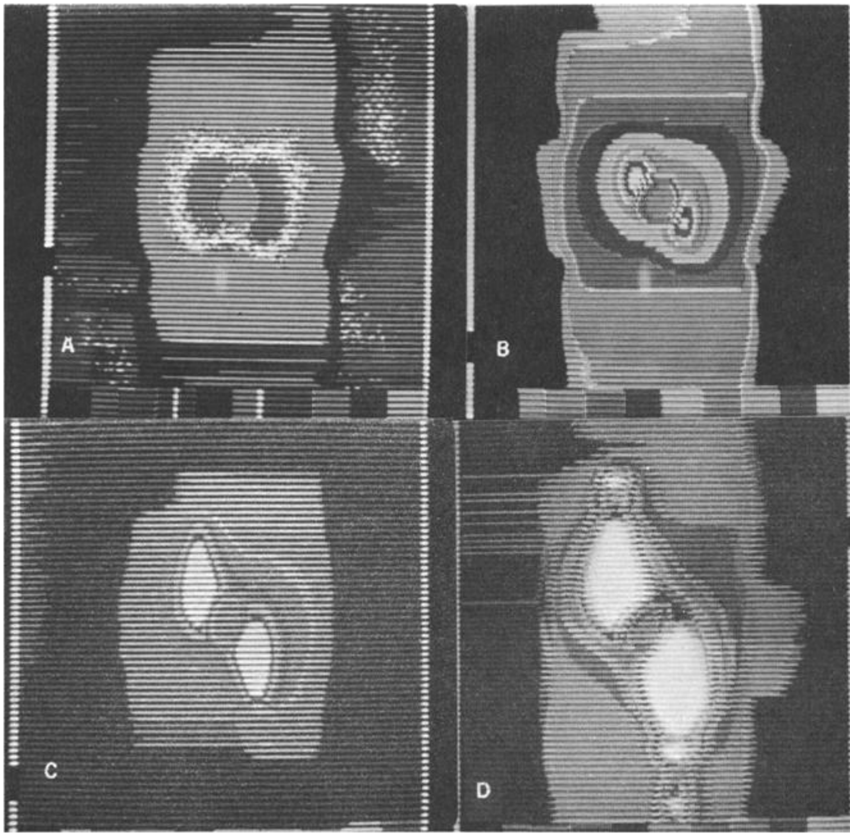

FIG. 12—*Reproductions of color thermographs showing preferential heat development due to fatigue damage:* (a) *Symmetric heat distribution around hole during early stages of cyclic straining.* (b) *Locally high heat generation associated with damage development.* (c) *Preferential heat development as damage develops longitudinally.* (d) *Thermograph of highly damaged specimen.*

Discussion

In view of the nonlinear frequency dependent behavior shown by these two materials, the question of a possible testing system resonance must be answered. After an extensive investigation consisting, in part, of an analysis of the power density spectrum over a wide range of frequencies, including the imposed forcing frequencies, it was concluded that the fatigue response reported previously was not caused by a testing system resonance condition. However, considerably more information through investigative study is necessary before a complete understanding of the nonlinear frequency dependence reported herein can be developed although some preliminary observations can be made.

Since hysteresis heating and attendant frequency dependence are present, a first inclination is to attempt to explain these results on the basis of time-dependent (viscous creep) response, especially in the case of the polymeric matrix material. Our tests [*2,3*] and others [*4*] have shown that some rate dependent heating does occur in these materials during fatigue loading. Also, Broutman and Gaggar [*4*] have shown that there is some strength and modulus change in epoxy at elevated temperatures. It might appear that the result of these data could be translated into degraded fatigue resistance (at least in polymer-matrix composites) cycled at high frequencies for which hysteresis heating is most severe. There is some data to support this premise, especially in the low cycle region [*10*]. However, while rate-dependent response certainly contributes to our findings, at least through an initial elevation of specimen temperature, the present results cannot be explained solely on the basis of time-dependent response. None of the constituent materials shows a significant amount of viscous behavior at the temperatures and frequencies involved. It has been shown, for example, that the fatigue response of pure epoxy under these conditions is truly cycle-dependent and not time-dependent [*4*]. Also, temperature related time-dependent effects in composites are generally small compared to the present variations under these conditions [*4,10*]. Rate test data [*11*] on B/Ep specimens with ply orientations identical to the B/Ep specimens in the present study reveal that the response of these materials is not significantly influenced by the loading rates imposed here or by the locally higher rates associated with calculated stress concentrations around the hole [*6*]. The nonlinear frequency dependence reported here is not consistent with the classical models of (temperature related) time-dependent or rate-dependent fatigue response.

Although all of the details are not yet clear, cycle-dependent arguments based on the mechanical development of damage appear to be more pertinent to the present data. The results presented in Figs. 2–9 show that the cycle-dependent change in stiffness, energy dissipation, and specimen temperature are closely related to material damage as established by the residual strength values obtained in the post-mortem cyclic stress-strain tests. The nonlinear frequency dependent extrema of the magnitudes of these effects is consistent throughout all of these data. The damage-related cycle-dependence is further substantiated by Figs. 10–12. Because 30 Hz represents a damage rate maximum in B/Al in these tests, and because of the stochastic aspects of these phenomena [*8*], the 15 and 45-Hz response of B/Al was frequently similar. The tests shown in Figs. 10 and 11 were, in fact, quite similar from the standpoint of cycle-dependent mechanical property change as shown by the near coincidence of the curves. It so happens that these three tests are the same three which have the quite similar post-mortem cyclic stress-strain curves and residual strength values shown in Fig. 9. Figure 12 provides further evidence in support of these ideas. The time-resolved video-thermography patterns allow us to quantitatively identify the damage events as the test continues, to monitor the dissipated energy (in the form of heat emission) caused by the damage development and to correlate this process with our other observations of mechanical property changes. Although this correlation is still underway and will be more completely reported in a subsequent paper, we can say at this point that a definite correlation does exist and that it does support the idea of explaining the nonlinear frequency dependence on the basis of damage related cycle-dependent response.

Summary and Conclusions

The present work reports the discovery and initial investigation of a new class of mechanical response characteristics in composite materials based on the effect of cycled load (or strain) frequency on their fatigue behavior. These characteristics were most easily categorized as a nonlinear dependence on cycle frequency which effects every major aspect of the fatigue response of the materials tested to the extent that stiffness, strength and energy dissipation changes were altered by as much as an order of magnitude. The most salient consequence of these findings is the fact that the nonlinear aspect of the dependence results in the occurrence of maxima in the variation of these mechanical properties with frequency. Consequently, a 30-Hz-cyclic frequency may be more damaging than a 15 or 45-Hz, etc. The present data have established a correlation between the changes in material properties attendant to the frequency-dependent response and the development of damage as indicated by heat emission patterns during testing and residual strength tests. It is conjectured that the dominant aspects of this nonlinear frequency dependence are cycle-dependent. It is further conjectured that these effects are affected by, but are not peculiar to, the materials tested for the test conditions, that is, they are to be expected in other crossply or biasply composite materials. This latter observation is based on the fact that the materials tested here were quite different in many respects but quite similarly affected by cycle frequency.

Much more work needs to be done before these findings can be extrapolated to engineering consequences. However, some of the greatest potential for the engineering use of composite materials lies in the area of vehicular structures where cyclic loads of various types are nearly always present. It would appear, then, that this large nonlinear frequency dependence will require additions to our understanding of the response of these materials if further progress towards applications is to be made.

Acknowledgments

We would like to gratefully acknowledge the support of this investigation by the Air Force Office of Scientific Research under grant number AFOSR-72-2358, monitored by Jacob Pomerantz and extend our thanks to Robert Simonds and Michael Richardson for their laboratory assistance and the shop personnel of the Engineering Science and Mechanics Department for their services.

References

[1] Salkind, M. J., in *Composite Materials: Testing and Design (Second Conference), ASTM STP 497,* American Society for Testing and Materials, 1972, pp. 143–169.

[2] Reifsnider, K. L., Stinchcomb, W. W., Williams, R. S., and Marcus, L. A., "Heat Generation in Composite Materials During Fatigue Loading," VPI-E-73-21, College of Engineering, Virginia Polytechnic Institute and State University, Blacksburg, Va.

[3] Reifsnider, K. L. and Williams, R. S., "Determination of Fatigue-Related Heat Emission in Composite Materials," Paper No. 2255A, Society for Experimental Stress Analysis Fall Meeting, Indianapolis, Ind., 16–19 Oct. 1973.

[4] Broutman, L. J. and Gaggar, S. K., *International Journal of Polymeric Materials,* Vol. 1, 1972, pp. 245–316.

[5] Marcus, L. A., "Comparison of the Theoretical Initial Stress Distribution with Observed Fatigue Phenomena in a Boron-Epoxy Plate with a Circular Hole," Master's thesis, College of Engineering, Virginia Polytechnic Institute and State University, Blacksburg, Va.

[6] Marcus, L. A. and Stinchcomb, W. W., "Measurement of Fatigue Damage in Composite Materials," Paper No. 2254A, Society for Experimental Stress Analysis Fall Meeting, Indianapolis, Ind., 16–19 Oct. 1973.

[7] Stinchcomb, W. W., Reifsnider, K. L., Marcus, L. A., and Williams, R. S., "Effects of Cyclic Frequency on the Mechanical Properties of Composite Materials," VPI-E-73-25, College of Engineering, Virginia Polytechnic Institute and State University, Blacksburg, Va., June, 1973.

[8] Reifsnider, K. L. and Henneke, E. G., "Stochastic Aspects of Frequency Effects on the Fatigue and Fracture of Bias-ply Composite Flawed Plate Specimens," *Proceedings,* Symposium on Stochastic Problems in Mechanics, University of Waterloo, Waterloo, Ontario, 23–26 Sept. 1973.

[9] Raske, D. T. and Morrow, J. D., in *Manual on Low Cycle Fatigue Testing, ASTM STP 465,* American Society for Testing and Materials, 1969, pp. 1–26.

[10] Eudo, K., Yano, A., and Okuda, Y., *Proceedings,* Ninth Japan Congress on Testing Materials, Non-Metallic Materials, March, 1966, pp. 104–108.

[11] Heller, R. A. et al, "Time and Temperature Dependence of Boron-Epoxy and Graphite-Epoxy Laminates," AFML-TR-73-261, Air Force Materials Laboratory, Dayton, Ohio, Nov. 1973.

R. W. Landgraf[1] *and R. H. Richman*[1]

Fatigue Behavior of Carburized Steel

REFERENCE: Landgraf, R. W. and Richman, R. H., **"Fatigue Behavior of Carburized Steel,"** *Fatigue of Composite Materials, ASTM STP 569,* American Society for Testing and Materials, 1975, pp. 130–144.

ABSTRACT: This paper represents the first part of a systematic investigation of factors affecting the fatigue resistance of surface-hardened steel components. The adopted approach is to view a surface-hardened member as a composite material consisting of a high strength, low ductility case and a lower strength, higher ductility core. A series of smooth axial specimens, representing case and core carbon contents, were prepared to determine cyclic stress-strain and strain-life curves. The cyclic properties obtained from these tests were then used to analyze and interpret the cyclic behavior of carburized specimens. Both axial and bend specimens were carburized and subjected to constant amplitude, strain-controlled fatigue tests. A discontinuity in the resulting strain-life curves, representing a shift from surface to subsurface crack initiation, is predictable from comparison of the strain-life curves for simulated case and core material. Finally, a relation is developed to determine optimum case:core ratios taking into account cyclic material properties, residual stresses, strain gradient, and applied stress or strain level.

KEY WORDS: composite materials, fatigue tests, steels, fatigue (materials), crack initiation, stress distribution, strain distribution, surface hardening

Selective surface hardening is commonly used to improve the fatigue resistance of steel components. The beneficial effects obtained depend complexly upon a variety of metallurgical and mechanical considerations. In carburized steel, for example, the chemical compositions of case and core influence transformation kinetics and tempering responses, and, hence, the resultant microstructure. This, in turn, determines the ensuing cyclic properties and residual stress patterns obtained in a particular case and core combination.

Although numerous efforts have been directed at evaluating the fatigue resistance of surface-hardened members [*1–3*],[2] there have been few systematic investigations that could lead to useful quantitative general-

[1] Scientific Research Staff, Ford Motor Company, Dearborn, Mich. 48121.

[2] The italic numbers in brackets refer to the list of references appended to this paper.

izations. This paper represents the first part of such a systematic program to establish material selection and processing guidelines to optimize fatigue resistance in surface-hardened components.

In this adopted approach a surface-hardened member is viewed as a composite consisting of a high strength, low ductility case and a lower strength, higher ductility core. Krotine et al [4] and McGuire et al [5], in two related studies, have usefully applied this concept to the analysis of monotonic deformation and fracture behavior of carburized bend specimens. While admittedly a simplified view, their success suggests that it is a reasonable starting point for understanding the cyclic responses of carburized members. In the present work, the cyclic deformation and fracture behavior of steels representative of the case and the core are determined first. These results are then used to analyze and interpret the cyclic behavior of carburized axial and bend specimens.

Experimental Program

Materials

Laboratory heats of AISI 4027 and what would correspond to 4076 steel were prepared to simulate commonly encountered core and case compositions. Compositions and heat treatments are given in Table 1. Axial and bend specimens of 4027 were carburized together to ensure identical surface layer properties; the carburizing process parameters likewise appear in Table 1. Three groups of specimens, with measured case depths (at 0.45 carbon) of 0.008, 0.015, and 0.035 in. were prepared all with a surface carbon content of 0.71. Carbon and hardness gradients for the three groups are shown in Fig. 1. Carbon profiles were determined by an electron probe technique [6], and hardness gradients were obtained from Knoop microhardness traverses which were converted to diamond pryamid hardness values. Higher case carbon contents

TABLE 1 – *Compositions and processing.*

Alloy	C	Mn	Si	Mo
4027	0.27	0.80	0.28	0.27
4076	0.76	0.78	0.26	0.27

Heat Treatment
austenitize: 1550–1600°F, 30 min, oil quench
temper: 350°F, 1h.

Carburizing treatment
1650°F, endothermic atmosphere, 25°F dew point, 0.5 to 5 h
cool to 1550°F, oil quench
temper 350°F, 1 h

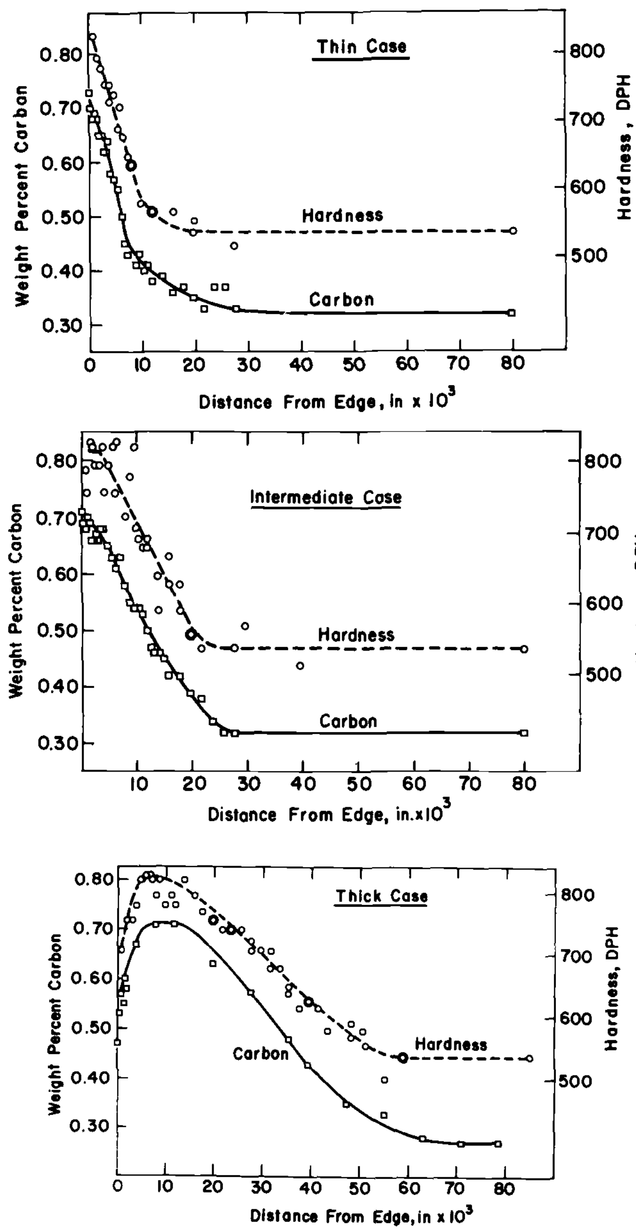

FIG. 1—*Carbon and hardness gradients for three case depths.*

were avoided because of problems associated with high retained austenite and transformation microcracking during heat treatment. Retained austenite levels were always ≤ 5 percent, and no microcracking was detected.

Test Methods

Monotonic tension and compression and strain-controlled fatigue tests were performed on axial specimens of cylindrical configuration with 0.2 in. diameter and 0.5 in. gage length. Axial testing was done on a closed-loop, servo-controlled test system with the capability for accurate measurement, control and recording of loads and strains.

Bend specimens had a test section 0.375 in. thick, 0.5 in. wide, and 2.8 in. long. Tests were conducted in a specially designed four-point bending apparatus installed on a servo-hydraulic actuator as shown in Fig. 2. Tests can be run under load (moment), stroke (deflection), or surface strain control.

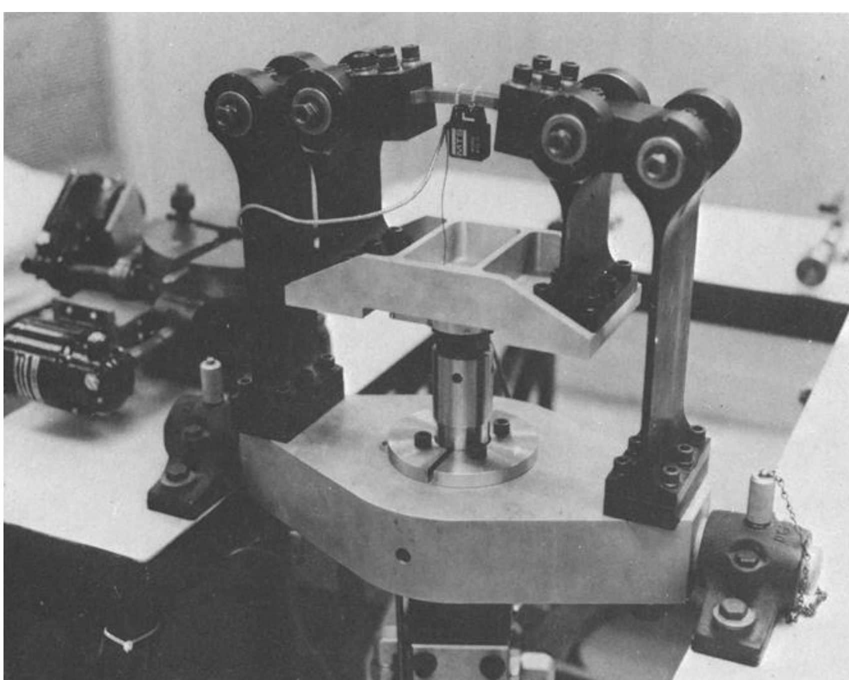

FIG. 2—*Four-point bending apparatus installed on servo-hydraulic actuator.*

Results

Axial Behavior

Stress-strain curves for the 4027 and 4076 steels are shown in Fig. 3. A pronounced strength differential between the tensile and compressive flow curves is evident for the 4076 steel. The cyclic stress-strain curve, determined by the tips of stable hysteresis loops from constant amplitude fatigue tests [*7*], lies between the two monotonic curves.

Although the 4027 steel displays a tensile curve higher than that of the 4076 (a consequence of 10 percent retained austenite in the 4076), it experiences cycle-dependent softening under reversed loading which results in a lower cyclic flow curve. It is the cyclic curve that defines the proper stress-strain relation for fatigue analysis; it is also appropriate for determining stress distributions in bending and for estimating the magnitude and stability of residual stresses.

Axial fatigue results are summarized in the strain-life plot of Fig. 4. The 4027 steel is seen to offer superior low-cycle fatigue resistance on the basis of its greater ductility, while the stronger 4076 steel is superior at long lives. Intersection of the life curves for simulated case and core materials accounts for a shift of failure location in carburized members. This is clearly demonstrated by the behavior of the carburized axial specimen data shown in Fig. 4. At short lives, the data points fall between the simulated case and core curves since, in this regime, cracks form in the brittle case early in the life and then propagate through the softer core.

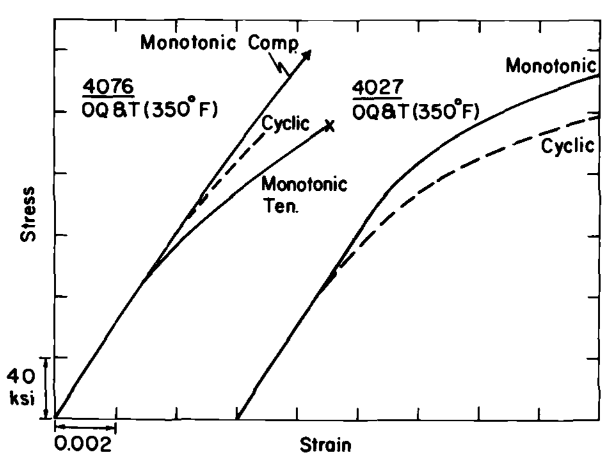

FIG. 3—*Monotonic and cyclic stress-strain curves for steels simulating case and core material.*

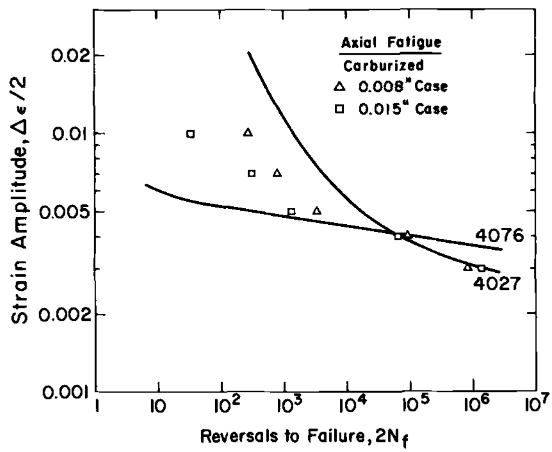

FIG. 4—*Axial fatigue results for 4076, 4027, and carburized 4027 specimens.*

At the crossover point all lives are nearly identical. In the long life regime, the data points fall on the simulated core line, which suggests that now the core has become the weak link. This is confirmed by the fractograph in Fig. 5 which shows that, indeed, this long life failure initiated below the surface. In this case an inclusion provided the initiation site.

Reversed Bend Tests

Bending fatigue data for 4027 uncarburized and with three carburized case thicknesses are summarized in Fig. 6. Again, the tendency for the curves to cross at some intermediate life is apparent. Moreover, the intersection point occurs at nearly the same strain level and life as was observed for the axial specimens. At short lives the carburized steel is seen to be inferior to the uncarburized with the deepest case giving the shortest life.

The beneficial effect of case depth becomes significant at long lives. The thin case displays slightly better fatigue resistance than uncarburized 4027 at lives just beyond the crossover, but, then, the resistance decreases abruptly to the 4027 line with the occurrence of subsurface initiation. The intermediate case thickness shows improvement but still suggests that subsurface initiation occurs since the thick case is significantly more fatigue resistant.

Discussion

The results of this study tend to confirm the usefulness of correlations between the responses of the separate case and core materials and the

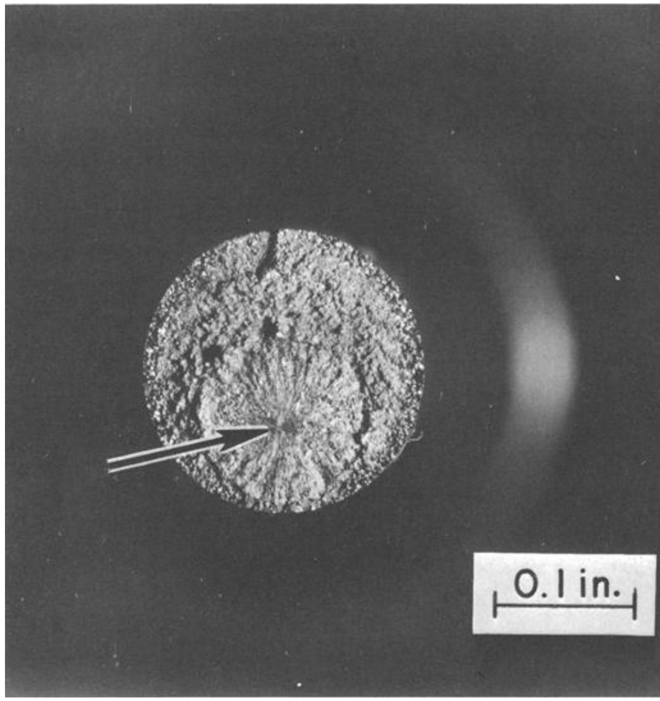

FIG. 5—*Fractograph of carburized axial specimen fatigued at a strain amplitude of 0.003* ($2N_f = 1.6 \times 10^6$ *reversals) showing subsurface failure initiation* (*arrow*).

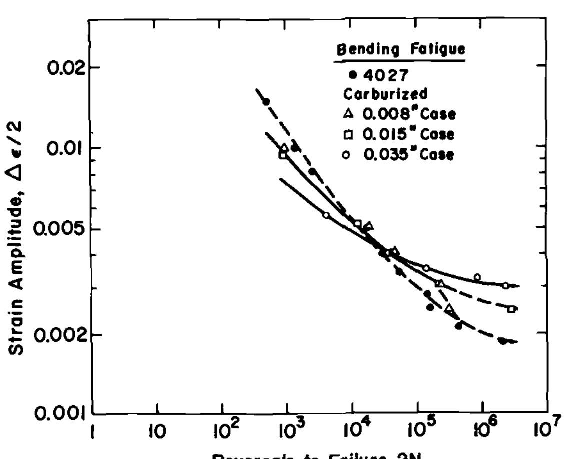

FIG. 6—*Bending fatigue results for uncarburized and carburized 4027 steel.*

behavior of carburized specimens. A pertinent example is the relation of the crossover point in the strain-life curves to the shift in failure location. For the designer, this observation provides bounds, either in terms of strain level or life, within which carburizing can be expected to enhance fatigue resistance.

In general, evaluation of carburized members for a service environment is of most interest at long lives. Therefore, it is useful to next consider ways of estimating optimum case depths for maximum fatigue life. This can be accomplished, when possible, by assuring that there is equal likelihood of failure in case or core for a given geometry and loading situation. As will be seen, not every deformation mode is amenable to such decisions.

Axial Fatigue

It will be immediately appreciated that with uniform strain fields, it is invariably the weakest element of a composite that fails first unless persistent residual stresses can compensate for the differential in resistance to reversed loading. Thus, in the long life regime we can expect core failure always to be the limiting factor. While carburizing will enhance wear resistance in such instances, little improvement in long-life fatigue resistance can be anticipated.

At short lives, two factors allow some manipulation of fatigue resistance. The residual stress pattern across a section is a sensitive function of the case thickness and carbon content [*8*]. Crack initiation can be forestalled by selecting a carburizing treatment to produce the highest compressive residual stresses in the surface layers. Such stresses will relax, however, in the presence of reversed plastic strains. Also, the duration of crack propagation will be increased the greater is the stressed area represented by the core. Nevertheless, it may be concluded that carburizing is not a logical technique for significantly improving axial fatigue resistance.

Bending Fatigue

For a simple beam in pure bending, as shown in Fig. 7, the axial strain, ϵ_x, at any point through the thickness is given by

$$\epsilon_x = \epsilon_s \left(\frac{y}{c}\right) \tag{1}$$

where

ϵ_s = maximum strain at the surface,
y = distance from neutral axis, and
c = one half the beam thickness.

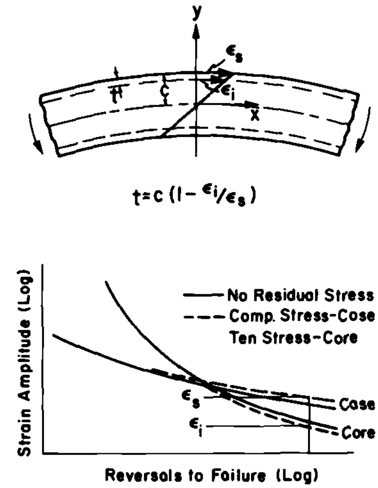

FIG. 7—*Schematic representation of analysis used to determine optimum case depth.*

The strain at the case-core interface, ϵ_i, is then

$$\epsilon_i = \epsilon_s \left(\frac{c-t}{c}\right) \tag{2}$$

where t = case thickness.

Solving for case thickness gives

$$t = c\left(1 - \frac{\epsilon_i}{\epsilon_s}\right) \tag{3}$$

By introducing the appropriate strain values from the simulated case and core life curves, the optimum case thickness can be determined from Eq 3.

If we restrict our attention to long fatigue lives, stresses can be assumed proportional to strains, and Eq 3 is rewritten as

$$t = c\left(1 - \frac{\sigma_i}{\sigma_s}\right) \tag{4}$$

where

σ_i = stress at case-core interface, and

σ_s = maximum stress at surface.

The stress cycling resistance of steel can be described by the following relation [9]

$$\sigma_a = (\sigma'_f - \sigma_o)(2N_f)^b \tag{5}$$

where

σ_a = stress amplitude,
σ_o = mean (residual) stress,
$2N_f$ = fatigue life in reversals,
σ'_f = fatigue strength coefficient, and
b = fatigue strength exponent.

Solving for life

$$2N_f = \left(\frac{\sigma_a}{\sigma'_f - \sigma_o}\right)^{1/b} \tag{6}$$

To maximize fatigue resistance, there should be equal likelihood of failure in case and core. Thus, for equal lives

$$\left(\frac{\sigma_a}{\sigma'_f - \sigma_o}\right)^{1/b}\Bigg|_{\text{case}} = \left(\frac{\sigma_a}{\sigma'_f - \sigma_o}\right)^{1/b}\Bigg|_{\text{core}} \tag{7}$$

The value of b has been shown to vary little for a variety of heat-treated steels [10]. Setting $b_{\text{case}} = b_{\text{core}}$ yields

$$\left(\frac{\sigma_a}{\sigma'_f - \sigma_o}\right)_{\text{case}} = \left(\frac{\sigma_a}{\sigma'_f - \sigma_o}\right)_{\text{core}} \tag{8}$$

The maximum σ_a in the case is σ_s, whereas in the core the maximum $\sigma_a \approx \sigma_i$. Thus,

$$\frac{\sigma_i}{\sigma_s} = \frac{(\sigma'_f - \sigma_o)_{\text{core}}}{(\sigma'_f - \sigma_o)_{\text{case}}} \tag{9}$$

and substitution of Eq 9 into Eq 4 gives

$$t_{opt} = c\left[1 - \frac{(\sigma'_f - \sigma_o)_{\text{core}}}{(\sigma'_f - \sigma_o)_{\text{case}}}\right] \tag{10}$$

Introduction of the appropriate fatigue properties and residual stresses for case and core into Eq 10 allows the optimum case thickness for maximum bending fatigue resistance to be determined. This same development can be used in analyzing torsional members, and it is also applicable to geometries which do not exhibit a linear strain gradient (for example, notched members) as long as the appropriate strain gradient relation is employed.

When this approach is applied to the present bend specimen in conjunction with the strain-life curves in Fig. 4, an optimum case depth of approximately 0.030 in. is obtained. This result is certainly not inconsistent with the test data in Fig. 6.

A more complete development of the treatment leads to consideration of the actual stress-strength profiles in carburized bending members. Such profiles are portrayed for the thin and thick cases in Fig. 8. Values for the fatigue strength coefficient, σ'_f, were estimated from the hardness measurements, and the residual stress profiles are based upon X-ray measurements on specimens similar to those of the present study.

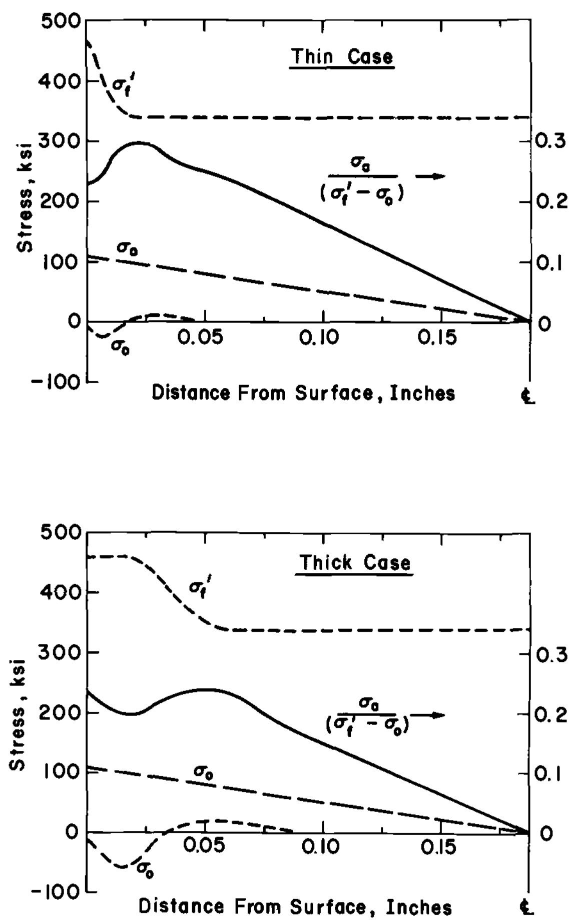

FIG. 8—*Stress-strength profiles for carburized bend specimens of two case depths.*

The varying effects of applied stress level, σ_a, material fatigue strength, σ'_f, and residual stress, σ_o, are conveniently combined in the previously introduced parameter $\sigma_a/(\sigma'_f - \sigma_o)$. Failure would be expected to initiate wherever this parameter is a maximum. For the thin case in Fig. 8, this point occurs unambiguously below the surface. In contrast, the distribution is much flatter and the peak values are lower for the thick case, and, thus, the fatigue resistance is much improved. Indeed, the indicated profile implies equal likelihood of failure at surface and subsurface locations.

Concluding Remarks

The treatment developed above is based upon a simplified mechanics view of what is, seemingly, an extremely complex problem. The qualitative agreement with observed behavior and, at least for the limited data available, the quantitative predictive capability of the approach suggests that it has considerable merit.

The concepts presented here would appear to have most immediate value to designers who presently are without well-established guidelines for the design and processing of surface-treated components. In the longer term, this viewpoint should provide a useful framework within which to assess and interpret more complex or subtle metallurgical effects associated with selective surface hardening.

Summary

Carburized AISI 4027 steel specimens were subjected to constant amplitude, strain controlled, fully reversed deformation in either axial or bending modes. A discontinuity, indicative of a shift from surface to subsurface crack initiation, was observed in the resulting strain-life curves. This observation is predictable from the strain-life relations determined from two groups of axial specimens separately representing case and core compositions. The experimental results were also used to evaluate an analytical model of a simple composite in bending fatigue. The model is capable of predicting optimum case:core ratios, extendable to other loading situations, and found to be qualitatively consistent with the observations.

Acknowledgments

The authors are indebted to B. T. Crandall, J. P. Ingall, and S. Merhav for performance of most of the experiments, and M. K. Brachaczek for supervision of the carburizing treatments.

References

[1] Love, R. J., *Proceedings,* Symposium on Properties of Metallic Surfaces, Institute of Metals, 1953, p. 161.
[2] Roberts, J. G. and Mattson, R. L. in *Fatigue Durability of Carburized Steel,* American Society for Metals, 1957, p. 68.
[3] DePaul, R. A., *Metals Engineering Quarterly,* Vol. 10, 1970, p. 25.
[4] Krotine, F. T., McGuire, M. F., Ebert, L. J., and Troianc, A. R., *Transactions,* American Society for Metals, Vol. 62, 1969, p. 829.
[5] McGuire, M. F., Troiano, A. R., and Ebert, L. J., *Transactions,* Series D, American Society of Mechanical Engineers, Vol. 93, 1971, p. 699.
[6] Eichen, E., Tabock, J., and Kinsman, K. R., *Metallography,* Vol. 5, 1972, p. 151.
[7] Landgraf, R. W., Morrow, JoDean, and Endo, T., *Journal of Materials,* Vol. 4, 1969, p. 176.
[8] Koistinen, D. P., *Transactions,* American Society for Metals, Vol. 50, 1958, p. 227.
[9] Landgraf, R. W. in *Achievement of High Fatigue Resistance in Metals and Alloys, ASTM STP 467,* American Society for Testing and Materials, 1970, p. 3.
[10] Landgraf, R. W. in *Proceedings,* 1971 International Conference on Mechanical Behavior of Materials, Vol. 11, Kyoto, Japan, 1972, p. 334. See also T & AM Report No. 320, Department of Theoretical and Applied Mechanics, University of Illinois, Urbana, Nov. 1968.

DISCUSSION

J. F. Throop[1]—The authors have adopted the view that a surface-hardened member is a composite material consisting of a high strength, low ductility surface layer and a lower strength, higher ductility core. This is comparable to laminar metal composites in which fatigue crack retardation or arrest or both have been reported at the interface between lamellae. McCartney, Richard and Trozzo[2] related this capacity for retardation or arrest to the gradient of interfacial fracture strength, expressed either in units of shear strength per micron or units of tensile strength per micron across the internal interfaces. In cyclic bending they found that fatigue cracks propagated through an interface having an interfacial tensile strength gradient of 4 ksi/μ without delamination, but, in another laminate with larger gradient of 50 ksi/μ delamination occurred when the fatigue crack reached the interface, and the crack advance was arrested. They concluded that ultrahigh-strength steel composites containing a macrostructure of internal interfaces can confine cracks within geometrical compartments by a delamination mechanism ahead of the crack tip. Throop and Miller[3] discuss this in relation to compact specimen fatigue crack propagation studies of steel and aluminum laminates. We found that the retardation or arrest results from a crack-blunting process occurring as the crack approaches the lower strength higher-ductility material at the interface, and change from Mode I to combined Mode I–Mode II failure involved in the delamination process.

Landgraf and Richman observed a discontinuity in the strain-life curves representing a shift from surface crack initiation at short life (high cyclic strains) to subsurface initiation at long lives (low cyclic strains). In optimizing case-core relationships, it may be useful to take into con-

[1] Benet Weapons Laboratory, Watervliet Arsenal, Watervliet, N. Y. 12189.

[2] McCartney, R. F., Richard, R. C., and Trozzo, P. S., *Transactions*, American Society for Metals, Vol. 60, 1967, pp. 384–394.

[3] Throop, J. F. and Miller, J. J., "Fatigue Crack Propagation and Fracture in Compact Specimens of Metal Laminates," presented at the American Society for Testing and Materials Symposium on Fatigue of Composite Materials, 3–4 Dec. 1973.

sideration the interfacial gradient of strength, or of microhardness since it is almost directly related to strength in steels. Certain limiting gradients of strength or microhardness may be effective in confining the fatigue cracking to the lower strength tougher core material, thereby extending the fatigue life of the part and enhancing the effectiveness of the carburized case. It is interesting that the authors' concept of the laminar-composite nature of a carburized case-core may add considerably to our understanding of this well accepted metallurgical treatment of metal parts.

R. W. Landgraf and R. H. Richman (author's closure)—We agree that crack retardation can be important in composites with discrete interfaces. Carburized steels, however, cannot be characterized by such discernible interfaces between the constituents. The sharpest gradients reported here, and they are quite typical, are 0.24 ksi/μ in fracture strength. This is far below the reported threshold for delamination. Thus, we conclude that improvements of fatigue resistance in carburized parts must rely principally upon manipulation of the rheological interactions between the composite elements.

G. J. Dvorak[1] *and J. Q. Tarn*[1]

Fatigue and Shakedown in Metal Matrix Composites

REFERENCE: Dvorak, G. J. and Tarn, J. Q., "**Fatigue and Shakedown in Metal Matrix Composites,**" *Fatigue of Composite Materials, ASTM STP 569*, American Society for Testing and Materials, 1975, pp. 145–168.

ABSTRACT: Simple mechanical models of unidirectional metal matrix composites are used to analyze elastoplastic deformation and shakedown in the matrix under cyclic composite loads. Both axial and off-axis loadings of a lamina are considered. It is shown that the fatigue limits of as-fabricated boron-aluminum, beryllium-aluminum, tungsten-copper, and other composites generally coincide with the composite shakedown limits because the matrix yield stresses and fatigue limits are equal.

In heat-treated composites, the matrix yield stress is usually much higher than the fatigue limit, and matrix fatigue failure can take place in the shakedown state. The residual microstresses caused by heat treatment are estimated, and their influence on fatigue is discussed. A method for improvement of the fatigue resistance of heat-treated composites is discussed.

The theoretical predictions of fatigue limits are verified by an extensive comparison with available experiments, and a very good agreement is obtained. It is concluded that, in principle, the composite fatigue failure can be avoided if each of the constituents is stressed within its particular fatigue limits during a cyclic loading program of the composite.

KEY WORDS: composite materials, fibers, aluminum, beryllium, boron, copper, tungsten, reinforcement (structures), fatigue (materials), fatigue limit, cyclic loads

Nomenclature

E_c Young's modulus of the composite (in the fiber direction)

E_f Young's modulus of the fiber

[1] Professor of civil engineering and graduate assistant, respectively, Department of Civil Engineering, Duke University, Durham, N. C. 27706

E_m	Young's modulus of the matrix
N_F or N_f	Number of cycles to failure
R	S_{min}/S_{max}
S	Uniaxial stress applied at a composite
S_{max}	Maximum value of S applied in a fatigue test
S_{min}	Minimum value of S applied in a fatigue test
S_{PR}	Composite prestress
S_Y	Composite proportional limit
$\Delta S = S_{max} - S_{min}$	Composite stress range
ΔS_{SH}	Shakedown stress range
V_f	Fiber volume fraction
$V_m = 1 - V_f$	Matrix volume fraction
ϵ^c	Normal composite strain in the fiber direction
$\epsilon_{max}{}^c$	Maximum value of ϵ^c applied in a fatigue test
$\epsilon_{PR}{}^c$	Composite prestrain
ϵ^f	Axial normal strain in the fiber
ϵ^m	Normal strain in the matrix, in the direction of the fibers
θ	Angle between the load and fiber directions in off-axis tests
σ^f	Axial normal stress in the fiber at a given value of S
$\sigma_{max}{}^f$	Maximum value of σ^f supported by the fiber in a fatigue test
$\sigma_{FL}{}^f$	Fatigue limit of the fiber ($N = 10^6$)
$o_R{}^f$	Residual fiber stress in a heat-treated composite
$o_u{}^f$	Ultimate tensile strength of the fiber
$\sigma_Y{}^f$	Tensile yield strength of the fiber
σ^m	Axial normal stress in the matrix (in the fiber direction) at a given value of S
$\sigma_{max}{}^m$	Maximum value of σ^m supported by the matrix in a fatigue test
$\sigma_{min}{}^m$	Minimum value of σ^m supported by the matrix in a fatigue test
$\sigma_{FL}{}^m$	Fatigue limit of the matrix ($N = 10^6$)
$\sigma_R{}^m$	Residual matrix stress in a heat treated composite
$\sigma_Y{}^m$	Tensile yield strength of the matrix
$\sigma_{YR}{}^m$	Reduced yield strength of the matrix in off-axis tests

During the last decade of intensive research of the mechanical behavior of fiber-reinforced composites, the mechanisms of fatigue failure have received relatively little attention. Accordingly, the fatigue resistance criteria are much less adequate than the design guidelines for composite structures under static load. The lack of understanding of fatigue processes and the resulting reliability problems have been among the major obstacles to certain applications of composites as structural materials [*1*].[2] One of the principal reasons for this situation can be found in the almost total absence of analytical work in the micromechanics of composites under cyclic loading. Indeed, it appears that such analytical approaches would permit a quantitative interpretation of available experimental results and a generalization of these results for use in design. In this paper we shall attempt to develop a simple analysis of the several modes of fatigue behavior in metals reinforced with unidirectional, continuous fibers. A comparison with available fatigue experiments will be presented to identify the mechanisms of fatigue in both axial and off-axis tests under unidirectional cyclic loads. A relationship between the properties of the constituents and the fatigue limit of a composite will be established, and fatigue resistance criteria for design with metal matrix composites will be summarized. Although the composites may not have an endurance limit, the term fatigue limit will be used here to indicate the maximum stress which does not cause failure at 10^6 to 10^7 cycles.

Theoretical Considerations

Selection of the Composite Model

The composite is assumed to consist of straight, elastic, continuous, cylindrical fibers, with parallel axes, which are embedded in a metal matrix. The distribution of the fibers in the matrix is approximately uniform, the fiber volume fraction is denoted as V_f. The matrix is an isotropic, elastic-plastic material. A perfect bond is tentatively assumed at the fiber-matrix interface; however, this assumption can be frequently relaxed. Finally, the material properties of the constituents, namely, their elastic moduli, yield stresses, hardening properties, ultimate strengths, and fatigue limits under steady-state uniaxial cyclic loads are considered as known quantities.

Among the various composite models which have been proposed in the literature, Dvorak et al [*2–4*] analyzed the elastic, elastoplastic, thermoplastic, and shakedown behavior of the regular hexagonal fiber

[2] The italic numbers in brackets refer to the list of references appended to this paper.

array models and of the model consisting of right circular composite cylinders, in which the fibers are surrounded by uniform layers of the matrix material. Both these models permit an accurate evaluation of the three-dimensional microstress and microstrain states which exist in the composite after a particular loading program. Some of the model analysis results which are pertinent to the present discussion can be summarized as follows:

(*a*) In initially stress-free composites which are loaded in the direction z of the fibers, the microstresses σ_z^f and σ_z^m in the fiber and matrix, respectively, are nearly uniform in the elastic region. The stresses in the transverse plane, σ_r^m and σ_θ^m, are of the order of 10^{-2} of the axial stresses. Under these circumstances, the axial σ_z^f and σ_z^m stresses can be determined quite accurately from the rule of mixtures.

(*b*) If the uniaxial loading continues beyond the proportional limit of the composite, the transverse stresses σ_r^m and σ_θ^m start to increase due to the plastic straining of the matrix. However, they do not reach appreciable values until the composite stress is much higher than the proportional limit. Therefore, an essentially uniaxial stress state exists in the composite during the initial stage of plastic deformation, and the rule of mixtures is still applicable for determination of the axial stresses σ_z^f and σ_z^m.

(*c*) The initial yield surface of the composite [*2,3*] experiences rigid body translation in the direction of the loading vector in the composite stress space when the composite is loaded along any radial path by composite stresses which are symmetric with respect to the fiber axis. Axial tension and compression, a uniform temperature change, and a hydrostatic stress can be combined to produce such axisymmetric composite stress states. It can be shown that the translated initial yield surface is identical both with the unloading and shakedown surfaces of the composite. Therefore, in the case of uniaxial tension in the fiber direction, the rule of mixtures can also be used in the plastic region, to find the proportional and shakedown limits of the composite.

The foregoing conclusions justify the use of a simple two-parameter rule of mixtures model of the composite in the analysis of uniaxial fatigue tests. The model is shown schematically in Fig. 1. It should be noted that in the plastic region, the model can determine only the axial stresses, σ_z^f and σ_z^m, accurately and that it neglects the stresses in the transverse plane. A similar model had been used by a number of authors, for example, by Kelly et al [*5,6*], Baker and Cratchley [*7*], and others, although the limitations of the model in the plastic region have not been well understood. The following equations are presented only to facilitate the discussion of the experimental results.

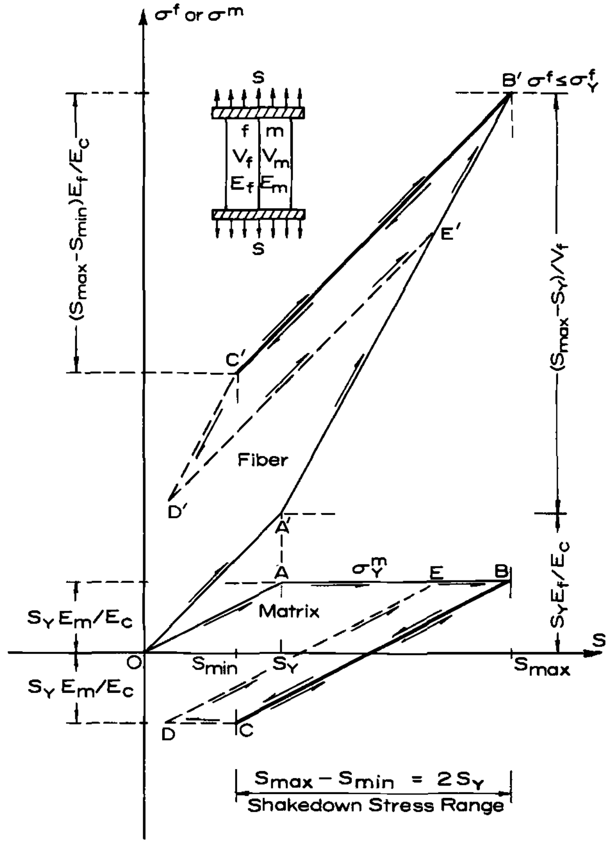

FIG. 1—*Deformation and shakedown of a two-parameter composite model in a stress-controlled uniaxial test.*

Determination of Shakedown Limits

If one wants to avoid fatigue failure in general, and low cycle fatigue failure in particular, it is essential to ensure that the cyclic applied load will produce only elastic strains in both constituents. However, it is permissible to allow local plastic straining in the composite during the first few load cycles, providing that the composite shakes down during this initial loading period. The shakedown state is reached if, and only if, residual microstresses are generated during the cyclic plastic straining, and reach such magnitudes that only elastic deformation can eventually take place under the applied load.

The determination of the shakedown stress range for the two-parameter composite model is shown in Fig. 1. Let S denote the uniaxial composite stress, σ^f; σ^m, the normal microstresses in the fiber direction, in the fiber and matrix, respectively; and, ϵ^f and ϵ^m, the respective microstrains. Then, at any instant of loading, the strains must be compatible, and the stresses must be in equilibrium, that is

$$\begin{gathered}\epsilon^f = \epsilon^m = \epsilon^c \\ \sigma^f V_f + \sigma^m V_m = S\end{gathered} \tag{1}$$

where ϵ^c is the composite strain and V_f and $V_m = 1 - V_f$ are the volume fractions of the constituents. If E_f and E_m denote the instantaneous Young's moduli of the constituents, the instantaneous Young's modulus of the composite is

$$E_c = E_f V_f + E_m V_m \tag{2}$$

Let $\sigma_Y{}^m$ denote the magnitude of the uniaxial yield stress of the matrix material. Then the proportional limit of an initially stress free composite is

$$S_Y = \sigma_Y{}^m E_c / E_m \tag{3}$$

One can assume, without the loss of generality, that the $\sigma_Y{}^m$ = constant, and select the appropriate value with regard to the previous loading history of the matrix. For $0 \leqslant S \leqslant S_Y$, the composite deforms elastically, the matrix follows the loading path OA, the fiber the path OA', Fig. 1. For $S_Y \leqslant S \leqslant S_{\max}$, the respective paths are AB and $A'B'$. It is assumed that at B', the fiber stress does not exceed either the yield or ultimate strength of the fiber, that is, $\sigma^f < \sigma_Y{}^f \leqslant \sigma_U{}^f$.

One can find that along the path $A'B'$, the stress in the fiber is

$$\sigma^f = (S - S_Y)/V_f + S_Y \frac{E_f}{E_c} = (S - \sigma_Y{}^m V_m)/V_f \tag{4}$$

When the composite is unloaded at $S = S_{\max}$, the unloading paths are BC and $B'C'$. In the absence of the Bauschinger effect, the matrix will remain elastic on the BC path, providing that

$$S_{\max} - S_{\min} \leqslant 2S_Y \tag{5}$$

This equation defines the shakedown stress range of the composite. It is obvious that the magnitude of this stress range does not depend on the position of the origin O on the S axis, or on the initial stresses which may exist in the composite prior to the plastic straining of the matrix, or on the stress ratio $R = S_{\min}/S_{\max}$.

For example, for $R = -1$, the path CB would pass through the origin O, and the composite may experience only cyclic strain hardening before shakedown. If the shakedown stress range is exceeded upon unloading, the matrix resumes plastic straining along the path CD, and the cyclic loading paths $BCDE$ and $B'C'D'E'$ are followed in the matrix and in the fiber, respectively. Under such circumstances, the matrix does not shake down. In the absence of sufficient cyclic strain hardening, which could restore the shakedown state within several load cycles [*6*], the matrix will experience cyclic plastic straining, and the attendant low cycle failure. In a composite, this process is usually demonstrated by initiation of many fatigue microcracks in the matrix or at the fiber-matrix interface, which can propagate through the fibers and cause low cycle fatigue failure of the composite [*8–10*].

Another loading regime which is frequently used in fatigue experiments involves the application of a constant cyclic composite strain range $0 \leqslant \epsilon^c \leqslant \epsilon_{max}{}^c$. Figure 2 shows the respective responses of the matrix and the composite. It is assumed that an initial residual stress, $\sigma_R{}^m$, exists

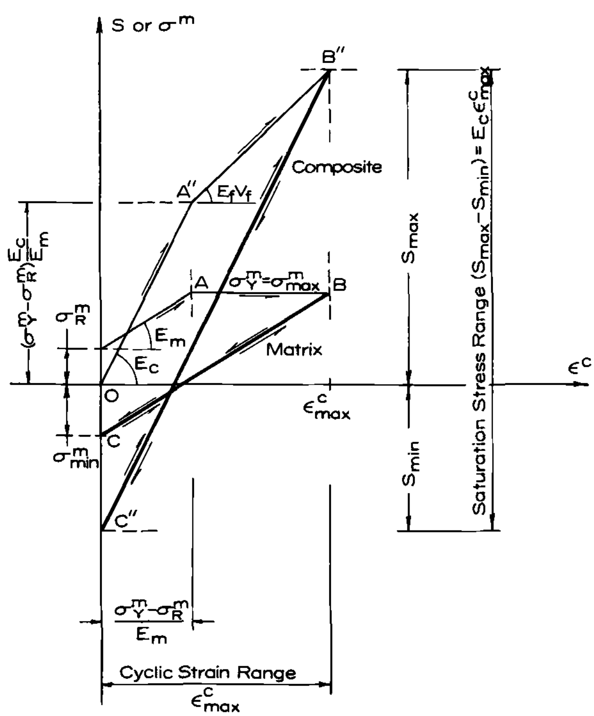

FIG. 2—*Deformation and shakedown of a composite in a strain-controlled uniaxial test.*

in the matrix. The path BC in the matrix and $B''C''$ in the composite will remain within a shakedown stress range as long as Eq 5 is satisfied. Then one finds that the saturation composite stress range corresponding to the applied strain range is

$$S_{\max} - S_{\min} = E_c \epsilon_{\max}{}^c \tag{6}$$

Assuming that plastic straining took place in the matrix along the path AB, the composite stresses are

$$\begin{aligned} S_{\max} &= \epsilon_{\max}{}^c E_f V_f + (\sigma_Y{}^m - \sigma_R{}^m) V_m \\ S_{\min} &= (\sigma_Y{}^m - \sigma_R{}^m) V_m - \epsilon_{\max}{}^c E_m V_m \end{aligned} \tag{7}$$

and the extreme matrix stresses are

$$\sigma_{\min}{}^m = \sigma_{\max}{}^m - \epsilon_{\max}{}^c E_m \geqslant -\sigma_Y{}^m \tag{8}$$

It may be noted that the saturation stress range is nonsymmetric. $S_{\max} \neq S_{\min}$, if $\epsilon_{\max}{}^c < 2\sigma_Y{}^m/E_m$, that is, if the matrix shakes down. On the other hand, when the saturation range is symmetric, and $\epsilon_{\max}{}^c > 2\sigma_Y{}^m/E_m$, there is no shakedown and low cycle fatigue failure of the composite follows. The magnitude of the initial matrix stress $\sigma_R{}^m$ affects the apparent proportional limit of the composite, but has no effect on $S_{\max}$, $S_{\min}$, or $\sigma_{\max}{}^m$ if the matrix deforms plastically. On the other hand, if $S_{\max} < (\sigma_Y{}^m - \sigma_R{}^m)E_c/E_m$, the matrix remains elastic, and Eq 8 must be replaced by

$$\begin{aligned} \sigma_{\max}{}^m &= \sigma_R{}^m + S_{\max} E_m/E_c = \sigma_R{}^m + \epsilon_{\max}{}^c E_m \\ \sigma_{\min}{}^m &= \sigma_R{}^m \end{aligned} \tag{9}$$

Matrix-Limited Fatigue Behavior

Although shakedown of the matrix is always a necessary condition for prevention of a fatigue failure, it may not be a sufficient one if the matrix yield stress exceeds the fatigue limit of the matrix, $\sigma_{FL}{}^m < \sigma_Y{}^m$. Under such circumstances, the fatigue limit stress range

$$S_{\max} - S_{\min} \leqslant 2\sigma_{FL}{}^m E_c/E_m \tag{10}$$

Figure 3 shows the behavior of both fiber and matrix in this case, the notation is analogous to that used in Fig. 1. One possible measure which can lead to the satisfaction of Eq 9, on the path GF, after the matrix has experienced straining into the plastic region, is the application of one or more stress cycles within the shakedown stress range such that the maximum composite prestress

$$S_{PR} = S_{max} + (\sigma_Y{}^m - \sigma_{FL}{}^m)E_c/E_m \tag{11}$$

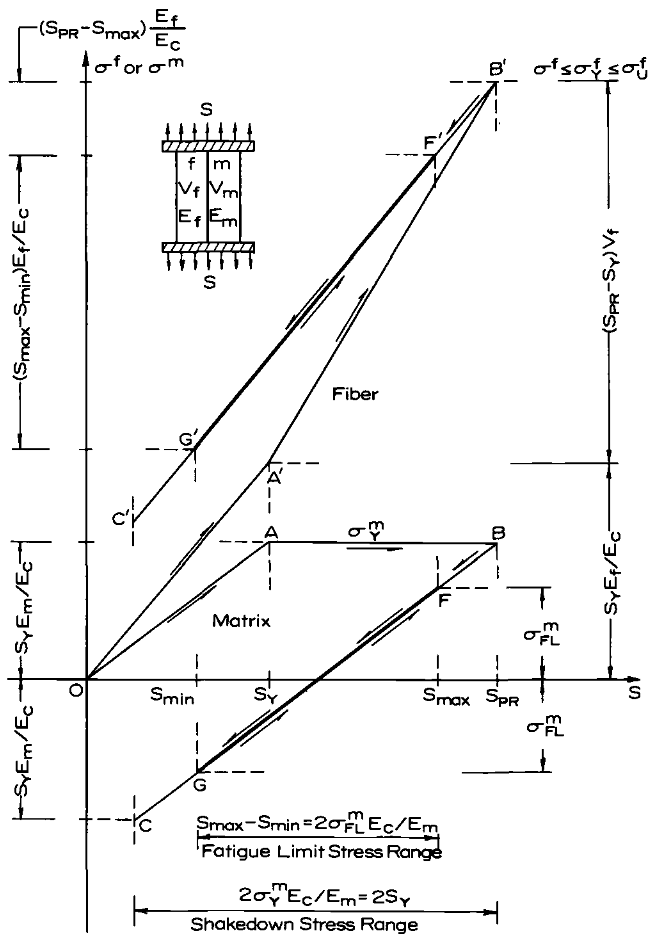

FIG. 3—*Reduction of matrix stress amplitude in the shakedown state by prestressing of the composite.*

A similar result can be achieved in a strain controlled test, Fig. 2, when the total cyclic strain range is expanded for few cycles, so that $\epsilon_{PR}^c > \epsilon_{max}^c$. The required magnitude of ϵ_{PR}^c can be found from Eqs 7 and 11.

In the absence of plastic deformation of the matrix, the composite stresses which will keep the matrix within its fatigue limits are

$$\begin{aligned} S_{max} &= (\sigma_{FL}^{m+} - \sigma_R^m)E_c/E_m = \sigma_{max}^m E_c/E_m \\ S_{min} &= (\sigma_{FL}^{m-} + \sigma_R^m)E_c/E_m = \sigma_{min}^m E_c/E_m \end{aligned} \tag{12}$$

where σ_R^m is an assumed initial residual stress in the matrix, as in Fig.

2, and $\sigma_{FL}{}^{m+} - \sigma_{FL}{}^{m-}$ is the allowable stress amplitude within fatigue limits of the matrix at the particular value of $R = \sigma_{\min}{}^{m}/\sigma_{\max}{}^{m}$. The path FG of Fig. 3 now passes through the origin O. Equation 12 suggests a beneficial influence of $\sigma_R{}^m < O$. Analogous equations can be derived for strain controlled tests, Fig. 2, where the stress path in the matrix can be nonsymmetric even after the matrix has deformed plastically.

Fiber-Limited Fatigue Behavior

The above considerations involving shakedown and the imposition of limits on the stresses in the matrix, were made under the assumption that the stresses in the fibers are lower than the fatigue limit, the yield stress, or the ultimate strength of the fiber. That was already suggested in Figs. 1 and 3. Also, the compressive stresses in the fiber must not cause fiber buckling [*11*].

In the presence of plastic yielding of the matrix, one finds from Fig. 1 that

$$\begin{aligned} S_Y \leqslant S_{\max} &\leqslant (\sigma_{\max}{}^{f} - S_Y E_f/E_c)V_f + S_Y \\ &= (\sigma_{\max}{}^{f} - \sigma_Y{}^{m} E_f/E_m)V_f + \sigma_Y{}^{m} E_c/E_m \end{aligned} \tag{13}$$

If the matrix remains elastic

$$S_{\max} \leqslant \sigma_{\max}{}^{f} E_c/E_f \leqslant S_Y \tag{14}$$

In Eqs 13 and 14, $\sigma_{\max}{}^{f}$ is the maximum allowable fiber stress.

Shakedown in Off-Axis Tests

The results of the shakedown analysis of unidirectional composites have shown that substantial shakedown effects can be achieved only with respect to stress states which are symmetric about the fiber axis [*4*]. Other stress states, which may cause failure of the composites in longitudinal or transverse shear, do not contribute to shakedown, but they can reduce the effective yield stress which determines the magnitudes of the shakedown limits for the axial loads.

Similar considerations were applicable in the determination of initial yield surfaces of unidirectional composites [*3*], where the effect of the longitudinal shear stresses on initial yielding was expressed by means of a reduced yield stress of the matrix. Inasmuch as the translated initial yield surface is identical with the shakedown surface for axisymmetric loading states, the reduced yield stress can be also used to account for the influence of shear composite stresses on shakedown.

In particular, let us consider that a unidirectional composite is loaded by a cyclic stress, S, which contains an acute angle, θ, with the fiber direction in the lamina. Furthermore, let us introduce a cartesian coordinate system, x_1, x_2, x_3, associated with the lamina, such that the x_3 axis is in the fiber direction, and the x_2 axis is perpendicular to it in the plane of the lamina. Then, the axisymmetric stress in the lamina can be denoted as S_{33}, while S_{23} and S_{12} are the longitudinal and transverse shear stresses, respectively. The magnitudes of these stresses can be found in terms of S and θ as

$$\begin{aligned} S_{33} &= S \cos^2\theta \\ S_{23} &= S \sin\theta \cos\theta \\ S_{12} &= \tfrac{1}{2} S \sin^2\theta \end{aligned} \tag{15}$$

Following the derivation presented in Ref *3*, the reduced yield stress of the matrix can approximately be defined as

$$\sigma_{YR}{}^m = \sigma_Y{}^m \left[1 - \left(\frac{S_{23}}{S_{23}{}^Y}\right)^2 - \left(\frac{S_{12}}{S_{12}{}^Y}\right)^2\right]^{1/2} \tag{16}$$

where $S_{23}{}^Y$ and $S_{12}{}^Y$ are the magnitudes of the shear stresses at initial yield. It was found that for metal matrix composites with a low volume fraction of fiber [*2*,*3*]

$$S_{23}{}^Y \doteq 0.4\ \sigma_Y{}^m,\ S_{12}{}^Y \doteq 0.45\ \sigma_Y{}^m \tag{17}$$

Equations 16 and 17 define the reduced yield strength of the matrix, which can be used in the evaluation of shakedown limits on S_{33}, in the same way as $\sigma_Y{}^m$ was used to evaluate the limits $S_{\max}$ and $S_{\min}$ on S in Fig. 1. From Eqs 3 and 5, the shakedown condition can be written as

$$S_{\max} - S_{\min} \leqslant 2\ \sigma_{YR}{}^m E_c/E_m = 2S_Y \tag{18}$$

The proportional limit S_Y for a unidirectional lamina loaded in an off-axis direction can be found from Eqs 15 to 17 in the implicit form

$$S_Y \cos^2\theta = \sigma_Y{}^m \left[1 - \left(\frac{S_Y \sin\theta \cos\theta}{0.4\ \sigma_Y{}^m}\right)^2 - \left(\frac{S_Y \sin^2\theta}{0.9\ \sigma_Y{}^m}\right)^2\right]^{1/2} \frac{E_c}{E_m}$$

The resulting S_Y can be substituted into Eq 18, and the fatigue limit $S_{\max}$ can be evaluated for any given $R = S_{\min}/S_{\max}$ as

$$S_{\max} = \frac{2E_c}{(1 - R)E_m}\ \sigma_Y{}^m \left[\cos^4\theta + \left(\frac{\sin\theta \cos\theta}{0.4\ E_m/E_c}\right)^2 + \left(\frac{\sin\theta^2}{0.9\ E_m/E_c}\right)^2\right]^{-1/2} \tag{19}$$

The initial yield stresses (Eq 17) were calculated for a perfect interface bond; somewhat different results would be expected for composites with degraded interfaces. It should be emphasized that Eqs 16, 17, and 19 are only approximate expressions for the evaluation of $S_{\max}$, but it will be seen that they predict experimental results quite well. A more accurate analysis of the off-axis shakedown problem is beyond the scope of this paper.

Interpretation of Experiments

It is convenient to divide the experimental results into two major groups, one which contains the results obtained on composites in the as-fabricated state, and one which includes the results for heat-treated composites. The reason for this division lies in the following differences between the two groups, which can have a strong influence on the fatigue behavior of the composites:

(*a*) The fatigue limits of certain matrices in the as-fabricated state, such as aluminum and copper, are either equal to or somewhat larger than the initial yield stresses, and their magnitude is small [*12*]. Therefore, shakedown is likely to take place and control the fatigue behavior in these composites, providing that the fiber stresses do not exceed allowable limits. The initial residual stresses, if they exist, can be neglected since they do not affect the shakedown limits.

(*b*) Composites with heat-treated matrices may contain residual stresses of large magnitudes. The matrix yield strength is high and usually much greater than the fatigue limit. Therefore, if shakedown takes place in these composites, the matrix is loaded above its fatigue limit and can serve as a nucleation source for fatigue microcracks. If the composite is loaded only in the elastic manner, within the proportional limits of the matrix, the actual loading regime of the matrix is affected by the residual stresses. Therefore, it may be difficult to evaluate both the proportional limit of the composite and the composite stresses which would prevent fatigue cracking in the matrix. Each of these complications is, of course, resolvable. For example, a composite prestress can reduce the matrix stresses in the shakedown state, Fig. 3. The initial residual stresses can be evaluated for any known thermal loading path and considered in the evaluation of the allowable composite stresses for which $|\sigma^m| \leq \sigma_{FL}{}^m$, Eq 12. An extensive investigation of the residual microstresses in heat-treated composites has been recently completed by Dvorak and Rao, and will be published in the near future. The residual stress values used here were found in that study.

In what follows, the properties of fiber and matrix materials will be taken from Table 1, and supplemented when necessary.

Fatigue Behavior of As-Fabricated Composites

Boron-Aluminum Composites—These composites have been tested extensively by several investigators. As indicated earlier, shakedown is

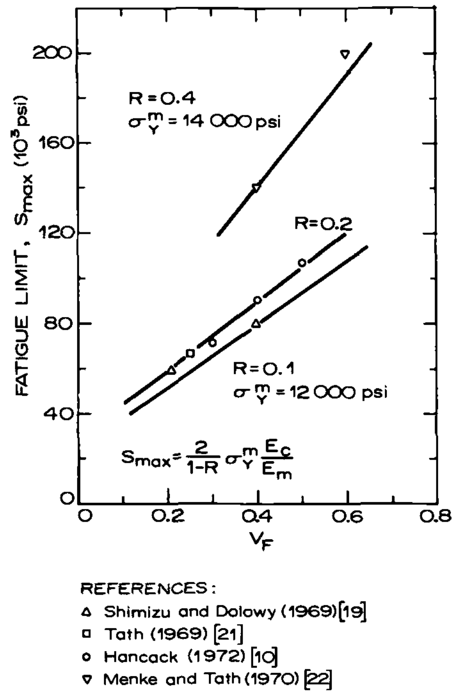

FIG. 4—*Comparison of predicted and measured fatigue limits for 6061-O Al-B composites.*

expected to take place in these composites during cyclic loading at or below the composite fatigue limit, if both the fiber and the matrix are loaded below their respective fatigue limits in the shakedown state. In particular, from Fig. 1 and Eqs 1 and 5, one finds that the fatigue limit of the composite should be equal to

$$S_{max} = \frac{2}{1 - R}\,\sigma_Y{}^m\, E_c/E_m \tag{20}$$

providing that $\sigma_Y{}^m = \sigma_{FL}{}^m$, and $\sigma_{max}{}^f$ is admissible.

Equation 20 was used to evaluate the composite fatigue limits of eight materials used in testing programs performed by four different groups of investigators on the 6061-O Al-B composites, Fig. 4. It was found that for $R = 0.1$ and 0.2 the best match was obtained for $\sigma_Y{}^m = \sigma_{FL}{}^m = 12\,000$ psi, whereas for the two tests at $R = 0.4$, $\sigma_Y{}^m = \sigma_{FL}{}^m = 14\,000$ psi. Both these values are within the limits indicated in Table 1. Figure 5 illustrates the relationship between the S-N curves of three composites and the respective shakedown limits. The experiments were performed by Hancock [*10*].

TABLE 1—*Mechanical properties of fiber and matrix materials.*

Fibers					
Material	E_f, 10^6 psi	$\sigma_Y{}^f$, 10^3 psi	$\sigma_{FL}{}^{f\,a}$, 10^3 psi	$\sigma_U{}^f$, 10^3 psi	References
B	60	...	...	400 to 570	[*8–10*]
Be	42	62 to 75	...	124 to 150	[*13*]
W	58	...	80	237	[*14,15*]
355 stainless steel	30	50	53.5	101	[*16*]

$^a\,R = \sigma_{min}{}^f/\sigma_{max}{}^f = -1$, $N = 10^6$.

Matrices				
Material	E_m, 10^6 psi	$\sigma_Y{}^m$, 10^3 psi	$\sigma_{FL}{}^{m\,a}$ 10^3 psi	References
1235-O Al	10.5	5	5	[*9,12*]
6061-W Al	10.5	10 to 15	...	[*12*]
6061-O Al	10.5	10 to 15	12 to 15	[*12,17*]
6061-T6 Al	10.5	40	25	[*12,19*]
7075-W Al	10.5	20	...	[*12*]
7075-T6 Al	10.5	70 to 75	38	[*19*]
2024-W Al	10.5	20 to 35	...	[*12*]
2024-T8 Al	10.5	65	18	[*16*]
X7002-T6 Al	10.5	40	24 ($R = 0.1$)	[*13*]
OFHC-Cu Al	17	5	14	[*18*]

$^a\,R = -1$, $N = 10^6$.

Two important conclusions can be derived from Figs. 4 and 5. The first is that the presence of the fibers did not affect the magnitude of the fatigue limit of the matrix. The second suggests that the contribution of the fibers to the elevation of the composite fatigue limit above that of the matrix is due only to the reduction of the matrix stresses in the presence of the fibers. Finally, one can find from Eq 13 that in the tests shown in Fig. 4, $\sigma_{max}{}^f \leqslant 365\,000$ psi which is equal to 90 percent of the lower bound of boron fiber strength, Table 1.

Table 2 presents a comparison of the theoretical and experimental fatigue limits for a group of off-axis tests on unidirectional 6061-O Al-B composites, with $V_f = 0.25$. The experimental values were reported by Toth [*21*]. The theoretical predictions were made from Eqs 15 to 19, assuming that $\sigma_Y{}^m = 12\,000$ psi, as in Fig. 4. It is observed that the theoretical values are slightly higher than the experimental ones. These differences can be attributed to the approximate nature of Eqs 16, 17,

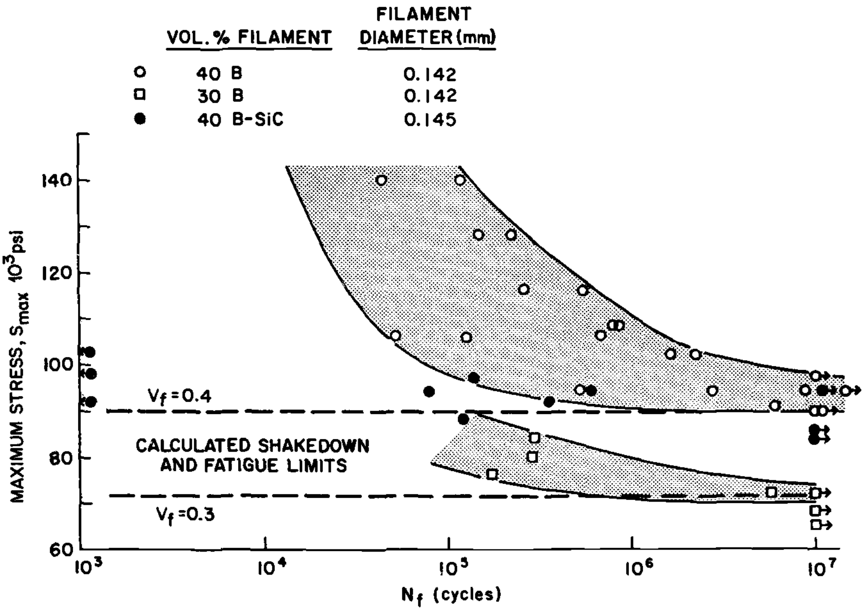

FIG. 5—*Predicted shakedown and fatigue limits, and results of uniaxial fatigue tests in 6061-O Al-B composites obtained by Hancock* [10], (R = *0.2*).

and 19. The off-axis behavior is apparently controlled by the shakedown condition only, since it is doubtful that the introduction of the reduced matrix yield stress, $\sigma_{YR}{}^m$, in the fiber direction, Eq 16, implies a similar reduction in the $\sigma_{FL}{}^m$. Specimens loaded above the shakedown limit experience incremental plastic collapse and low-cycle fatigue failure. This suggests that the S-N curves for the off-axis specimens should be rather flat, especially at higher values of θ, which was indeed observed in the experiments, Fig. 6.

TABLE 2—*Fatigue limits in off-axis tests (unidirectional 6061-O Al-B*, V_f = *0.25*, R = *0.2*).

	Fatigue Limits	
Fiber-Load Angle, θ deg	Measured, Ref [*21*], 10^3 psi	Predicted, Eq 19, 10^3 psi
0	65	67
5	52	58
20	27	31
45	16	19.5

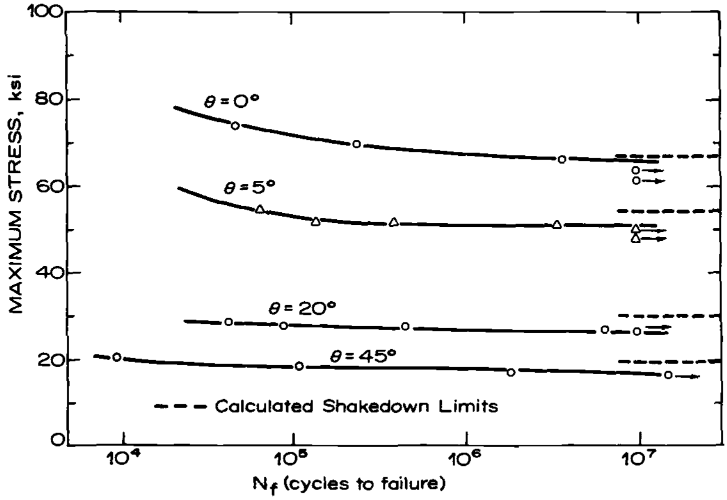

FIG. 6—*Predicted shakedown and fatigue limits, and results of off-axis uniaxial fatigue tests on 6061-O Al-B composites obtained by Toth* [21]; (R = *0.2*, V_f = *0.25*).

Tungsten-Copper Composites—These composites, tested by Ham and Place [*15*], exhibited fatigue behavior similar to that of the 6061-O Al-B composites. Cyclic hardening apparently takes place prior to shakedown, since the fatigue limit is almost three times as high as the initial yield stress, Table 1.

Using the material parameters for tungsten and copper from Table 1 in Eq 20 for $R = 0$, one finds the comparison between the predicted and theoretical fatigue limits shown in Table 3. Again, the agreement is very satisfactory.

The conclusions about the mechanism of fatigue which were derived from the behavior of the boron-aluminum composites are valid here as well, that is, the fatigue limit of the composite is controlled by the matrix and the magnitude of the stresses supported by the matrix at a given reinforcement.

It is of interest to note that the resistance of the fibers to microcrack propagation is not greatly affected by the magnitude of the stresses supported by the fibers. In the boron-aluminum composite, we found that ${\sigma_{max}}^f < 365\,000$ psi or 90 percent of ${\sigma_U}^f$, whereas in the tungsten-copper composites ${\sigma_{max}}^f \leqslant 45\,000$ psi, or about 19 percent of average tensile strength of the tungsten fiber, Table 1. Similarly, the ratio of Young's moduli of the constituents, E_f/E_m seems to have no effect on the composite fatigue limit. For boron-aluminum, this ratio is equal to 6, and for tungsten-copper, it is equal to 3.4.

TABLE 3—*Fatigue limits for W-Cu composites* (R = *0*).

	Fatigue Limits	
V_f	Measured, Ref *15*, (10^3 psi)	Predicted, Eq 20, (10^3 psi)
0.074	16.6	16.6
0.230	20.2	21.5

Beryllium-Aluminum Composites—These composites in the as-fabricated state were tested by Hancock [*8,9*], and the results are described in Table 4. These were strain-controlled tests. The cyclic strain range $\epsilon_{max}{}^c$ varied from 0.0045 to 0.012 but was kept constant in each test. The stress range corresponding to the imposed strain became symmetric after several cycles, that is, $R = S_{min}/S_{max} = -1$. One can easily find from Eq 8 that the elastic strain range of the matrix is $\epsilon_e{}^m = 2\ \sigma_Y{}^m/E_m$, that is, for $\sigma_Y{}^m = 5000$ psi, and $E_m = 10.5 \times 10^6$ psi; Table 1, $\epsilon_e{}^m = 0.00095 \ll \epsilon_{max}{}^c$. Also, the elastic strain range for the ductile beryllium filament is about $\epsilon_e{}^f = 0.004$ [*13*]. It follows that in all tests described in Table 4, the imposed strain range caused cyclic plastic straining in both fiber and matrix, which resulted in the observed low cycle fatigue failure.

Fatigue Behavior of Heat-Treated Composites

One of the major difficulties in the prediction of fatigue limits of these composites is caused by the presence of initial stresses. Preliminary results obtained in a simulation of the T6 temper in boron-aluminum and beryllium-aluminum composites have shown that, in the matrix, the

TABLE 4—*Fatigue behavior of as-fabricated Be-Al composites in controlled strain tests.*[a]

Material	V_f	$\sigma_Y{}^m$, ksi	S_Y, ksi	$\epsilon_{max}{}^c$ $\times 10^3$	ΔS, ksi ($R = -1$)	N_F, cycles	References	Predicted Mechanism of Fatigue Failure
Be-1235 Al	0.34	5	9.17	5.0	42.0	22 000	[*9*]	$\epsilon_e{}^m \doteq 0.00095 \ll \epsilon_{max}{}^c$
Be-1235 Al	0.34	5	11.265	5.2	53.1	47 000	[*9*]	$\epsilon_e{}^f \doteq 0.004 < \epsilon_{max}{}^c$
Be-1235 Al	0.34	5	...	6.0	47.0	20 000	[*9*]	low cycle fatigue failure
Be-1235 Al	0.34	5	...	7.0	...	7 000	[*9*]	of both matrix and
Be-Al	0.34	5[b]	...	4.5	42	3 000	[*8*]	fibers, propagation of
Be-Al	0.34	5[b]	...	10.2	58	2 000	[*8*]	matrix microcracks
Be-Al	0.34	5[b]	...	12.7	60	1 000	[*8*]	through the fibers

[a] $\Delta S = S_{max} - S_{min}$.
[b] Estimated values.

normal residual stresses in the fiber direction are positive and equal to about one half of the matrix yield stress in the as-quenched (*W*) state. These yield stresses are given in Table 1 for several aluminum alloys. It will be assumed that the residual stress in the matrix, $\sigma_R{}^m = 0.5\ \sigma_Y{}^m$ in (*W*) state, Table 5. Then, the residual stress in the fiber is $\sigma_R{}^f = -\sigma_R{}^m V_m/V_f$.

The fatigue properties of matrices are usually known only for comparable homogeneous metals. Assuming that the effect of the different fabrication procedures is negligible, one can find the fatigue limits of the 6061-T6 and 7075-T6 aluminum matrices for any loading regime from the Goodman diagram [*19*]. It is convenient to express the fatigue limits in the form

$$\begin{aligned} \sigma_{\max} &\leqslant \sigma_m + \sigma_a \\ \sigma_{\min} &\geqslant \sigma_m - \sigma_a \end{aligned} \tag{21}$$

where σ_m and σ_a are the mean and alternating stresses, respectively. From Ref *19* one can find the following approximations.

For 6061-T6 Al

$$\begin{aligned} \sigma_a &= 25 - 0.50\ \sigma_m \text{ for } 0 \leqslant \sigma_m \leqslant 20 \text{ ksi} \\ \sigma_a &= 30 - 0.75\ \sigma_m \text{ for } 20 \leqslant \sigma_m \leqslant 40 \text{ ksi} \end{aligned} \tag{22}$$

For 7075-T6 Al

$$\begin{aligned} \sigma_a &= 38 - 0.43\ \sigma_m \text{ for } 0 \leqslant \sigma_m \leqslant 40 \text{ ksi} \\ \sigma_a &= 49 - 0.70\ \sigma_m \text{ for } 40 \leqslant \sigma_m \leqslant 70 \text{ ksi} \end{aligned} \tag{23}$$

These expressions will be used for evaluation of the matrix fatigue limits in the boron-aluminum and beryllium-aluminum composites.

It can be easily established from Eqs 22 and 23, and from the corresponding yield stresses for the two alloys, that elastic straining within the shakedown limits will always cause matrix microstresses larger than the fatigue limits. Therefore, it is expected that fatigue limits of heat treated composites will be always lower than the shakedown limits, in contrast to the behavior of as-fabricated composites.

Boron-Aluminum Composites—These composites in the T6, M-T6, and M-PFZ states were tested by Hancock [*8,9,23*]. The experimental results are shown in Table 5. Except for the last boron-aluminum test, all experiments were performed under a controlled applied strain. The first specimen, T6, reached the saturation stress of 97 ksi within the first few cycles and did not harden or soften during the test period of 40 000 cycles. Although the experimental information does not include the magnitude of the maximum applied stress, $S_{\max}$, one can calculate the maxi-

TABLE 5—*Fatigue behavior of heat-treated composites.*

	Experimental Results									Theoretical Analysis					
Material and Heat Treatment	V_f	$\sigma_Y{}^m$, ksi	S_Y, ksi	$\epsilon_{max}{}^c$ $\times 10^3$	ΔS, ksi	S_{max}, ksi	ΔS_{SH} or S_{SH}	N_F cycles	Ref	$\sigma_R{}^{m*}$, ksi	$\epsilon_e{}^m$ $\times 10^3$	$\sigma_{max}{}^f$, ksi	$\sigma_{max}{}^m$, ksi	$\sigma_{FL}{}^m$, ksi	Predicted Mechanism of Fatigue Failure
B-7075 Al (T6)	0.30	65	56.6	4.5	97	97	310	>>40000	[9]	10	5.25	247	57	55 [b]	no failure
B-7075 Al (M-T6)	0.30	75	...	6.0	145	...	356	19151	[8,23]	10	6.2	360	73	58 [b]	
B-7075 Al (M-PFZ)	0.30	42	51.6	6.0	145	...	200	20000 [a]	[8,23]	10	3.0	360	42	30 [c]	matrix fatigue and
B-7075 Al (M-PFZ)	0.30	42	55.6	7.2	164	...	200	20000 [a]	[8,23]	10	3.0	432	42	27 [c]	cracking of fibers
B-7075 Al (M-PFZ)	0.30	42	...	...	101	125	200	18800	[23]	10	3.0	323	42	25 [c]	
Be-6061 Al (T6)	0.34	40	38.1	5.0	92	...	75 [d]	1889	[8,23]	5	3.3	125	40	25 [c]	low cycle fatigue
Be-6061 Al (M-T6)	0.34	40	24.4	5.2	90	...	75 [d]	2895	[8,23]	5	3.3	125	40	25 [c]	of fibers and matrix fatigue
Be-X7002 Al (T6)	0.30	38	63	...	33	37	143	10^7	[13]	5	...	64	23	24 [f]	no failure
Be-X7002 Al (*T6*)[e]	0.30	...	...	...	33	37	...	10^7	[13]	0	...	74	13.7	13 [f]	no failure
355 SS-2024 Al (T8)	0.25	60	...	...	51	25.6	60	10^7	[16]	0	...	57	17	18 [f]	no failure

[a] Estimated magnitudes.
[b] Calculated from Eq 23.
[c] Calculated from Eq 22.
[d] Limited by $\sigma_Y{}^f \doteq 75$ ksi.
[e] Tested at 500°F.
[f] Measured values.
$\Delta S = S_{max} - S_{min}$, ΔS_{SH} — shakedown stress range.

mum elastic strain of the matrix as $\epsilon_e{}^m = (\sigma_Y{}^m - \sigma_R{}^m)/E_m = 0.00525$. Inasmuch as this strain is greater than the applied strain and the fiber stress is within acceptable limits, one may conclude that the composite remained elastic during the entire test. Equation 9 can be used to evaluate the $\sigma_{\max}{}^m$ and Eqs 21 and 22 to find the appropriate fatigue limit, $\sigma_{FL}{}^m$. These two stresses are approximately equal; thus, no fatigue failure is expected.

The remaining four boron aluminum specimens failed after about 20 000 cycles. The saturation stress range was never stable for more than 200 cycles or so, and decreased continuously thereafter. An analysis of the response of these composites reveals that $\sigma_{\max}{}^m \doteq \sigma_Y{}^m$ during the first loading cycle. Although all load ranges were well within the shakedown limits, the maximum stress in the matrix exceeded the fatigue limit during each cycle, Fig. 2. Therefore, fatigue failure of the matrix was expected. It is doubtful, however, that matrix fatigue alone could result in the short fatigue life of the composite. The maximum stresses in the fibers are quite high, and it may be assumed that fiber failure was also a cause of the short fatigue life. That was indicated also by the progressive cyclic softening of these composites. Swanson and Hancock [*24*] reported boron fiber strengths (as delivered) in the range from 316 to 529 ksi, which overlaps with the stress range calculated in Table 5.

Beryllium-Aluminum Composites—These composites with the 6061-T6 and X7002-T6 matrices were tested by Hancock [*8,23*] and Toy [*13*], respectively. The 6061-T6 Al-Be specimens were tested in the controlled applied strain mode. The fatigue life was extremely short. The tensile properties of beryllium filaments, both in as delivered and extracted conditions, were tested by Toy [*13*]. From these results one finds that the strain range applied in the tests was larger than the elastic strain range of both the filament and the matrix.

The B-X7002 Al(T6) composite was tested more extensively so that both the *S-N* curve and the fatigue limit were established. The prediction of the composite fatigue limit was possible because the fatigue limit of the matrix was also measured in the experiments. The matrix stresses were obtained from Eq 9. The equality of the composite fatigue limits at 70 and 500°F appeared to be surprising. However, experimental measurements showed that $E_c = 21.0 \times 10^6$ psi at both temperatures, whereas $E_m = 10.5 \times 10^6$ psi at 70°F, and 7.8×10^6 psi at 500°F. Viscous flow was not mentioned. Considering that $\sigma_R{}^m \rightarrow 0$ at the higher temperature, one obtains from Eq 9 the fatigue limits shown in Table 5.

355 Stainless Steel-2024 T8 Aluminum Composite—This composite was tested by Varschavsky and Tamayo [*16*]. The fatigue limit of the matrix material was again measured, and it is seen that the calculated $\sigma_{\max}{}^{m}$ is equal to the $\sigma_{FL}{}^{m}$.

The significant result which can be derived from Table 5 is that at the composite stress which was equal to the composite fatigue limit, the maximum stress in the matrix $\sigma_{\max}{}^{m}$ was equal to the fatigue limit of the matrix $\sigma_{FL}{}^{m}$.

Discussion

The principal conclusion which emerges from the present work is that unidirectionally reinforced metal matrix composites examined here can be considered as bimaterial structures, the fatigue resistance of which is determined by the fatigue strengths of the constituents. It appears that the reinforcing fibers do not significantly improve the fatigue limit of the matrix, and the matrix does not greatly improve the strength of the fibers. The superior fatigue properties of the composite are achieved through favorable internal stress distribution which reduces the stresses supported by the weaker matrix and transfers them to the stiffer fiber. The fatigue limit of a composite can be determined from the requirement that the stresses, acting in the constituents during a particular loading program, do not exceed the respective fatigue limits of either the matrix or the fiber.

Apart from the mechanical considerations, substantial progress in the development of fatigue-resistant composites has been achieved by metallurgical means. An authoritative survey of the subject has been recently prepared by Hancock [25]. The properties of the fiber-matrix interfaces are of key importance. For example, as shown in Fig. 5, the silicon carbide (SiC) coating on the boron fiber can substantially degrade the composite properties. The present "state of the art" composites, for example, those shown in Fig. 4, appear to perform as expected from simple mechanical considerations. More recent results indicate that improvements in composite properties can be expected by perfection of fabrication procedures [25]. However, it may be useful to examine if the more sophisticated fabrication process does also improve the properties of the constituents.

Further refinement in analytical prediction techniques can be also expected. It should help to provide more accurate estimates of fatigue limits of composites, especially in the case of heat treated matrices, in laminated structures, in the presence of geometrical stress concentrations, etc. The present exposition of the effectiveness of the simplest mechanical models in predicting the composite fatigue limits certainly indicates the promise of the continuum mechanics approach which is indispensable for efficient structural applications of composites.

Conclusions

Rules for Design of Fatigue-Resistant Composites

The results of the present work suggest that fatigue limits of metal matrix composites may be improved by the following measures.

1. The fiber should have both high stiffness and strength, and the fiber volume fraction should be high. For a given matrix, the allowable cyclic stress range is directly proportional to the ratio E_c/E_m of the composite and matrix Young's moduli, Eq 10. Brittle, high strength fibers are preferable; ductility of the fibers does not seem to elevate composite fatigue limits.
2. The matrix should have a low Young's modulus and a high fatigue limit which is not lower than the matrix yield stress. This is usually the case in as-fabricated composites. Then, the fatigue limit of the composite can be evaluated from the requirement that the matrix must shake down under the applied composite loading program.
3. Low cycle fatigue of as-fabricated composites is always associated with cyclic plastic straining of the matrix or ductile fibers, beyond the shakedown limits of either constituent.
4. The present results indicate that both the ratio of the elastic moduli, E_f/E_m, and the maximum stress in the fiber, $\sigma_{\max}{}^f$, have no effect on the magnitude of the fatigue limit of a composite.
5. Matrices with higher yield stresses can be used profitably, provided that they have also a high fatigue limit which can be smaller than the yield strength. Such composites may be prestressed above the service load. The prestress should reduce the stress range applied to the matrix and improve the composite fatigue limit. This procedure can also help eliminate residual stresses caused by heat treatment.
6. The fatigue limits for off-axis loading can be predicted on the basis of shakedown analysis.
7. The characteristics of the fiber-matrix interface do not appear to affect the magnitude of the axial fatigue limit of a composite. However, if the composite is loaded above its fatigue limit, the interfaces can have a very significant effect on the rate of fatigue microcrack propagation in the constituents and on the fatigue life.
8. In general, the allowable cyclic stress range or the fatigue limit of a given composite can be determined from the fatigue limits of the constituents and the internal microstress distribution in the composite. As a

rule, fatigue failure of the composite can be avoided when each of the constituents is stressed below its particular fatigue limit during the composite loading program. However, more recent results on boron-titanium composites obtained by Toth[3] suggest that the composite fatigue limits can be much smaller than those of the titanium matrix. It is possible, therefore, that other fatigue mechanisms are present in these composites which are distinguished by the high yield strength of the matrix.

Acknowledgments

We wish to acknowledge the support of this work by the U.S. Army Research Office, the encouragement by Saibel and J. J. Murray of the U.S. Army Research Office, and the scientific supervison by John Slepetz of the U.S. Army Materials and Mechanics Research Center. M. S. M. Rao made many useful suggestions when the work was in progress.

References

[*1*] Salkind, M. J., in *Composite Materials: Testing and Design (Second Conference), ASTM STP 497,* American Society for Testing and Materials, 1972, pp. 143–169.
[*2*] Dvorak, G. J., Rao, M. S. M., and Tarn, J. Q., *Journal of Composite Materials,* Vol. 7, April 1973, pp. 194–216.
[*3*] Dvorak, G. J., Rao, M. S. M., and Tarn, J. Q., *Journal of Applied Mechanics,* Vol. 41, March 1974, pp. 249–253.
[*4*] Tarn, J. Q., Dvorak, G. J., and Rao, M. S. M., "Shakedown of Unidirectional Composites," *International Journal of Solids and Structures* to be published.
[*5*] Kelly, A. and Davies, G. J., *Metallurgical Reviews,* Vol. 10, No. 37, 1965, pp. 1–77.
[*6*] Kelly, A. and Bomford, M. J., *Physics of Strength and Plasticity,* A. S. Argon, Ed. Massachussetts Institute of Technology Press, Cambridge, Mass., 1969, pp. 339–350.
[*7*] Baker, A. A. and Cratchley, D., *Applied Materials Research,* Vol. 3, No. 4, 1964, pp. 215–222.
[*8*] Hancock, J. R. *Proceedings,* Air Force Conference on Fatigue and Fracture of Aircraft Structures and Materials, Technical Report AFFOL TR-70-144, Air Force Flight Dynamics Laboratory, Dayton, Ohio, 1970, pp. 285–300.
[*9*] Hancock, J. R., *Composite Materials: Testing and Design (Second Conference), ASTM STP 497,* American Society for Testing and Materials, 1972, pp. 483–502.
[*10*] Hancock, J. R., "Fatigue of Boron-Aluminum Composites," Midwest Research Institute Preprint, Midwest Research Institute, Kansas City, Mo., July 1972.
[*11*] Schuerch, H., *American Institute of Aeronautics and Astronautics Journal,* Vol. 4, 1966, p. 102.
[*12*] *Aluminum,* Vol. 1, Van Horn, K. R., Ed. American Society for Metals, Metals Park, Ohio, 1967.
[*13*] Toy, A., *Journal of Materials,* Vol. 3, No. 1, March 1962, pp. 43–58.
[*14*] Morris, A. W. H. and Steigerwald, E. A., *Metallurgical Transactions,* American Institute of Mining, Metallurgical, and Petroleum Engineers, Vol. 239, May 1967, pp. 730–739.

[3] Toth, I. J., private communication, 1973.

[15] Ham, R. K. and Place, T. A., *Journal of the Mechanics and Physics of Solids*, Vol. 14, 1966, pp. 271–280.
[16] Varschavsky, A. and Tamayo, P., *Journal of Materials Science*, Vol. 4, 1969, pp. 653–657.
[17] *Aerospace Structural Metals Handbook*, Vol. 2, 3rd revision, Syracuse University Press, Syracuse, N. Y., March 1966.
[18] OFHC Brand Copper, Technical Survey, The American Metal Company, Ltd., 1959, p. 122.
[19] Shimizu, H. and Dolowy, J. F., Jr., in *Composite Materials: Testing and Design, ASTM STP 460*, American Society for Testing and Materials, 1969, pp. 192–202.
[20] *Metals Handbook*, Vol. 1, American Society for Metals, Metals Park, Ohio, 1961.
[21] Toth, I. J., in *Composite Materials: Testing and Design, ASTM STP 460*, American Society for Testing and Materials, 1969, pp. 236–253.
[22] Menke, G. D. and Toth, I. J., "The Time Dependent Mechanical Behavior of Composite Materials," Technical Report AFML-TR-70-174, Air Force Materials Laboratory, Dayton, Ohio, 1970.
[23] Hancock, J. R., "The Initiation and Growth of Fatigue Cracks in Filament-Reinforced Aluminum Alloys," Technical Report No. 1, Contract No. N00014-70-C-0212, NR 031-743, Midwest Research Institute, Kansas City, Mo., March 1971.
[24] Swanson, G. D. and Hancock, J. R., in *Composite Materials: Testing and Design (Second Conference), ASTM STP 497*, American Society for Testing and Materials, 1972, pp. 469–482.
[25] Hancock, J. R., "Fatigue of Metal Matrix Composites," *Fatigue and Fracture of Composites*, Chapter 6, to be published by Academic Press.

Fatigue Fracture Mechanisms and Environmental Effects

C. K. H. Dharan [1]

Fatigue Failure Mechanisms in a Unidirectionally Reinforced Composite Material

REFERENCE: Dharan, C. K. H., "**Fatigue Failure Mechanisms in a Unidirectionally Reinforced Composite Material,**" *Fatigue of Composite Materials, ASTM STP 569,* American Society for Testing and Materials, 1975, pp. 171–188.

ABSTRACT: The fatigue failure mechanisms in a unidirectional glass fiber-epoxy material were studied. Specimens were made by filament winding the glass fiber roving and vacuum impregnating with a low viscosity room temperature curing resin. The fatigue response could be divided into three distinct life ranges. In the first region (< 200 reversals), there was a small dependence of the fatigue life on cycling. Behavior here was believed to be dependent upon the fiber mean strength and strength distribution. In the second region (200 to 10^6 reversals), the logarithm of the applied stress decreased almost linearly with the logarithm of the number of cycles. Fatigue failure in this region occurred by the growth of matrix microcracks, which lead to preferential fiber failure, and was followed by interfacial shear failure. In the third region (> 10^6 reversals), the applied stress was below the microcrack initiation stress and none of the few specimens tested failed. Unlike behavior in the first two regions, where defects were formed in the first cycle and subsequently propagated, most of the cycles in this region were used in crack nucleation.

KEY WORDS: composite materials, failure, fatigue (materials), fibers

Cyclic deformation processes in fiber-reinforced materials differ widely from those in homogeneous isotropic materials. For example, crack nucleation plays a significant role in the latter; in the former, cracks and failure zones are often formed in the very first few cycles. In fact, there are often voids and defects in the material even before cycling begins. Secondly, fiber-reinforced materials are characterized by a high degree of anisotropy; the ratio of longitudinal to transverse moduli varies from about 5 for glass fiber-polymers to about 25 for graphite or boron fiber-

[1] Metallurgy Department, Scientific Research Staff, Ford Motor Company, Dearborn, Mich. 48121.

polymers. The stress field around a flaw in such a highly anisotropic medium is significantly different from one in an isotropic material [*1*].[2] Consequently, while homogeneous isotropic materials usually fail in fatigue by the nucleation of a crack which propagates in a single mode, composite materials generally exhibit a variety of failure modes including matrix crazing or microcracking, individual fiber failures resulting from statistically distributed flaw strengths, debonding, delamination, void growth, etc. In addition, several of these failure modes are generally present at any given time prior to failure.

Further, failure mechanisms in the fiber are different from those in the matrix. It is well established, for example, that glass by itself does not exhibit dynamic fatigue failure but fails in "static" fatigue as a result of thermally activated stress corrosion reactions of water vapor at surface flaws [*2,3*]. The apparent activation energy from glass fracture is in good agreement with activation energy values for sodium-ion transport which is the probable controlling mechanism for crack propagation [*2*]. When glass fibers are enclosed in a polymer matrix, however, and subjected to cyclic loading, it is not clear whether there would be reactions at the entire glass-polymer interface due to moisture absorption through the polymer layer, or whether matrix microcracks, alone (resulting from cyclic failure), would provide a conduit for preferential attack by water vapor over a localized area on the fibers at the crack front leading to further crack growth and eventual fatigue failure of the composite.

It is not surprising that, with the large number of variables involved, the relative significance of each to the controlling mechanisms of fatigue failure is not well understood. The investigations that have been reported have concentrated on obtaining general fatigue performance data, the bulk of which concerns the most common class of composite materials, glass fiber-reinforced polymers. In the early work of Boller, a significant amount of data was generated by conducting flexural fatigue tests at 30 Hz on a wide variety of unidirectionally reinforced glass fiber-polymers and laminates [*4*]. While these results do indicate the relative significance of variables such as fiber orientation, fiber and matrix content, and matrix composition, subsequent investigations have indicated that high frequency fatigue tests can lead to significant temperature rises in the specimens being tested [*5*]. Such tests are then no longer isothermal and observations of failure mechanisms cannot distinguish between cyclic and thermal causes. Other investigators have studied the effects of lamination order [*6*], matrix properties [*7*], aspect ratios (for short fibers) [*8*], and reinforcement configurations of woven cloth [*9*] and

[2] The italic numbers in brackets refer to the list of references appended to this paper.

chopped fibers [*10*] on fatigue life. However, the actual mechanisms of fatigue failure are difficult to deduce from the results of these studies that have generally been aimed at obtaining a broad data base in which the effects of the many variables could be evaluated.

The present investigation was conducted in an effort to determine the controlling failure mechanisms in a simple (that is, analyzable) composite system in which the variables could be closely controlled. At the same time, the material that was chosen for study (a unidirectional glass fiber-epoxy) was one that was realistic enough to have been used in actual high-strength structural applications and was not, therefore, a model system. The choice of the actual constituents was dictated by factors that ensured good wetting between fiber and resin, low residual stresses, lack of voids, and uniform fiber distribution.

Experimental Procedure

Glass fiber roving [3] was used as the reinforcement. It consisted essentially of an untwisted bundle of 2040 continuous glass filaments, 0.50 to 0.55 by 10^{-3} in. in diameter. The filaments were surface-treated (by the manufacturer) with an epoxy-compatible silane finish and held together in an approximately rectangular bundle 0.10 by 0.008 in. in cross section. The roving spool was sealed in a plastic bag and refrigerated until it was ready to be used.

The epoxy resin used as the matrix material was Epon 815 [4] cross-linked by 13 parts per hundred per weight of the resin (phr) of triethylene-tetramine (TETA). This resin is commonly used in filament winding applications since its low viscosity (500 to 900 cps at 25°C) facilitates impregnation and wetting. It is also a low exothermic room temperature curing system.

Figure 1 shows a schematic of the filament winding apparatus. The roving, as it unwinds from the spool, passes over two rollers, together, acting as a tensioning device. The rollers are spring loaded; varying the spring tension allows the application of any desired tension load during winding. The roving then passes over a small spindle whose purpose is to break the sizing that holds the bundle together and separate the individual filaments to enhance wetting. The spindle is so arranged that this is done while it dips into a resin bath. The wetted roving passes next over a tetrafluoroethylene roller fitted with a wiper to remove the excess resin and is then wound into the mold.

The roving is wound around two pins in the mold which is slowly

[3] Supplied by Owens-Corning Fiberglas Corporation, Type K836AA-675.
[4] Shell Chemical Company.

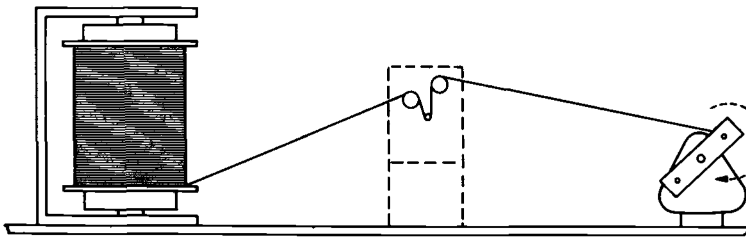

FIG. 1—*Schematic diagram of the filament winding apparatus.*

rotated. After the required number of turns (determined by the volume fraction of fiber desired), the mold is removed from its fixture and the side plates are assembled. When filament winding in air was done, the mold was allowed to sit at room temperature for 24 h followed by a post cure of 24 h at 66°C. This was all that was necessary to produce a finished specimen. When vacuum impregnation was desired, however, the roving was wound dry into the mold, the side plates were assembled, and the entire mold was placed in a vacuum chamber which was evacuated to about 5 mm Hg. Appropriate quantities of the resin and the hardener were mixed thoroughly, and, after degassing the mixture in a separate vacuum chamber, the catalyzed resin was forced into the mold through a neoprene tube. When the mold was filled, the vacuum was removed and the same cure schedule was applied. The side plates of the mold in contact with the specimen were covered before use by a layer of adhesive-backed tetrafluoroethylene tape.[5] This resulted in smooth specimen surfaces which did not require any further polishing. Figure 2 shows the mold containing the cured specimen.

The strong anisotropy of a high-strength unidirectional composite makes conventional dog-bone specimen shapes impractical since shear failures will occur in the grip sections. The usual rectangular shaped specimens with end tabs used for testing composites are also often unsuitable in fatigue testing since failure and crack propagation frequently occur in the highly stressed regions under the grips. The specimen shape (shown in Fig. 3 held by the testing machine grips) was used after several trials with various geometries and proved quite satisfactory. In this design, the wedge-shaped grips provided a uniform compressive stress

[5] Scotch Plastic Tape No. 549, The 3M Company.

FIG. 2—*Specimen mold.*

predominantly transverse to the fibers to balance the tensile stress in the gage section.

All the specimens had a nominal fiber volume fraction of 0.48. The average gage cross-sectional area (nominally,$^3/_8 \times ^1/_{16}$ in.) was 0.02212 in.^{2}. Slices from representative specimens were made for thermomechanical analysis to determine the glass transition temperature, T_g. A Perkins Elmer TMA unit was used with the probe tip perpendicular to the fiber direction and the average T_g over several runs at 2.5 Cpm was 85 ± 1°C.

In addition to the glass fiber-epoxy specimens, several tension specimens of epoxy alone were made by vacuum-casting the resin. The specimen shape used corresponded to ASTM D638 Type I with a gage length of 2 in. and a rectangular crosssection 0.125 by 0.500 in.

All mechanical tests were performed in air at room temperature in an electrohydraulic closed-loop test system. Details of the experimental

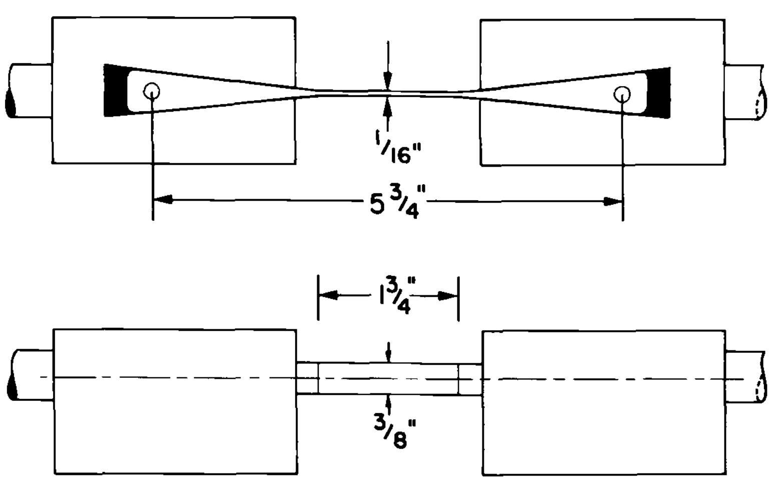

FIG. 3—*Specimen and tension grips.*

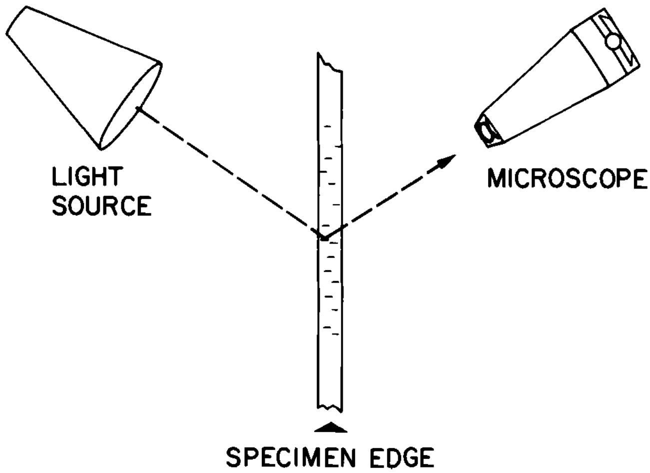

FIG. 4—*Oblique microscope set-up for detecting microcracks and fiber breaks.*

arrangement and test equipment are given elsewhere [*11*]. Tension tests to failure were conducted at a constant strain rate of 10^{-4} s^{-1} on both the composite and epoxy specimens. Fatigue tests were performed in zero tension (between load limits) at a "constant" strain rate of 10^{-2} and 10^{-1} s^{-1}. The actuator in this mode moved from zero load at constant velocity until the set maximum load limit was reached at which it reversed its motion and moved at the same constant velocity towards zero load. This resulted in a triangular waveform of the strain versus time profile in which the slope was always constant. An increase in the maximum load limit, therefore, resulted in a decrease in the cyclic frequency. In all tests, an extensometer was mounted directly to the specimen to monitor the strain and provide feedback to the servo-controller. In the fatigue tests, the cycling frequency varied from approximately 0.25 Hz in the low region to 6 Hz for the long life tests.

The apparent modulus was continuously monitored at all cycling speeds by using a peak storage circuit and a double pen strip chart recorder that plotted the envelope of the maximum and minimum strain peaks with time [*11*]. When a significant change in the material occurred it was immediately detected as an increase in the strain range and was recorded. For a linear material, this corresponded to a decrease in the apparent modulus since the load limits were kept constant.

During all tests, the specimen was illuminated by a light source and observed obliquely through a low power microscope as shown in Fig. 4. This arrangement was remarkably effective in detecting microcracks in the matrix, as well as individual fiber breaks, by specular reflection off the newly fractured surfaces within the translucent material.

Results and Discussion

Specimen Micrographs

Micrographs of transverse and longitudinal sections of a few specimens that were filament wound in air (the conventional technique) revealed the presence of a large number of voids. Figures 5 and 6 show representative specimens. The voids had the appearance of elongated bubbles which are caused by air entrapped in the roving bundle as it is pulled over the spindle immersed in the resin. In fact, as the winding progressed, small bubbles were seen to accumulate in the resin bath itself. While no attempt was made to quantitatively determine void content, estimates of 10^7 and 10^9 voids in.^{3} have been made for conventional filament-wound glass fiber-epoxy composites by Bascom and co-workers [*12,13*]. They have also noted an inverse linear relationship between the

FIG. 5—*Transverse micrograph-filament wound in air.*

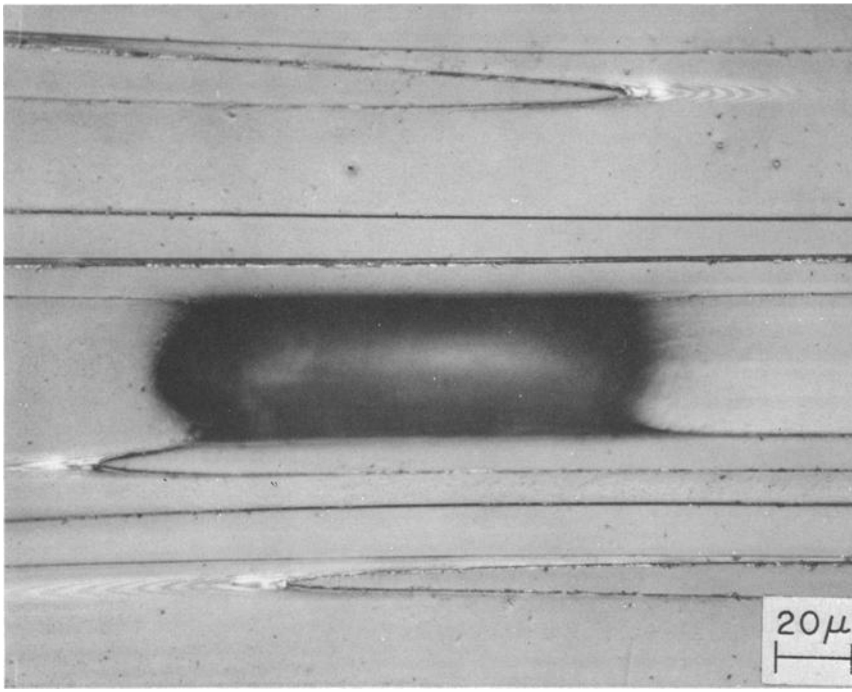

FIG. 6—*Longitudinal micrograph-filament wound in air.*

void content and the interlaminar shear strength from tests conducted on Naval Ordnance Laboratory (NOL) rings. Reducing the void content from the normal 5 to 0.5 volume percent resulted in 40 to 100 percent increases in the interlaminal shear strength. This is not surprising since the stress concentration around a void is liable to be more effective in reducing shear fracture strength which is matrix-dependent rather than tensile strength which is primarily fiber-dependent. In fatigue, voids can be expected to act as crack nucleation sites and promote interfacial shear failure.

Use of the vacuum impregnation technique described earlier resulted in essentially void-free specimens as shown in Figs. 7 and 8. These micrographs reveal several interesting features. One is the variation in fiber diameter that is observed. Diameters ranging from 0.00044 to 0.00072 in. were measured. This introduces an additional variable that would affect the fiber strength distribution since the variation in size would depend upon manufacturing tolerances on spinneret sizes, drawing speeds, ambient temperature control, etc., and can be expected to vary with the batch. It is well known that mean glass fiber strengths are, to a limit, inversely proportional to the diameter to which the fiber is drawn [14]. In addition, there is a strength distribution associated with each given fiber size. The effect of the combination of varying fiber sizes and associated strength distributions is unclear at present.

Another feature to be noted relates to the fiber distribution in the matrix. Clearly, the distribution is not uniform but consists instead of sections of resin-rich areas adjacent to high concentrations of fibers where each fiber generally contacts two other fibers resulting in a chain-like distribution. Capillarity, as the driving force during infiltration by the resin, appears to be the cause of such a distribution. It is evident, from a consideration of load transfer in the matrix, that where fibers are bunched together, fracture of one fiber will necessarily impose very high interfacial shear stresses on its adjacent neighbors leading to debonding.

Tension Tests

Observations during tensile loading indicated that the earliest observed local failures were random fiber fractures which began to occur at stresses

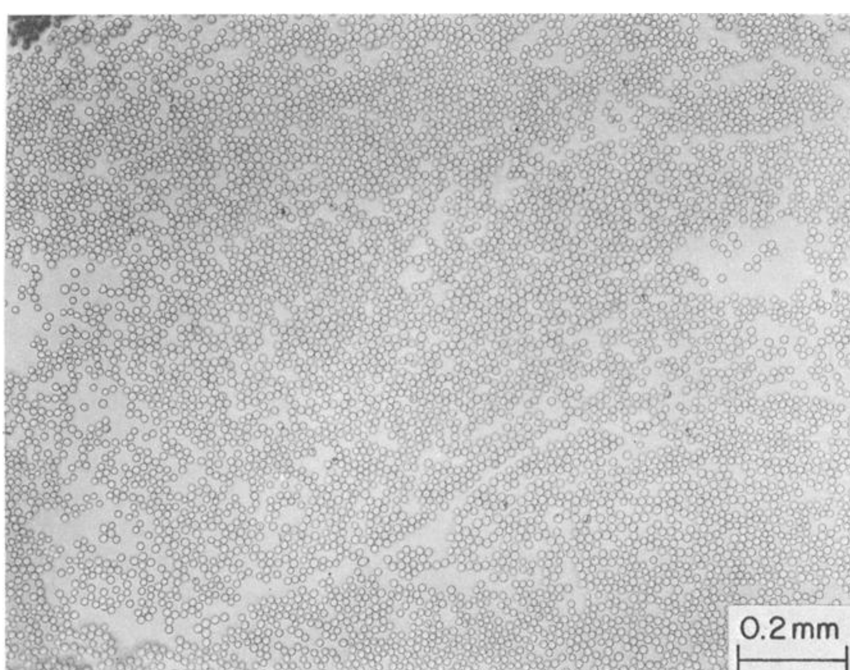

FIG. 7—*Transverse micrograph-filament wound dry followed by vacuum impregnation.*

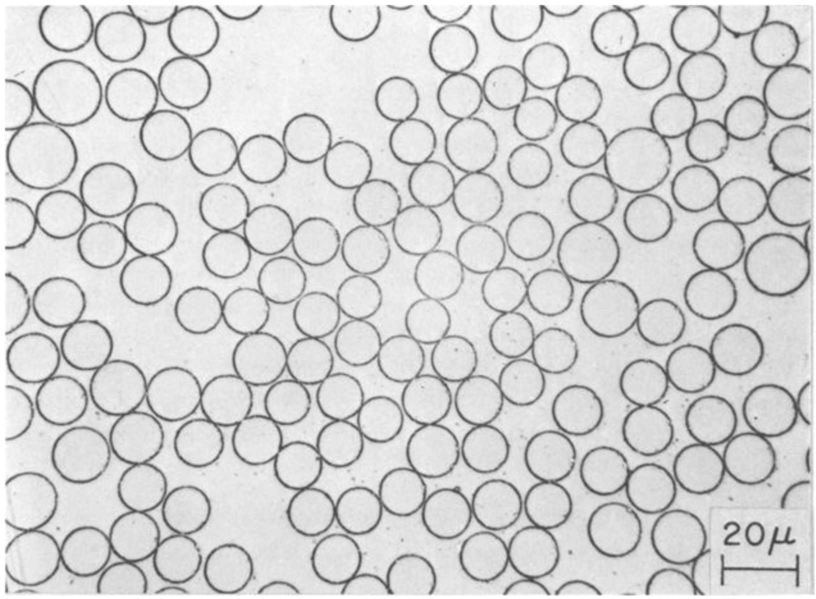

FIG. 8—*Transverse micrograph-filament wound dry followed by vacuum impregnation.*

as low as 25 000 psi. Increasing the load did not cause a proportional increase in fiber breaks, suggesting that the earliest fractures were at fibers that were more highly flawed and also, perhaps, more highly stressed during filament winding which, subsequently, failed at their weakest flaw locations. These fractures were observed to be in the shape of circular penny-shaped cracks 0.0005 to 0.001 in. in diameter. Since the average fiber was approximately 0.0005 in. in diameter, this indicated that the fiber fracture did extend into the matrix to some extent. When the stress was removed, the reflected light off the local fracture surface was seen to decrease in intensity and area, suggesting that the fracture surfaces in the matrix closed back on themselves when the load was released, leaving the still detectable, newly created fracture surfaces in the fiber.

Increasing the stress to about 35 000 psi caused the appearance of fine craze-like microcracks in the matrix. Most of these appeared to originate at the surfaces of the specimen, and all were perpendicular to the tensile axis. As the stress was increased, more microcracks appeared. Their numbers increased in direct proportion to the increase in the stress level. These defects occurred with an even distribution over the length and width of the specimen. Observations of several specimens indicated that a specific stress was necessary before microcracks were formed.

Figure 9 shows the fiber fracture and matrix microcrack pattern observed in the arrangement shown in Fig. 4. The photograph was taken while a stress of 69 000 psi was applied to the specimen. This particular specimen had undergone 70 000 cycles in zero-tension fatigue testing. The pattern is, however, quite similar to that observed in a monotonic test.

It appears possible that the microcracks observed are actually crazes occurring in the epoxy resin matrix. Crazes are regions of high local strain which are visible as crack-like defects. They are not cracks, however, since they can carry load and are known to consist of strips of highly oriented polymer material interspersed with voids [*15*]. Observation of crazes in glassy thermoplastics is well established. Bevis and Hull, for example, have observed craze formation in a region surrounding a crack tip in polystyrene [*16*]. The crazes were oriented around the crack in directions perpendicular to the maximum tensile stress, the specific pattern depending upon load history and crack tip geometry.

Crazes have not been conclusively identified in highly cross-linked polymers like epoxies. In the present study, the fact that a uniform distribution of microcracks was observed and that there appeared to be little interaction between adjacent defects suggests that the defects are load-bearing. Recent observations by Lilley and Holloway of what

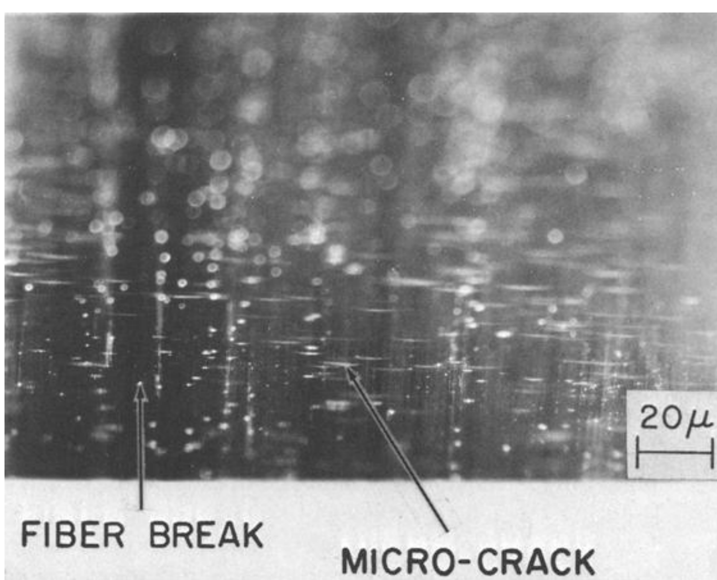

FIG. 9—*Fiber fracture and matrix microcrack pattern in a specimen cycled at 69 000 psi through 70 000 cycles.*

appeared to be crazing (at 350 K) in Araldite CT200/HT901 and Epikote 828/NMA/BDMA, which are general purpose Bisphenol A/epichlorhydrin resins like the Epon 815/TETA used in the present study, seem to confirm the present observations [17]. Craze patterns were observed near loaded crack tips and crack arrest positions. Further work, such as electron micrographs of thin transverse sections, is required, however, to conclusively verify these observations.

At stresses approaching the fracture stress (90 000 to 120 000 psi) the rate of fiber breaks increased dramatically, often occurring in clumps throughout the specimen. Just before fracture, cracks were observed to connect the breaks in a transverse fashion before propagating in a shearing mode parallel to the fibers. The release of strain energy at fracture was large enough to completely destroy the specimen when it fractured.

The sequence of failure modes leading to tensile fracture may be summarized as follows: early formation of local fiber breaks which probably correspond to the lower tail of the probability distribution of the strengths of the weakest flaws in the fibers; development of matrix crazes or microcracks beyond a certain initiation stress; a rapid increase in fiber failures; and, finally, coalescence of fiber breaks by transverse cracking followed by interfacial shearing and failure.

Figure 10 shows the tensile stress-strain curves of both the composite and matrix. The regions where the various failure modes made their appearance are noted. It is clear that the strain levels corresponding to microcracking in the epoxy matrix in the composite lie well below the ultimate strains of the bulk epoxy. Observations of bulk epoxy during straining did not reveal the presence of microcracks before failure. Fracture in the epoxy, in typical circumstances, initiated from a local imperfection. In each case, the fracture surface exhibited a smooth region extending from the initial imperfection (the slow crack growth region) surrounded by a rougher surface caused by rapid crack extension. The transition line from slow to fast crack growth was clearly visible.

Fatigue Tests

In testing highly anisotropic materials, the definition of failure is important. In isotropic materials, failure can be readily defined as physical separation of the specimen into two or more pieces so that it can no longer carry the applied load. Usually this happens due to the propagation of a single crack during the last few cycles of the fatigue test. In anisotropic materials, however, specimen degradation, in the form of microcrack growth, delamination, and subsequent mixed mode crack propagation, is often well established before complete fracture occurs. It is difficult to accurately define the point at which the specimen can be considered to

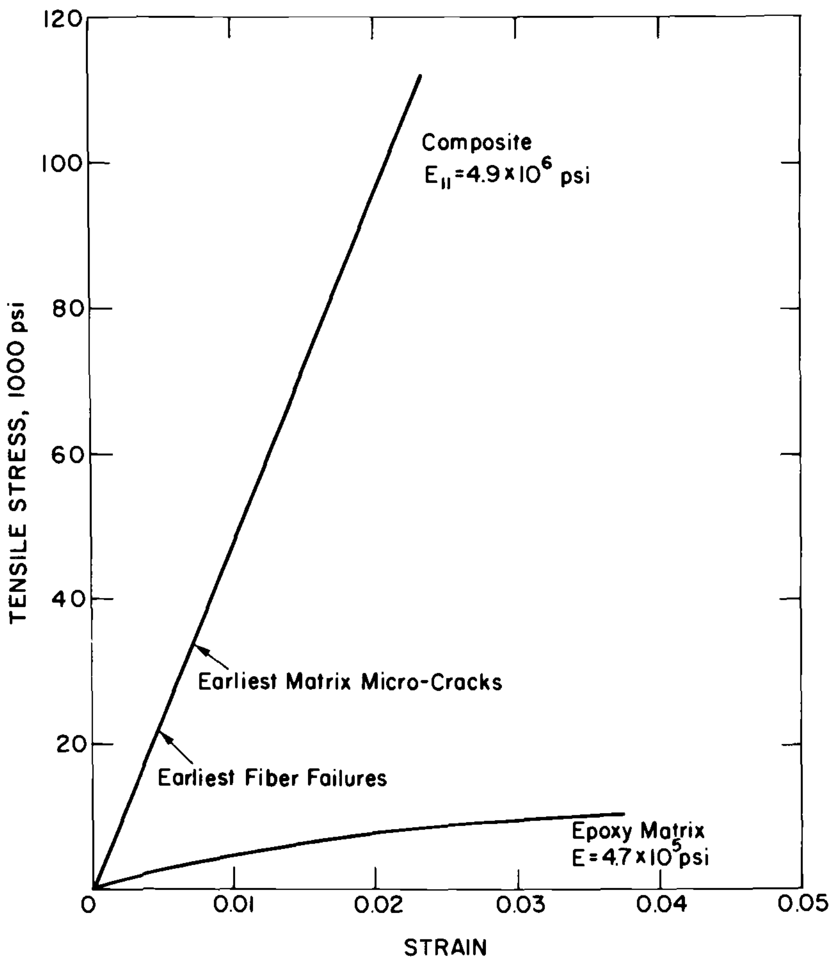

FIG. 10—*Tensile stress-strain curves of composite and epoxy specimens.*

have failed, and it is this difficulty that results in a considerable degree of experimental scatter. To avoid this problem, the loss in the apparent modulus was used as a criterion to define fatigue failure in this investigation. In addition to providing a reasonable measure of the degree of fatigue damage, this criterion was also useful for those applications where meeting a specified stiffness is the primary design requirement, as in chassis frames, helicopter and turbine blades, leaf springs, etc. In such components, a decrease in the stiffness, which can occur well before fracture, will quickly result in component failure.

Figure 11 shows the apparent modulus that was monitored during cycling as a function of the number of elapsed cycles for a specimen that was cycled through a stress amplitude of 50 300 psi. Figure 12 summarizes the fatigue data in a plot of the logarithm of the stress amplitude against the logarithm of the number of reversals (twice the number of cycles) to failure. The data point at one reversal is tensile fracture. Also shown are the stresses at which fiber failure and matrix microcracking begin. The fatigue response can be conveniently divided into three regions of interest corresponding to regions of markedly different slopes on the plot in Fig. 12.

Region I—In the short life region (less than about 200 reversals) the applied stress level is only slightly dependent upon cycling. Observation of the specimen during the first cycle showed that in addition to a progressive increase in matrix microcracks with stress, the peak stress was high enough to precipitate large numbers of fiber failures within the material. In this region, the stress in the fibers was sufficiently within the fiber-flaw strength distribution to produce a high-fiber failure density. Failure then occurred by the coalescence of local fiber breaks which then propagated in a few cycles to connect other such regions until the specimen failed catastrophically in a manner similar to tensile fracture. The first half cycle significantly weakened the material often producing large

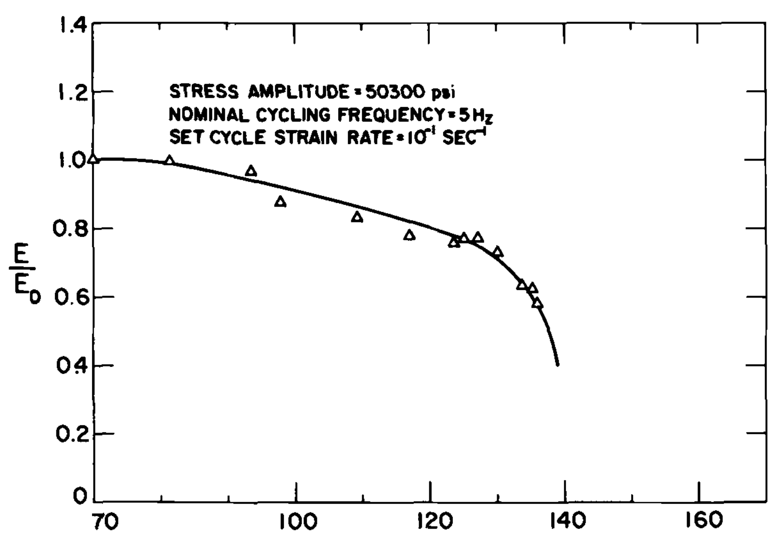

FIG. 11—*Ratio of final to initial moduli monitored during a fatigue test as a function of the number of elapsed cycles.*

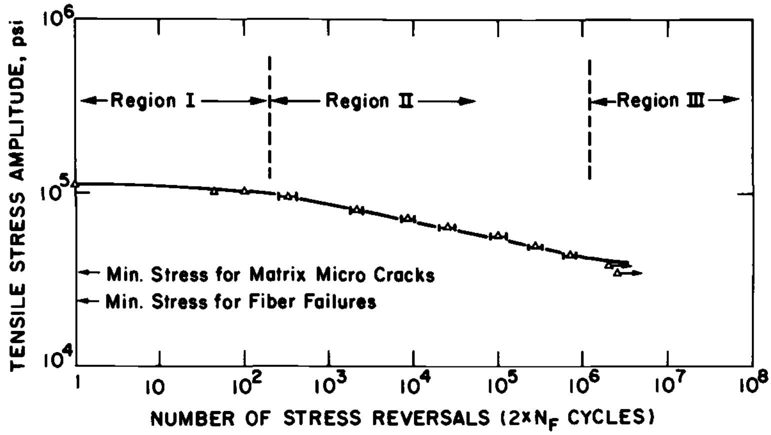

FIG. 12—*Logarithm applied stress versus logarithm number of stress reversals.*

cracks. Reversals accelerated the breakdown process by crack propagation that connected weak zones so that the failure mechanism in this region was most properly described as combined static fiber fracture and fatigue. The fiber mean strength and strength distribution would appear to profoundly affect the extent of this region, a narrower distribution producing a longer region and vice versa.

Although failure is fiber controlled since fiber breaks occur at random throughout the volume of the material in sufficiently large numbers to cause incipient failure, it is highly accelerated by cycling. In one experiment, a specimen was held at 100 000 psi as in a creep test; and, while it was highly damaged and consisted of extensive fiber breaks, the time to fracture was greater than 10 h, much larger than the approximately 100 cycles required to cause fatigue failure at this stress level. It should be noted that the tensile data shown in Fig. 12 (at $2N_F = 1$) represent the average of tests conducted at a strain rate of 10^{-4} s^{-1}, while the fatigue tests were performed at 10^{-1} s^{-1}. One should expect higher values for the tensile strength at the higher strain rate which would have the effect of bringing the failure curve more in line with that in Region II. From the little data in this region, however, it is difficult to come to any definite conclusions on failure mechanisms except to note that specimens which survived the first cycle when stressed to the tensile fracture range, exhibited macroscopic failure zones in the first cycle and required additional stress reversals for subsequent failure to occur within this region.

Region II—From 200 to 10^6 stress reversals, a linear relationship was obtained between the logarithm of the applied stress and the logarithm of the number of reversals. In this region, matrix microcracks were still formed in the first half cycle since the stress exceeded the minimum microcrack initiation stress. Several random fiber breaks were also observed, but not in the large numbers that caused the condition of incipient failure in Region I. Instead, the fiber breaks within the material appeared to play a small role in fatigue behavior in this region. As cycling progressed, one (or more) of the surface microcracks were seen to propagate perpendicular to the tensile axis (in Mode I) breaking glass fibers in its path until it was large enough to satisfy the criterion for shearing-type propagation parallel to the fibers. When this occurred, delamination began, leading to a loss in the apparent modulus and eventual failure.

A reasonable hypothesis may be formulated that propagation of the microcracks is governed by the rate at which the glass fibers at their fronts fail as a result of the thermally activated stress corrosion mechanisms proposed by Charles [*2*] to explain delayed fracture in glass. Once microcracks are formed, stress corrosion fiber failures would then be the rate-controlling process that governed fatigue failure. The microcracks in the matrix play an important dual role, since they not only produce a condition of intense local strain at the crack tip at the fiber-matrix interface, but also serve to open the interface to preferential attack by water vapor in the atmosphere. This makes it possible for Mode I propagation to occur until a condition is reached when interfacial shearing begins. The criterion for this would be a function of the crack energy release rate for shear mode propagation.

Figure 13 shows schematically the sequence of fatigue failure: formation of microcracks at the surface; preferential failure of the fibers at the tip of a microcrack leading to its growth; and, finally, interfacial shear failure and delamination. The data in Region II (Fig. 12) fit the equation

$$\sigma N^n = C$$

for a value of $n = 10$.

Region III—In this region (greater than 10^6 reversals), the maximum applied stress was close to the microcrack initiation stress. The few specimens tested in this region did not fail. A few fiber failures were observed to form in the first half cycle, but these did not increase with subsequent cycling. No microcracks were observed initially; however, after several cycles, well into the test, some microcracks were nucleated. When the test was stopped (at about 2×10^6 reversals), the specimens were totally undamaged except for the additional nucleation of a few microcracks. One can speculate that, in this region, the stress level is below that required to propagate a crack through the glass fibers since

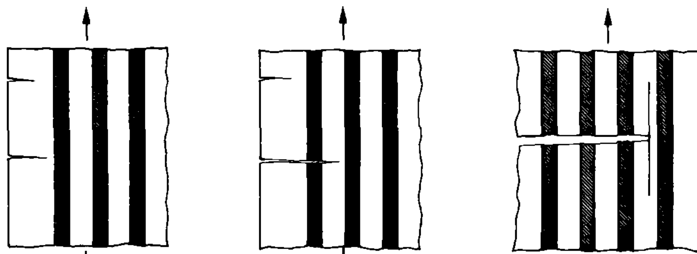

FIG. 13—*Schematic of the sequence of fatigue failure in Region II.*

the stress corrosion mechanism requires a minimum stress below which the crack tip radius in glass increases, resulting in little further crack growth [*2*].

Conclusions

1. Vacuum-impregnation was necessary to produce unidirectional glass fiber-epoxy composite specimens with a minimum of voids.

2. During tension testing, the earliest fiber breaks were observed at stresses as low as 25 000 psi. At about 35 000 psi, this was followed by the appearance of matrix microcracks whose frequency of occurrence appeared to be proportional to the applied strain on the specimen. Comparison with the stress-strain behavior of the bulk epoxy showed that microcracking in the composite began well before the failure strain of the bulk epoxy was reached. The microcracks may have initiated from crazes; further work is needed, however, to verify this conjecture.

3. The fatigue response could be divided into three distinct life ranges. In the first region (less than 200 reversals), there was a small dependence of the fatigue life on cycling. Behavior here was believed to be dependent upon the fiber mean strength and strength distribution. In the second region (200 to 10^6 reversals), the logarithm of the applied stress decreased almost linearly with the logarithm of the number of cycles. Fatigue failure in this region occurred by the growth of matrix microcracks leading to proferential fiber failure followed by interfacial shear failure. In the third region (greater than 10^6 reversals), the applied stress was below the microcrack initiation stress and none of the few specimens tested failed. Unlike behavior in the first two regions where defects were formed in the

first cycle and subsequently propagated, most of the cycles in this region were used in crack nucleation.

References

[1] Lekhnitskii, S. G., *Theory of Elasticity of an Anisotropic Body*, Holden-Day, San Francisco, 1963.
[2] Charles, R. J., *Journal of Applied Physics*, Vol. 29, No. 11, 1958, pp. 1549–1560.
[3] Ritter, J. E., *Journal of Applied Physics*, Vol. 40, No. 1, 1969, pp. 340–344.
[4] Boller, K. H., *Modern Plastics*, Vol. 41, No. 10, 1964, pp. 145–151.
[5] Cessna, L. C., Levens, J. A., and Thomson, J. B., *Polymer Engineering and Science*, Vol. 9, No. 5, 1969.
[6] Fujii, T. and Mizukawa, K., *Proceedings*, 24th Society of Plastics Industries Conference, Paper 14-D, Feb. 1969.
[7] Lavengood, R. E. and Anderson, R., *Proceedings*, 24th Society of Plastics Industries Conference, Paper 11-E, Feb. 1969.
[8] Lavengood, R. E. and Gulbransen, L. B., *Journal of Polymer Engineering and Science*, Vol. 9, No. 5, 1969.
[9] James, T. K., Appl, F. J., and Bert, C. W., *Experimental Mechanics*, July 1968.
[10] Dally, J. W. and Carrillo, D. H., *Journal of Polymer Engineering and Science*, Vol. 9, No. 6, 1969, pp. 434–444.
[11] Dharan, C. K. H. and Colvin, A. D., *Review of Scientific Instruments*, Vol. 44, No. 3, 1973, pp. 326–330.
[12] Bascom, W. D. and Romans, J. D., *Industrial and Engineering Chemistry*, Vol. 7, No. 3, 1968, pp. 172–178.
[13] Kohn, E. J., Sands, A. G., and Clark, R. C., *Industrial and Engineering Chemistry*, Vol. 7, No. 3, 1968, pp. 179–183.
[14] Bartenev, G. M., *The Structure and Mechanical Properties of Inorganic Glasses*, Walters-Noordhoff Publishing, Groningen, The Netherlands, 1970, p. 204.
[15] Kambour, R. P., *Journal of Polymer Science*, Vol. 3, 1965, pp. 1713–1724.
[16] Bevis, M. and Hull, D., *Journal of Materials Science*, Vol. 5, 1970, pp. 983–987.
[17] Lilley, J. and Holloway, D. G., *Philosophical Magazine*, Vol. 28, No. 1, 1973, pp. 215–220.

M. F. Henry [1] *and N. S. Stoloff* [2]

High Strain Fatigue in a Ni(Cr)-TaC Fibrous Eutectic

REFERENCE: Henry, M. F. and Stoloff, N. S., "**High Strain Fatigue in a Ni(Cr)-TaC Fibrous Eutectic,**" *Fatigue of Composite Materials, ASTM STP 569,* American Society for Testing and Materials, 1975, pp. 189–209.

ABSTRACT: The eutectic Ni(Cr)-TaC has been directionally solidified to yield a fibrous composite. The material was studied in strain-limited low-cycle fatigue at room temperature and 1000°C. The eutectic with brittle fibers and a ductile matrix was found to obey the Coffin-Manson law at both temperatures. The hysteresis behavior is explained and related to tensile deformation. Surface studies of highly polished cyclic-bend specimens revealed the fatigue crack nucleation and early growth characteristics. The data are compared to conventional materials, and the fatigue resistance is found to be essentially equivalent.

KEY WORDS: fatigue tests, eutectics, composite materials, solidification, life prediction, crack initiation, hysteresis

Work reported to date on fatigue of directionally solidified eutectics is limited. Some fatigue work has been done on Al-Al_3Ni [*1–3*],[3] Al-$CuAl_2$ [*1*], Ag_3Mg-AgMg [*4*], Fe-Fe_2B [*5*], Ni-Ni_3Cb [*6*], Ni_3Al-Ni_3Cb [*7*], Co-CbC [*8*], and nickel- and cobalt-based tantalum carbide (TaC) eutectics [*9*]. But, except for a few specimens of Al-Al_3Ni [*1*], the work has been zero-tension (or tension-tension) or reversed bending, stress-limited cycling. The majority of the fundamental work on composite fatigue has been in the area of artificial composites. The artificial composites, however, are vastly different in interface characteristics and rod size. Thermally induced residual stresses in eutectics are known to affect monotonic loading behavior [*10*] and may play an important role in plastic strain-limited fatigue.

[1] Metallurgist, General Electric Corporate Research and Development Center, Schenectady, N. Y. 12301.

[2] Professor of Materials Engineering, Rensselaer Polytechnic Institute, Troy, N. Y. 12181.

[3] The italic numbers in brackets refer to the list of references appended to this paper.

The potential for the most immediate application of directionally solidified eutectics probably lies in providing high temperature strength, reasonable ductility, and good oxidation resistance for use in high temperature rotating machinery. An ideal system would be one which combined strong, stiff fibers or lamellae with a reasonably strong, ductile matrix that had adequate oxidation and hot corrosion resistance. Rather than just picking an arbitrary model system, it seemed desirable to study a model system which was a good mechanical behavior model of a class of material system that could see use in high temperature operating hardware in the next 5 to 15 years [*11,12*].

It has been shown that certain monocarbides can be alloyed with either nickel- or cobalt-base alloys and then directionally solidified to give a fibrous eutectic structure [*13–16*]. The monocarbide TaC has the highest melting point, approximately 4000°C, of any substance known [*17*]. The elastic modulus at room temperature in the <100> direction is between 69 and 73 million psi depending on the precise carbon-to-tantalum ratio [*18*].

The pseudo-binary eutectic between near stoichiometric TaC and an alloy of nickel-12 percent chrome [*15*] was selected as the primary alloy for this study. Currently available information indicates a eutectic freezing temperature of approximately 1350°C. This Ni(Cr)-TaC alloy was directionally solidified at 0.635 cm/h through a temperature gradient of approximately 70°C/cm to give a good fibrous structure of predominately square TaC rods in a Ni(Cr) matrix. The fibers and matrix both have a <100> growth direction and have a common interface plane of {110} [*19*]. The resulting structure has rods approximately 1.5 to 2.0 μm square with an average interrod spacing of 7.5 to 8.0 μm. The aspect ratio of the rods is 10 000 to 1 or greater. The structure is shown in Fig. 1. This figure is a section taken perpendicular to the growth direction, polished, and, then, etched to reveal the rods. Note that the etch is preferential and the {111} planes in the matrix have been left behind [*20*]. The fibers are strong and stiff, and the matrix is ductile. The volume fraction of rods, while low at 5 percent, is sufficient for significant strengthening, particularly at elevated temperatures. Use of this alloy will allow studies to be conducted at temperatures up to 1000°C without swamping out the mechanical response with oxidation. The 1000°C regime will have matrix strength and strain hardening very different from low temperatures, and it is anticipated that this strain hardening difference will play a major role.

This paper reports results of an examination of the strain-controlled low cycle behavior of this Ni(Cr)-TaC eutectic in the directionally solidified condition.

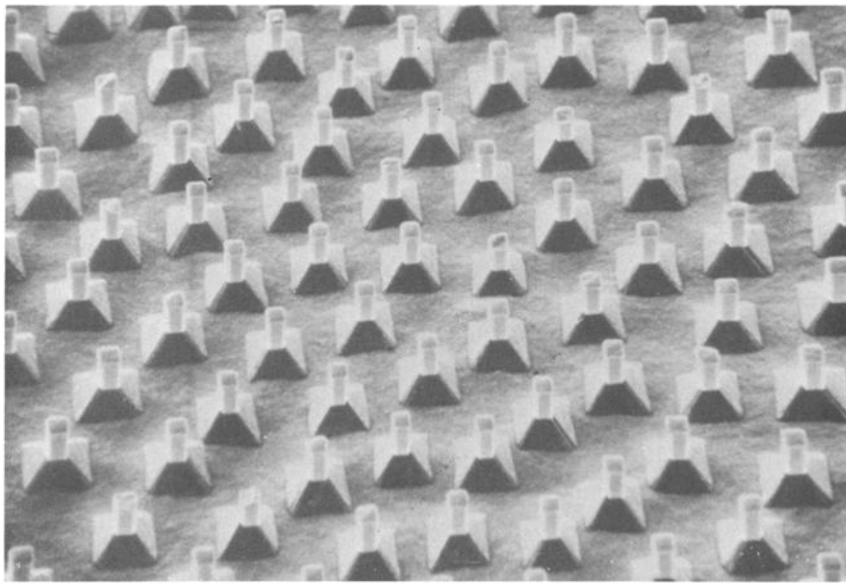

FIG. 1—*Etched, transverse scanning electron micrograph of Ni(Cr)-TaC. Etch facets {111} planes in matrix at base of each fiber (X2000).*

Experimental Procedure

The axial fatigue specimens were hourglass-shaped with a minimum gage section of 0.2 in. and an overall length of 4.25 in. The hourglass shape was achieved by grinding with a radius of 1.5 in. A few specimens were ground with a 0.5-in. wheel. After final grinding, the specimens were then longitudinally polished to a finish of 4 μin. or better. This was done to prohibit the opportunity for circumferential grinding marks to act as micronotches, provide a smooth surface for crack nucleation, and remove surface residual stress that might have been induced by the grinding operation. All fatigue specimens were prepared with the specimen axis coincident with the growth axis of the directionally solidified ingot.

The tests were fully reversed, axial, cyclic tests operating between fixed diametral strain limits. Two test temperatures were selected, room temperature and 1000°C (1832°F). Equipment scheduling and availability required the low cycle fatigue tests to be performed on three different machines. The room temperature tests were done on a hydraulic closed-loop 20 000-lb machine and a 20 000-lb screw machine with a hydraulic piston in the crosshead to give a closed-loop machine. All the 1000°C low cycle fatigue tests were conducted on a 20 000-lb screw machine. The elevated temperature tests were done at 1.0 cpm.

Diametral strain was measured using a scissors-type gage [*21*]. One of these gages and a specimen are shown in Fig. 2. One side of the pivot point has alumina gage rods which are put around the minimum diameter of the specimen. On the other side of the pivot point is a standard clip gage which is used to record the scissors gage displacement. The setup was calibrated in a master fixture before each test.

Observations on fatigue crack nucleation and early growth were made at room temperature with a technique previously used by Henry [*22*] to study conventional superalloys. The tests consisted of fully reversed, cyclic bending tests. The specimen was side-notched to prevent nucleation of fatigue cracks at the edge. The bottom was notched to confine the high strain region to a reasonably localized area. Both notches had a 0.5-in. radius. The flat side of the specimen gage section was polished to a metallographic finish to allow high magnification observations of the fatigue crack nucleation and early growth. Each test was interrupted frequently and acetate plastic replicas were made of the polished gage section each time. One could then examine the replicas in the reverse order

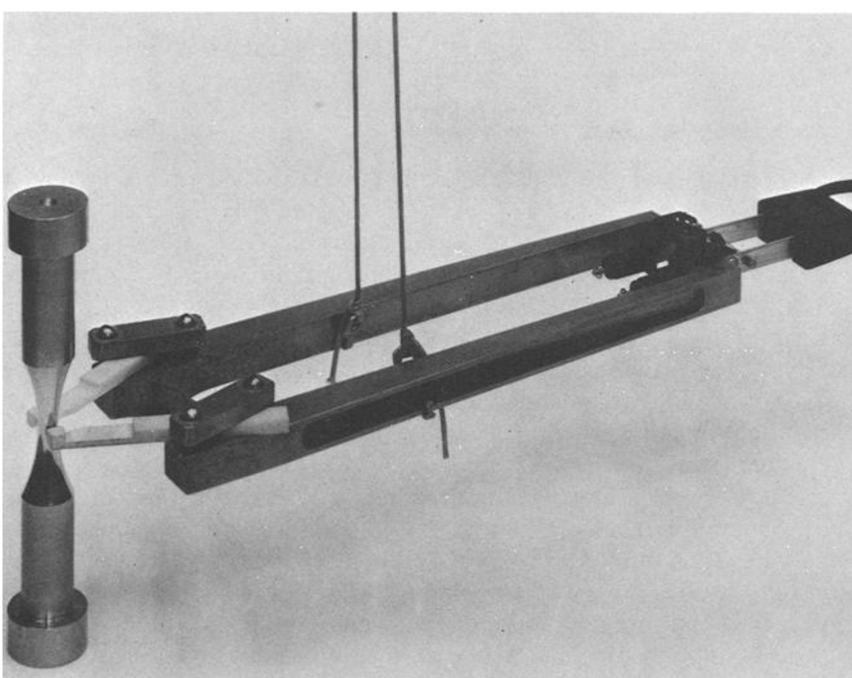

FIG. 2—*Simulated setup showing axial fatigue specimen and diameter gage.*

that they were taken and simulate "uncycling" of the specimen. This allowed the observer to trace specific large cracks back to their origin and watch them until they disappeared. The details of this uncycling or "healing" technique and its general usefulness are given in Ref *23*.

It should be noted here that these cyclic bending tests were performed to gather qualitative information on mechanisms and all quantitative information was left for the axial fatigue tests.

Results

The axial fatigue machines used had analog plastic strain computers that allow limiting on a desired value of plastic strain range during cycling of a conventional alloy. This is done through the analog computer by calculating the plastic diameter range as

$$\Delta d_p = \Delta d - KP \tag{1}$$

where

Δd_p = plastic diameter range,
Δd = total diameter range,
P = load, and
K = compliance setting in the plastic strain computer.

The value of K is determined experimentally for each test. The specimen is load-cycled well within the elastic range and K is searched until $\Delta d_p = 0$ for all values of P swept. The computer output, Δd_p, is then used to limit cycling. With the background of the tension tests on Ni(Cr)-TaC, it was realized that the specimen stiffness would go down as fibers segmented [*24*]. Then if fibers broke during the test, the required value of K would be continually changing. It was decided, therefore, to utilize the technique that was used before the development of the plastic strain computer and plastic strain limiting. Total diametral strain was limited by limiting total diameter change as measured directly by the diametral scissors gage extensometer. The summary data for each test was then taken at half-life. If total strain range is constant throughout life, then the distribution between elastic and plastic strain changes as the material cyclic hardens or cyclic softens, or in the case of a fibrous composite, as fibers segment. Cyclic hardening or softening generally saturates fairly early in life, and load range dropoff due to crack propagation is generally not significant until late in life. Thus, the use of half-life behavior to characterize the material behavior and, in particular, the breakdown of total strain into elastic and plastic is reasonable.

The summary raw data from the twelve successful axial tests run are given in Table 1. This table identifies the specimen, machine used, test temperature, specimen minimum gage diameter, d_o, diameter range limited, Δd, load range, ΔP, at half-life, and, cycles to failure.

Tests on the seven standard room temperature specimens included a determination of the quantity E/μ. Before elastic-plastic strain cycling was started, the specimens were load-cycled in the elastic range. For each specimen, an average of two to three sets of load range, ΔP, and diameter range, Δd, was taken. Diametral strain range, $\Delta\epsilon^d$, may be related to stress range, $\Delta\sigma$, by

$$\Delta\epsilon^d = \frac{\mu}{E}\,\Delta\sigma \tag{2}$$

where E = longitudinal elastic modulus and μ = Poisson's ratio. Using $\Delta\sigma = \Delta P/A_o$ and $\Delta\epsilon^d = \Delta d/d_o$ for the small strains involved, then the desired ratio may be written as

$$\frac{E}{\mu} = \frac{\Delta P}{A_o} \times \frac{d_o}{\Delta d} \tag{3}$$

where A_o = original gage section area and d_o = original diameter. The values of E/μ for specimens FT1, FT2, and FT12 through FT16 ranged from 60.4×10^6 psi to 70.4×10^6 and the arithmetic mean was 67.0×10^6 psi. Using a value of $E = 22.0 \times 10^6$ psi [25], the value of $\mu = 0.328$ was calculated.

With this information, the total strain range could be distributed into

TABLE 1—*Ni(Cr)-TaC raw fatigue data.*

Specimen Number	Machine	Test Temperature, °C	d_o, in.	Δd, mil	ΔP at $N = \frac{N_f}{2}$, lb	N_f
FT1	MTS	RT [b]	0.1979	3.34	7 120	390
FT2	MTS	RT [b]	0.1981	2.46	6 440	955
FT3	Instron	1000	0.1974	3.96	2 250	45
FT4	Instron	1000	0.1975	1.062	1 930	470
FT5	Instron	1000	0.1972	2.12	1 880	124
FT10	Instron	1000	0.1980	0.562	1 680	1 500
FT11	Instron	1000	0.1984	0.356	1 260	4 000
FT12	ICL [a]	RT [b]	0.1984	1.40	5 980	2 500
FT13	ICL [a]	RT [b]	0.1983	0.800	5 480	14 000
FT14	ICL [a]	RT [b]	0.1996	6.00	9 440	85
FT15	MTS	RT [b]	0.1994	0.569	5 060	155 000
FT16	ICL [a]	RT [b]	0.1993	16.02	11 260	16

[a] ICL = Instron closed loop.
[b] RT = room temperature.

elastic and plastic and longitudinal strain data could be calculated from the diametral data. The total diametral strain range, $\Delta\epsilon^d$, was taken as

$$\Delta\epsilon^d = \frac{\Delta d}{d_o} \tag{4}$$

where Δd = diameter range and d_o = original diameter. The elastic diametral strain range was calculated as

$$\Delta\epsilon_e{}^d = \frac{\mu}{E}\,\Delta\sigma \tag{5}$$

Since the total strain range is the sum of the elastic and plastic ranges, the plastic diametral strain range, $\Delta\epsilon_p{}^d$, could be calculated as

$$\Delta\epsilon_p{}^d = \Delta\epsilon^d - \Delta\epsilon_e{}^d \tag{6}$$

Using a constant volume assumption, the longitudinal plastic strain range, $\Delta\epsilon_p$, is then given by

$$\Delta\epsilon_p = 2\Delta\epsilon_p{}^d \tag{7}$$

The longitudinal elastic strain range, $\Delta\epsilon_p$, is simply the ratio of the stress range to elastic modulus

$$\Delta\epsilon_p = \frac{\Delta\sigma}{E} \tag{8}$$

Again, taking total equals elastic plus plastic yields the last required quantity, longitudinal total strain range, $\Delta\epsilon$

$$\Delta\epsilon = \Delta\epsilon_e + \Delta\epsilon_p \tag{9}$$

The strain ranges from Eqs 4–9 are shown in Table 2 for the twelve

TABLE 2—*Ni(Cr)-TaC fatigue strain ranges.*

Specimen Number	N_f	$\Delta\epsilon^d$	$\Delta\epsilon_e{}^d$	$\Delta\epsilon_p{}^d$	$\Delta\epsilon$	$\Delta\epsilon_e$	$\Delta\epsilon_p$	Temperature, °C
FT1	390	0.01688	0.00345	0.01343	0.0374	0.0105	0.0269	RT[a]
FT2	955	0.01242	0.00312	0.00930	0.0281	0.0095	0.0186	RT[a]
FT3	45	0.0201	0.00161	0.01849	0.04188	0.0049	0.03698	1000
FT4	470	0.00538	0.00138	0.00400	0.0122	0.0042	0.00800	1000
FT5	124	0.0108	0.00135	0.00945	0.0230	0.0041	0.01890	1000
FT10	1 500	0.00284	0.00119	0.00165	0.00693	0.00363	0.00330	1000
FT11	4 000	0.00179	0.00089	0.00090	0.00451	0.00271	0.00180	1000
FT12	2 500	0.00706	0.00289	0.00417	0.01713	0.00879	0.00834	RT[a]
FT13	14 000	0.00403	0.00264	0.00139	0.01084	0.00806	0.00278	RT[a]
FT14	85	0.03006	0.00450	0.02556	0.0648	0.0137	0.0511	RT[a]
FT15	155 000	0.002854	0.002421	0.000433	0.008239	0.007373	0.000866	RT[a]
FT16	16	0.08038	0.00539	0.07499	0.1664	0.0164	0.1500	RT[a]

[a] RT = room temperature.

axial tests. A scan of the data reveals that tests at each temperature encompass a wide enough set of strain ranges to include the transition fatigue life.

Discussion

Tensile Background

The low strain tensile deformation of Ni(Cr)-TaC is that of a classic composite material. This behavior is shown in Fig. 3, which is a plot of the low strain portion of an engineering stress-strain curve at room temperature. Region A of this figure represents composite elasticity, that is, both fibers and matrix are deforming elastically. Region B consists of elastic-plastic behavior, that is, the fibers are deforming elastically and the matrix is deforming plastically. The upper yield point represents onset of significant fiber failure. After the low strain portion shown here in Fig. 3, the composite strain hardens to an ultimate of approximately 100 ksi at 20 percent elongation. Composite failure at room temperature occurs at approximately 35 percent elongation or a true strain from areal measurements of approximately 80 percent [*24*].

The low strain behavior at 1000°C is similar to that at room temperature. This low strain behavior is seen in Fig. 4, an engineering stress-

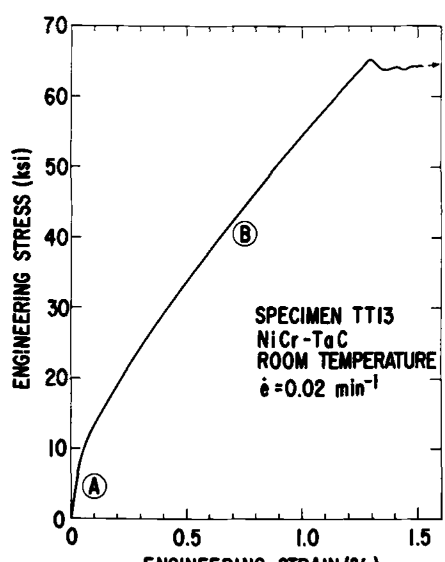

FIG. 3—*Low strain portion of a Ni(Cr)-TaC tension test at room temperature. Ultimate tensile strength equals 100 ksi. Elongation to failure equals 35 percent.*

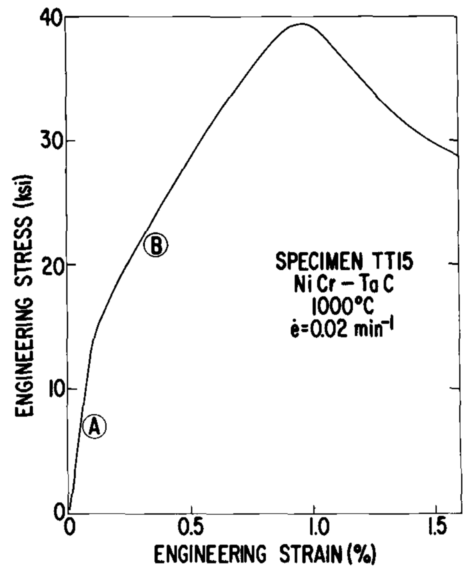

FIG. 4—*Low strain portion of a Ni(Cr)-TaC tension test at 1000°C. Ultimate tensile strength equals 39 ksi. Elongation to failure equals 15 percent.*

strain plot. The directionally solidified eutectic at this temperature also shows the region of composite elasticity, A, followed by a region of matrix plasticity plus fiber elasticity, B. The peak at approximately 1 percent strain represents onset of significant fiber failure. Beyond the strain regime shown here, the composite load-carrying capacity continually drops off. Composite failure at 1000°C at this strain rate is at approximately 15 percent elongation or approximately 60 percent true strain from areal measurements [*24*].

Hysteresis

The diameter-change signal from the extensometer of Fig. 2 was plotted directly against the signal from the load cell on an *X-Y* recorder to monitor specimen hysteresis in these high strain fatigue tests. The shapes of these hysteresis loops are consistent with the monotonic deformation just described.

Figure 5 shows this hysteresis for the first two cycles of specimen FT4, a 1000°C test where fibers did not fragment until near end of life. Note from Table 2 that this specimen still has $\Delta\epsilon_p > \Delta\epsilon_e$. The startup shows the same Region A and Region B type behavior observed in tension in Fig. 4. During compressive straining, the composite also exhibits the regions of elastic-elastic and elastic-plastic behavior. Since the strain

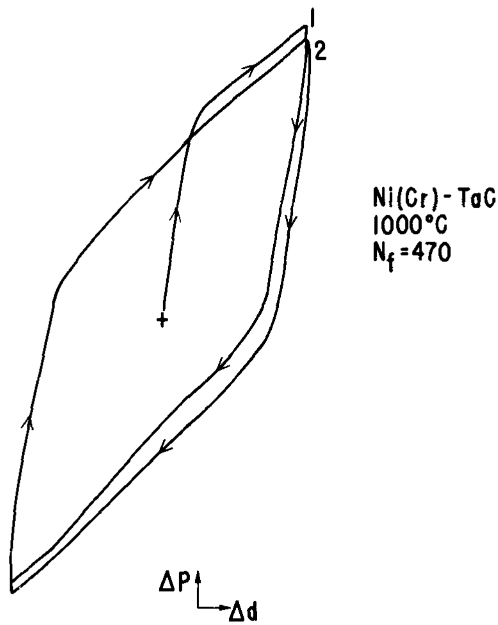

FIG. 5—*First two hysteresis loops for specimen FT4 at 1000°C. Strain range is insufficient to cause early fiber failure.*

range is insufficient to cause significant fiber failure, this four-sided loop becomes the stable loop shape (with some cyclic hardening) until macrocrack propagation.

Figure 6 shows selected hysteresis loops for specimen FT3 tested at 1000°C. The first cycle was done at a low strain range just to obtain additional data on the low strain loop shape. After the second cycle, the strain range was expanded to that desired for this specimen. The tensile loading on the second cycle looks qualitatively just like the low strain portion of the tension test of Fig. 4. Note that the hysteresis loops represent more of a true stress-true strain curve and that this is, therefore, more than just a drop in load-carrying capacity due to a necking instability. The dropoff in load is due to fiber cracking and a loss of load sharing in the second phase. On the third cycle, the maximum tensile load and, thus, the stress range, have decreased. This qualitative shape then remains until macrocrack propagation. Careful examination of Fig. 6 shows a cusp on the compression side of even the second cycle. This is more obvious at high strains at room temperature and is discussed next.

Figure 7 shows hysteresis loops from a test at room temperature where the strain range was not sufficient to cause early fiber failure. This speci-

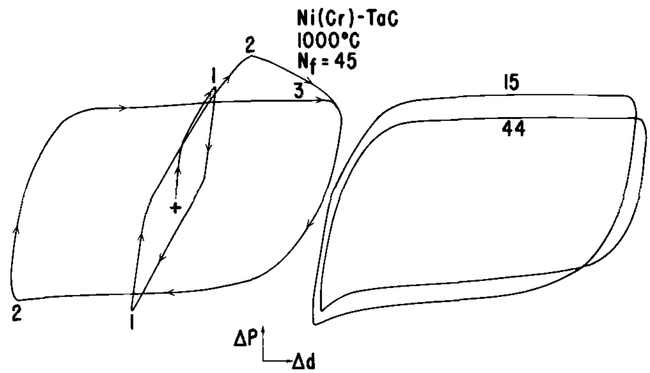

FIG. 6—*Selected hysteresis loops for specimen FT3 at 1000°C. Strain range is sufficient to cause early fiber failure.*

men does not appear in Table 1 or 2 because shortly after 1000 cycles, a machine malfunction terminated the test. The loops show cyclic hardening. Regions A and B are not as clearly defined in tension as in compression. Note, also, in comparing Figs. 3 and 4 that these regions were also less clearly defined in tension at room temperature than at 1000°C. This is also consistent with the hysteresis loops of Figs. 5 and 7.

Figure 8 shows selected hysteresis loops of specimen FT2, a room temperature specimen, where the strain range was large enough to cause significant fiber failure on the first cycle. Compare these to the loops of Fig. 7. Note now the absence of a clear Region B (matrix plasticity with

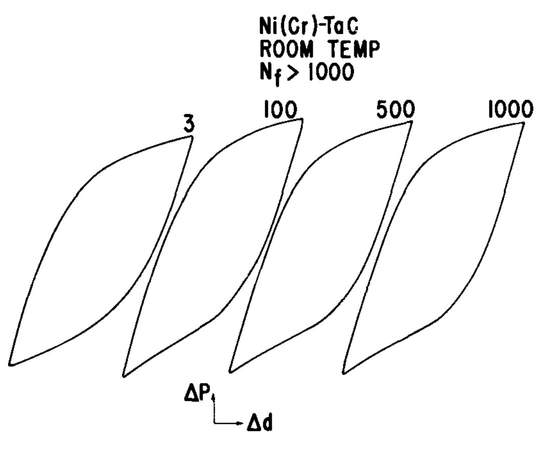

FIG. 7—*Selected hysteresis loops at room temperature where the strain range was insufficient to cause early fiber failure.*

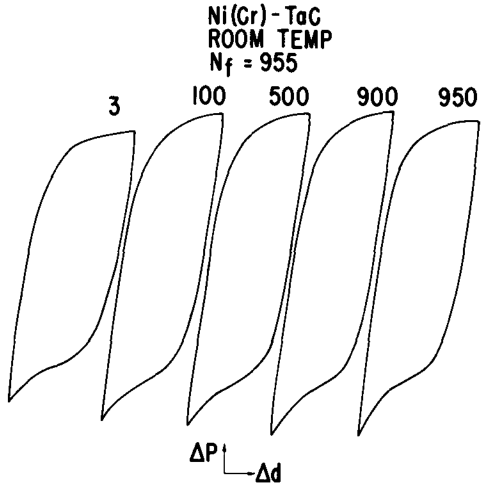

FIG. 8—*Selected hysteresis loops for specimen FT2 at room temperature. Strain range is sufficient to cause early fiber failure.*

fiber elasticity) in compression. Instead, there is a clear compression cusp very early in life. This cusp, now, does not relate to macrocrack propagation but to compliance differences at the sites of fiber failure as the microvoids are closed until the fractured fiber ends butt and begin to share load. The cusp becomes much more exaggerated later in life and is most probably beginning to reflect crack propagation.

Crack Initiation

The reversed bend tests described previously were used to study fatigue crack nucleation at room temperature. Observations from replicas of the polished free surface will be discussed here.

A specimen tested to give 509 cycles to failure had a sufficient strain range to give severe fiber failure in the first cycle. Figure 9 shows a surface replica taken after 1.5 cycles or 0.3 percent of life. The micrograph shows the fiber segmentation. Subsequent matrix crack initiation and early or Stage I growth is from the fiber crack sites.

If the strain range is dropped enough, then the strong fibers cycle in their elastic regime. This forces crack initiation to occur in the Ni(Cr) matrix by conventional mechanisms. Figure 10 shows a surface replica taken after 14 000 or 82 percent of life on a bend specimen with 17 000 cycles to failure. The strain range did not cause significant fiber failure until near end of life. Examination shows that fatigue crack initiation has been at extrusion sites on slip bands in the matrix as in some conventional materials [22]. This replica also shows that the fatigue crack propagation in this specimen is causing fiber failure only where the microcrack crosses the fibers. The fibers are uncracked elsewhere. Note the tongues of replica material that were down in the crack on the actual specimen.

Phenomenology

As demonstrated by the well-known Coffin-Manson law [26]

$$N_f^{\beta}\,\Delta\epsilon_p = C \tag{10}$$

the fundamental correlation for low cycle fatigue life of conventional alloys is the plastic strain range. Here $\Delta\epsilon_p$ and N_f are plastic strain range

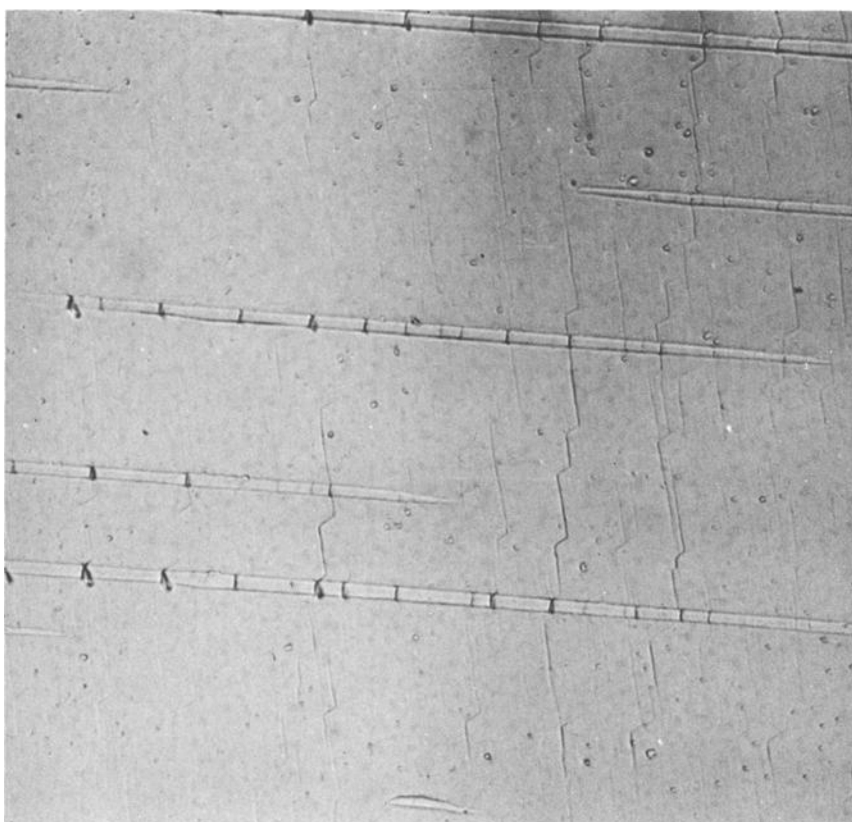

FIG. 9—*Surface replica of bend specimen with* $N_f = 509$. *Replica at 0.3 percent of life (1.5 cycles).*

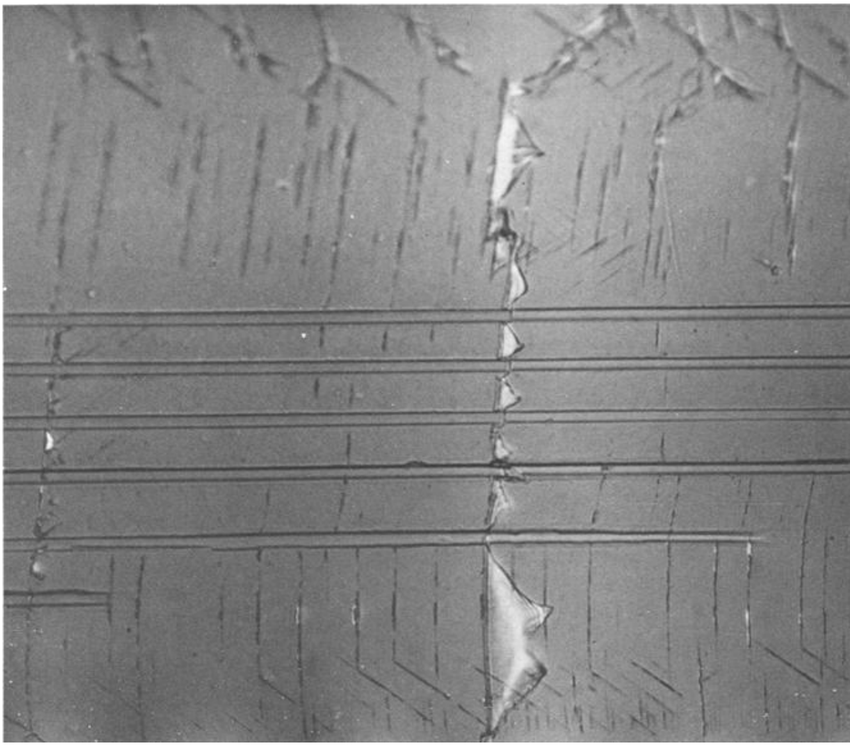

FIG. 10—*Surface replica of bend specimen with* $N_f = 17\,000$. *Replica at 82 percent of life (14 000 cycles).*

and cycles to failure, respectively, and β and C are constants. Since this equation can be rewritten as

$$\log (\Delta\epsilon_p) = C_1 - \beta \log (N_f) \qquad (11)$$

where C_1 is a constant, then a logarithm-logarithm plot of $\Delta\epsilon_p$ and N_f yields a straight line for conventional alloys. It has also been shown that for many conventional materials the elastic strain range, $\Delta\epsilon_e$, may be related to cycles to failure, N_f, by [*27*]

$$N_f^{\alpha}\, \Delta\epsilon_e = C_2 \qquad (12)$$

where α and C_2 are constants. Since this can also be transformed to the format of Eq 11, a straight line logarithm-logarithm plot of $\Delta\epsilon_e$ and N_f can be expected for many materials.

The room temperature longitudinal strain range data of Table 2 is plotted against cycles to failure on a logarithm-logarithm scale in Fig. 11. As can be seen, the straight line correlation for plastic strain is excellent. A computer regression curvefit of Eq 10 gives an index of determination of 0.994 and a value of $\beta = 0.566$. A perfect fit has an index of determination of 1.0. The fit of the elastic strain range data is moderately good. A regression on Eq 12 yields an index of determination of 0.912 and a value of $\alpha = 0.089$.

This fit to the Coffin-Manson law is excellent even across the zone where the strain range is sufficient to cause significant fiber failure on the first cycle. This indicates that the fatigue response is matrix-controlled. The four higher strain tests on Fig. 11 had fiber failure on the first cycle and the three lower strain tests had no significant fiber failure until final macrocrack propagation. This fibrous eutectic with a ductile matrix and brittle fibers, thus, does obey the Coffin-Manson law at room temperature. The total strain range data are also shown.

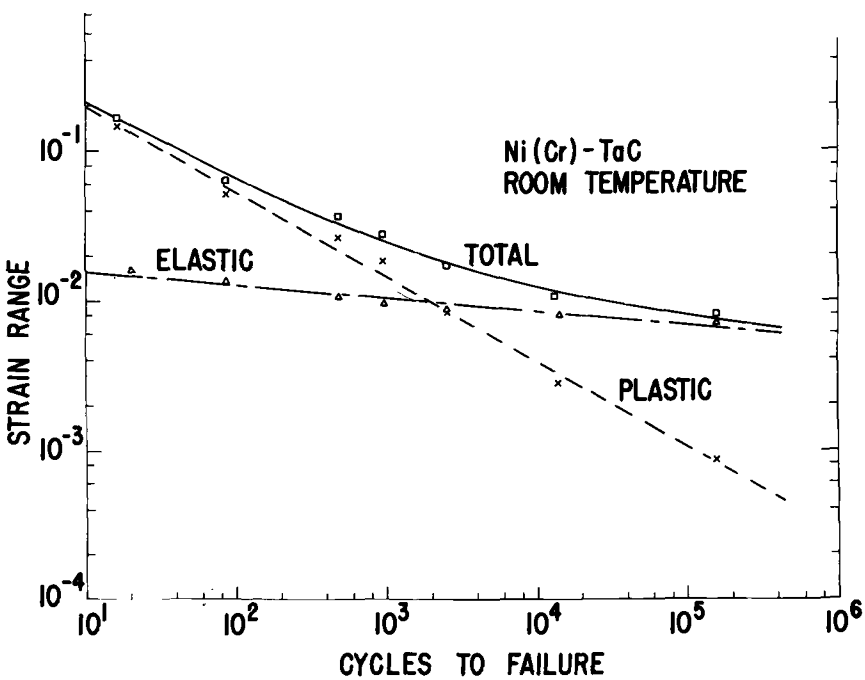

FIG. 11—*Strain range versus life for Ni(Cr)-TaC at room temperature. Included are elastic, plastic and total strain.*

The longitudinal strain range data of Table 2 for 1000°C tests in air are plotted against cycles to failure on a logarithm-logarithm scale in Fig. 12. At this temperature, the straight-line correlation on plastic strain range is also excellent. A regression analysis yields an index of determination of 0.999 and a value of $\beta = 0.680$. This eutectic, then, in the directionally solidified condition, also obeys the Coffin-Manson law at 1000°C, where the fibers account for a significant portion of the composite strength [*24*]. The data span two tests where there was severe fiber failure on the first cycle and three tests where there was no significant fiber failure until near end of life.

The elastic strain range data at 1000°C give a poor fit to Eq 12. A regression analysis of these data gives a value of 0.836 for an index of determination. The line drawn through the elastic data in Fig. 12 is schematic. While there is not sufficient data yet to support this shape solely on a phenomenological basis, examination of the hysteresis loops shows support for the general shape. When the strain range is low enough to not cause fiber failure on the first cycle, then the stress range, or elastic strain range, is sensitive to plastic strain range (see Fig. 5). Since there is a correlation on plastic strain range, then the elastic strain range decreases with increasing cycles to failure as seen in the high life region of Fig. 12. When the strain range is sufficient to cause severe fiber failure on

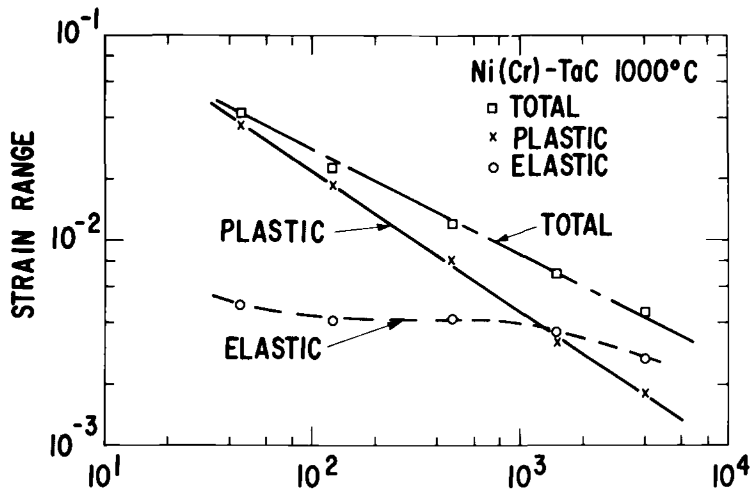

FIG. 12—*Strain range versus life for Ni(Cr)-TaC at 1000°C. Included are elastic, plastic and total strain. Frequency equals one cycle per minute.*

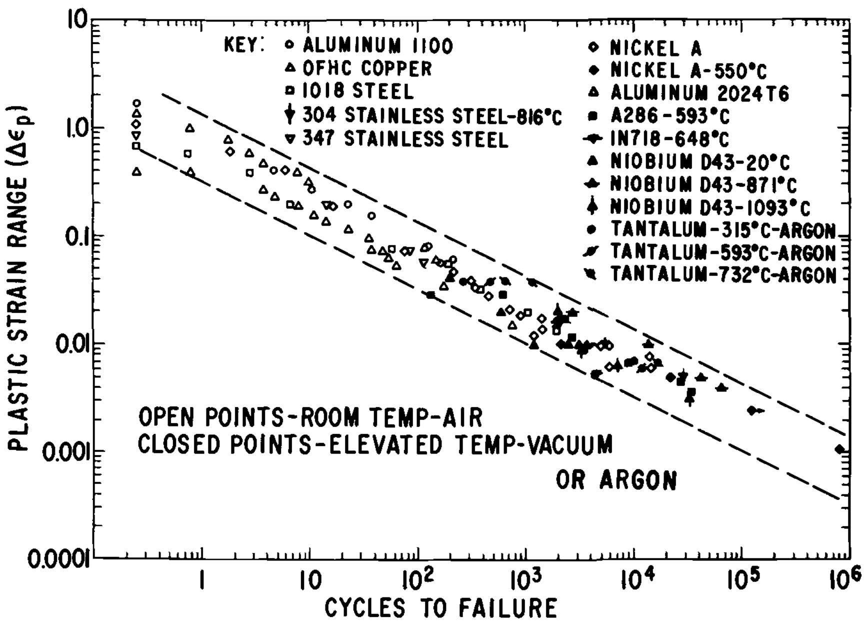

FIG. 13—*Generic fatigue data from Coffin* [28].

the first cycle, then the stress range, or elastic strain range, is relatively insensitive to the plastic strain range. This can be seen in the shape of the hysteresis loop shape of Fig. 6. Since there is a correlation on plastic strain range, one would expect $\Delta\epsilon_e$ in this range to be relatively insensitive to N_f. This is seen in the intermediate life regime of Fig. 12. The slight upturn in the $\Delta\epsilon_e$ curve at the lowest life point appears to be due to severe cyclic hardening at the very high plastic strain range associated with that test. The sum of elastic plus plastic to give total strain yields a straight line at 1000°C, but this is judged to be purely coincidental.

Comparisons

While the Ni(Cr)-TaC system reported here is a model system, comparisons to conventional alloys are instructive. Coffin [*28*] has shown that room temperature strain-cycled fatigue data are generic for many conventional materials. One of Coffin's graphs is given here in Fig. 13. It demonstrates, for plastic strain range, a single scatter band for several materials at room temperature and several materials at elevated temperature where environment has been excluded. Because this plot contains a wide range of materials and many data points, that same plot is given again for clarity in Fig. 14 with only the scatter band plotted. Included now are the plastic strain points from this study. The Ni(Cr)-TaC points fall in that scatter band and, therefore, have a plastic strain versus life relation in low cycle fatigue like that of conventional materials despite the presence of the brittle TaC fibers.

Comparison of the 1000°C data is not as straightforward as at room temperature. Directionally solidified monocarbides eutectics, as a class, are currently under consideration as potential materials for high temperature gas turbine buckets. It was decided, therefore, to compare this model alloy to a current, conventional, as-cast superalloy bucket material. Data for such an alloy could not be found at 1000°C. The comparison was, thus, made between Ni(Cr)-TaC at 1000°C, a potential use temperature for a new class of materials, and cast René 80 at 870°C, a current, conventional alloy at its use temperature. The data on cast René 80 were obtained from Coffin [*29*]. The comparison on plastic strain range is shown in Fig. 15. The plot also shows the Ni(Cr)-TaC data at room temperature. Again, there is evidence that the Ni(Cr)-TaC low cycle fatigue behavior is matrix controlled. The 1000°C data in air are not far below the room temperature data and are above the cast René 80 curve at 870°C. Both elevated temperature curves are for one cycle per minute.

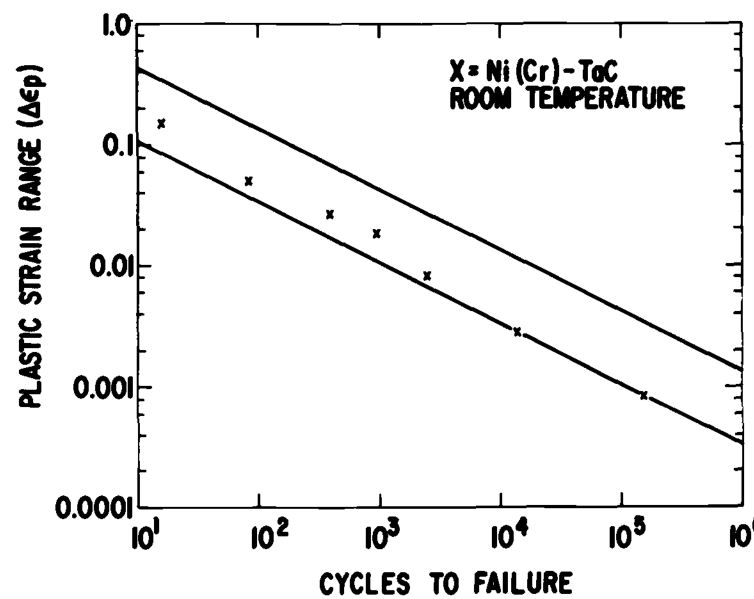

FIG. 14—*Scatter band of Fig. 13 with Ni(Cr)-TaC room temperature data.*

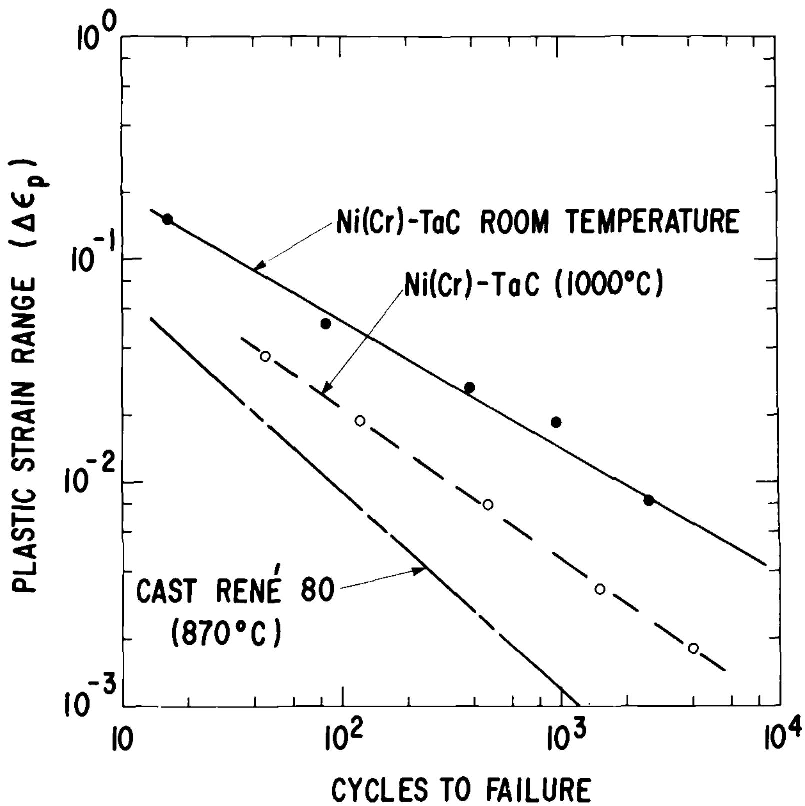

FIG. 15—*Plastic strain versus life for Ni(Cr)-TaC at room temperature and 1000°C, and cast René 80 at 870°C.*

It must be noted here that cast René 80 at 870°C is significantly stronger than Ni(Cr)-TaC at 1000°C. For completeness, therefore, the comparison is also made on the basis of total strain range (elastic plus plastic) in Fig. 16. The two materials can be seen to be essentially equivalent in fatigue resistance despite the 130°C higher temperature for the Ni(Cr)-TaC.

Conclusions

1. The directionally solidified eutectic Ni(Cr)-TaC obeys the Coffin-Manson law in high-strain/low-cycle fatigue at room temperature and 1000°C (1832°F).

2. The strain-cycled fatigue behavior of this fibrous eutectic is controlled by the matrix.

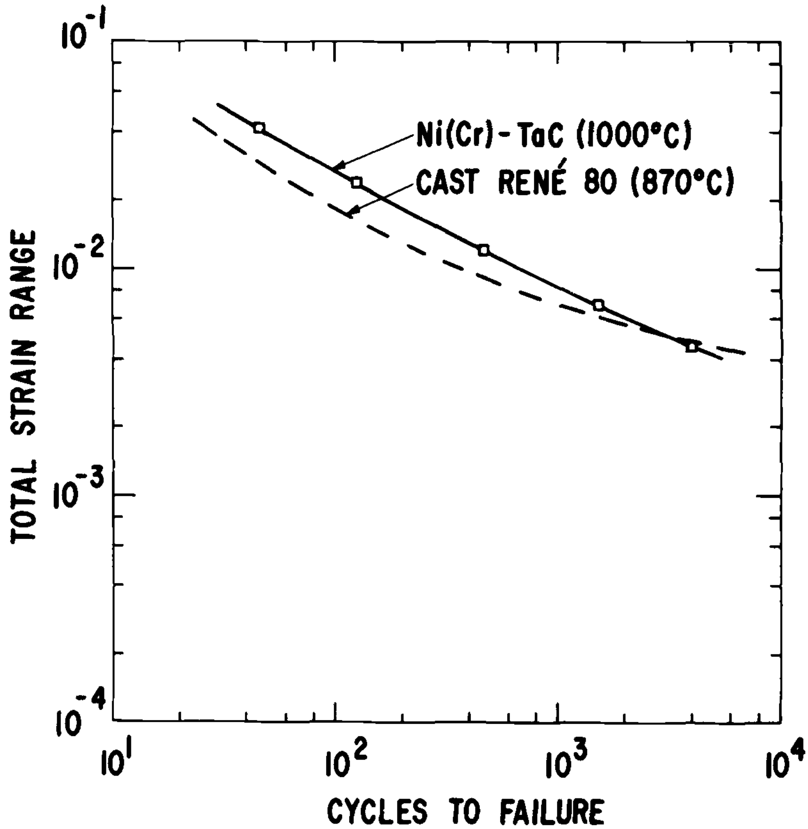

FIG. 16—*Total strain versus life for Ni(Cr)-TaC at 1000°C and cast René 80 at 870°C.*

3. The stress/strain hysteresis behavior is very different from that of conventional alloys.
4. The shape of the hysteresis loops may be used to judge fiber integrity.
5. Fatigue cracks initiate at broken fibers at high cyclic strain and at slip band extrusions in the matrix at low cyclic strains.
6. The strain cycled fatigue resistance of the directionally solidified eutectic Ni(Cr)-TaC is essentially equivalent to conventional superalloys.

Acknowledgments

We wish to thank W. J. Baxter and W. F. Moore for alloy preparation and G. E. Stebbins and C. P. Palmer for directional solidification. D. C.

Lord and P. T. Hill provided valuable consulting and assistance in testing. Numerous discussions with L. F. Coffin, Jr., H. D. Solomon, and L. A. Johnson were appreciated.

References

[1] Salkind, M. J., George, F. D., Lemkey, F. D., and Bayles, B. J., Final Report: Contract NOW 65-0384-d (AS633241), United Aircraft Research Laboratories, May 1966.
[2] Hoover, W. R. and Hertzberg, R. W., *Transactions*, American Society for Metals, Vol. 61, 1968, p. 769.
[3] May, G. J. and Chadwick, G. A., *Metal Science Journal*, Vol. 7, 1973, p. 20.
[4] Kim, Y. G., Maurer, G. E., and Stoloff, N. S., in *Fatigue of Composite Materials, ASTM STP 569*, American Society for Testing and Materials, 1975, pp. 210–225.
[5] de Silva, A. R. T. and Chadwick, G. A., *Metal Science Journal*, Vol. 4, 1970, p. 63.
[6] Mills, W. J. and Hertzberg, R. W., in *Fatigue of Composite Materials, ASTM STP 569*, American Society for Testing and Materials, 1974, pp. 5–27.
[7] Thompson, E. R., George, F. D., and Kraft, E. H., Report No. J910868-4, United Aircraft Research Laboratories, July 1970.
[8] Patarini, V. M. and Kattamis, T. Z., *Proceedings*, National Academy of Sciences, Vol. 2, 1973, p. 187.
[9] Bibring, H., Trottier, J. P., Rabinovitch, M., and Seibel, G., *Memoires Scientifiques de la Revue de Metallurgie*, Vol. 68, No. 1, 1971, p. 23.
[10] Koss, D. A. and Copley, S. M., *Metallurgical Transactions*, Vol. 2, 1971, p. 1557.
[11] Anonymous, *Materials Engineering*, Vol. 76, No. 7, 1972, p. 30.
[12] Vaccari, J. A., *Materials Engineering*, Vol. 77, No. 2, 1973, p. 19.
[13] Lemkey, F. D. and E. R. Thompson, *Metallurgical Transactions*, Vol. 12, 1971, p. 1537.
[14] Bibring, H., Rabinovitch, M., and LucMartin, J., *Comptes Rendus*, Vol. 270, 1970, p. 1937.
[15] Bibring, H., Rabinovitch, M., and Seibel, G., *Comptes Rendus*, Vol. 268, 1969, p. 1666.
[16] Walter, J. L. and Cline, H. E., *Metallurgical Transactions*, Vol. 4, 1973, p. 1775.
[17] Storms, E. K., *The Refractory Carbides*, Academic Press, New York, 1967.
[18] Rowcliffe, D. J. and Hollox, G. E., *Journal of Material Science*, Vol. 6, 1971, p. 1270.
[19] Henry, M. F. and Koch, E. F., *Practical Metallography*, Vol. 10, 1973, p. 439.
[20] Henry, M. F. and Stoloff, N. S., *Journal of Material Science*, Vol. 7, 1972, p. 1477.
[21] Slot, T., Stentz, R. H., and Berling, J. T., in *Manual on Low Cycle Fatigue, ASTM STP 465*, American Society for Testing and Materials, 1969, p. 100.
[22] Henry, M. F., Report No. 72CRD100, General Electric Company, March 1972.
[23] Henry, M. F., Report No. 71C338, General Electric Company, Nov. 1971.
[24] Henry, M. F., *Proceedings*, National Academy of Sciences, Vol. 2, 1973, p. 173.
[25] Henry, M. F., Ph.D. thesis, Rensselaer Polytechnic Institute, Sept. 1974.
[26] Coffin, L. F., Jr., *Annual Reviews of Materials Science*, Vol. 2, 1972, p. 313.
[27] Manson, S. S. and Hirschberg, M. H., *Fatigue—An Interdisciplinary Approach*, Syracuse University Press, 1964, p. 133.
[28] Coffin, L. F., Jr., *Metallurgical Transactions*, Vol. 3, 1972, p. 1777.
[29] Coffin, L. F., Jr., Report No. 73CRD137, General Electric Company, April 1973.

Y. G. Kim,[1] G. E. Maurer,[2] and N. S. Stoloff[2]

Fatigue Behavior of an Ag_3Mg-AgMg Eutectic Composite

REFERENCE: Kim, Y. G., Maurer, G. E., and Stoloff, N. S., "**Fatigue Behavior of an Ag_3Mg-AgMg Eutectic Composite,**" *Fatigue of Composite Materials, ASTM STP 569*, American Society for Testing and Materials, 1975, pp. 210–225.

ABSTRACT: The eutectic alloy Ag-32 atomic percent Mg has been directionally solidified at rates ranging from 0.8 to 27.7 cm/h to produce an aligned lamellar structure. The alloy, consisting of 40 volume percent AgMg and 60 volume percent of a solid solution of approximate composition Ag-27 atomic percent Mg, has been cycled in tension-tension loading at room temperature. Fatigue life increased sharply with both higher growth speeds and with the introduction of long range order into the Ag-27 atomic percent Mg phase by post-solidification heat treatment. Fractographic examination revealed a marked change in crack path and striation morphology as order was produced. It is concluded that improvements in fatigue life with growth speed were a consequence of decreased interlamellar spacing and the resulting rise in tensile strength of the alloy.

KEY WORDS: composite materials, eutectics, fractures, striations, range, order, silver, magnesium, yield strength

Previous studies have shown that the tensile and creep strength of directionally solidified eutectic alloys depend sensitively upon the fineness of microstructure achieved by varying growth rates [*1–3*].[3] However, studies of fatigue in Al-Al_3Ni [*4*,*5*] and in Al-$CuAl_2$ [*4*] reveal no effect of growth speed on fatigue life except for very high speeds where the yield stress is materially increased. Since we have shown that the yield stress of a silver-magnesium (Ag-Mg) eutectic alloy is very sensitive to post-solidification heat treatments which produce long range order in one

[1] Formerly graduate assistant, Rensselaer Polytechnic Institute; presently resident research associate, National Aeronautics and Space Administration, Lewis Laboratory, Cleveland, Ohio 44135.
[2] Graduate assistant and professor, respectively, Rensselaer Polytechnic Institute, Troy, N. Y. 12181.
[3] The italic numbers in brackets refer to the list of references appended to this paper.

phase [6,7], we have decided to utilize this system for a study of the relationships among fatigue life, microstructure and strength level.

The experimental program consisted of producing directionally solidified specimens of the Ag-Mg alloy at several growth rates, performing post-solidification heat treatments to produce long range order in one of the phases, and determining the room temperature fatigue properties as a function of growth rate and heat treatment.

Alloy Structure and Crystallography

The Ag-33.6 atomic percent Mg (nominal) eutectic transformation occurs at 759°C and yields a lamellar structure consisting of 40 volume percent of the ordered cesium chloride (CsCl) type phase AgMg, and 60 volume percent of a solid solution of approximate composition Ag-27 atomic percent Mg [8]. AgMg is ordered to its melting point (820°C), while Ag-27 percent Mg undergoes an ordering reaction from disordered face center cubic (fcc) to a face center tetragonal (fct) DO_{23} type superlattice below about 375°C [9]. No data are available concerning crystallographic relations between the co-existing phases. However, previous work has shown that the ordering treatment decreases the ease of slip propagation across interphase boundaries [10].

Experimental Procedure

Material Preparation

Starting materials were 99.999 percent silver and 99.995 percent magnesium. Ingots were melted in graphite crucibles under flowing argon in an induction unit. A shift in composition from Ag-33.6 atomic percent Mg to Ag-32.2 percent Mg was necessary to remove proeutectic magnesium. Ingots were hot swaged to 0.76 cm diameter directly after initially casting to 2.5 cm diameter.

Directional Solidification

Cylindrical rods of 0.76 cm diameter were directionally solidified in graphite crucibles inside an induction-heated Bridgeman apparatus through which argon was flowing. The crucible was withdrawn from the furnace, through a water-cooled collar, at rates, R, in the range 0.86 to 27.7 cm/h. The structure of Ag-Mg ingots selected for study always consisted of plates aligned nominally parallel to the growth direction.

The relationship between average plate spacing $\lambda = t_1 + t_2$, where t_1 and t_2 are the thickness of adjacent lamellae of the two phases, and growth rate, R, has previously been established [7]. The alloy obeys the relation $\lambda^2 R$ = constant, where the constant = 1.5×10^{-9} cm^3/s.

The eutectic grain size, d, was also measured as a function of growth rate. There was little variation in grain size over the range of growth speeds employed; the average value of d was about 0.06 cm.

Specimen Preparation and Testing

After unidirectional solidification, hour-glass shaped fatigue specimens, about 5 cm long, were machined parallel to the growth direction with a series 10-67 "Tensilkut" machine and a "Tensilathe" attachment. The minimum diameter of these specimens was approximately 0.33 cm.

Specimens of Ag-Mg eutectic in which long-range order was to be produced in the silver-rich phase were annealed in vacuum at 500°C for 1 h and then slow cooled to 370°C, held for 15 h, and cooled to room temperature over a period of 10 h. Specimens in which the silver-rich phase was to be disordered were quenched after a 1-h vacuum anneal at 500°C. This treatment disordered only the Ag-27 percent Mg phase. Complete long range order was retained in the AgMg phase.

Prior to testing, gage sections of the alloy were polished with Linde A and B, and then electropolished.

Fatigue tests were conducted on a closed-loop electrohydraulic system under load control. The cyclic frequency was 10 Hz, and a sinusoidal waveform was used. In most cases a tension-tension cycle with a constant mean stress of 28 000 psi (196 MN/m^2) was employed to minimize damage of fracture surfaces. Additional tests in tension-tension cycling were carried out at somewhat higher mean stresses.

Fractured tensile specimens were examined both by scanning electron microscopy and two-stage replication. Replicas were shadowed with chromium at 45 deg, and then backed with carbon at 90 deg. Fractured specimens to be examined metallographically were coated for edge preservation. The specimens were then mounted longitudinally so that crack paths could be examined. Interlamellar spacings were measured on cross sections cut from specimen shoulders.

Experimental Results

Fatigue Life

The results of fatigue tests on ordered specimens of Ag_3Mg-AgMg prepared at two growth speeds, 3.5 cm/h and 27.7 cm/h, are shown in Fig. 1. The more rapid growth speed, which produced a decrease in interlamellar spacing of 50 percent, caused considerable extension of

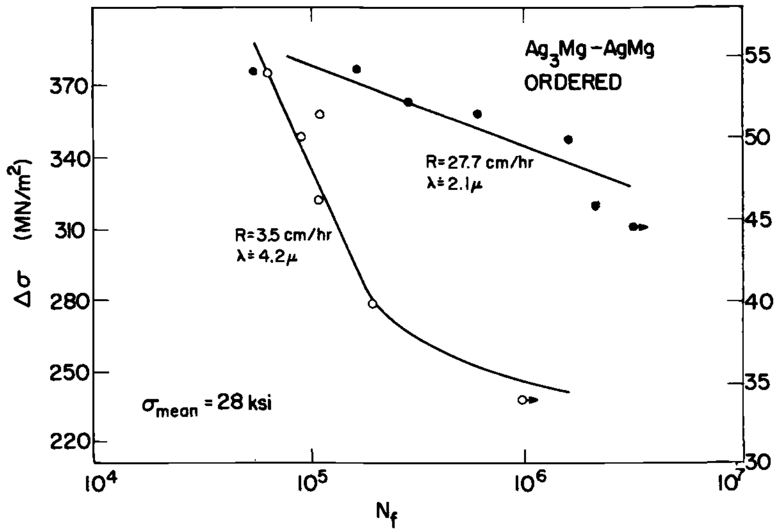

FIG. 1—*Effect of growth speed on fatigue life of ordered Ag_3Mg-AgMg.*

the fatigue lives, particularly at low cyclic stresses. A difference in fatigue limit (10^7 cycles) of some 10 ksi is indicated on the $\Delta\sigma$ scale.

The fatigue lives of Ag_3Mg-AgMg specimens as a function of long range order and specimen growth speed, R, are tabulated in Table 1. Most tests were carried out at a peak stress of 49 ksi (343 MN/m^2) and a mean stress of 28 ksi (196 MN/m^2). Considerable scatter was experienced, in part due to variations in interlamellar spacing due to growth

TABLE 1—*Effect of ordering on fatigue life.*

Growth Speed, cm/h	Condition	$\Delta\sigma$, ksi	N_f
1.7	ordered	42	2.12×10^5
1.7	disordered	42	8.0×10^4
3.5	ordered	42	5.6×10^4
3.5	disordered	42	4.7×10^4
6.9	ordered	42	1.16×10^5
6.9	ordered	42	2.3×10^6
6.9	disordered	42	8.5×10^4
19.6	ordered	42	1.6×10^6 [a]
19.6	disordered	42	4×10^5
27.7	ordered	52	6×10^5
27.7	disordered	52	6.8×10^4

[a] Did not fail.

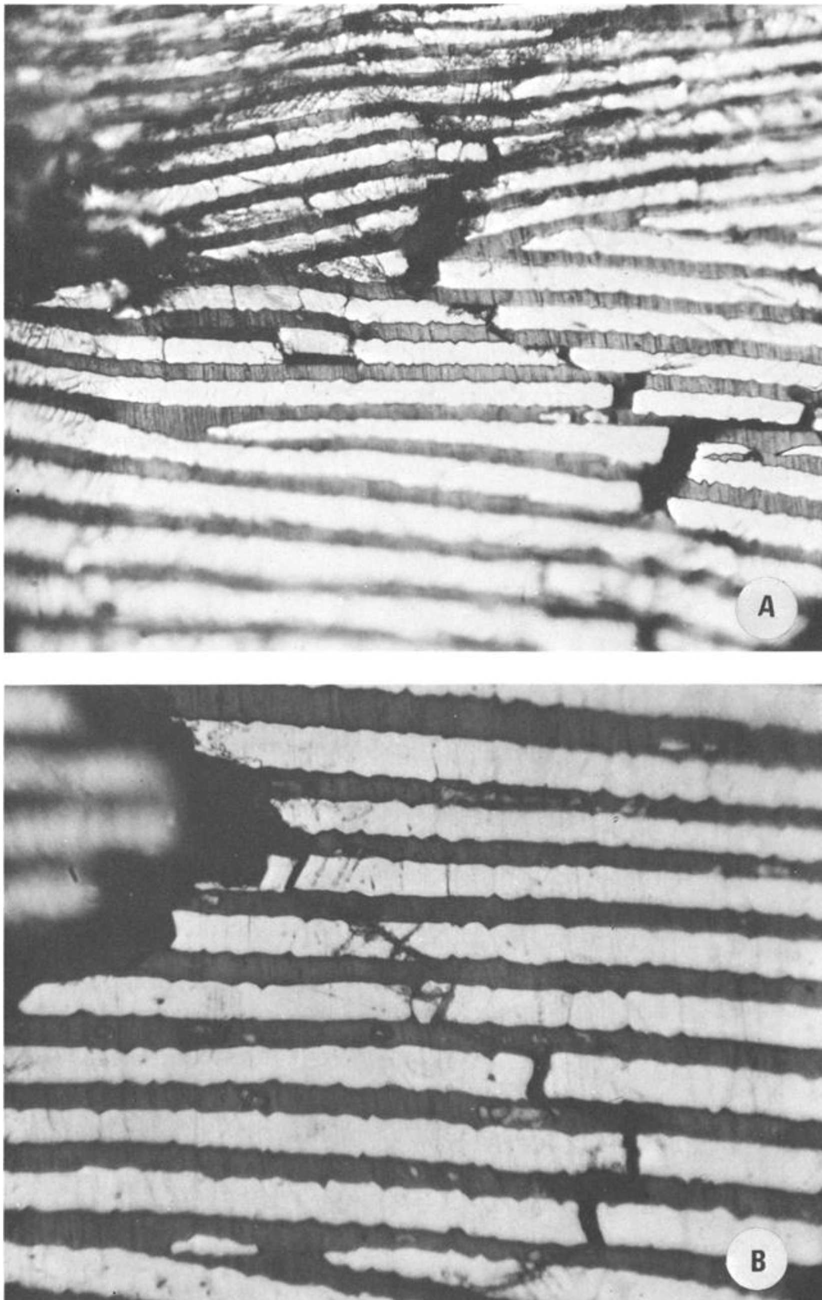

FIG. 2—*Secondary fatigue cracks in ordered specimen 1*AO, R = *0.86 cm/h:* (a) *cracking along interphase boundaries,* ×*410; and,* (b) *cracking along crystallographic planes,* ×*750.*

perturbations along the length of each ingot (up to three specimens were obtained per ingot). Tests on specimens containing obvious casting defects are not reported. In all cases no crack was visible until the specimen was very near final failure. At a constant growth speed, long range ordered specimens have greater fatigue resistance, particularly at rapid growth rates. Moreover, there is a sharp increase in fatigue life with growth speed for both ordered and disordered material, as has already been shown in Fig. 1. The greater effectiveness of ordering on life at high growth speeds is consistent with the effectiveness of interphase boundaries as barriers to slip when the Ag_3Mg phase is ordered [*6*]. That is, the finer the microstructure, the greater the strength of the eutectic alloy, with the interlamellar spacing causing more of an effect when Ag_3Mg is ordered.

One ordered specimen, *AO*, grown at $R = 6.9$ cm/h, was cycled in reversed tension-compression [$\sigma_{max} = 50$ ksi, (350 MN/m^2) $\sigma_{min} = -10$ ksi (−70 MN/m^2)]. The fatigue life was 3.1×10^4 cycles, compared to an average life of about 10^5 cycles experienced at $\sigma_{max} = 49$ ksi, (343

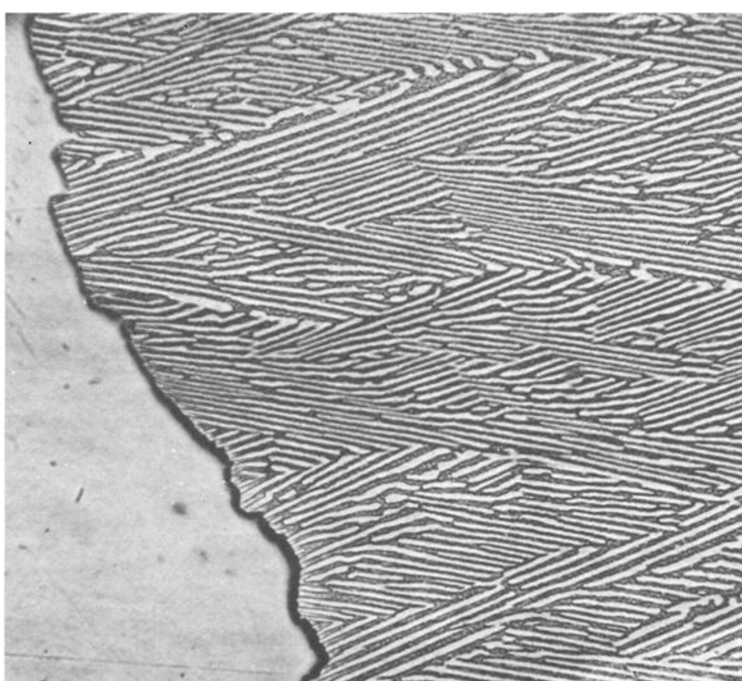

FIG. 3—*Crack profile in disordered specimen* 6BD, R = *27.7 cm/h, showing tendency for crack to lie perpendicular to individual lamellae, ×265.*

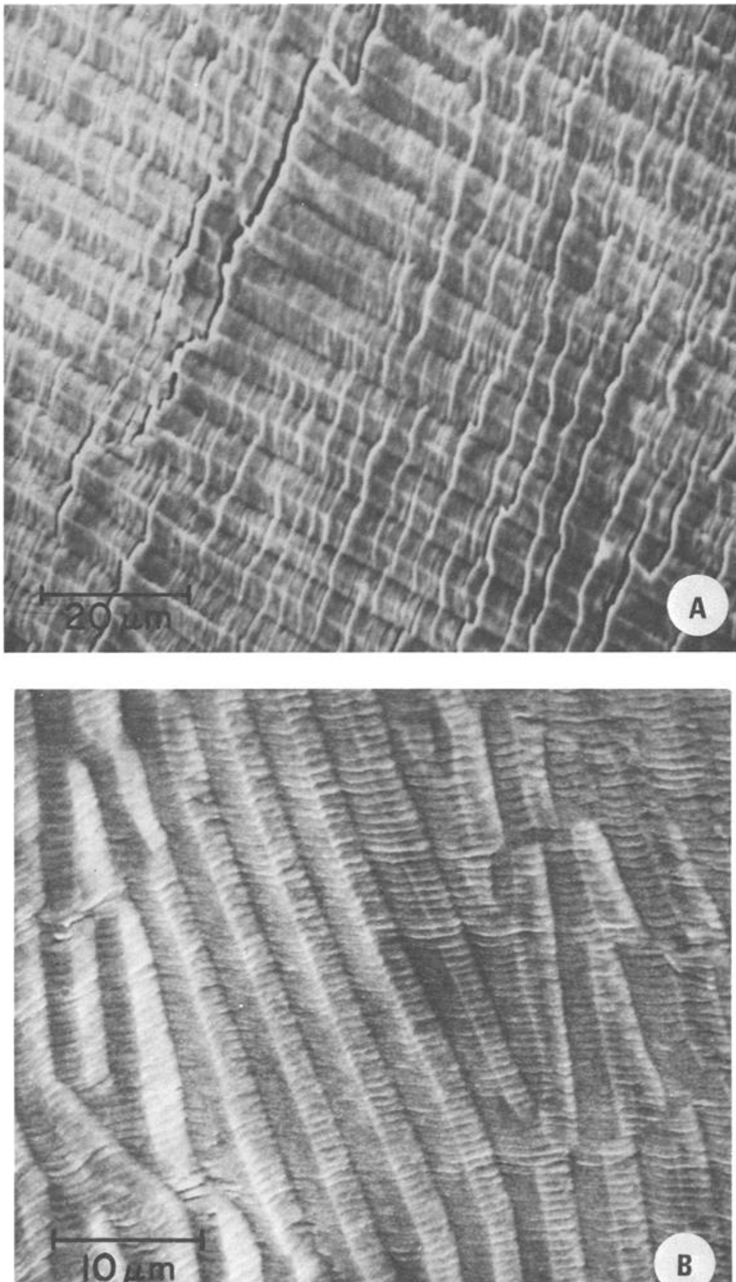

FIG. 4—*Fatigue striations in disordered specimens:* (a) *specimen* 3D, R = *6.9 cm/h, ×1000;* (b) *specimen* 7BD, R = *27.7 cm/h, ×2000; and,* (c) *specimen* 7 BD, R = *27.7 cm/h, ×2000.*

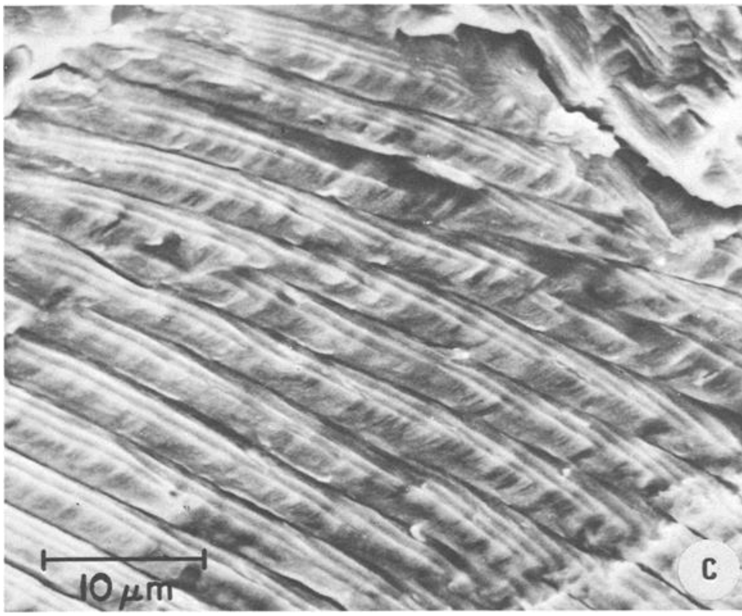

FIG. 4—(*continued*).

MN/m²) $\sigma_{min} = 8$ ksi (56 MN/m²) for two other specimens grown at the same speed. This suggests that although the mean stress was lower for specimen *AO* than for any other ordered specimen, the total stress range of 60 ksi (420 MN/m²) was sufficient to cause failure in a relatively short time span. Considerably more testing will be necessary to establish the importance of mean stress on fatigue life in this alloy.

Crack Paths

Ordered specimens fractured with a much more irregular surface topography than did disordered specimens. Extensive interphase delamination was noted in ordered specimens, particularly for slow growth speeds (see Fig. 2*a*). Note that the crack path is segmented with periodic diversion along interphase boundaries. Also, cracking in the lighter etching Ag_3Mg phase seems to occur along crystallographic planes (Fig. 2*b*). Delamination was noted also in disordered specimens, but only infrequently and on a very small scale near the overload portion of the failure. More usually, the crack path in disordered specimens was not parallel to the lamellae, as may be seen in detail in Fig. 3. Note that lamellae in adjacent eutectic grains are not parallel indicating that this

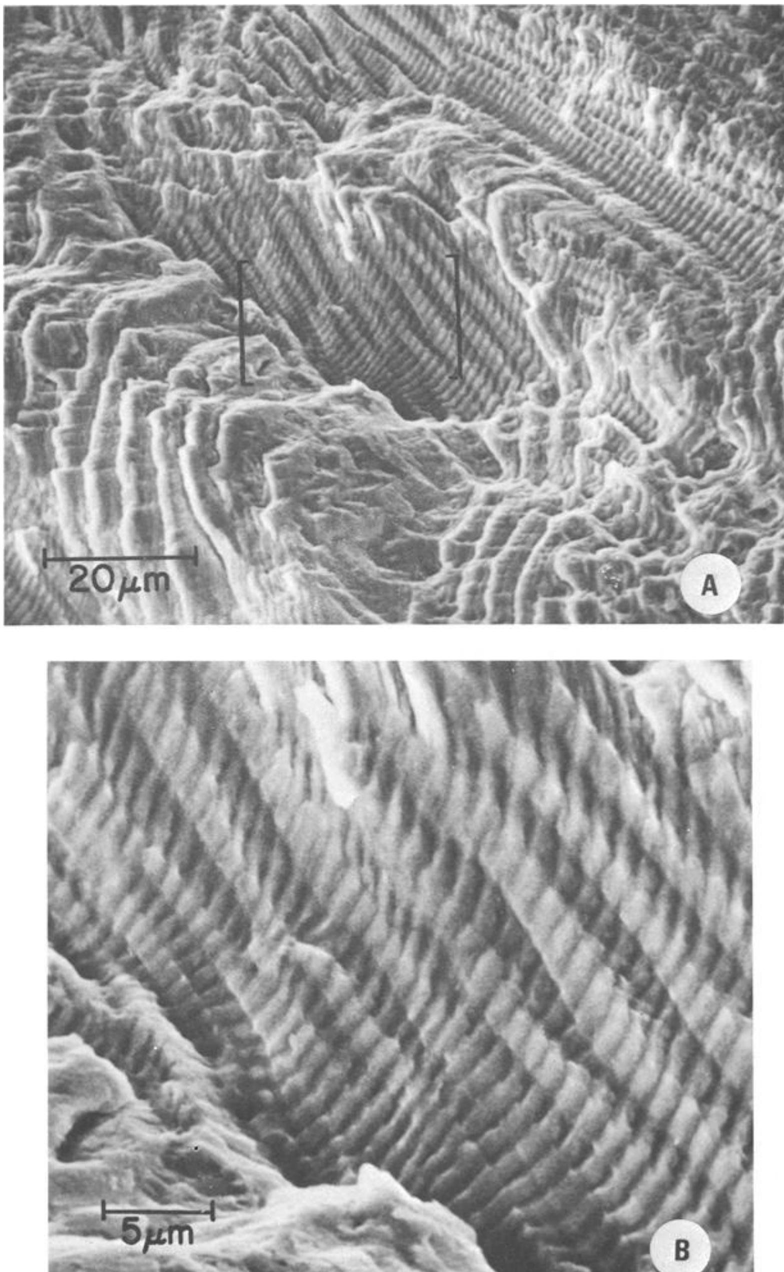

FIG. 5—*Fracture surface of disordered specimen* 6BD, R = *27.7 cm/h:* (a) *striations, general view,* ×*1000;* (b) *striations, magnified view of region* (a), ×*3000; and,* (c) *dimples in tensile overload region,* ×*2000.*

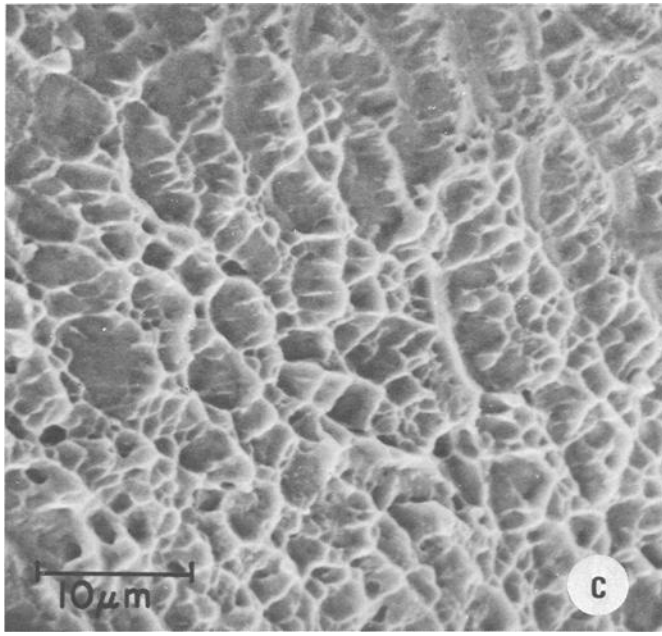

FIG. 5—(*continued*).

material is not perfectly aligned. The crack changes direction across eutectic grain boundaries in such a way as to remain nearly perpendicular to the lamellar axis in each grain. Secondary cracking in disordered specimens was relatively rare, precluding detailed observation of crack paths relative to the microstructure.

Fractographic Observations

The most notable feature on fracture surfaces of disordered specimens was the long, continuous striations which were essentially undiverted by interphase boundaries. Examples are found in Fig. 4*a* for $R = 6.9$ cm/h, and Fig. 4*b* for $R = 27.7$ cm/h. Both specimens exhibit striations which cross neighboring lamallae at approximately 90 deg. However, instances were occasionally noted where striations appeared nearly parallel to interphase boundaries, Fig. 4*c*. The morphology of striations is particularly apparent in Fig. 5*a* for a different disordered specimen grown at 27.7 cm/h. The regular striation patterns shown in Fig. 5*a* are viewed at higher magnification in Fig. 5*b*. Finally, for comparison, a portion of the tensile overload fracture surface is shown in Fig. 5*c*. Dimples are clearly visible but the underlying lamellar structure is not

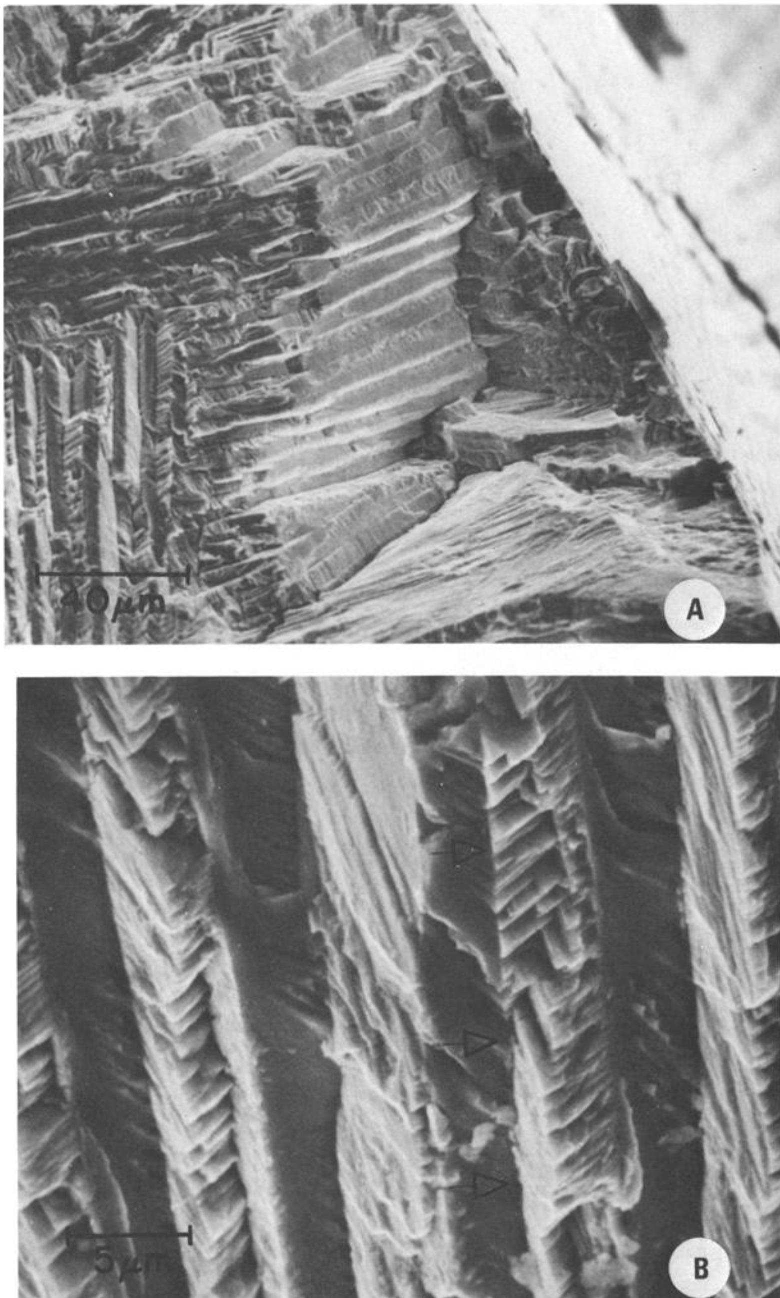

FIG. 6—*Fatigue fracture surface of ordered specimen* MB-*1*, R = *3.5 cm/h:* (a) *general view near specimen edge, revealing stepped fracture, ×500;* (b) *slip band cracking at arrows, ×3000; and,* (c) *slip steps, ×5000.*

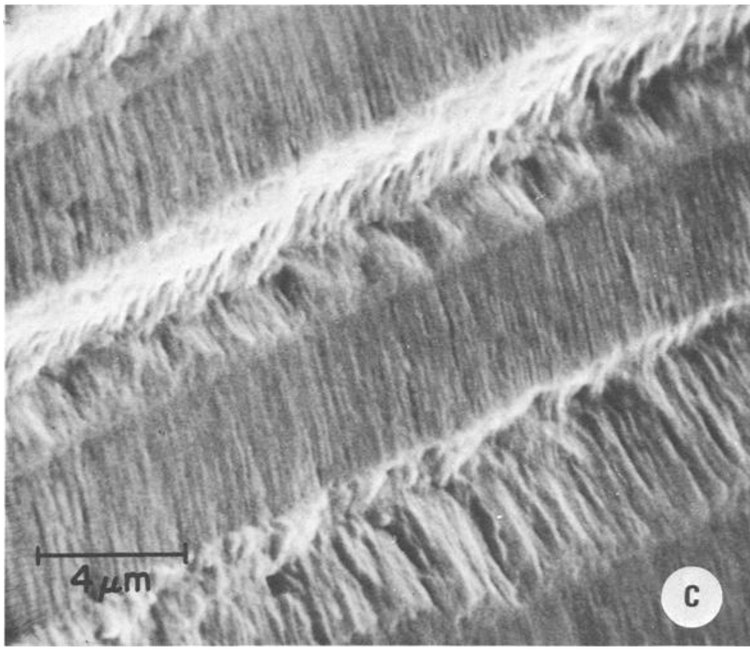

FIG. 6—(*continued*).

visible, indicating that interphase boundaries are not obstacles under the high monotonic strain conditions in microvoid coalescence.

A tendency for interphase delamination in both the fatigue region and the tensile overload region of ordered material was apparent, as in specimen *MB*-1 grown at 3.5 cm/h and which failed after 1.1×10^5 cycles. The fatigue region of specimen *MB*-1 is shown in Fig. 6*a* at low magnification and Fig. 6*b* at high magnification. The stepped nature of the fracture surface is apparent in Fig. 6*a* (fatigue regions of disordered specimens were relatively flat), indicating branching of the primary crack parallel to some lamellae or to eutectic grain boundaries. Figure 6*b* shows a near region of the same specimen but there are no visible striations, although there is evidence of some stepped form of fracture, probably along active slip planes within one of the phases. Elsewhere on the same fracture surface, evidence for faint slip was obtained (see Fig. 6*c*).

The discontinuous nature of markings in ordered material is revealed again in Fig. 7*a*, for sample *AO* grown at 6.9 cm/h and cycled between limits of +50 ksi and −10 ksi (350 and −70 MN/m²). The surface appears to be covered with slip markings and slip band cracks. However, in a few isolated instances, long striations were observed, Fig. 7*b*.

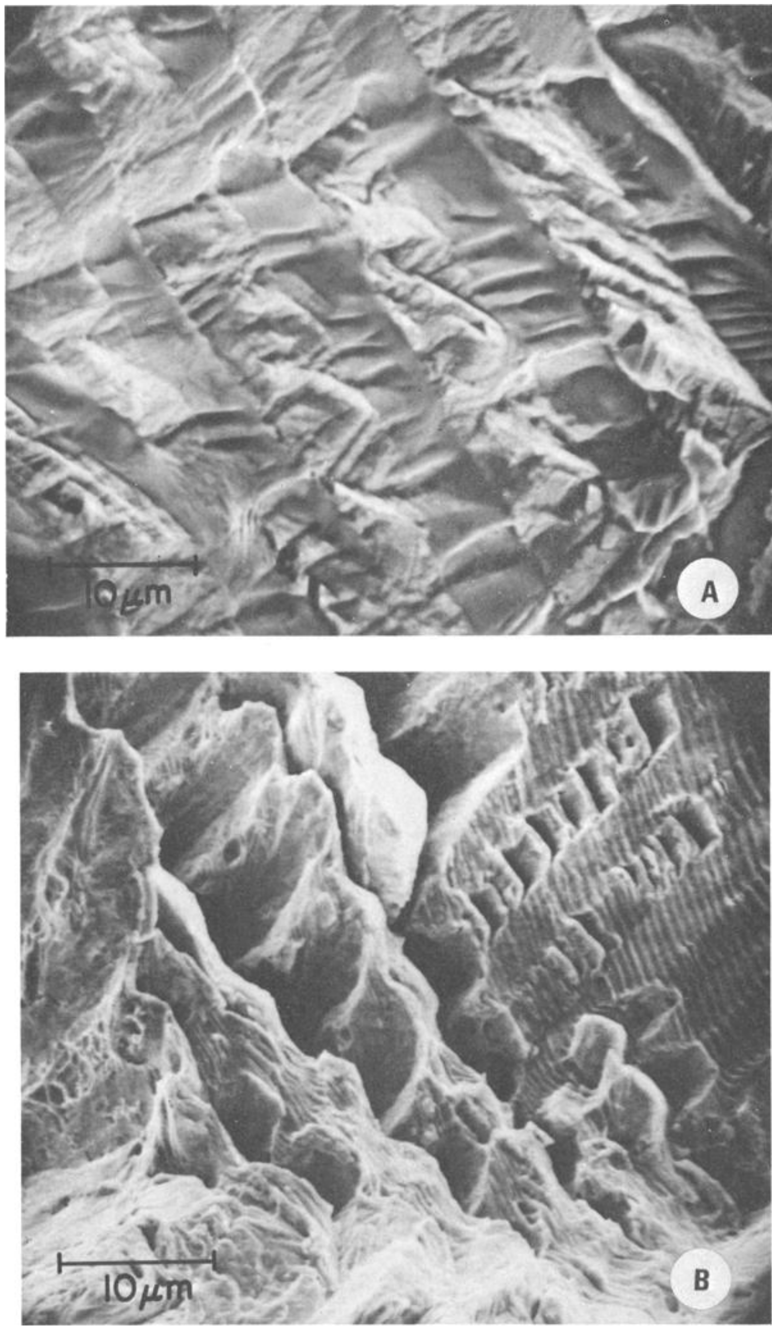

FIG. 7 — *Fracture surface of ordered specimen* AO, R = *6.9 cm/h,* ×*2000:* (a) *Stage I crack propagation; and,* (b) *striations.*

Discussion

The data summarized in Table 1 clearly indicate that long range order in the Ag-27 percent Mg phase produces a marked improvement in fatigue resistance of the eutectic alloy. Table 1 and Fig. 1 also demonstrate that refinement of the microstructure has a similar beneficial effect. Previous studies of growth speed effects in the fatigue of eutectics seems to have been done only on the Al-Al_3Ni and Al-$AlCu_2$ systems in the low cycle range [*4*]. Neither material revealed any effect of growth speed on life for speeds in the range 0.3 to 11 cm/h. In this range there is little change in yield strength for either alloy. Recent work at our laboratory has demonstrated, however, that increasing the growth speed to 25 cm/h *does* increase fatigue life of an Al-Al_3Ni eutectic alloy at several cyclic stress levels [*5*]. It appears, then, that while there may be no inherent effect of growth speed on fatigue life, it is possible to achieve appreciably higher fatigue lives in both fibrous and lamellar eutectics by suitable control of interphase spacings.

The explanation of ordering effects on fatigue life is not so direct. Previous work has revealed that slip character in the Ag-27 percent Mg phase changes from wavy to planar as long range order is produced [*10*]. The fractographs shown in this paper reveal a change in fatigue crack topography and striation morphology with order; striations being profuse, continuous and relatively undistorted for disordered material, and infrequently seen; and then restrained at interphase boundaries in ordered specimens. If interphase boundaries are more effective barriers to fatigue crack propagation when Ag-27 percent Mg is ordered, an increased fatigue life would be expected. However, another possible contributing factor to increased life is the increased tendency for interphase delamination of ordered material, Figs. 2*a* and 6*a*, leading to diversion of the crack from the shortest path across the specimen. Further work is required to establish the most critical of the three possible mechanisms for enhanced fatigue resistance in ordered material: yield stress increase, restricted propagation, and branching.

With regard to the fractographic observations made in this work, it is pertinent to recall the work of Hoover and Hertzberg [*11*] on the lamellar eutectic Ni-Ni_3Cb. At low and intermediate stresses (lives to 20 000 cycles) that alloy revealed fatigue striations which tended to lie parallel to, or to approach parallelism with, the interphase boundaries. At lower stress levels, the nickel matrix failed in a faceted manner somewhat similar to the behavior noted in ordered Ag_3Mg-AgMg, Fig. 6*b*. This faceted appearance also has been observed in the nickel base superalloy Mar M200 and has been attributed to Stage I fatigue crack growth along active slip planes [12,13]. There was clear evidence in the present work, Fig. 2, of crack growth in ordered specimens at about 45 deg to the stress axis along active slip planes. Consequently, it appears that fatigue crack growth in ordered Ag_3Mg-AgMg tends to occur in Stage I, with the overall crack propagation rate probably controlled in part by interface decohesion (crack blunting at interfaces). This behavior would account for the relatively few instances of striations in ordered material, since striations are more usually associated with Stage II growth at approximately 90 deg to the stress axis.

The absence of evidence for slip band cracking in disordered material, either on external surfaces or on fracture surfaces, is consistent with the wavy, diffuse slip mode of disordered Ag_3Mg [10]. The profuse striations observed on disordered material (Figs. 4 and 5), together with the tendency for the primary crack to lie perpendicular to the surface traces of the lamellae (Fig. 3), suggest, instead, that cracking proceeds largely in Stage II.

Summary and Conclusion

1. The fatigue life of Ag_3Mg-AgMg becomes progressively greater with an increase of growth rate and the occurrence of long range order in the Ag_3Mg phase.
2. The growth speed effect appears to arise from increased tensile strength of the eutectic with a decrease in the interlamellar spacing.
3. Long range order changes slip character and fracture surface morphology in such a manner as to suggest that cracking proceeds continuously in Stage I, the process being interrupted only at interphase boundaries. Cracking in disordered material, on the other hand, occurs as a Stage II process.
4. Cracking along interphase boundaries is a prominent feature of fatigue of ordered material.

Acknowledgments

We are grateful to M. Badawy for assistance with the experimental program and to D. Duquette for helpful discussions. This work was supported by the Office of Naval Research under Contract No. N00014-67-A-0117-0010, NR031-745.

References

[1] Shaw, B. J., *Acta Metallurgica*, Vol. 15, 1967, p. 1169.
[2] Hertzberg, R. W., Lemkey, F. D., and Ford, J. A., *Transactions*, The Metallurgical Society of the American Institute of Mining, Metallurgical, and Petroleum Engineers, Vol. 233, 1965, p. 342.

[3] Cline, H. E. and Stein, D. F., *Transactions,* The Metallurgical Society of the American Institute of Mining, Metallurgical, and Petroleum Engineers, Vol. 245, 1969, p. 841.
[4] Salkind, M. J., George, F. D., Lemkey, F. D. and Bayles, B. J., Final Report: Contract No. w-65-0384-d, United Aircraft Research Labs. (AD633241), May, 1966.
[5] Maurer, G., Rensselaer Polytechnic Institute, unpublished work.
[6] Kim, Y. G. and Stoloff, N. S., *Metallurgical Transactions,* Vol. 3, 1972, p. 1391.
[7] Bellows, R. H., Kim, Y. G., Stoloff, N. S., *Proceedings,* Conference on *In-Situ* Composites, Vol. 2, 1972, p. 121.
[8] Hansen, M. *Constitution of Binary Alloys,* McGraw-Hill, N. Y., 1958, p. 278.
[9] Gangulee, A. and Bever, M. B., *Transactions,* The Metallurgical Society of the American Institute of Mining, Metallurgical, and Petroleum Engineers, Vol. 242, 1968, p. 278.
[10] Kim, Y. G. and Stoloff, N. S., *Metallurgical Transactions*, Vol. 5, 1974, p. 809.
[11] Hoover, W. R. and Hertzberg, R. W., *Metallurgical Transactions*, Vol. 2, 1971, p. 1289.
[12] Gell, M. and Leverant, G. R., *Transactions*, The Metallurgical Society of the American Institute of Mining, Metallurgical, and Petroleum Engineers, Vol. 242, 1968, p. 1869.
[13] Gell, M. and Leverant, G. R., *Acta Metallurgica,* Vol. 16, 1968, p. 553.

H. T. Sumsion[1] *and D. P. Williams*[1]

Effects of Environment on the Fatigue of Graphite-Epoxy Composites

REFERENCE: Sumsion, H. T. and Williams, D. P., "**Effects of Environment on the Fatigue of Graphite-Epoxy Composites,**" *Fatigue of Composite Materials, ASTM STP 569,* American Society for Testing and Materials, 1975, pp. 226–247.

ABSTRACT: Torsional and flexural fatigue tests were performed on both uniaxial (0°) and crossplied (±45°) graphite-epoxy materials at temperatures of 24 and 74°C in environments of air and water. The results of the torsion testing showed that the number of cycles required to cause an initial decrease in stiffness as well as the rate of stiffness loss was a function of temperature and environment; the most significant losses were noted for tests at the higher temperature in water. The torsional fatigue specimens were subsequently tested in four-point bending to determine the effect of torsional damage on longitudinal properties. This damage caused changes in the flexural stiffness, failure stress, and failure energy, depending on the stress and environmental histories. The flexural fatigue tests also showed a significant effect of water (at 24°C) on the material behavior. These results are compared with the results of previous investigations and are discussed in terms of proposed damage mechanisms.

KEYWORDS: composite materials, fatigue tests, environmental tests, nonmetallic coatings

The time-dependent structural integrity of primary structural materials for aeronautical applications must be extremely well characterized. If advanced composites are to find general application in aircraft structures, these materials must demonstrate properties that are relatively predictable over long periods under expected use conditions. Therefore, tests on structural composites must be performed under conditions of aeronautical cyclic loading and in a variety of adverse service environments to determine if this class of materials has sufficient long-time integrity to be considered an important candidate for application in critical aircraft structures.

Most of the available data on the long-time fatigue properties of com-

[1] Research scientist and chief, Materials Science Branch, respectively, Ames Research Center, NASA, Moffett Field, Calif. 94035.

posites is highly encouraging in that it generally suggests that these materials are less prone to fatigue damage than engineering alloys. For example, both Beaumont and Harris [*1*] [2] and Owen and Morris [*2*] show that, under repeated pure tension loading, carbon-polyester composites exhibit no fractures in 10^7 cycles for stress levels less than 0.9 of the static failure stress (σ_f). Both studies also show that the materials behave well under flexural loading; failure occurs in 10^7 cycles only at flexure stresses above $0.6\sigma_f$. Additionally, the work of Beaumont and Harris indicates that neither the tensile nor the flexural fatigue lives were significantly affected by the test environments (100°C steam and vegetable oil at 100°C). However, these results, as well as the results of most other fatigue studies, give information on just one possible failure mode of the composite material, namely, failure by separation (fracture). Moreover, these good fatigue properties were noted when the only stress component was applied parallel to the direction of the reinforcing fibers. On actual aircraft applications, failure may occur by some mechanism other than separation (fracture) and pure uniaxial loading parallel to the fibers is not likely to occur. Many aircraft structures are "stiffness critical," that is, the stiffness of the component controls the design. Therefore, a significant loss in material stiffness due to repeated cycling (or environmental exposure) would constitute failure of this type of component. Moreover, it is well known that aerodynamic loads cause complex fluctuating stress fields that will surely have components in directions not parallel to the reinforcing fibers. While these secondary stresses may have relatively little effect on the overall fatigue failure behavior of isotropic metal alloys, they may contribute significantly to the failure properties of anisotropic composites. Additionally, the environment may have a significantly different effect on the off-axis properties of composites than on the properties in a directional parallel to the fiber reinforcements.

Beaumont and Harris [*1*] suggest that, in fact, carbon-fiber-reinforced composites did reduce the stiffness significantly under cyclic loading, especially when subjected to off-axis loads. Moreover, they found that materials exposed to moisture environments before testing were more sensitive to subsequent cyclic loading. They related the observed effects of both cyclic loading and environment to damage within the matrix material. These results suggest that, under anticipated aircraft conditions, structures of composite materials might be subject to failure because of fatigue and such failures might be sensitive to the environment.

To better characterize the effects of environment on the fatigue prop-

[2] The italic numbers in brackets refer to the list of references appended to this paper.

erties of typical advanced composite materials, both flexural fatigue and torsional fatigue of carbon-fiber-reinforced composites were studied in air and water environments. The intent of these initial studies was to: (1) verify the observations of Beaumont and Harris concerning the effects of cyclic, off-axis loads and environment on the stiffness of carbon-reinforced composites; (2) determine the relative effects of environment on the torsional versus flexural fatigue characteristics; (3) compare the relative effects of pretest exposure to moisture with those caused by exposure during the test; and, (4) compare the effects of moisture on the properties of uniaxial composites with those observed on crossply material.

Experimental

The material used in this investigation was formed from Hercules prepreg tapes containing 60 percent volume fraction (V_f) H fibers[3] in Hercules AS/3501 resin system. Fiber properties as given by the producer were UTS 448.3×10^3 psi (3.09 GN/m^2), modulus 32.27×10^6 psi (222.5 GN/m^2), and density 0.06514 lb · $in.^3$ (1.803 g/cm^3). The specimen stock was made by Lockheed Missiles and Space Corporation in the form of both 0 and ±45 deg sheets, approximately 1/8 in. thick (0.3 cm). The method of preparation was as follows. Release film was placed against a tool surface, followed by a peel ply of perforated glass Teflon. Then, 24 layers of fiber tape were placed per orientation requirement (for the ±45 deg material, 12 layers of ± layup, followed by 12 layers of ∓ layup) with 1 layer of bleeder cloth[4] for every 4 layers of tape. The layup was placed in bagging material and autoclaved at 100 psi (689.5 KN/m^2) and 350°F (117°C) for 2 h. The resulting sheets were then cut into specimen blanks that were finally machined into specimens having the dimensions indicated in Fig. 1*a* and *b*. The specimens with the parallel gage section were used for the torsion and four-point bend testing while the "dogbone" specimens were used for flexural fatigue. Thickness of both types was approximately 1/8 in.

Torsional fatigue tests were conducted at a frequency of about 1 Hz under conditions of controlled torsional strain. In these tests, the torque was monitored by a torque cell while the specimen was undergoing cyclic strain and was recorded periodically on a high-speed strip-chart recorder. In addition to the periodic recording of the torque, full hysteresis curves were recorded at intervals during the test. The cyclic deflection was set at the beginning of the test and was maintained constant, thereafter. The tests were continued until the torque had decreased to some predeter-

[3] manufactured by Fiberite Corporation.
[4] Mochburg paper or style 120 cloth.

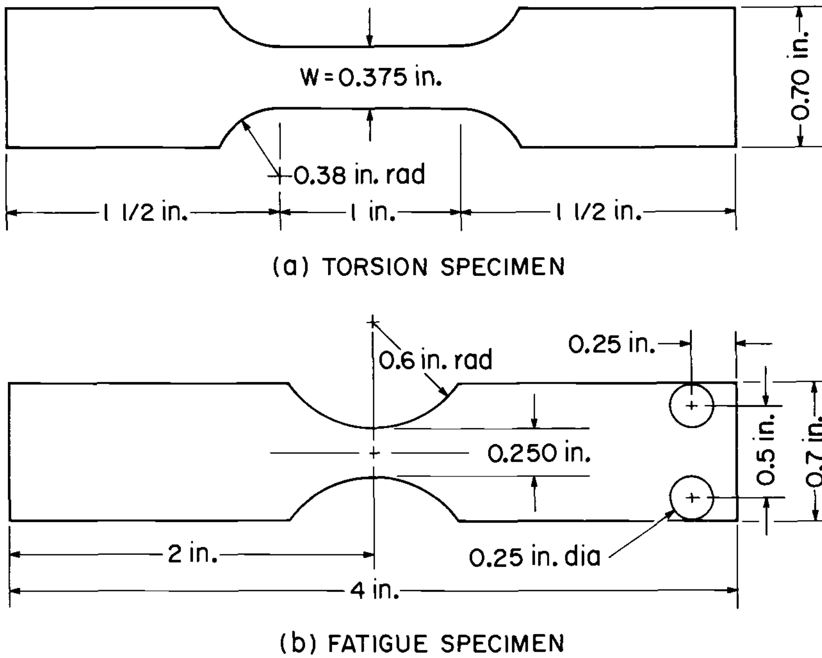

FIG. 1—*Test specimens.*

mined level or until a sufficient number of stress cycles was reached. For the torsional fatigue tests performed in water or at elevated temperatures or both, a controlled temperature chamber was installed in the load frame and a liquid container was fitted around the specimen. At elevated temperatures, the chamber heaters were used to heat the loading rods, the water or air, and the specimen. The temperature of the specimen was monitored with a thermocouple located adjacent to the specimen in the water bath or in air. Some of the specimens tested in water were exposed to water for a four-week period or longer before the test. In all cases, this pretest exposure was conducted at ambient temperatures.

After the torsional fatigue tests were completed, the specimens were subjected to a four-point bend test (to failure) using a hydraulic testing machine. The bend tests were conducted at room temperature to measure the residual longitudinal strength of the specimens and, therefore, were performed with a span-to-depth ratio of 32:1. Specimens that had been torsion-tested in water were stored in water before bend testing. Data were obtained in the form of bend load versus deflection curves from which failure energies (γ_f) could be calculated as the area under the curve divided by twice the cross-sectional area of the specimen gage section [1]. Failure energy is identified as that determined from the area under the curve for deflections up to the first significant load drop.

The flexural fatigue studies were performed on a standard commercial fatigue machine in cyclic, fully reversed, plane bending under constant maximum load (frequency of 30 Hz). The machine was modified by the addition of a second limit detector, designed to terminate the test when the specimen deflection at the free end exceeded the initial value by 50 percent. This 50 percent increase in deflection (decrease in stiffness) was then defined as the failure point for the test. Some specimens were tested in water by taping a small amount of absorbent cotton around the gage section. The cotton was moistened with distilled water before the test began, and this environment was maintained throughout the test by dripping water onto the cotton.

Results

The results of the torsional fatigue tests are shown in Figs. 2–7. These results are presented as curves that show instantaneous specimen stiff-

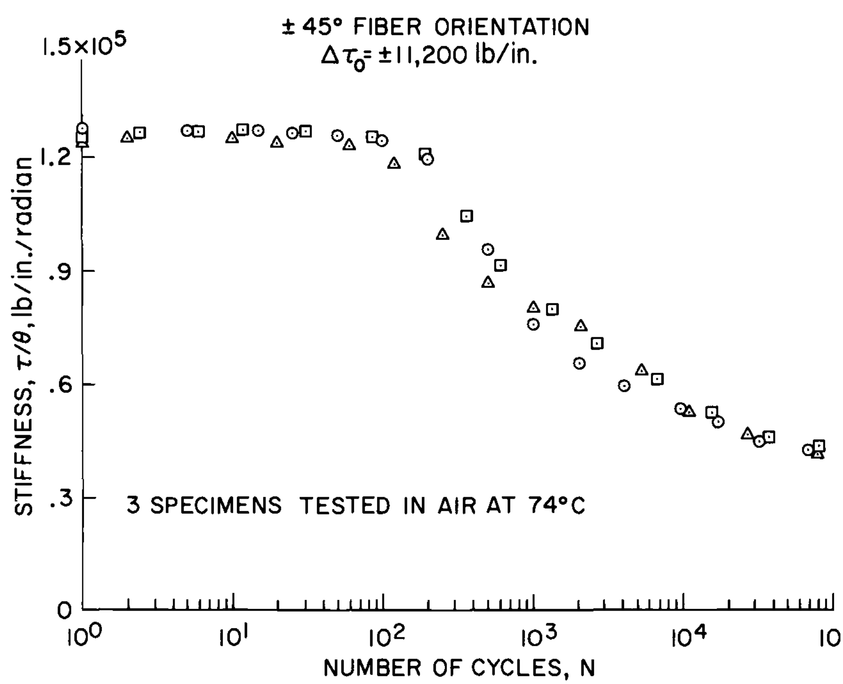

FIG. 2—*Torsion fatigue of ±45 deg fiber-oriented graphite-epoxy composite specimens. Decrease in stiffness* (τ/θ) *with number of cycles* (*log* N) *of three specimens tested in air at 74°C.*

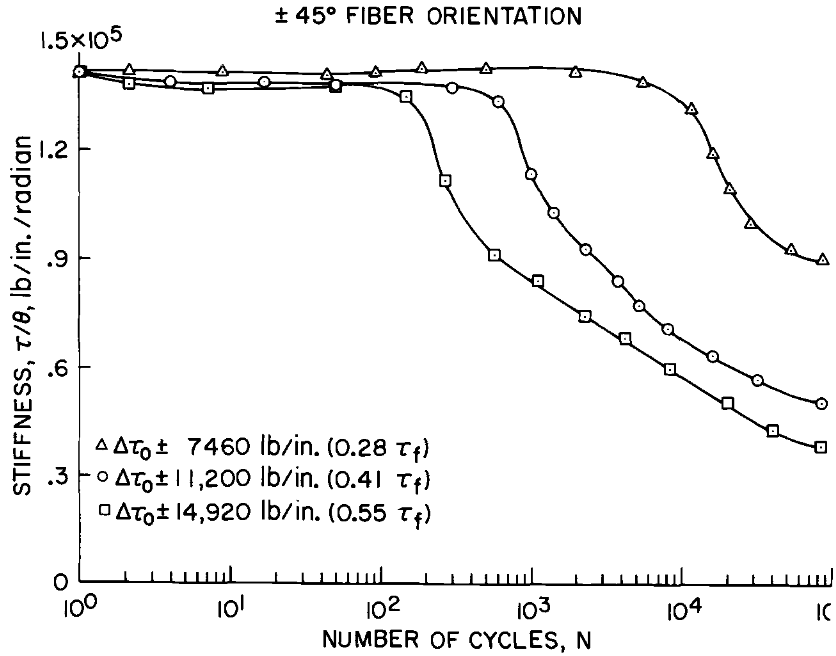

FIG. 3—*Torsion fatigue of ±45 deg fiber-oriented graphite-epoxy composite. Decrease in stiffness* (τ/θ) *with number of cycles* (*log* N) *as a function of initial applied stress* (τ_0).

ness, τ/θ, as a function of the number of applied stress cycles, where τ is the maximum applied shear stress [*3*] and θ is the torsional deflection in radians per unit length. Figures 2–5 show the results obtained on ±45 deg material and Figs. 6 and 7 are for 0 deg material. In all cases, the curves shown are taken from one of three specimens tested under identical conditions. An example of the good agreement between the triplicate tests is shown in Fig. 2. Because of the small scatter shown here and observed under all test conditions, an individual curve could represent the test results for any particular test condition.

Figure 3 indicates the effect of the initial torsional stress on the torsional fatigue behavior of crossplied (±45 deg) material. For each of the three initial stress levels studied, the material undergoes a decrease in stiffness on cycling. For tests at the lowest initial shear stress, $\pm\tau_0$ of 7460 psi (51.5 MN/m^2) — $\pm\tau_0 \approx 0.28$ of the static torsional fracture stress, (τ_f), the material appears to withstand greater than 10^3 stress cycles before experiencing any decrease in stiffness. With further cycling, the stiffness does, however, decrease until, at 10^5 cycles, the stiffness is decreased to about 60 percent of the initial value. Since these tests were

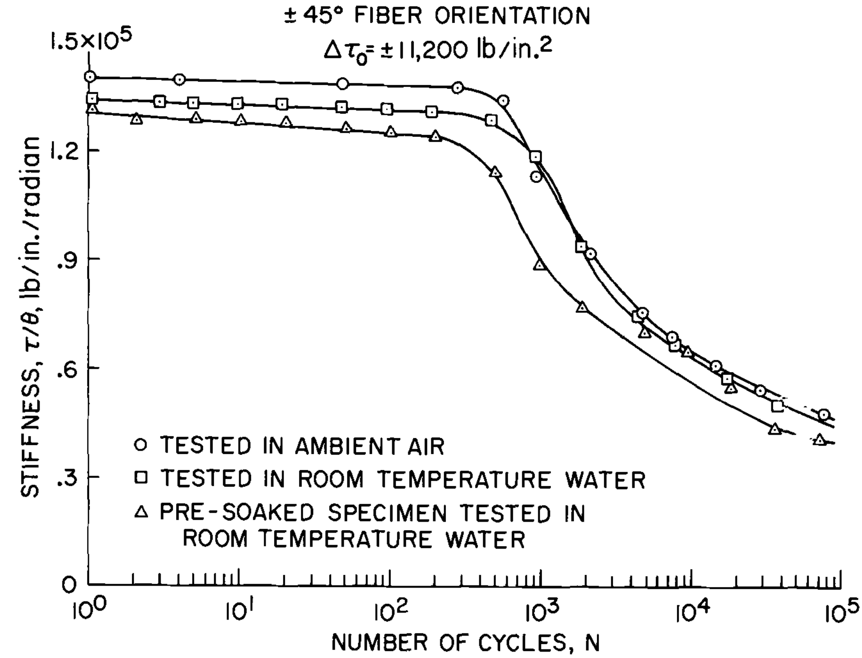

FIG. 4—*Torsion fatigue of* ±*45 deg fiber-oriented graphite-epoxy composite. Decrease in stiffness* (τ/θ) *with number of cycles* (*log* N) *as a function of environment and specimen history.*

performed under conditions of constant torsional deflection, this means that, in 10^5 cycles, the torsional stress decreases to about 60 percent of the initial value, that is, to $0.17\tau_f$. This curve indicates a "fatigue limit," namely, a limiting stress below which no further decreases in stiffness occur. However, since all tests were terminated at 10^5 cycles, it is not known if this behavior continued. The other two curves on Fig. 3 are for specimens stressed to $\pm\tau_0$ values of 11 200 psi (77 MN/m^2) ($0.41\tau_f$) and 14 920 psi (103 MN/m^2) ($0.55\tau_f$). For these specimens, the stiffness began to decrease after about 3×10^2 and 1×10^2 stress cycles, respectively. The stiffness of the specimen initially loaded to $0.41\tau_f$ decreased to about 36 percent of the initial value (τ decreased to about $0.15\tau_f$), and the stiffness of the specimen initially loaded to $0.55\tau_f$ decreased to about 26 percent of the initial value (τ decreased to about $0.16\tau_f$). The indication that the three specimens loaded to different initial stress levels are approaching a fatigue limit or condition of constant stress level suggests that this parameter may control the rate of accumulation of damage after many cycles.

Figure 4 compares the effect of water and air at room temperature (24°C) on crossplied ±45 deg material cycled at an initial stress, $\pm\tau_0$, of 11 200 psi (77 MN/m^2) ($0.41\tau_f$). The curve shown for air is the same as shown for the $\pm\tau_0 =$ 11 200 psi (77 MN/m^2) value in Fig. 3. Of the two specimens tested in water, one had been previously exposed to water at ambient temperature for four weeks, while the other had been maintained in a dry environment. As can be seen, the fatigue behavior was only slightly dependent on the environmental history, inasmuch as the specimen stored in the dry environment withstood somewhat more fatigue cycles before the onset of damage than the specimen stored in water. Both specimens tested in water had a somewhat lower initial stiffness than the specimen tested in air; however, in all other ways, the specimen that had been stored in air and cycled in water appeared identical to the specimen tested in air.

Tests were also run on ±45 deg material at 74°C (165°F) in air and water. For all tests in water at 74°C, the specimens had been presoaked in water at room temperature for four weeks. As can be seen in Fig. 5 (in comparison to the results shown in Figs. 3 and 4), the effect of temper-

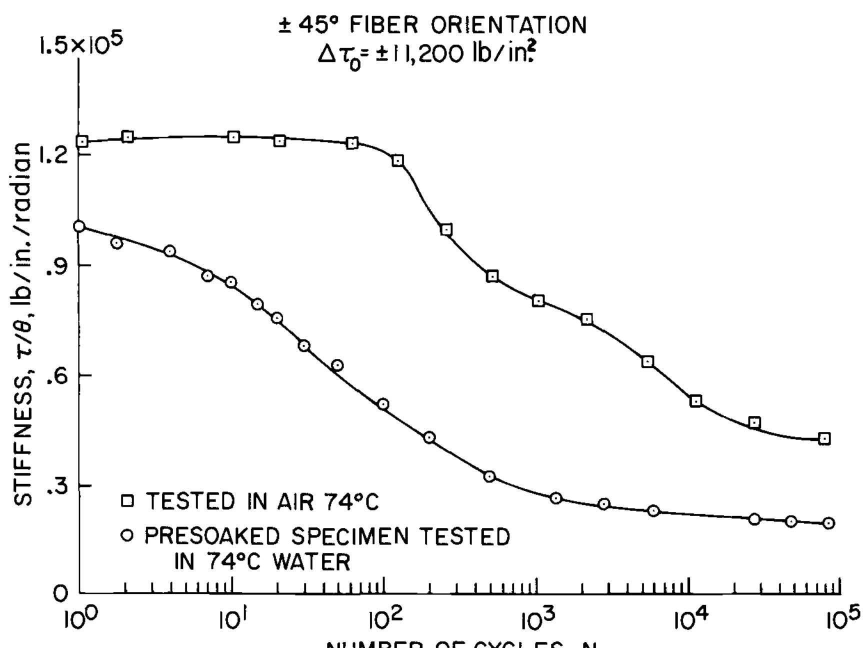

FIG. 5—*Torsion fatigue of ±45 deg fiber-oriented graphite-epoxy composite. Decrease in stiffness* (τ/θ) *with number of cycles* (*log* N) *as a function of temperature and water.*

ature is to decrease the initial stiffness of the material in both air and water, decrease the number of cycles before the onset of damage, and decrease the final stiffness after 10^5 cycles. The decrease in the initial stiffness of the presoaked specimen tested in water is especially noticeable being 20 percent less than the stiffness of the specimen tested in air at the same temperature and 24 percent less than the stiffness of the presoaked specimen tested in water at room temperature (Fig. 4).

Figures 6 and 7 show the torsional fatigue behavior of unidirectional (0 deg) material. This unidirectionally oriented material had an initial torsional stiffness about 50 percent lower than the ±45 deg material. Additionally, the 0 deg material exhibited a static torsional failure strength considerably lower than the torsional failure strength for the ±45 deg material (15 800 psi (103 MN/m²) versus 27 300 psi (188 MN/m²). Figure 6 shows the results of cyclic fatigue tests on 0 deg material at room temperature and at an initial torsional stress of about 5760 psi (40 MN/m²) ($0.36\tau_f$). The results of these tests show a considerably smaller effect of cyclic loading on torsional stiffness for the 0 deg material than was noted for the ±45 deg material (Fig. 4). For the speci-

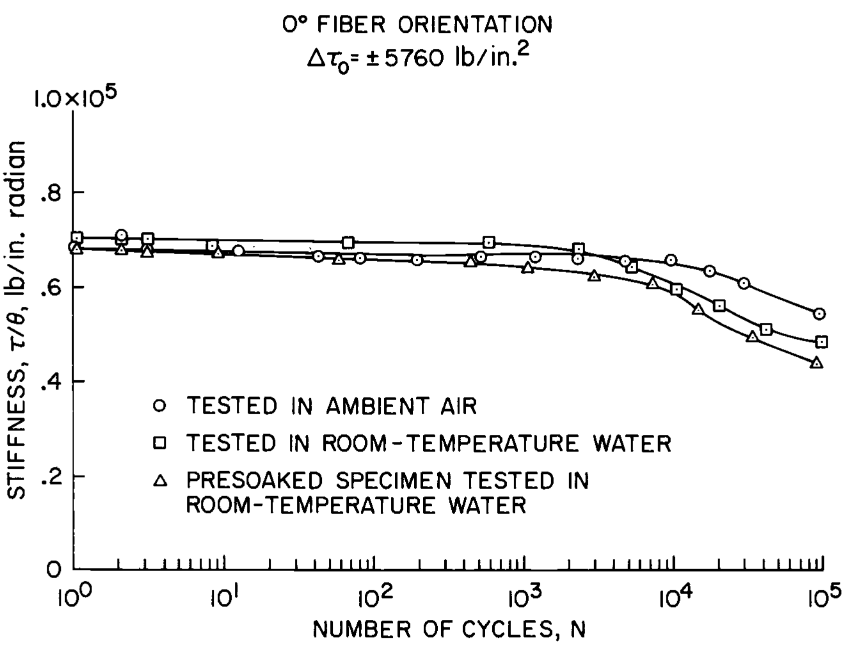

FIG. 6—*Torsion fatigue of 0 deg fiber-oriented graphite-epoxy composite specimens. Decrease in stiffness* (τ/θ) *with number of cycles* (*log* N) *as a function of environment and specimen history.*

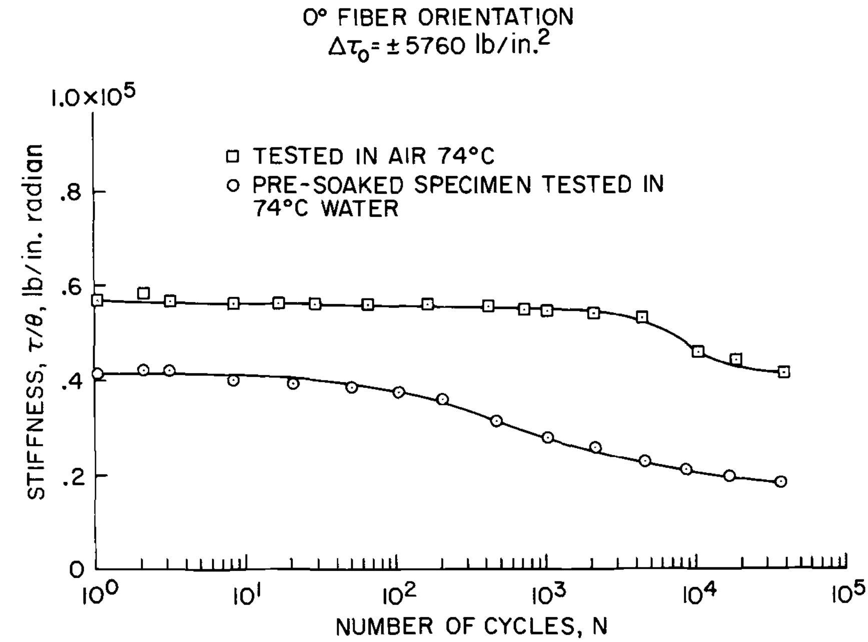

FIG. 7—*Torsion fatigue of 0 deg fiber-oriented graphite-epoxy composite specimens. Decrease in stiffness* (τ/θ) *with number of cycles* (*log* N) *as a function of temperature and water.*

mens tested in air, no decrease in stiffness was noted until the specimens had been subjected to 10^4 stress cycles; after that, the stiffness decreased very slowly. Both the presoaked and the unsoaked specimens tested in water began to decrease in stiffness somewhat earlier than those tested in air; however, they also decreased only slightly for test periods up to 10^5 cycles. No noticeable differences in the behavior of the unsoaked and the presoaked specimens tested in water could be determined.

Figure 7 shows the torsional fatigue behavior of the unidirectional material tested at 74°C in air and water. As for the ±45 deg material, the specimen tested in water at 74°C had been presoaked for four weeks before testing in water at ambient temperature. The effect of temperature on specimens tested in air was about a 20 percent reduction in the initial stiffness; however, the elevated temperatures did not seem to make the material much more prone to fatigue damage. No noticeable decrease in stiffness was noted until approximately 5×10^4 stress cycles had been applied. The most significant effect of testing in water at elevated temperatures is to decrease the initial stiffness, although the damage also appears to initiate at fewer stress cycles and proceed somewhat more rapidly than in air. This decrease in initial stiffness cannot be attributed to either the effect of temperature or the effect of water alone, but, rather, it appears to be a combined effect of the two.

A number of specimens (three specimens each for the various test environments) were tested at room temperature in four-point bending to determine the effect of prior stress and environmental history on the properties of the material in the longitudinal direction. Figures 8*a* and *b* and 9*a* and *b* show examples of the load deflection curves obtained in these bend tests. As shown, torsional stress cycling and environmental exposure can cause changes in such longitudinal material properties as: flexural stiffness; the failure stress in bending (S_{max}), determined from the maximum load; and the failure energy, determined from the area under the load deflection curve for deflections up to that corresponding to the first significant load drop. Maximum failure stresses for uniaxial specimens not previously torsion tested had an average range for the different

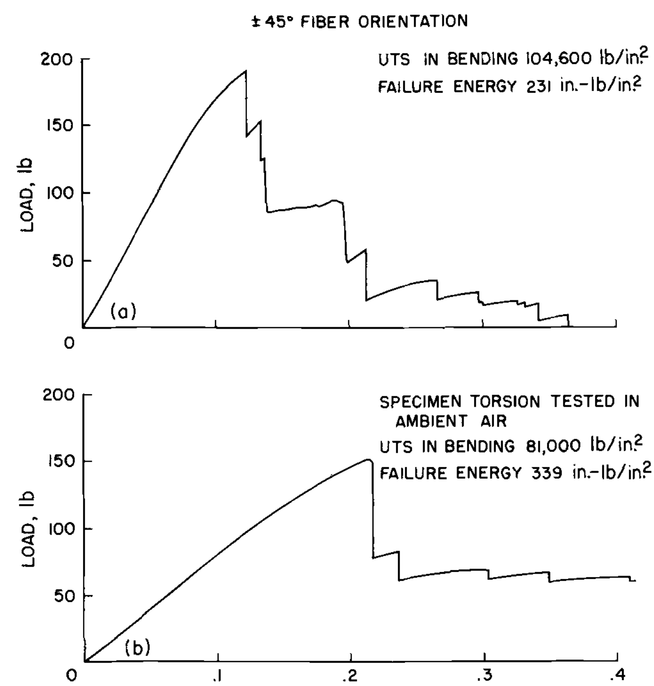

FIG. 8—*Bend tests in ambient air of* ±*45 deg fiber-oriented specimens:* (a) *specimen not previously tested in torsion; and,* (b) *specimen previously torsion-tested in ambient air at* $\Delta\tau_0 = \pm 11\ 200$ *psi (77 MN/m²).*

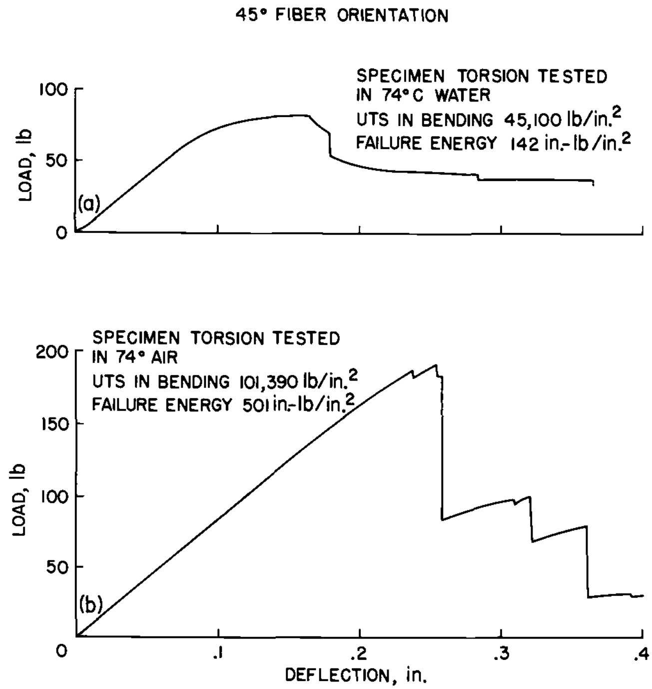

FIG. 9—*Bend tests in ambient air of ±45 deg fiber-oriented specimens:* (a) *specimen previously torsion tested in 74°C water at* $\Delta\tau_0 = \pm 11\ 200$ *psi* (77 MN/m^2); *and*, (b) *specimen previously torsion tested in air at 74°C at* $\Delta\tau_0 = \pm 11\ 200$ *psi* (77 MN/m^2).

test conditions of ±3 percent of the mean with a standard deviation of ±7 percent. Failure energy test results showed similar variations with an average range of ±5 percent and standard deviations of ±7 percent. For crossply material, the failure stress range was ±3 percent, and the standard deviation ±4 percent; the failure energy range averaged ±8 percent, standard deviation ±7 percent. Results of bend tests on specimens which had been torsion tested showed much greater variations than for the non-torsion-tested ones. Failure stress values for uniaxial material had an average range of ±13 percent, failure energy range of ±15 percent. For the crossply specimens, average failure stress ranges were ±8 percent and failure energy range of ±12 percent. Summaries of the failure stresses and failure energies for the ±45 and 0 deg materials are shown in Figs. 10 and 11 and Figs. 12 and 13, respectively. As seen in Fig. 8, torsion testing and the associated loss in torsional stiffness is accompanied by a corresponding decrease in flexural stiffness. Neither the bend test environment nor the pretest environmental history has a significant effect on the failure

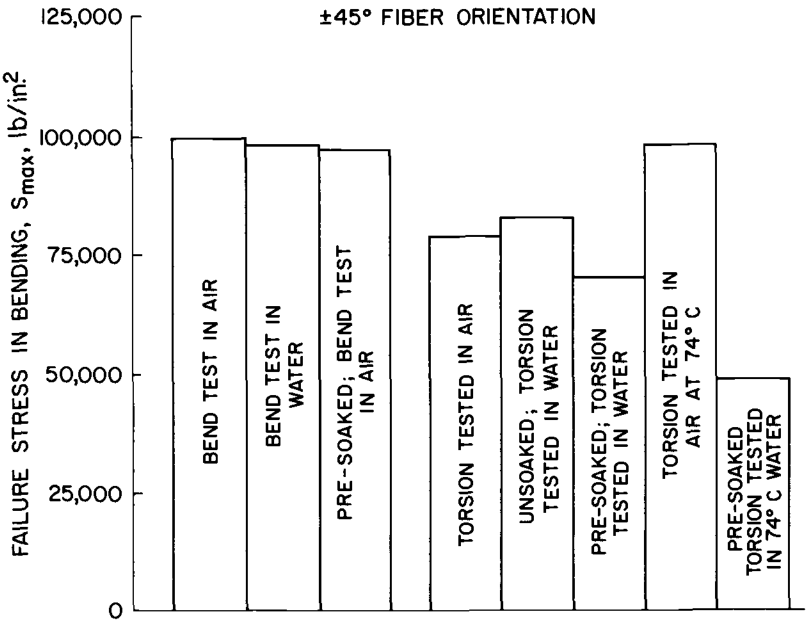

FIG. 10—*Failure stress in bending of ±45 deg fiber-oriented specimens. All bend tests at room temperature; torsion tested at room temperature except as indicated at 74°C.*

stress of the crossplied (±45 deg) material (Figs. 10 and 12). The four week presoak of the 0 deg specimens in water, however, did reduce the failure strength in bending somewhat. Those specimens subjected to cyclic torsional loading showed varying decreases in the failure stress in bending, depending on the torsion test conditions. All the ±45 deg torsion-tested specimens, except those tested in air at 74°C, exhibited a decrease in failure stress, with the specimen tested in water at 74°C showing the largest decrease. All 0 deg specimens subjected to torsional fatigue failed at reduced stresses.

The effect of torsional stress cycling on the failure energy of ±45 and 0 deg material is shown in Figs. 11 and 13, respectively. As shown in Fig. 11, the failure energy of previously unstressed ±45 deg specimens was increased by presoaking in water (at 24°C) for four weeks. This resulted from a decrease in the flexural stiffness of the material with no corresponding decrease in failure stress. The failure energies of all the torsion-tested specimens except those tested at 74°C in water were also observed to increase because of decreases in flexural stiffness. The failure energy of the specimen tested at 74°C in water did not increase, however, because the decrease in failure stress more than compensated for the decrease in flexural stiffness. In contrast to the crossply material, the failure energies of all previously unstressed specimens of 0 deg material were constant (Fig. 13). Moreover, the failure energies of 0 deg specimens that had been stress-cycled in torsion were lower than previously unstressed material because of a reduction in failure stress without a corresponding decrease in flexural stiffness.

Figures 14 and 15 show the results of flexural fatigue tests on unidirectional (0 deg) and crossplied (±45 deg) specimens tested at 24°C in air and water. Figure 14 shows that water reduces the fatigue life by nearly a factor of ten for unidirectional (0 deg) material. This reduction is somewhat larger at low stresses than at high. Over the flexural stress range for which data were obtained ($S_{max} = 41\,000 - 72\,000$ psi) (283 to 496 MN/m^2), no fatigue limit was indicated in either air or water. For crossplied (±45 deg) material (Fig. 15), the test environment has a smaller effect on the flexural fatigue behavior. For stress from 40 000 to 90 000 psi (275 to 620 MN/m^2), the effect of water is to reduce the fatigue life by factors from 3 to 1.5. Again, for this material, no evidence of a flexural fatigue limit was noted.

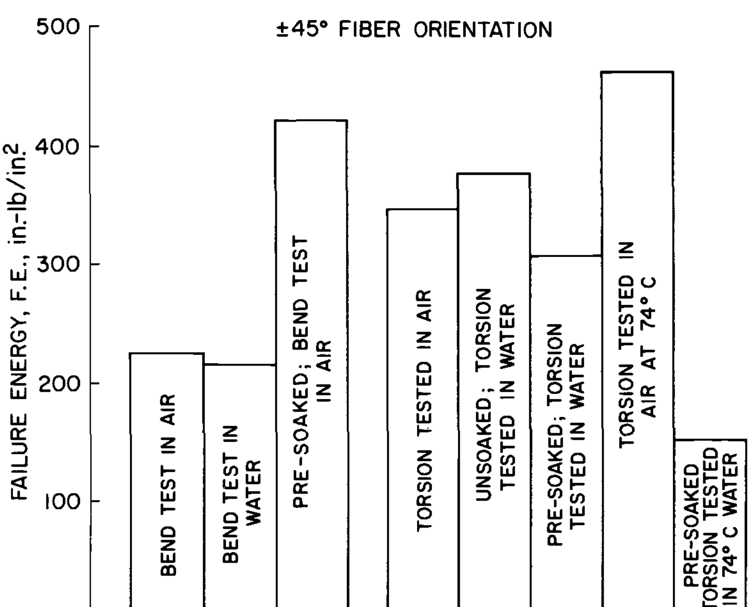

FIG. 11—*Failure energy in bending of ±45 deg fiber-oriented specimens. All bend tests at room temperature; torsion tested at room temperature except as indicated at 74°C.*

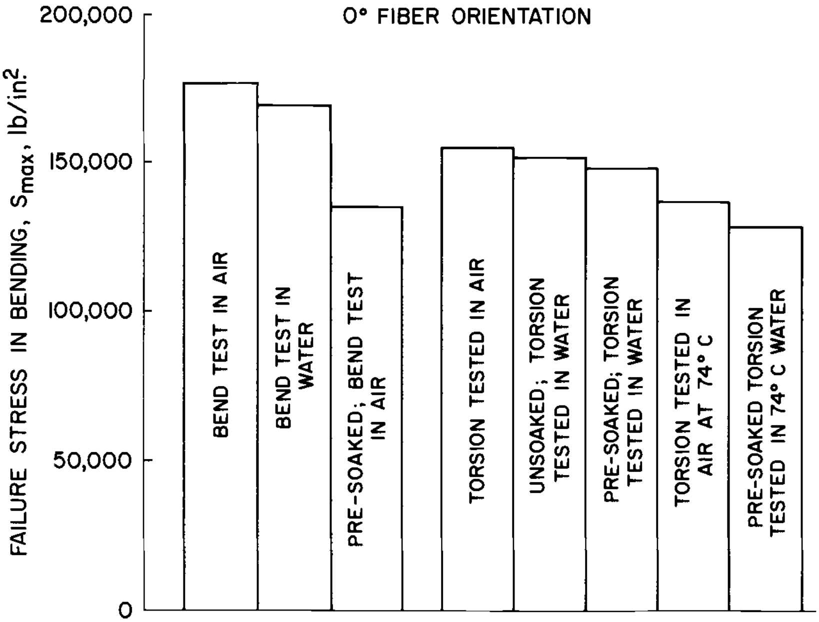

FIG. 12—*Failure stress in bending of 0 deg fiber-oriented specimens. All bend tests at room temperature; torsion tested at room temperature except as indicated at 74°C.*

Discussion

The results of this investigation clearly indicate that graphite-epoxy composite materials are prone to fatigue damage when subjected to cyclic torsional stresses. Since these stresses can be related to more general transverse loading stresses, it is anticipated that aeronautical structures may be subject to cyclic loads of the type used here. The damage caused by the cyclic stresses was distinguished primarily by a reduction in the torsional stiffness (τ/θ) of the material. For specimens of rectangular cross section this stiffness is, of course, related to the shear modulus, G, through the relationship [*4*]

$$\frac{\tau_{\max}}{\theta} = kc\ G$$

in which c is the thickness and k is an empirical constant which is determined by the specimen width-to-thickness ratio. Therefore, the torsional fatigue damage noted can be directly related to reductions in the transvẽrse stiffness of the material caused by cyclic transverse stresses. The importance of these stresses in determining the performance of real composite structures becomes apparent when the (limiting) stress levels required to cause this damage appear to be less than 15 percent of the transverse failure strength (Fig. 3). Since longitudinal failure strength of composites is about 15 times greater than this torsional failure strength, it is apparent that the observed torsional fatigue damage occurred at stress levels less than one percent of the longitudinal failure strength of these materials. Such stress levels are likely to be realized in real two-dimensional and three-dimensional structural components. For this reason, the results of this investigation seem to be of particular importance in evaluating the suitability of composite materials for aerospace applications.

For the most part, the present results are consistent with those of previous investigators. The torsional fatigue characteristics noted are in general agreement with the results of cyclic torsion tests by Beaumont and Harris [*1*] and with the results of interlaminar fatigue studies by Owen and Morris [*2*]. After an (apparently) damage-free period, the crossplied (±45 deg) material was found to undergo a decrease in torsional stiffness with increasing stress cycles. The length of the damage-free period (incubation period) and the rate of damage accumulation (stiffness

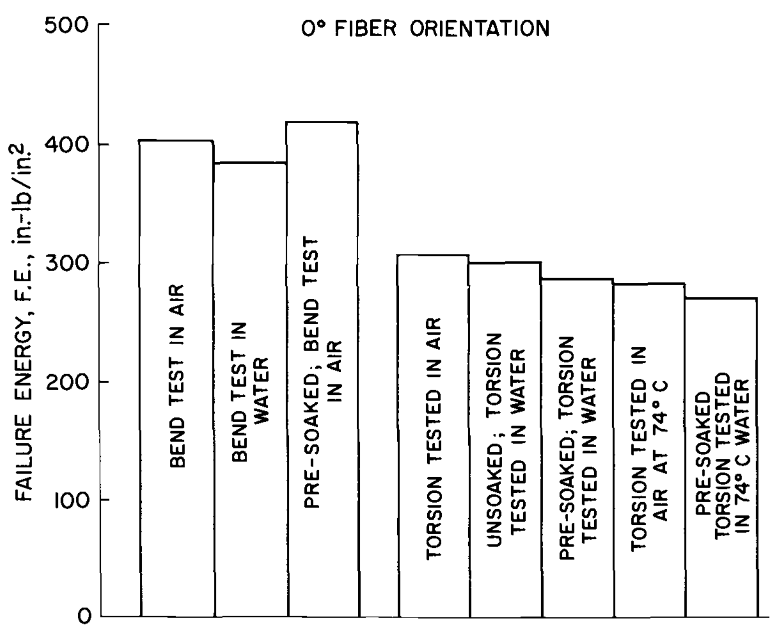

FIG. 13—*Failure energy in bending of 0 deg fiber-oriented specimens. All bend tests at room temperature; torsion tested at room temperature except as indicated at 74°C.*

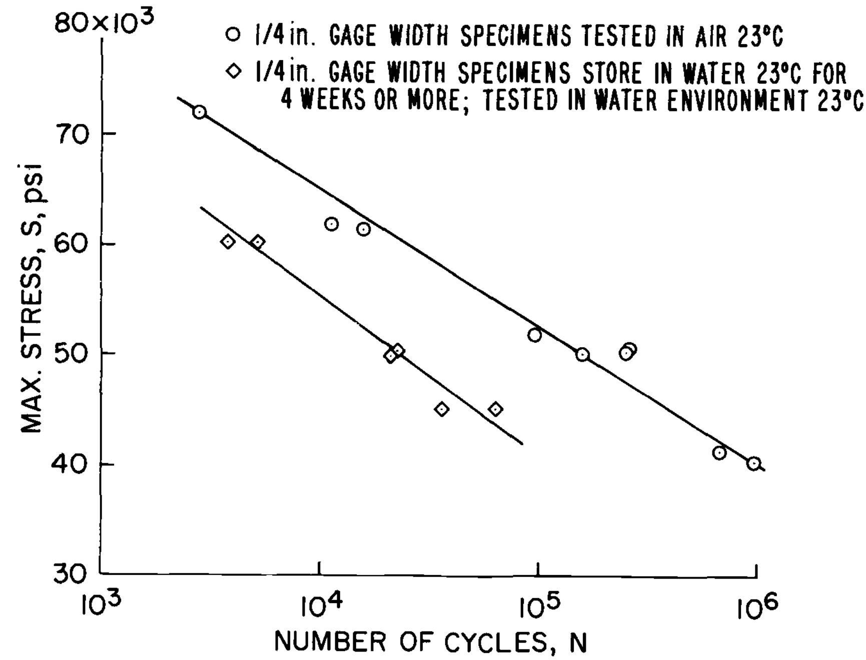

FIG. 14—*Flexure fatigue tests of 0 deg fiber-oriented specimens. All bend tests at room temperature; torsion tested at room temperature except as indicated at 74°C.*

decrease) were found to be a function of the initially applied torsional stress. At room temperature (24°C), damage appeared at all cyclic stress levels greater than about 0.15 of the static torsion failure stress, τ_f. A test environment of water at 24°C appeared to have no noticeable effect on either the incubation period or damage accumulation rate for specimens stored before testing in dry air. Specimens presoaked in water for four weeks at 24°C exhibited a slightly lower initial stiffness, a slightly shorter incubation period, and a slightly faster rate of damage accumulation than either the specimens stored and tested in air or those stored in air and tested in water. Tests at somewhat higher temperatures showed a greater effect of the water environment. Although the initial stiffness was slightly lower and the incubation period was slightly shorter, the general features of the fatigue damage curves for specimens tested in air at 74°C were unchanged from those at 24°C. For specimens tested in water at 74°C, however, the initial stiffness was decreased considerably as were the incubation period and the "apparent" fatigue limit. The decrease in initial stiffness must have occurred quite rapidly as the specimens were maintained in warm water for only 1 h (to allow the temperature to stabilize) before testing. Since specimens with identical pretest histories but tested in water at 24°C exhibited only a minor decrease in initial stiffness, the reduction at 74°C must be attributed to the 1-h temperature stabilization period. This effect of hot water exposure is similar to that noted by Beaumont and Harris, who exposed a number of specimens to steam at 100°C for 48 h before testing at room temperature in water. They noted somewhat smaller effects of water on both the initial interlaminar shear strength and on the fatigue damage curve. They did not observe any effect of the high-temperature steam pretreatment on the apparent fatigue limit. The comparison with the work of Beaumont and Harris appears to suggest that, although preexposure of the material to moisture at elevated temperatures can affect the fatigue damage behavior, exposure during testing represents a more severe condition.

The behavior of the unidirectional (0 deg) material subjected to cyclic torsional loads was similar to that noted for crossplied material; however, the amount and rate of accumulation of damage was less for 0 deg specimens loaded to equivalent relative stress levels (τ_o/τ_f) than for cross-

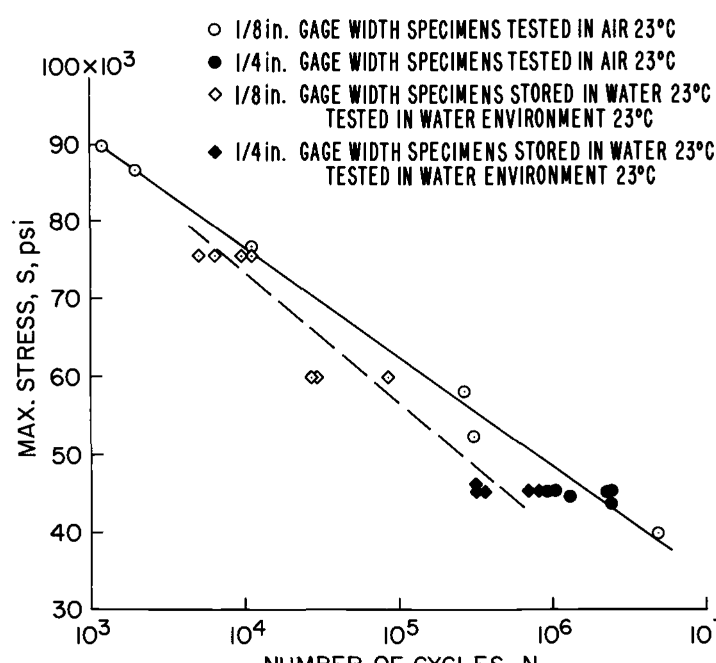

FIG. 15—*Flexure fatigue tests at ±45 deg fiber-oriented specimens. All bend tests at room temperature; torsion tested at room temperature except as indicated at 74°C.*

plied specimens. No effect of water and, indeed, very little fatigue damage were noted for unidirectional specimens cycled (at 24°C) at an initial torsional stress level of $0.36\tau_f$. At 74°C, the unidirectional specimens tested in air exhibited only a small reduction in initial stiffness and showed no increased propensity for fatigue damage. In water at this temperature, however, they exhibited a significant decrease in initial stiffness and showed signs of considerable fatigue damage during cycling.

The reasons for the large observed effect of stress cycling on the stiffness of crossplied material as compared to the effect on unidirectional material are not completely certain. Beaumont and Harris determined from their studies that matrix cracks were responsible for the decreases in stiffness of their (unidirectional) material. They found very little evidence of interfacial cracking. Therefore, the damage noted for the unidirectional material in the present study is also expected to be due to matrix cracking although microscopic examination of tested specimens has not yet been made. For the crossplied material, however, the higher measured torsional stiffness and higher torsional failure stress indicate that the fibers themselves contribute more significantly to the mechanical properties. Therefore, the cyclic stresses undoubtedly cause significant strains to occur in both the matrix and fibers of the crossplied specimens. These strains are expected to lead not only to the formation of cracks within the matrix material but also debonding at the fiber-matrix interface. In addition, these strains might cause the fracture of some of the fibers themselves. These latter two factors, when added to the first, would undoubtedly cause greater reductions in the transverse stiffness than would the formation of cracks only within the matrix. Support for the hypothesis that interfacial debonding might be the cause of the larger decreases is contained in the results of the bend tests on the torsion-tested and on the untested specimens of both crossplied (±45 deg) and unidirectional (0 deg) materials (Figs. 10–13). In general, the torsion-tested specimens of crossplied material exhibit a substantially larger decrease in failure stress in bending than do the unidirectional specimens for any number of reasons. More importantly, however, the crossplied specimens show an increase in fracture energy after torsion testing, while the unidirectional specimens show a decrease. On the basis of previous theoretical predictions [*5*] and experimental observations [*6*], this behavior might be expected if the torsion testing caused a decrease in the interfacial energy of the crossplied material and no appreciable change in the interfacial energy of the unidirectional material. Debonding in torsion testing of some fraction of the interfacial area in the crossplied material would reduce the remaining "average" interfacial energy. This hypothesis should be tested by a thorough examination of stress-cycled specimens to identify or refute the occurrence of debonding in torsion testing.

The observation that water at 24°C had relatively little effect on the properties of graphite-epoxy composites was consistent with the very small changes noted in previous investigations [1]. Based on these observations, it seems likely that the absorption rate of water by the epoxy at room temperature is simply too slow to cause any significant changes in material properties. The effects of water at 74°C were somewhat larger than expected based on the study of Beaumont and Harris [1]. They found that the interlaminar shear strength (measured at room temperature) was virtually unchanged after exposure to steam at 100°C for 1 h. The results of the present study show a large effect on initial torsional stiffness when tested in water at 74°C. These tests were run within 1 h after the specimen was placed in 74°C water. Beaumont and Harris also found that the torsional fatigue behavior was affected much less significantly by the pretest exposure to the 100°C steam than was the behavior noted here for specimens tested in water at 74°C. These results suggest that there is a synergistic effect of loading the material in the environment, probably caused by the stress-assisted absorption of water in the epoxy. This effect should be considered when characterizing composite materials for use in anticipated service environments.

The flexural fatigue results were perhaps the most surprising obtained during this study (Figs. 14 and 15). Investigators [1,2] who had previously performed flexural fatigue work generally found that composite materials are relatively insensitive to damage so long as the flexural stresses are applied perpendicular to the longitudinal axis of the fibers. However, these investigators used either three- or four-point cyclic bend testing techniques. In the present study, flexural fatigue loading, using fully reversed plane bending, led to significant fatigue damage at stress levels down to at least 50 percent of the static (flexural) failure stress. Even at these stress levels, no fatigue limit was indicated. Moreover, the unidirectional material and, to a lesser extent, the crossplied material showed a significant effect of testing in water at room temperature. This is in contrast to results of other investigators [1,2] and the results of the torsional fatigue tests that showed no appreciable effect of water at room temperature. The reason for this difference in behavior is unclear, although it is expected that the mechanism of damage in these specimens is different from those loaded in torsion and that the influence of moisture on the two mechanisms might also be different. The reason for a greater amount of fatigue damage in these flexural tests than in those previously reported may be related to two factors. First, the definition of failure for the present data was based on a decrease in flexural stiffness of 50 percent, while that for the earlier studies appears to have been a fracture criterion. Second, the fully reversed method of loading, ($R = -1$), may well be more damaging to composite materials than the three- or four-point bend methods generally used ($R > 0$). (These factors require further study.)

Based on the present results which show that both flexural and torsional fatigue can occur in smooth specimens of graphite-epoxy composites, it seems reasonable that further fatigue studies should be conducted. These studies should investigate the effect of cyclic loads and environment on the fatigue behavior of small specimens that contain holes and cracks representative of material cutouts and of larger specimens that are more representative of structural panels.

Conclusions

1. Both unidirectional (0 deg) and crossplied (±45 deg) specimens of graphite-epoxy composites undergo fatigue damage, as evidenced by reductions in torsional stiffness when subjected to cyclic torsional stresses of 5760 psi (40 MN/m^2) for unidirectional and 11 200 psi (77 MN/m^2) for crossplied material.
2. For the constant torsional deflection tests used, the fatigue damage curves are characterized by: initial incubation period before damage begins; an accumulation of damage evidenced by a significant reduction in stiffness; and, a decrease in the rate of accumulation of damage evidenced by the approach to constant stiffness value.
3. The effect of exposure to a water environment during torsion testing at 74°C and, to a lesser extent at 24°C is to decrease the incubation period and to increase the rate of accumulation of damage; at 74°C, water also appears to decrease (lower) the limiting torsional stiffness.
4. The limiting stiffness in crossplied specimens that were torsion tested at 24°C appears to correspond to a limiting torsional stress level equal to about 15 percent of the torsional failure strength (τ_f); this stress level may then be equivalent to a "fatigue limit" for these composite materials.
5. The crossplied specimens are more prone to fatigue damage in torsion than the unidirectional specimens.
6. The reductions in torsional stiffness caused by stress cycling are accompanied by reductions in failure strength in bending; the extent of the reductions depends on the stress and environmental histories.
7. The graphite-epoxy specimens showed significant flexural fatigue damage in both air and water when subjected to fully reversed plane bending.

8. In contrast to the torsion fatigue results, the results of the flexural fatigue studies showed a greater effect of water on the unidirectional specimens than on the crossplied specimens.

Acknowledgments

We wish to thank Richard Blomseth and S. T. Houck for their invaluable assistance in the experimental and data reduction programs.

References

[*1*] Beaumont, P. W. R. and Harris, B., "The Effect of Environment on Fatigue and Crack Propagation in Carbon Fibre Reinforced Epoxy Resin," Paper 49, International Conference on Carbon Fibres, Their Composites and Applications, Plastics Institute, London, Feb. 1971.
[*2*] Owen, M. J. and Morris, S., "Some Interlaminar Shear Fatigue Properties for CFRP," Paper 8, Conference on Reinforced Plastics Research Projects III, Plastics Institute, London, Nov. 1971.
[*3*] Singer, F. L., *Strength of Materials,* Harper & Brothers, New York, 1951, pp. 69.
[*4*] Timoshenko, S. and Young, D. H., in *Elements of Strength of Materials*, 4th Ed., Van Nostrand, Princeton, N. J., 1962, Chapter IV.
[*5*] Cook, I. and Gordon, J. E., *Proceedings,* Royal Society, Vol. A282, 1964, pp. 508.
[*6*] Harris, B., Beaumont, W. R., and Moncunill de Ferran, E., *Journal of Material Sciences,* Vol. 6, 1971, pp. 238.

Prediction, Reliability, and Design

N. L. Person[1] *and T. N. Bitzer*[2]

Flexural-Fatigue Evaluation of Aluminum-Alloy and Kraft-Paper Honeycomb-Sandwich Beams

REFERENCE: Person, N. L. and Bitzer, T. N., "**Flexural-Fatigue Evaluation of Aluminum-Alloy and Kraft-Paper Honeycomb-Sandwich Beams,**" *Fatigue of Composite Materials, ASTM STP 569,* American Society for Testing and Materials, 1975, pp. 251–261.

ABSTRACT: Flexural static and fatigue tests were conducted on 3¼-in.-thick honeycomb-sandwich beams having either aluminum-alloy or kraft-paper cores and identical aluminum facings. When the beams have relatively small ratios of length to thickness (short spans, thick cores), the static and fatigue strengths are determined primarily by the shear properties of the core material. In this case, the aluminum honeycomb sandwich was stronger than the kraft-paper honeycomb sandwich. With longer beams, the strengths are dependent mainly on the properties of the facing materials. Since the facings were the same for the two types of sandwiches, the respective static and fatigue properties were approximately equal.

KEY WORDS: fatigue tests, composite materials, aluminum, papers, honeycomb structures, structural forms

Honeycomb cores have been used in sandwich construction for a wide range of applications for many years. Over these years, a number of fatigue studies of aluminum and kraft-paper honeycomb-sandwich structures have been reported. A few representative studies are referenced herein [*1–4*].[3] In most cases, the studies have been conducted on relatively short beams, in which shear in the core was the critical mode of failure. Also, some plate-shear fatigue tests (pure shear) have been conducted. The core was usually less than 1 in. thick in these cases.

Thus, when fatigue properties were required for the confirmation of

[1] Senior research engineer, Kaiser Aluminum and Chemical Corporation, Center for Technology, Pleasanton, Calif. 94566.

[2] Supervisor, Structural Design and Testing, Hexcel Corporation, Dublin, Calif. 94566.

[3] The italic numbers in brackets refer to the list of references appended to this paper.

the design of a honeycomb-sandwich highway van trailer, the available published data appeared inappropriate. The main structural element in the design was the floor panel which was a honeycomb sandwich much thicker than those tested in Refs *1–4*. Also, improvements in honeycomb sandwiches have been made in recent years.

In this study, sandwich panels with 3-in.-thick cores were evaluated as short beams (shear-mode tests) and relatively long beams (with respect to thickness). In long beams, the bending stresses predominate over the shear stresses. All the panels had aluminum facings but the cores were made of aluminum-alloy or kraft-paper honeycomb.

Experimental Program

Test Materials

Both types of honeycomb sandwiches evaluated in this program had identical facings of 5052-H34 alloy sheet. The facing loaded in tension during flexure was 1/8 in. thick and the one in compression, 3/16 in. thick. Both facings were of "doubler" construction; that is, they were built up from two thinner sheets (1/8-in. facing from two 1/16-in. sheets and 3/16-in. facing from 1/16 and 1/8-in. sheets).

Both the aluminum and kraft-paper cores were 2.93 in. thick, giving an overall thickness of about 3 1/4 in. for the sandwiches. The aluminum core was made from 0.0047-in.-thick 5052-H39 foil. It had a cell size of 1/4 in. and a density of 7.9 lb/ft^3. For the resin-impregnated kraft-paper core, the cell size was 3/16 in. and the density was 8.0 lb/ft^3 (Hexcel TUF-200-3/16-8.0 honeycomb made by proprietary process). Both cores had the *L* (ribbon) direction orientated parallel to the span length. Table 1 gives typical mechanical properties of the core materials. The core and facings were press-bonded using a modified epoxy liquid adhesive. Press-bonding

TABLE 1—*Typical mechanical properties of honeycomb cores.*

Honeycomb Material	Honeycomb Density, lb/ft^3	Stabilized[a] Compressive Strength, psi	Plate-Shear Properties[b] *L* Direction Strength, psi	*L* Direction Modulus, ksi	*W* Direction Strength, psi	*W* Direction Modulus, ksi
Aluminum	7.9	1420	700	130	440	52.8
Kraft-paper	8.0	1600	650	37	360	17.0

[a] Facings adhesively bonded to core.
[b] Tested in accordance with ASTM Shear Test in Flatwise Plane of Flat Sandwich Constructions or Sandwich Cores (C 273-61(1970)). Data for 0.625-in.-thick aluminum core and 0.500-in.-thick paper core.

was done at 250°F for 1 h with a pressure of 20 psi. Test beams, 6 in. wide and either 30 or 70 in. long, were sawed from the 3¼-in.-thick sandwich panels (panel size 70 by about 48 in.).

Test Procedure

A schematic representation of the loading arrangement for the 30 and 70-in. beams is given in Fig. 1. The shear load was constant between the outer support point and the nearest inner point of the 17-in. span (Fig. 1*a*) and zero between the inner load points. With three-point loading of the 70-in. beams (Fig. 1*b*), the maximum bending moment occurred at midspan. The shear load in this case was of constant absolute magnitude over the entire span length; but this was inconsequential since, as mentioned previously, the shear stresses were overshadowed by the bending stresses in the long beam.

Static strength was determined for both beam lengths using a 50-kip electrohydraulic machine and the test arrangements shown in Figs. 2 and 3. As Fig. 1 shows, 3 by 6-in. pieces of ¼-in.-thick steel plate at each loading point distributed the concentrated loads and, thus, prevented crushing of the core. The beams were placed in the test machine with the ⅛-in.-thick facings down so that the thinner facing would be stressed in tension. Duplicate static tests were conducted on each type of core and each beam length.

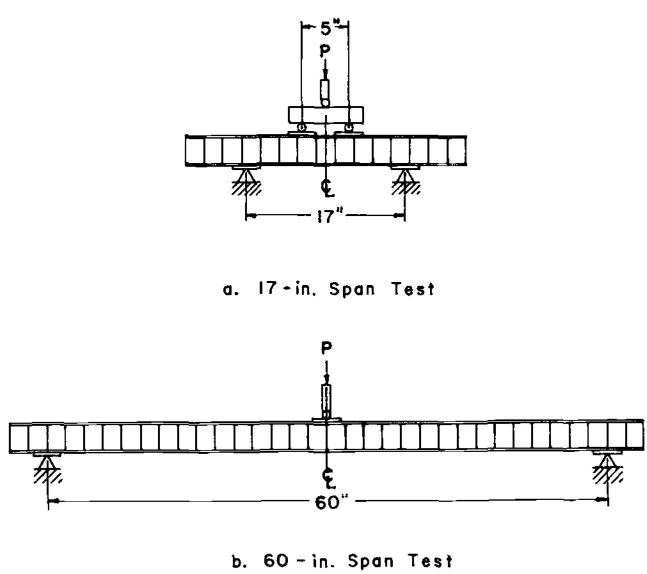

FIG. 1—*Schematic of beam flexure tests.*

The same test arrangement was used for the flexural-fatigue tests (Figs. 2 and 3). Since failure of the short beams was expected to occur in the cores, the sawed edges of the facings in those beams were not dressed. They were filed smooth, and the sharp corners were rounded slightly, in the long beams. The corners on the inside of the facings (side against core) could not be rounded, and slight burrs from the sawing and filing remained there.

Cyclic loads for the fatigue tests were set at percentages of the average static strength for each type of beam. The ratio of minimum load to maximum load, R, was maintained at zero for all tests on the short beams. For the long beams, R was 0.1. The test frequency was about 6 and 2 Hz for the short and long beams, respectively.

Results and Discussion

Static-Strength Tests

The results of the static tests are presented in Table 2. With the exception of the kraft-paper short beams, the scatter between the dupli-

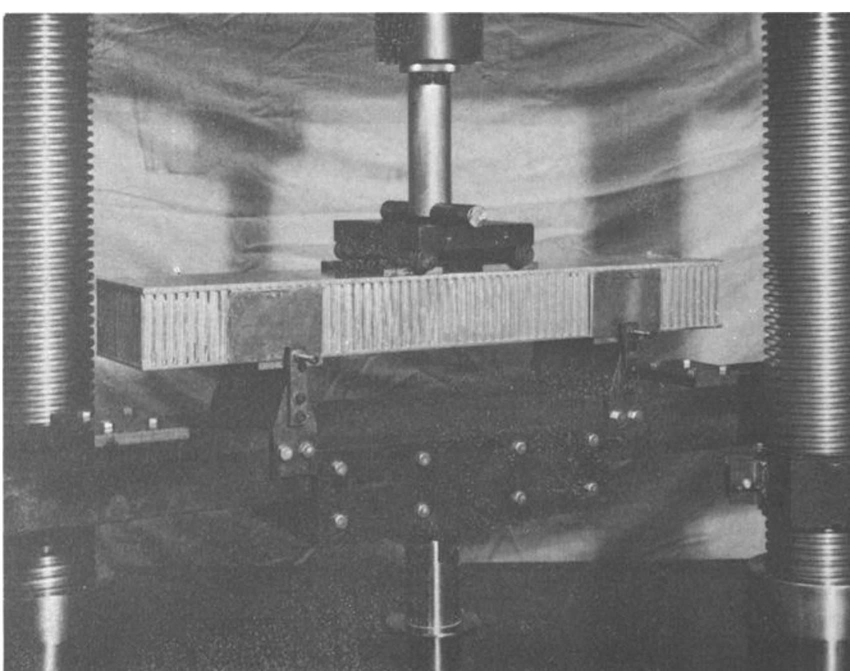

FIG. 2—*Four-point-loading test setup for short beams.*

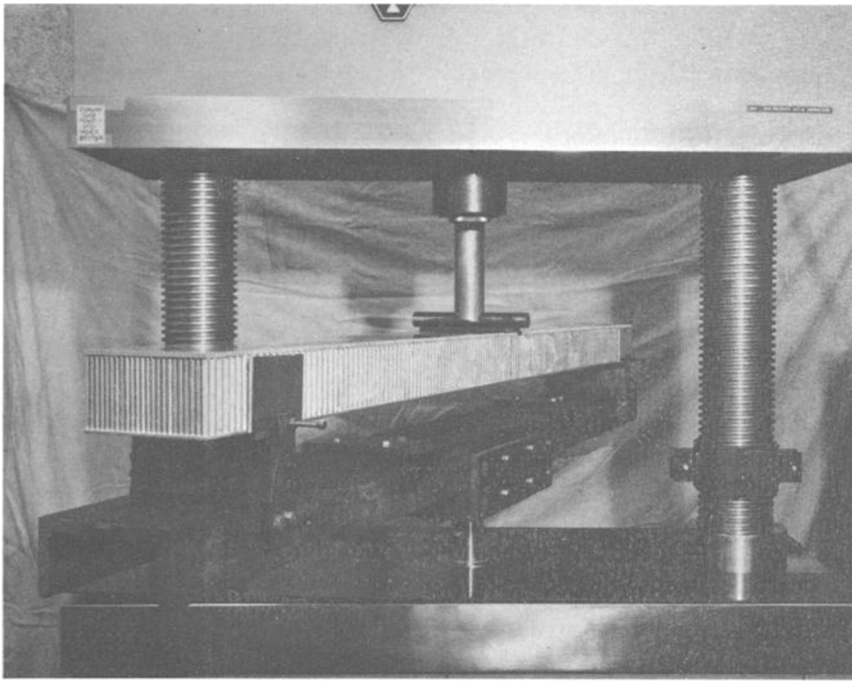

FIG. 3—*Three-point-loading test setup for long beams.*

TABLE 2—*Static strength of $3\frac{1}{4}$-in.-thick all-aluminum and aluminum kraft-paper honeycomb-sandwich beams.*

Core Material	Span Length, in.	Specimen Number	Static Strength, lb	Remarks
Aluminum	17	1	27 490	45-deg-shear failure through core
		2	27 860	
		Average	27 680	
Kraft-paper	17	1	17 580	45-deg-shear failure through core
		2	18 520	
		Average	18 050	
Aluminum	60	1	5 860	tensile failure in facing
		2	5 860	
		Average	5 860	
Kraft-paper	60	1	5 680	tensile yielding of facing, then core collapsed
		2	5 550	
		Average	5 620	

cate test results was less than 2½ percent of the average value. The scatter for the 17-in.-kraft-paper beams was about 5 percent of the average strength. For both span lengths, the aluminum-core beams showed less scatter than the kraft-paper beams.

As expected, failure of the short beams occurred by shear in the core on a plane 45 deg from the plane of the sandwich as shown in Fig. 4. Thus, the short-beam static strengths are a reflection of the shear strengths for the two honeycomb materials. The aluminum beams (17-in. span) supported a 53 percent greater load than the kraft-paper short beams (27 680 lb for aluminum and 18 050 lb for kraft-paper). These values equate to core ultimate shear strengths of 747 and 487 psi, respectively. The typical L plate-shear strengths (Table 1) for ⅝-in.-thick aluminum and ½-in.-thick paper cores are 700 and 650 psi, respectively.

L and W honeycomb shear strengths normally drop off with increasing core thickness (typical values in Table 1 are for thin honeycomb cores). Thus, for 3-in.-thick honeycomb, the L plate-shear strengths are approximately 505 psi and 430 psi for the 7.9 lb/ft^3 aluminum and 8.0 lb/ft^3 paper cores, respectively. When the honeycomb is tested in short-beam flexural specimens, the core starts to yield and then some of the shear loads are transferred to the facings, thus increasing the ultimate shear

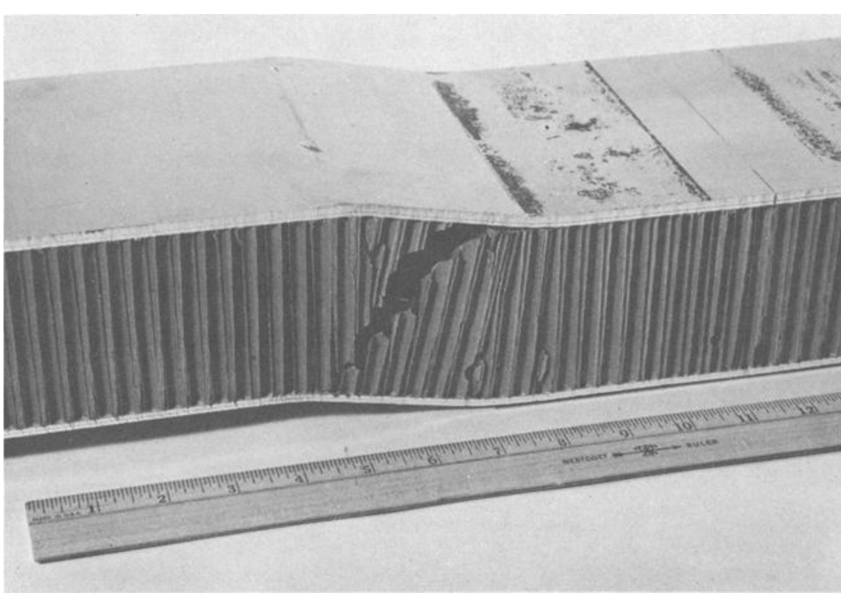

FIG. 4—*Shear failure in core of short beam.*

load capacity of the beam. Aluminum honeycomb exhibited more yielding than the more brittle resin-impregnated kraft-paper core; therefore, it was able to distribute more shear load to the skins. The paper-honeycomb product tended to fail with just a slight amount of yielding (a somewhat brittle-type failure). Therefore, it was not able to transfer as much shear load to the aluminum facings and, thus, the beam's ultimate strength was lower than that of the aluminum-honeycomb beam.

For the long beams (60-in. span), the aluminum-core sandwich failed when the bottom facing broke in tension. This occurred at an average load of 5860 lb. The kraft-paper-core beams, on the other hand, exhibited tensile yielding of the bottom skin with the core ultimately collapsing in compression. These beams supported an average maximum load of 5620 lb, which is about 4 percent lower than the static strength of the aluminum beams. Normally, one expects essentially equal strengths for these two types of beams since their respective core thicknesses were equal and their facing materials were identical.

Fatigue Tests

Tables 3 and 4 list the flexural-fatigue test results for the 17 and 60-in.-span tests, respectively. The data are plotted as *S-N* curves in Figs. 5–8. Two types of curves are given: load in percent of static strength (Figs. 5 and 7), and load in pounds (Figs. 6 and 8).

TABLE 3—*Fatigue test results for four-point loading on 17-in. span* (R = 0).

Specimen Number	Load: Percent of Static Strength	Load: Lb	Number of Cycles	Remarks
			ALUMINUM HONEYCOMB	
3	80	22 100	4 720	45-deg-shear failure mode
4	60	16 600	114 000	45-deg-shear failure mode
5	60	16 600	253 000	45-deg-shear failure mode
6	54	14 900	447 000 to 547 000	Test machine did not shut off at failure. 45-deg-shear failure mode
7	50	13 800	1 710 000	fatigue failure in facing
			KRAFT-PAPER HONEYCOMB	
3	80	14 400	5 800	45-deg-shear failure mode
4	60	10 800	71 200	45-deg-shear failure mode
5	60	10 800	76 400	45-deg-shear failure mode
6	50	9 020	365 000	45-deg-shear failure mode
7	45	8 120	2 620 000	45-deg-shear failure mode

TABLE 4—*Fatigue test results for three-point loading in 60-in. span* (R = *0.1*).

Specimen Number	Load: Percent of Static Strength	Load: Lb	Number of Cycles	Remarks
		ALUMINUM HONEYCOMB		
3	95	5 570	26 500	fatigue failure in lower facing
4	95	5 570	46 200	
5	80	4 690	166 000	
6	60	3 520	98 900	
7	60	3 520	647 000	
8	60	3 520	751 000	
		KRAFT-PAPER HONEYCOMB		
3	95	5 330	61 000	fatigue failure in lower facing
5	80	4 490	203 000	
6	60	3 370	752 000	
7	60	3 370	>1 680 000 [a]	

[a] > indicates "greater than"; specimen did not fail.

Span Tests, 17 In.—With load expressed in percent of static strength (Fig. 5), the aluminum-core sandwich had a higher fatigue strength at 10^5 to 10^6 cycles than the kraft-paper sandwich. At shorter lives, the curves converged, since at one-half cycle they must meet at 100 percent of the static strength. When these same data were plotted with load expressed in pounds, the dependence of fatigue strength on static strength became quite evident (Fig. 6). At 10^6 cycles, the fatigue strength for the aluminum beam was nearly double that of the kraft-paper beam. Furthermore, the 6000 to 8000-lb-fatigue-strength differential between these types of beams was apparently maintained down to very short cycles.

As noted in Table 3, all fatigue failures except one occurred in 45-deg-shear mode. The exception, an aluminum-core beam tested at 50 percent of its static strength (13 800 lb, Table 3), failed at about 1.7 million cycles from a fatigue crack that developed in the lower facing. As noted previously, the 30-in.-long beams were tested with the facings left in the "as-sawed" condition. This might have led to a premature failure of the sawn specimen and to the failure mode. This exception aside, the fatigue-failure mode of the short span beams was identical to that in the static tests.

Span Tests, 60 In.—For loads expressed in percent of static strength, the *S-N* curve for the kraft-paper beam lies slightly above that for the aluminum beams (Fig. 7). This is contrary to normal expectations. The fatigue strength should depend primarily upon the static strength of the

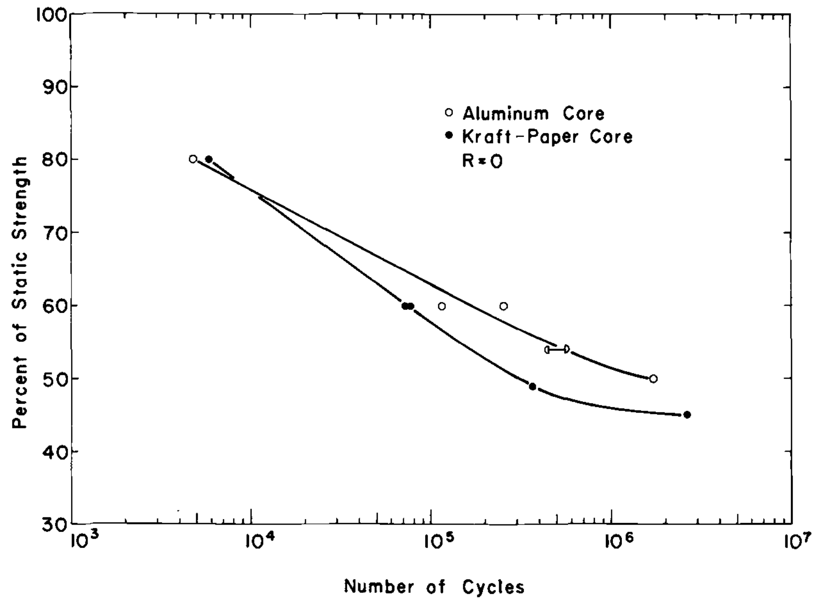

FIG. 5—*Flexural-fatigue* S-N *curves based on percent of static strength for aluminum and kraft-paper honeycomb sandwiches using 17-in. span and four-point loading.*

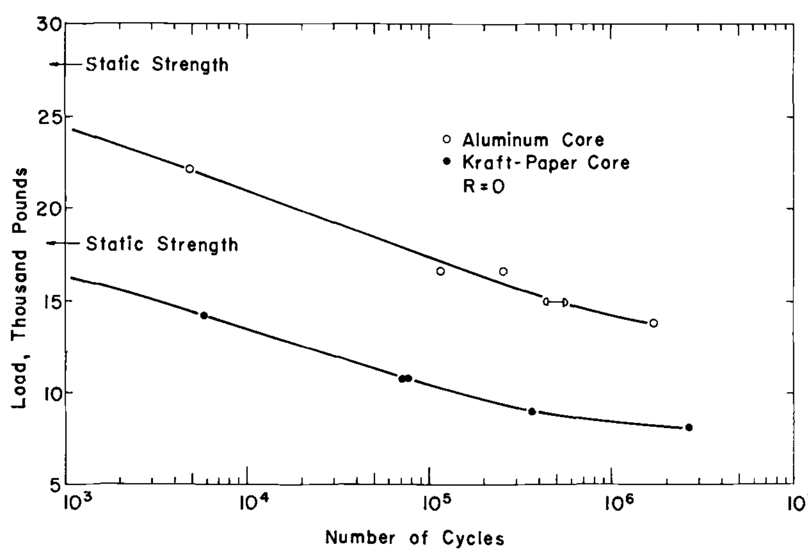

FIG. 6—*Flexural-fatigue* S-N *curves based on load in pounds for aluminum and kraft-paper honeycomb sandwiches using 17-in. span and four-point loading.*

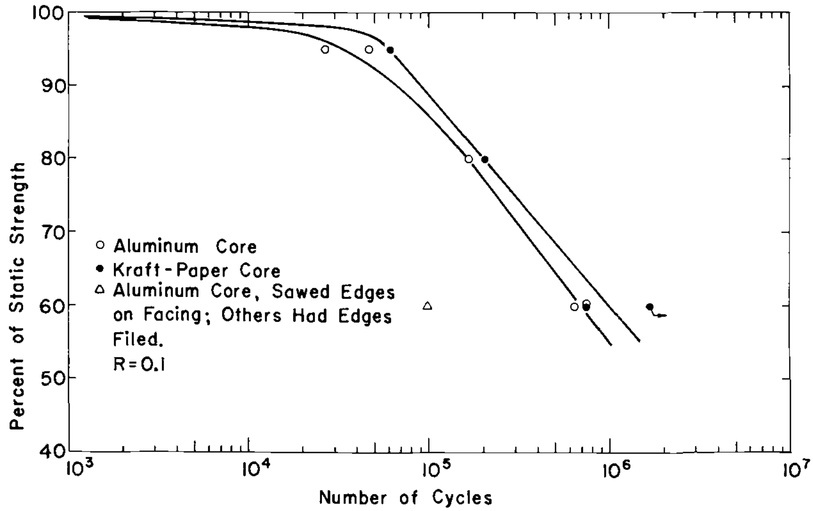

FIG. 7—*Flexural-fatigue* S-N *curves based on percent of static strength for aluminum and kraft-paper honeycomb sandwiches using 60-in. span and three-point loading.*

facings, and the facings were identical for both beam types. The explanation for the behavior shown in Fig. 7, however, is the difference in the static strengths of the beams caused by collapse of the core in the kraft-paper-core beams. Thus, when viewed on an absolute load basis, the *S-N* curves of the two types of beam should be virtually identical to one another. This is shown to be the case in Fig. 8.

A beam, 60 in., with an aluminum core was tested without the facing edges filed smooth. The results of that test (Figs. 7 and 8) illustrate the strong dependence of the fatigue strength of long beams on the edge condition of the facing. In this case, the fatigue life of the beam with sawed edges was only one seventh than that of beams with the facings filed smooth.

All beams fatigue tested over a 60-in. span failed when fatigue cracks initiated at one edge of the lower facing. Crack initiation usually occurred at the corner of the inner sheet of the doubler facing where it was impossible to remove the slight burrs that remained after filing the edges. The crack would then propagate across the inner sheet of the facing until the net load on the outer sheet reached the ultimate strength of that layer.

Summary and Conclusions

The static strength and the flexural shear fatigue strength of 3¼-in.-thick aluminum honeycomb-sandwich beam tested over a 17-in. span were substantially higher than those of a similar sandwich made with kraft-

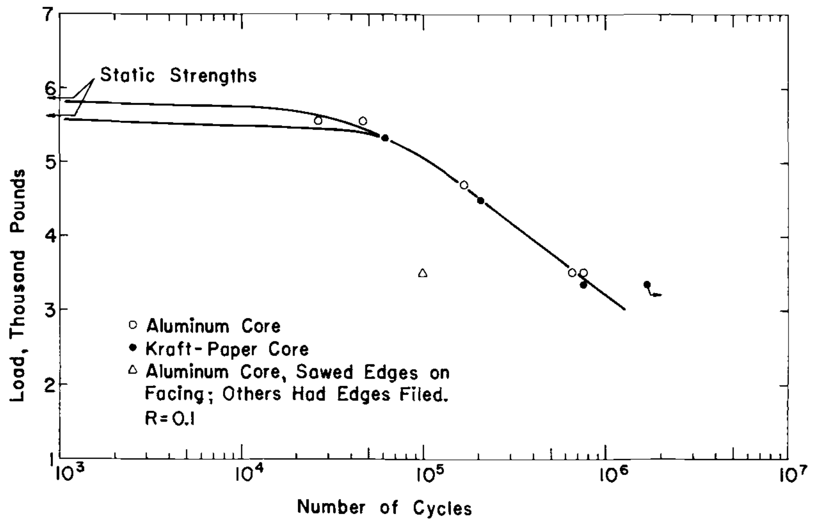

FIG. 8—*Flexural-fatigue* S-N *curves based on load in pounds for aluminum and kraft-paper honeycomb sandwiches using 60-in. span and three-point loading.*

paper honeycomb (core shear-mode failures). For tests over a 60-in. span, in which bending stresses predominated over shear stresses, the two types of beams had comparable fatigue strengths. The roughness of the cut edges of the sandwich facings, as in the fatigue tests of solid-metal specimens, influences fatigue strength.

Acknowledgments

We wish to thank R. C. Jordan of Hexcel Corporation for supplying the test materials, and J. R. Schultz of Kaiser Aluminum and Chemical Corporation's Center for Technology for conducting the experimental work. The authors also thank their respective corporations for permission to publish this work.

References

[*1*] Werren, F., "Fatigue of Sandwich Constructions for Aircraft, Aluminum Face and Paper Honeycomb Core Sandwich Material Tested in Shear," FPL 1559-A, Forest Products Laboratory, Madison, Wis., 1947.

[*2*] Werren, F., "Fatigue of Sandwich Construction for Aircraft, Aluminum Facing and Expanded Aluminum Honeycomb Core Sandwich Material Tested in Shear," FPL 1559-K, Forest Products Laboratory, Madison, Wis., 1952.

[*3*] Apodaca, D. R. and Preston, J. L., "Fatigue in Shear by Bending of Structural Sandwich Constructions," Technical Report No. ASD-TR-61-338. Part II, Northrop Corporation, Hawthorne, Calif., March 1963.

[*4*] Jenkinson, P. M. and Kuenzi, E. W., "Fatigue Properties of Some Aluminum and Stainless Steel Sandwich Construction," Technical Documentary Report No. ASD-TDR-62-1003, Forest Products Laboratory, Madison, Wis., March 1963.

T. D. Gray[1]

Foreign Object Damage and Fatigue Interaction in Unidirectional Boron/Aluminum-6061

REFERENCE: Gray, T. D., "**Foreign Object Damage and Fatigue Interaction in Unidirectional Boron/Aluminum-6061,**" *Fatigue of Composite Materials, ASTM STP 569,* American Society for Testing and Materials, 1975, pp. 262–279.

ABSTRACT: An experimental program was conducted to study the effects of foreign object damage (FOD) on the bending fatigue characteristics of a composite material, unidirectional boron/aluminum-6061. Fatigue curves were generated for a control group and each of four levels of FOD. The composite was further characterized by static tensile and nondestructive tests. All tests were carried out at room temperature. A similar damage and fatigue experiment was done for a titanium alloy, Ti-6Al-4V, to provide baseline data with which to compare the composite. It was concluded that the composite suffers a greater percentage reduction in fatigue strength than does Ti-6Al-4V for a given impact energy.

KEY WORDS: composite materials, boron, aluminum, fatigue tests, titanium alloys, foreign object damage, ballistic impact

Fiber-reinforced composites are candidate materials for use in high performance, structural applications such as jet engine compressor blades. Composites offer substantial weight reductions in rotating components which lead to further weight reductions in the form of lighter disks, shafts, and bearings. The composites are generally anisotropic and can be specifically designed to take advantage of their directionality of strength and stiffness. One drawback has been the lack of knowledge of the composites' residual strength after foreign object damage (FOD) has occurred. Composite materials were well on their way to application in production quantities when Rolls Royce Ltd. discovered that a carbon

[1] Captain, United States Air Force, graduate student, Mechanics Department, Air Force Institute of Technology, Wright-Patterson Air Force Base; now assigned to Air Force Flight Dynamics Laboratory, Wright-Patterson Air Force Base, Dayton, Ohio 45433.

fiber/epoxy material planned for use in jet engine fan blades was so deficient in FOD resistance that titanium blades had to be substituted.

The service life of a structure such as a compressor blade is directly determined by its fatigue characteristics. If a composite blade incurs FOD that is great enough to cause immediate failure, then the question of its residual service life does not exist. But if the blade incurs only slight damage, then how is its service life affected? Information in needed on the time dependent, structural response of composite materials when they are subjected to foreign object hits.

The purpose of this experimental study was to investigate the effects of foreign object damage on the bending fatigue characteristics of a metal-matrix composite material, unidirectional boron/aluminum-6061. For four levels of foreign object damage, a fatigue curve or *S-N* curve (maximum tensile stress versus number of cycles to failure) was generated. Foreign object damage was simulated by impacting specimens of the composite with a spherical projectile fired from a variable pressure, gas-powered launch tube. One *S-N* curve was generated for undamaged composite specimens to provide a control group. The composite was further characterized by static tension tests. Nondestructive testing (NDT) techniques, radiographic and ultrasonic, were used to inspect the composite specimens in the lowest damage level. All tests were carried out at room temperature.

A damage and fatigue experiment similar to that for the composite was done for a titanium alloy, Ti-6Al-4V. This material is presently used in compressor blades. It was intended that the damage and fatigue experiment for Ti-6Al-4V would provide a baseline with which to compare the composite.

Background

The two most important causes of compressor blade failure are foreign object damage and fatigue [*1,2*].[2] FOD can result when an engine ingests anything other than air, for example, rocks, fasteners, tools, birds. Fatigue is caused by start-up and shut-down cycling, inherent vibrations, and pulsations in the compressor airflow. The airflow pulsations, due mainly to rotating stall and stall flutter, cause bending fatigue in the blades.

Previous studies [*3,4*] have shown that FOD caused by hard objects such as fasteners can be duplicated by impaction with a standard steel BB. Residual ultimate tensile strength (after impaction with a steel BB) in boron/aluminum composites has been shown to be controlled by the extent of filament damage [*5*]. That is, as the FOD impact energy in-

[2] The italic numbers in brackets refer to the list of references appended to this paper.

creases, progressively more fibers are broken until an energy is reached where no additional damage is done. The hole size does not grow significantly with velocity above that required to just punch out a hole of the diameter of the projectile. Above this velocity no significant additional reduction in ultimate tensile strength takes place. Some additional energy is imparted to the material as the impact energy is increased, but this shows up as delamination, splitting, and strain hardening of the matrix; all these effects are insignificant compared to the strength of the fibers.

Fatigue crack growth in boron/metal-matrix composites is decidedly different from fatigue crack growth in monolithic metallic materials. Due to the anisotropic and heterogeneous nature of composites, the growth of a single, continuous, fatigue crack rarely, if ever, occurs.

Studies carried out by the Air Force Materials Laboratory indicate that boron fibers, when tested singly, are not susceptible to fatigue damage.[3] In accordance with these results, the axial fatigue behavior of boron/aluminum composites has been postulated to be controlled by the matrix fatigue behavior as opposed to being controlled by the filaments [*6–11*]. More specifically, fatigue cracks initiate in the matrix at random sites of stress concentration (voids, broken filaments, and disbonds). As the cyclic loading continues, the matrix fatigue cracks propagate normally until they impinge upon a filament. A stress concentration is induced at the fiber surface and the fiber fractures. The fatigue process continues until a dominant, weak zone is produced and the load-bearing capacity of the remaining material is exceeded. The fatigue fracture surfaces are irregular due to the randomness of initiation sites and the tendency for crack branching to occur.

The behavior of boron/aluminum composites in bending fatigue has been postulated to be controlled by the matrix, as in the case of axial fatigue. However, the actual process of fatigue damage buildup is slightly different [*9,11,12,13*]. In bending fatigue, the outer layers of matrix develop fatigue cracks which propagate parallel to the fibers causing matrix delamination and fiber disbonding. These discontinuities induce stress concentrations in affected fibers, ultimately causing singular fiber failure. The process continues until the load is too great for the remaining unbroken fibers, whereupon catastrophic failure occurs. Large-scale delamination, disbonding, and fiber breakage occur in the latter portion of the fatigue life.

[3] K. D. Shimmin, private communication, 20 Feb. 1973.

Materials

The composite material used in this study was a diffusion-bonded, boron/aluminum composite, 6061 aluminum symmetrically reinforced with five plies of unidirectional, continuous, boron filaments. The filaments were 0.0056 in. (0.0142 cm) in diameter and constituted 50 percent of the volume of the composite. Nominal thickness for the composite was 0.038 in. (0.097 cm). Figure 1 is a scanning electron micrograph of a cross section of the material.

A diamond cut-off wheel was used to cut rectangular test specimens from a panel of the composite. Final dimensions were 3.000 in. (7.620 cm)

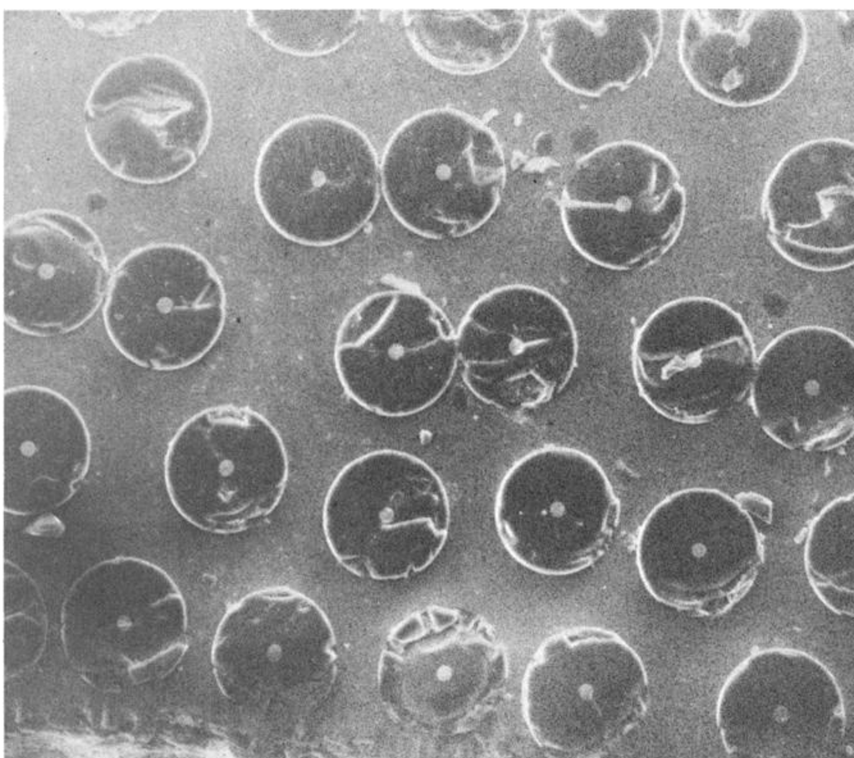

FIG. 1—*Cross-sectional view of unidirectional B/Al-6061, ×100.*

long by 0.700 in. (1.778 cm) wide by 0.038 in. (0.097 cm) thick with the lengthwise direction of the specimens parallel to the filaments.

The titanium test specimens were machined from annealed Ti-6Al-4V sheet, nominally 0.040 in. (0.102 cm) thick. Final dimensions were approximately equal to those of the composite specimens with the lengthwise direction of the specimens parallel to the rolling direction.

Aluminum doublers were adhesively bonded to both the composite and the titanium test specimens to reduce the influence of grip stresses. The doublers were rectangular with one edge beveled at 45 deg. Figure 2 shows a schematic of a test specimen complete with aluminum doublers. This specimen configuration was used for both static tension tests and bending fatigue tests.

Procedures

Figure 3 shows a schematic of the ballistic impaction apparatus. The basic test instrument is a smooth bore, launch tube with a variable pressure gas supply to propel the projectile. The launch tube has a bore diameter of 0.30 in. (0.76 cm) and a length of 60 in. (152 cm).

The projectile is carried in a small plastic cup called a "sabot" through the launch cycle. The sabot is a plastic cylinder made to bore diameter and one diameter in length. The front end of the cylinder is hollowed out to form a seat for the projectile. The additional rear surface area of the sabot makes possible a more efficient launch without having the projectile or the launch tube damaged during the launch cycle. After launch, the sabot is deflected so that it does not contact the specimen.

The projectile is launched into a flight tube. Along the flight path, the projectile interrupts two sets of laser beams and photocells. The signals

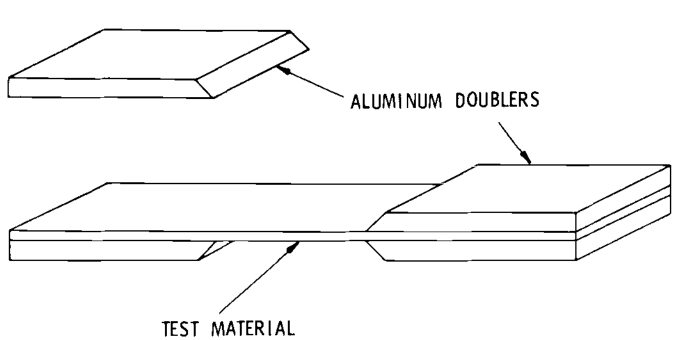

FIG. 2—*Test specimen schematic.*

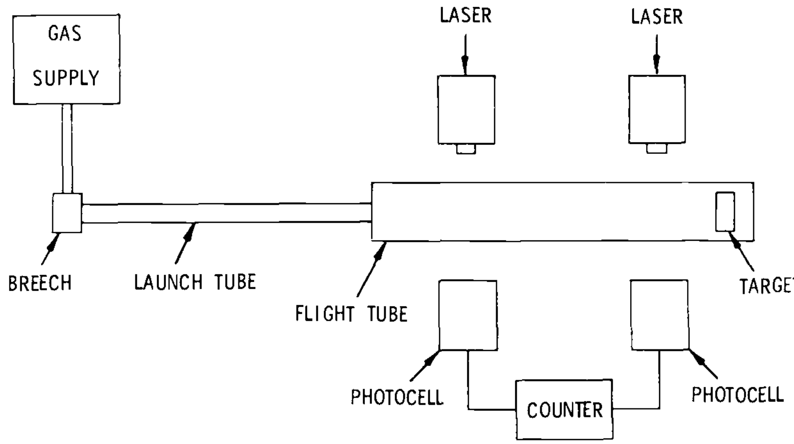

FIG. 3—*Impact apparatus schematic.*

thus generated start and stop an electronic counter, thereby measuring initial projectile velocity. At the end of the flight tube is a chamber in which the specimen is taped to a wooden backup block. A 0.5-in.-(1.3-cm) diameter hole was drilled in the center of the block to allow specimen deformation due to impact to occur freely. A high speed framing camera provides a measure of projectile velocity after impact.

In each ballistic impact test, the impact angle was 90 deg, and the aim point was the center of the specimen. Although edge impacts at angles other than 90 deg would have more realistically simulated FOD in compressor blades, it was felt that the variables inherent in such a test might obscure the results. All projectiles were steel BB's of diameter, 0.177 in. (0.450 cm) and mass, 350 mg. To characterize impact damage, impact dent diameters on specimen front faces and crack lengths on specimen rear faces, where applicable, were measured with a ×10 toolmaker's microscope.

A Sonntag universal fatigue testing machine, model SF-01-U, was used for all fatigue tests. The unit is of the controlled load type, using a linear, coil spring for static load and a rotating weight for cyclic load. The machine was fitted with a 1-in.-(2.54-cm) (lever arm) bending fixture. The type of loading induced by this fixture is essentially four point bending, that is, pure bending with constant moment across the gage length. The cyclic frequency of this machine is 30 Hz.

S-N plots were generated for damaged and undamaged groups of both B/Al-6061 and Ti-6Al-4V specimens. The data are, in all cases, presented in terms of a predicted or theoretical stress computed by using the familiar beam equation, $\sigma = Mc/I$, where M is moment on the specimen, c is distance away from the neutral axis, and I is area moment of inertia (computed using original or pre-impact specimen dimensions). The R value (minimum stress divided by maximum stress) for all tests was arbitrarily chosen to be 0.1. This loading cycle results in one side of the specimen always being in varying degrees of tension while the other side is always in compression. Unless indicated otherwise, all specimens were fixtured so that the impact side of the specimen was always in tension.

Results and Discussion

Ballistic Impaction

Table 1 contains the results of the ballistic impaction tests listed by damage level or group. Each group was made up of approximately ten specimens. Preliminary tests showed that impacting the B/Al-6061 with a velocity of 150 ft/s (45.7 m/s) produced an impact dent that was similar in size to the dent produced by impacting Ti-6Al-4V with a velocity of 350 ft/s (106.7 m/s). The preliminary tests also showed that the upper

TABLE 1—*Ballistic impaction test results.*

Group	Desired Impact Velocity, ft/s (m/s)	Average Impact Velocity, ft/s (m/s)	Rebound [a] Velocity, ft/s (m/s)	Impact Energy, ft · lb (J)	Average Damage Measurement, in. (cm)
			B/Al-6061		
I	no impact	0	0	0	0
II	150(45.7)	154(46.9)	46(14.0)	0.259(0.351)	0.056(0.143) [b]
III	225(68.6)	230(70.1)	65(19.8)	0.584(0.791)	0.153(0.389) [b]
IV	300(91.4)	300(91.4)	61(18.6)	1.035(1.403)	0.270(0.686) [b]
V	450(137.2)	454(138.4)	34(10.4)	2.458(3.333)	0.450(1.143) [b]
			Ti-6Al-4V		
VI	no impact	0	0	0	0
VII	350(106.7)	349(106.4)	35(10.7)	1.446(1.960)	0.068(0.172) [c]
VIII	500(152.4)	502(153.0)	75(22.9)	2.955(4.006)	0.086(0.220) [c]
IX	650(198.1)	667(203.3)	114(34.7)	5.180(7.022)	0.105(0.267) [c]
X	800(243.8)	813(247.8)	96(29.3)	7.816(10.597)	0.126(0.321) [d]

[a] Rebound velocity was measured for only one test in each group.
[b] Transverse crack length.
[c] Dent diameter.
[d] Hole diameter.

velocity limit for projectile containment was approximately 450 ft/s (137.2 m/s) for the B/Al-6061 and 800 ft/s (243.8 m/s) for Ti-6Al-4V. The upper velocity limit for projectile containment is defined as the maximum impact velocity for which the projectile rebounds from the test material; above the velocity, the projectile penetrates and passes through the material. In addition to the upper and lower impact velocities, intermediate velocities were chosen to obtain a range of impact damage for each material. The relative dispersion (standard deviation divided by sample mean) of the impact velocities was always less than six percent. In Table 1, impact energy for each group is the projectile average initial kinetic energy minus the (rebound) kinetic energy of the projectile after impact. As an aside, the rebound kinetic energy was less than ten percent of the average initial kinetic energy for all cases.

The physical damage that occurred in the B/Al-6061 was varying degrees of a circular dent on the impact or front face of the specimen and a raised area of material with a transverse crack through the center on the back face. Dent diameter and crack length increased with impact velocity. Figure 4 shows an impact-induced crack on the back face of a Group IV (see Table 1) B/Al-6061 specimen; also evident is a lesser degree of longitudinal cracking. The highest impact velocity in the B/Al-6061 produced a petalling-type hole with transverse and longitudinal cracking, but the projectile did not penetrate the specimen.

The damage characteristic to Groups VII and VIII Ti-6Al-4V was a circular dent on the impact face and a circular raised area on the back face. Damage to Group IX specimens was similar but more severe, and cracks around the periphery of the impact area were evident. At this stage a shear plug was beginning to develop. In specimens of Group X, formation of a shear plug was complete, and a circular hole was produced in the specimens. Even though a plugging-type failure occurred, the projectile did not penetrate but instead rebounded.

Material Characterization Tests

Static tension tests on unimpacted B/Al-6061 specimens showed the composite to have reproducible strength properties. Average ultimate tensile strength (load at fracture divided by original cross-sectional area) was 199.2 ksi (1.373×10^9 N/m^2). The load versus strain plots for the tensile tests were generally linear to fracture; average modulus of elasticity measured over the entire strain range was 24.9×10^6 psi (1.72×10^{11} N/m^2).

Nondestructive tests were done only on Group II B/Al-6061 specimens. Ultrasonic tests on Group II specimens *before* impact showed that the composite was of high quality; no disbonding or delamination was

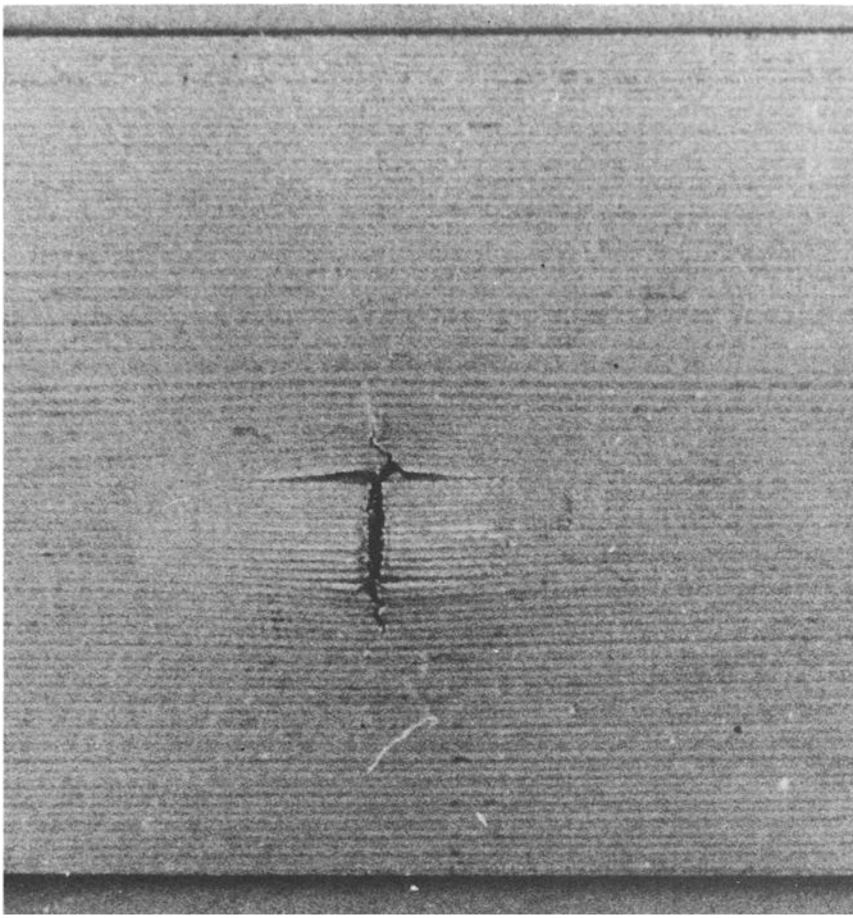

FIG. 4—*Impact-induced crack on the back face of a B/Al-6061 specimen, ×4.*

detected. Radiography showed that there was slight fiber misalignment in some areas, but no broken fibers were detected.

Viewing the radiographs of *impacted* Group II B/A1-6061 specimens with a ×10 toolmaker's microscope showed a transverse crack that was essentially through the thickness. The average percentage difference between crack lengths measured optically on the back surface of Group II specimens and crack lengths measured from the radiographs was less than seven percent. Thus, a fairly accurate estimate of the actual through-the-thickness crack is simply the length of the surface crack.

Bending Fatigue Tests, Unidirectional B/Al-6061

Results of the bending fatigue tests conducted on the B/Al-6061 are presented separately by group in Figs. 5–9. Figure 10 is a plot of the fitted curves from Figs. 5–9. The data are in the form of *S-N* curves or maximum stress versus number of cycles to failure. The general effect of increasing FOD on fatigue strength is obvious.

The two extremes of the *S-N* curves, 1 cycle to failure (actually failure occurred at one quarter of the first cycle) and 10^7 cycles to failure, are well defined and constitute a good measure of FOD effects. Fatigue strengths of Groups I through V at 1 and 10^7 cycles (taken from Fig. 10) are plotted against impact energy (from Table 1) in Fig. 11. Data for 10^4 cycles are included for comparison.

In Fig. 11, the 1 cycle to failure curve is essentially a plot for an ultimate bending test loaded at the rate of the fatigue tests; this curve shows the relation between ultimate bending strength and foreign object impact energy. The 10^7 cycles to failure curve of Fig. 11 shows the relation between fatigue strength at 10^7 cycles and foreign object impact energy. In the portion of the 10^7 cycles to failure curve that ranges from zero to

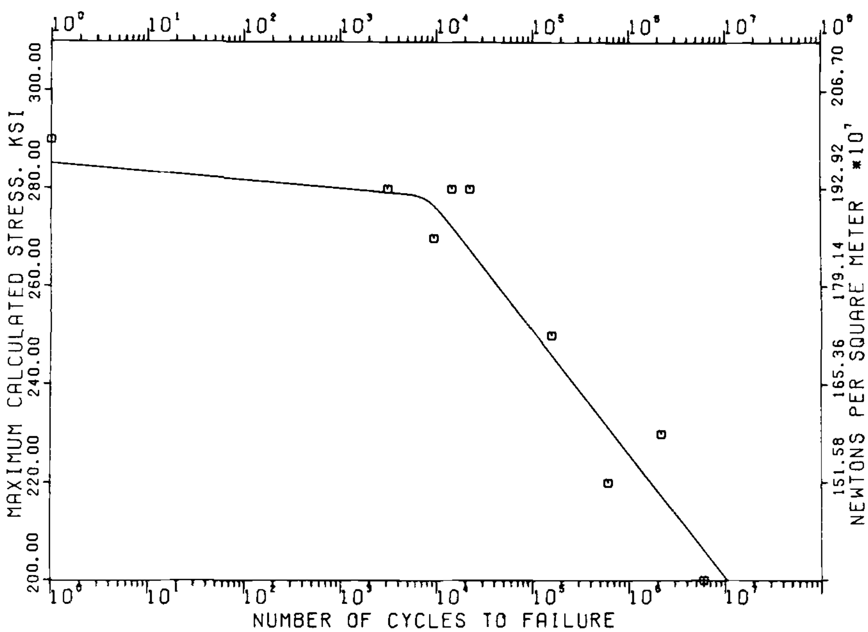

FIG. 5—S-N *plot for Group I B/Al-6061, undamaged.*

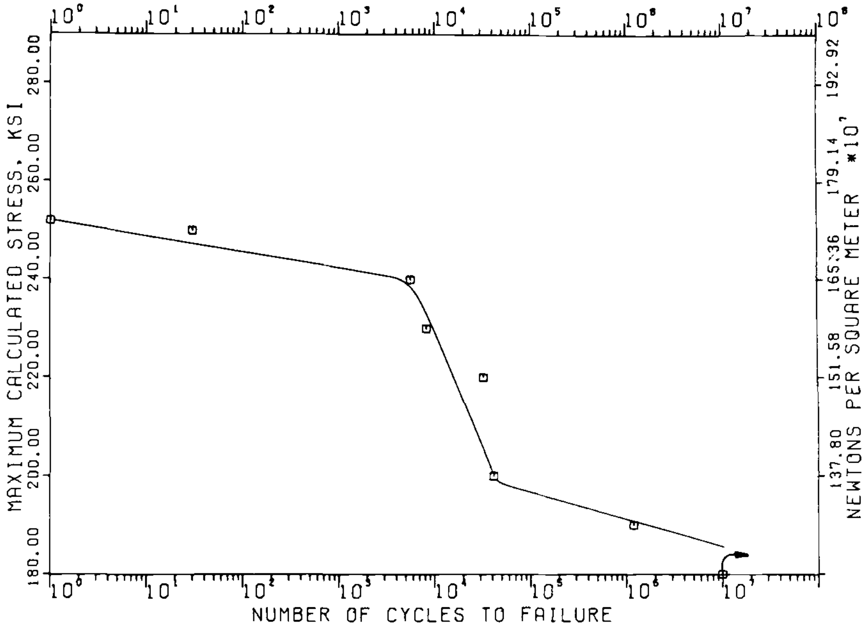

FIG. 6—S-N *plot for Group II B/Al-6061, average impact velocity = 154 ft/s (46.9 m/s).*

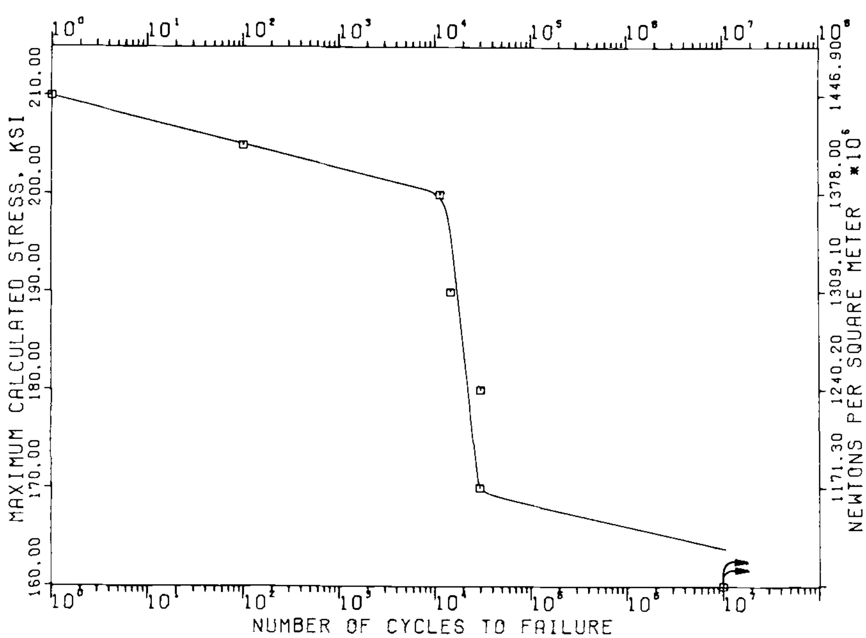

FIG. 7—S-N *plot for Group III B/Al-6061, average impact velocity = 230 ft/s (70.1 m/s).*

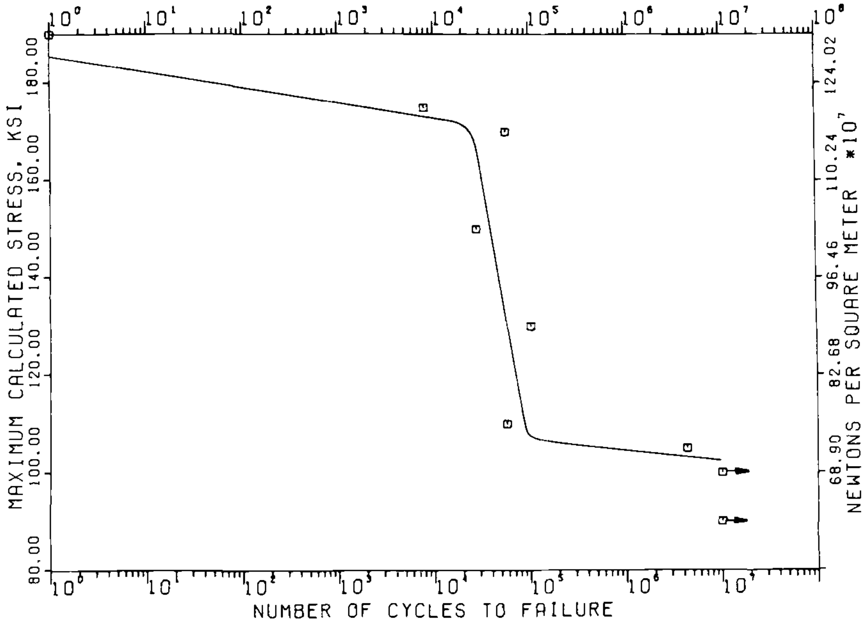

FIG. 8—S-N *plot for Group IV B/Al-6061, average impact velocity = 300 ft/s (91.4 m/s).*

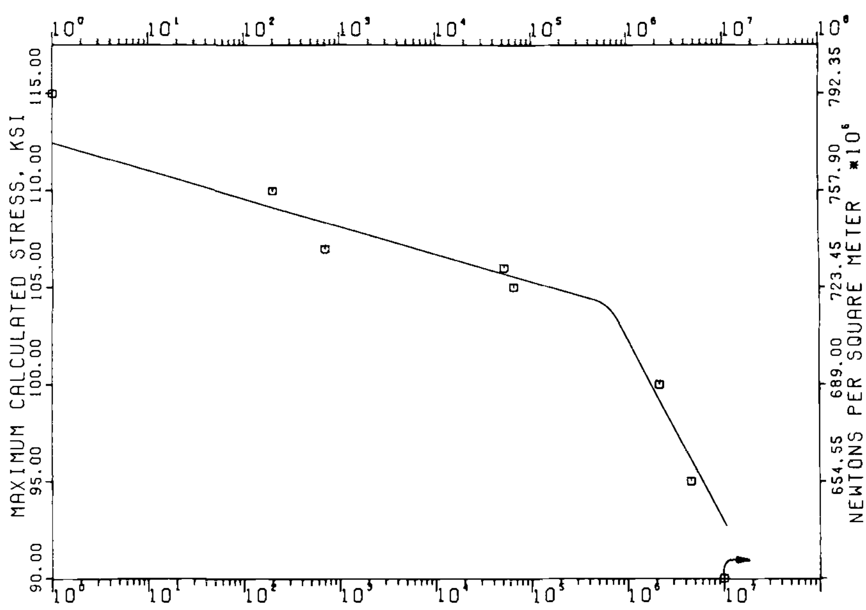

FIG. 9—S-N *plot for Group V B/Al-6061, average impact velocity = 454 ft/s (138.4 m/s).*

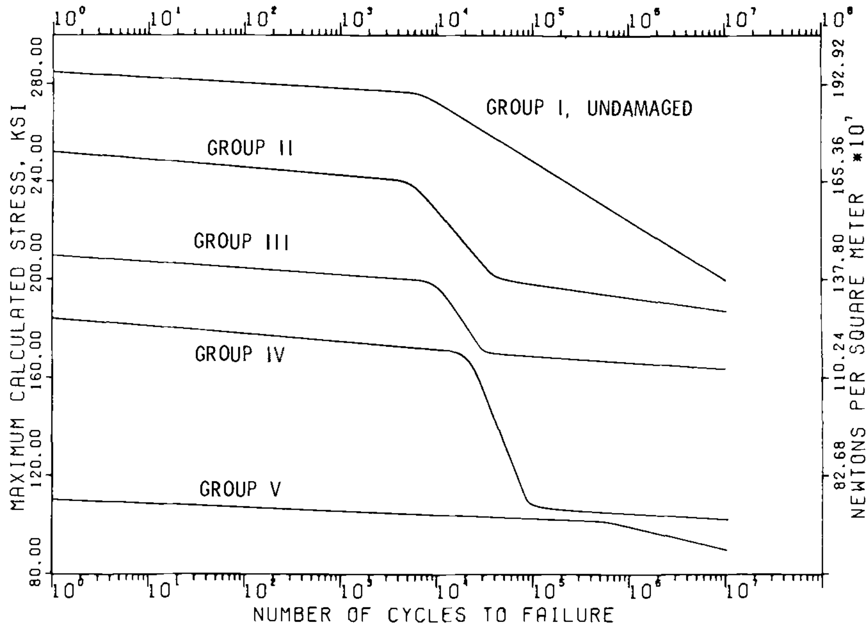

FIG. 10—S-N *plot for Groups I through V B/Al-6061.*

about 1.0 ft · lb (1.4 J), the reduction in fatigue strength is approximately proportional to the cube of the increase in impact energy. At higher impact energies, the 10^7 cycles to failure curve becomes asymptotic to a value of approximately 90 ksi (6.2×10^8 N/m^2); no significant decrease in fatigue strength (10^7 cycles) occurs for an increase in impact energy above 2.0 ft · lb (2.7 J).

A comparison of the ultimate strengths of the B/Al composite (undamaged) in tension and bending yields an apparent incongruity. Tension tests indicate an ultimate strength of approximately 200 ksi (1.4×10^9 N/m^2), while bending tests indicate an ultimate strength closer to 300 ksi (2.1×10^9 N/m^2). The equations used to determine stress in uniaxial tension and bending, σ = load divided by cross-sectional area and $\sigma = Mc/I$, apply only to linearly elastic, homogeneous, isotropic materials. A composite may be linearly elastic, but it is definitely not homogeneous or isotropic. When the above equations are applied to composites, the result is not a true stress but rather a "composite stress," which depends on the constituent materials and the geometry of the composite. Therefore, these equations generally should not be applied to composites for design; however, the equations do characterize material load-carry capacity and, thus, may be used for comparative purposes as was done in this study.

The failure mode of the composite was quite different from that of conventional, homogeneous materials. A single, continuous, transverse, fatigue crack was never observed for any of the composite specimens. Damaged and undamaged specimens tested at high stress levels (short fatigue lives) tended to fail in a manner similar to Fig. 12. At low stress levels (long fatigue lives), much more delamination and longitudinal cracking occurred. Figure 13 shows an undamaged (no impact) specimen that failed at 5 991 700 cycles. Damaged (impacted) specimens tested at low stress levels tended to have longitudinal cracks that initiated at both sides of the original, impact-induced, transverse crack and grew parallel to the filaments until they reached the aluminum doublers. This situation occurred early in the fatigue life leaving the specimen with two undamaged portions of material on either side of an H-shaped crack in the center of the specimen.

The failure criteria for this study has been complete material separation in the transverse direction such that the load-carrying capacity of the specimens was zero for the particular test mode. In another context,

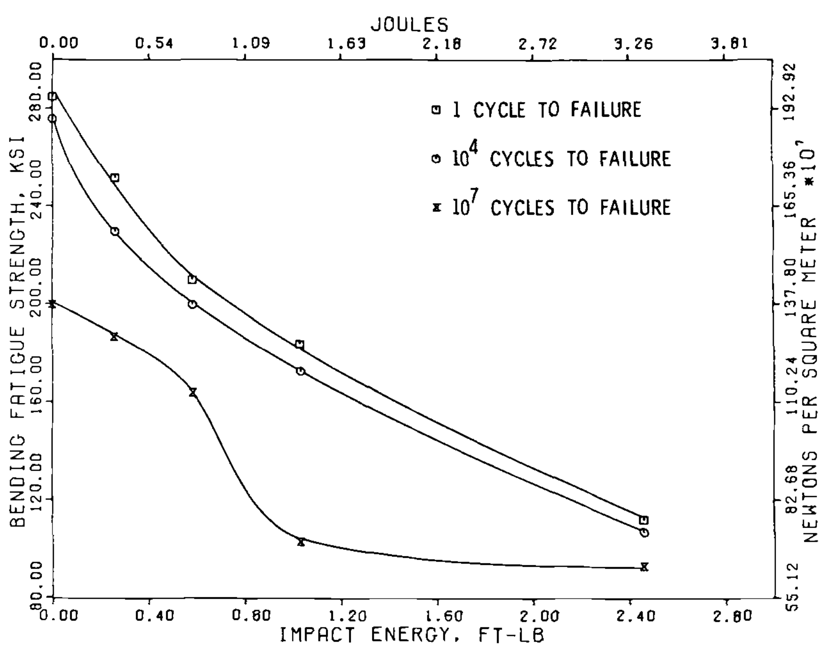

FIG. 11—*Fatigue strength versus impact energy, B/Al-6061.*

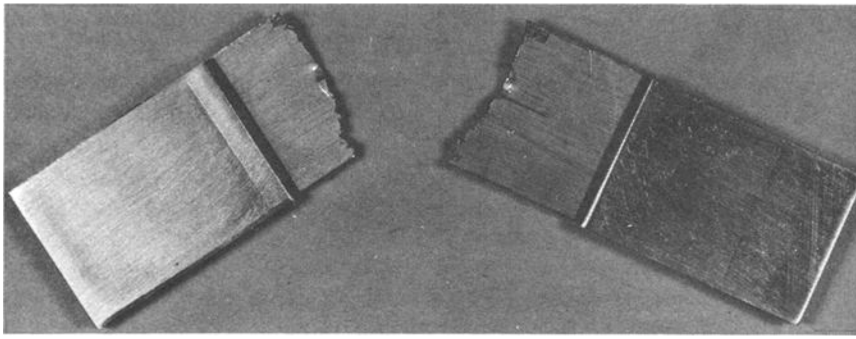

FIG. 12—*Typical high stress fatigue failure, 102 300 cycles, B/Al-6061.*

growth of longitudinal cracks out to the doublers might constitute failure. If this were the case, an accurate method of longitudinal crack measurement, perhaps an electrical potential method, would be necessary.

Bending Fatigue Tests, Ti-6Al-4V

Bending fatigue tests conducted on Ti-6Al-4V specimens in conjunction with least squares curve fitting indicated that there was no difference between the *S-N* curves for Groups VI (undamaged control group), VIII, and X. Fatigue failures in damaged specimens occurred away from the damaged area where the material was essentially unaffected, see Fig. 14. It is theorized that the ballistic impact had caused, in the immediate impact area, compressive residual stresses on the impact face that, when coupled with the type of loading (impact face always in tension),

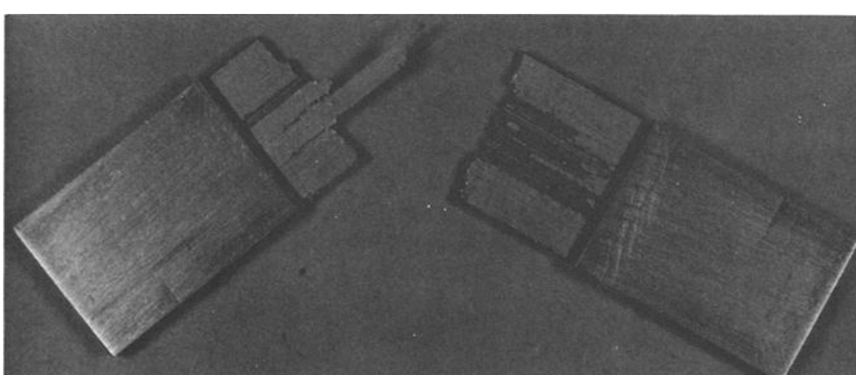

FIG. 13—*Typical low stress fatigue failure (unimpacted specimen), 5 991 710 cycles, B/Al-6061.*

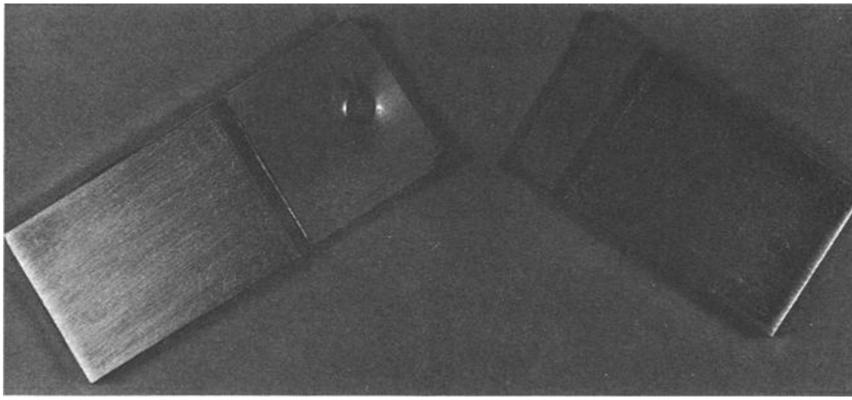

FIG. 14—*Typical fatigue failure, impacted Ti-6Al-4V specimen.*

caused a lower actual stress than in the surrounding undamaged material. Another possible contribution to failure away from the damaged material is an increased area moment of inertia, I. The ballistic impaction caused out-of-plane deformation of the specimen in the immediate impact area such that the moment of inertia would be increased. Since bending stress is inversely proportional to I, an increase in I would cause a decrease in bending stress in the immediate impact region. Since the applied moment was constant across the specimen gage length, the undamaged material (no increase in I) would experience a higher stress; hence, failure would occur in the undamaged region.

As the test results could be influenced by having the impacted (front) face always in tension, fatigue tests were done for Group VII specimens mounted in an inverted position, that is, mounted so that the back face of the specimen was always in tension. In this series of tests, three specimens failed away from the damaged area, while two specimens failed exactly through the damaged area. The results were compared to the results for Groups VI, VIII, and X, and again no noticeable difference in *S-N* curves existed. Since tests on Groups VI, VII, VIII, and X were essentially tests on undamaged material, all results were grouped together.

Fatigue tests were conducted on inverted Group IX specimens, but a machine malfunction rendered the results inconclusive. Additional Group X specimens were coded Group XB and fatigued in the inverted position. In these tests, all failures occurred through the damaged area. *S-N* curves for Group XB and all other specimens are shown in Fig. 15.

From Figs. 15 and 10 it is obvious that FOD degrades the fatigue characteristics of Ti-6Al-4V less severely than it does unidirectional

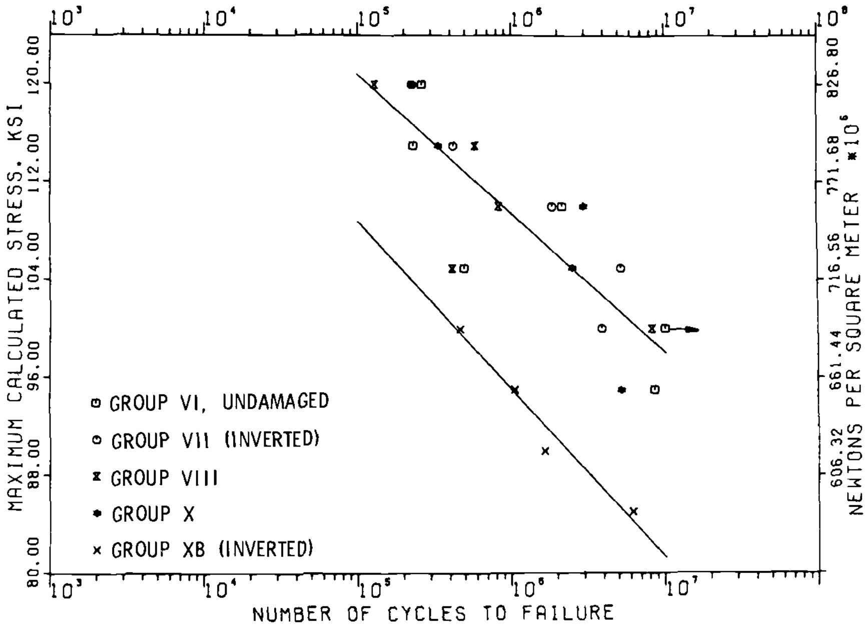

FIG. 15—S-N *plot, Ti-6Al-4V.*

B/Al-6061 fatigue characteristics. As an example, for the B/Al-6061 fatigued in the normal position (impact face always in tension), an impact velocity of 454 ft/s (138.4 m/s) caused a 54 percent reduction in fatigue strength (10^7 cycles). An impact velocity of 813 ft/s (247.8 m/s) caused no reduction in the fatigue strength (10^7 cycles) of Ti-6Al-4V fatigued in the normal position and only a 17 percent reduction when Ti-6Al-4V was fatigued in the inverted position.

Summary

An experimental program was conducted to study the effects of foreign object damage on the bending fatigue characteristics of a composite material, unidirectional boron/aluminum-6061. A similar damage and fatigue experiment was done for a titanium alloy, Ti-6Al-4V, to provide baseline data with which to compare the composite.

Simulated foreign object impacts reduced the bending fatigue strength of the composite by inducing cracks in the material. For the range of impact energies studied, the composite suffered a greater percentage reduction in bending fatigue strength than did Ti-6Al-4V.

Acknowledgments

This report was prepared for presentation to the faculty of the School of Engineering at the Air Force Institute of Technology in partial fulfillment of the requirements of the degree of Master of Science. The author wishes to express his sincere thanks to P. J. Torvik for his initial problem definition and enthusiastic guidance. In addition, the invaluable technical assistance of C. E. Acton, Robert Crane, Alan Hopkins, Thomas Lee, William Shelton, and David Stuber is gratefully acknowledged.

References

[*1*] Akins, R. J., "Composite Materials for Turbine Compressors," Solar Report No. RDR 1492, Solar Company, San Diego, Calif., Aug. 1966.
[*2*] "Factors That Affect Operational Reliability of Turbojet Engines," Technical Report R-54, National Aeronautics and Space Administration, Washington, D.C., 1960.
[*3*] "Minutes of Air Force Materials Laboratory Foreign Object Damage Meeting," Air Force Materials Laboratory, Dayton, Ohio, 21 April 1972.
[*4*] Young, J. H. and Carlson, R. G., "Advanced Composite Material Structural Hardware Development and Testing Program," Technical Report AFML-TR-70-140, Air Force Materials Laboratory, Dayton, Ohio, July 1970.
[*5*] "Foreign Object Damage Progress" Report No. 1, Air Force Materials Laboratory, Dayton, Ohio, 1972.
[*6*] Toth, I. J., "An Exploratory Investigation of the Time Dependent Mechanical Behavior of Composite Materials," Technical Report AFML-TR-69-9, Air Force Materials Laboratory, Dayton, Ohio, April 1969.
[*7*] Menke, G. D. and Toth, I. J., "The Time Dependent Mechanical Behavior of Composite Materials," Technical Report AFML-TR-70-174, Air Force Materials Laboratory, Dayton, Ohio, June 1970.
[*8*] Hancock, J. R., "The Initiation and Growth of Fatigue Cracks in Filament-Reinforced Aluminum Alloys," Technical Report AFML-TR-7a-82, Air Force Materials Laboratory, Dayton, Ohio, March 1971.
[*9*] Menke, G. D. and Toth, I. J., "The Time Dependent Mechanical Behavior of Composite Materials," Technical Report AFML-TR-71-102, Air Force Materials Laboratory, Dayton, Ohio, Sept. 1971.
[*10*] Hancock, J. R., "Fatigue of Boron-Aluminum Composites," Technical Report AFML-TR-72-113, Air Force Materials Laboratory, Dayton, Ohio, May 1972.
[*11*] Menke, G. D., Scheirer, S. T., and Toth, I. J., "The Time Dependent Mechanical Behavior of Composite Materials," Technical Report AFML-TR-71-149, Air Force Materials Laboratory, Dayton, Ohio, Sept. 1972.
[*12*] Kreider, K. G. and Leverant, G. R., "Boron Fiber Metal Matrix Composites by Plasma Spraying," Technical Report AFML-TR-66-219, Air Force Materials Laboratory, Dayton, Ohio, July 1966.
[*13*] Herman, M. et al, "Research and Development of an Advanced Composite Technology Base and Component Fabrication Program for Gas Turbine Compressor and Fan Blades," Technical Report AFML-TR-68-258, Air Force Materials Laboratory, Dayton, Ohio, March 1969.

J. L. Christian [1]

Axial Fatigue Properties of Metal Matrix Composites

REFERENCE: Christian, J. L., "**Axial Fatigue Properties of Metal Matrix Composites,**" *Fatigue of Composite Materials, ASTM STP 569,* American Society for Testing and Materials, 1975, pp. 280–294.

ABSTRACT: Axial fatigue properties were determined on a number of filament reinforced metal matrix composite materials. Results indicated that each of the composite materials possessed excellent fatigue properties when tested parallel with reinforcing filaments (that is, fatigue strengths at 10^6 cycles of 50 to 80 percent of ultimate tensile strengths). Transverse fatigue properties were found to be similar to those of the unreinforced matrix material. The type and size of filaments and the matrix material and its condition were found to significantly affect fatigue properties. For example, boron-reinforced composites possess higher fatigue strengths than Borsic-reinforced composites at high-stress, low-cycle fatigue, but the reverse is true in the low-stress, high-cycle region; large diameter (5.6-mil) filaments impart superior fatigue properties to composites than do 4.0-mil filaments; aluminum matrix composites possess better fatigue properties in the longitudinal direction (that is, parallel with reinforcing filaments), however, titanium matrix composites possess higher fatigue strengths in off-axis directions; disbonds result in lower fatigue strengths; and, heat treatment of the matrix improves transverse fatigue properties but has little or no effect on longitudinal fatigue strength. The fatigue properties of boron 6061 aluminum, Borsic 6061 aluminum, boron stainless steel 6061 aluminum, Borsic stainless steel 6061 aluminum, Borsic titanium 6061 aluminum, and Borsic 6Al-4V titanium are presented and compared to facilitate use by design and materials engineers.

KEY WORDS: composite materials, fibers, boron, aluminum, titanium

Advanced composite materials show considerable promise for weight and volume-critical applications, for example, aircraft and space vehicles. Metal matrix composites are particularly attractive because of their very desirable properties (high tensile, compression, and shear strengths, and modulii), stability (retention of properties at cryogenic and elevated temperatures, and resistance to degradation in various environments

[1] Staff scientist, General Dynamics Corporation, Convair Division, San Diego, Calif. 80807.

such as humidity, radiation, lightning, etc.), and fabricability (ability to be joined by welding, brazing, diffusion bonding, adhesive bonding, mechanical fastening or combinations of the foregoing plus ability to be formed into structural shapes and machined by a variety of methods).

There does appear, however, to be a dearth of information on the properties, particularly axial fatigue properties, of metal matrix composites in the literature. The objectives of this paper are to provide basic fatigue properties on several metal matrix composite materials and to compare these properties as a function of filaments, matrix, layup, volume content, and heat treatment.

Test Materials and Procedure

Axial fatigue properties were determined on a number of promising metal matrix composite materials. The test materials, constituents, layups, and tensile strength and modulus properties are given in Table 1. All of the test materials were diffusion-bonded sheet material, 0.040 to 0.050 in. thick. Details of the raw materials, processing, and quality assurance testing are given in Refs *1-3*. Composite materials were tested in the as-received (*F*) and heat treated (*ST* and *A*) conditions. The heat treatment consisted of solution treating at 980°F for 30 min and aged at 350°F for 8 h. Fatigue test specimens were straight-sided, 6 in. long by 1/2 in. wide with adhesively bonded 2-in.-long tapered aluminum tabs for longitudinal specimens, and 4 in. long by 1/2 in. wide with 1-in.-long tabs for transverse specimens.

A Sonntag SF-1U fatigue machine was used for testing. The cyclic mode was sinusoidal and operated at a frequency of 1800 cpm. Since the load capacity of this machine was lower than that required for the composites, a load multiplier was attached to the machine which magnified the cyclic loads by a factor of five.

Previously used gripping techniques were found to be inadequate at the higher cyclic loads required for composites. A technique was developed that was successful at all cyclic loads required to obtain *S-N* curves. Both grip ends of the specimens were placed between two L-shaped steel fixtures that were bolted to the machine loading platens. Drilled through the steel fixtures were two 9/16-in.-diameter holes. These holes were located in such a manner that when two 9/16-in. bolts were inserted in these holes, the bolts straddled the edges of the grip ends of the specimen. To further increase the gripping power of the fixtures, a special abrasive cloth was placed between each specimen-to-fixture interface. The abrasive cloth has the appearance of standard open-weave wire screen. This cloth has two beneficial features for a secure grip:

TABLE 1 – *Test materials.*

Test Material	Constituents[b]	Layup	Longitudinal Strength, ksi	Longitudinal Modulus, psi × 10^6	Transverse Strength, ksi	Transverse Modulus, psi × 10^6
Boron aluminum	50 v/o 4-mil boron 50 v/o 6061 aluminum	unidirectional	168	33.2	15	19.8
Boron aluminum	45 v/o 4-mil boron 55 v/o 6061 aluminum	0–90 deg crossply	79.7	19.1	...	...
Boron aluminum	48.7 v/o 5.6-mil boron 51.3 v/o 6061 aluminum	unidirectional	199	30.8	21	21.6
Boron stainless steel aluminum	43.4 v/o 4-mil boron 4.8 v/o 2-mil stainless steel wire 50.8 v/o 6061 aluminum	unidirectional boron (stainless steel at 90 deg to boron)	170	29.8	37	16.6
Borsic[a] aluminum	47.3 v/o 4.2-mil Borsic 52.7 v/o 6061 aluminum	unidirectional	168	32.5	14.5	19.6
Borsic[a] stainless steel aluminum	42.1 v/o 4.2-mil boron 5.6 v/o 2-mil stainless steel wire 52.3 v/o 6061 aluminum	unidirectional Borsic (stainless steel at 90 deg to Borsic)	161	32.4	32.4	19.2
Borsic[a] titanium aluminum	49.1 v/o 4.2-mil Borsic 23.6 v/o 1-mil beta-3 titanium 37.3 v/o 6061 aluminum	unidirectional	157	30.8	26.2	14.6
Borsic[a] titanium	37.6 v/o 5.7-mil Borsic 62.4 v/o Ti-6Al-4V	unidirectional	147	28.1	56	21.2

[a] Silicon-carbide coated boron filament.
[b] v/o = volume percent.

(1) open-weave design that increases the frictional holding force; and, (2) abrasive coating on both surfaces of the cloth that becomes embedded in the contact surfaces of both the fixtures and tabs. The two bolts were torqued to a level that just secured the specimen.

Before the fatigue test was started, the alignment of the specimen was determined to ensure axial loading. A preload was used to obtain a minimum/maximum load ratio (R) of +0.10. Fatigue tests were continued to failure or a maximum of one to ten million cycles with the maximum tension stress used for each specimen being based on a percent of the ultimate tensile strength. All failures occurred in the gage length, although, generally, near the edge of the doublers. The test data were then plotted on semi-logarithmic paper to obtain the characteristic S-N curves.

Results and Discussion

The test results are plotted as S-N curves in Figs. 1–10. Tabular results may be found in Refs *1–3*. Figures 1 and 2 present axial fatigue data on 4.0-mil boron aluminum composite material in the longitudinal and transverse directions. Figure 3 presents similar data on 5.6-mil boron aluminum. Figures 4 and 5 give the fatigue properties of boron stainless steel aluminum in both the longitudinal and transverse directions, while Fig. 6 gives longitudinal fatigue data on Borsic aluminum. Figures 7

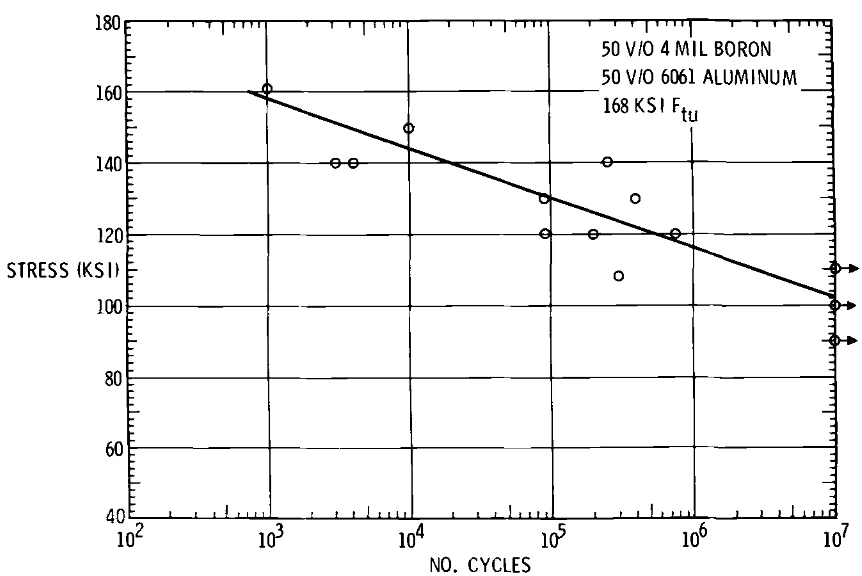

FIG. 1—*Fatigue properties of boron aluminum, longitudinal.*

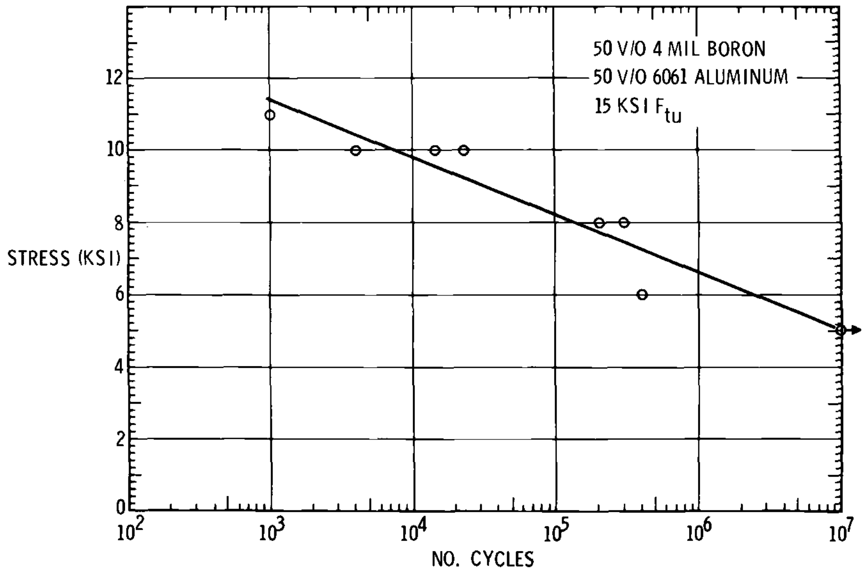

FIG. 2—*Fatigue properties of boron aluminum, transverse.*

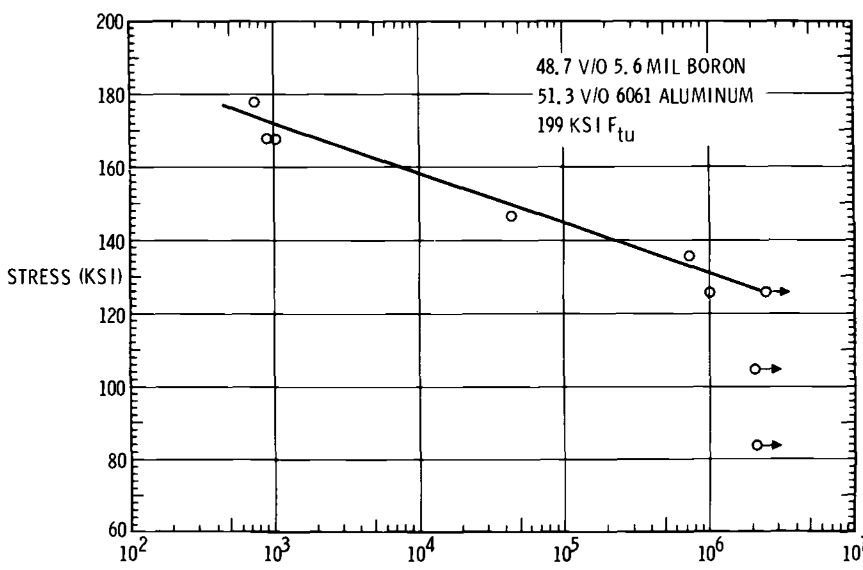

FIG. 3—*Fatigue properties of 5.6-mil boron aluminum, longitudinal.*

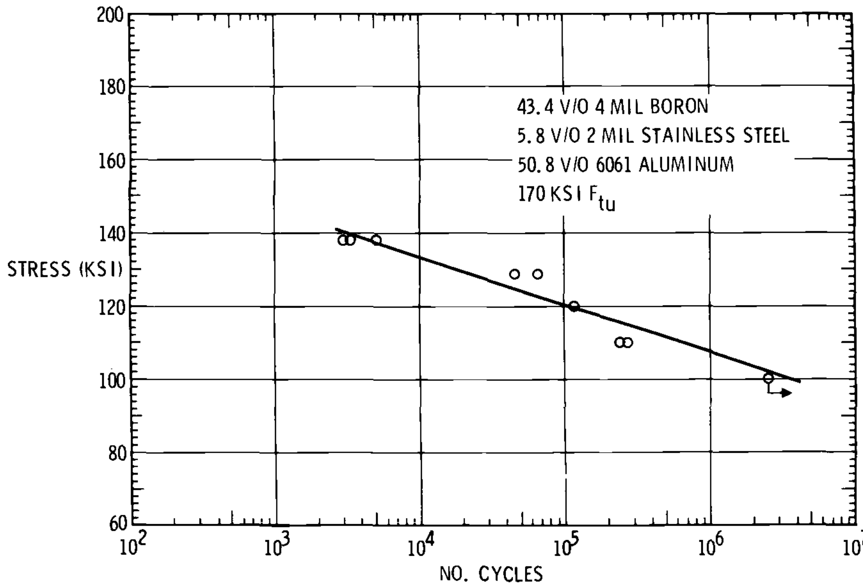

FIG. 4—*Fatigue properties of boron stainless steel aluminum, longitudinal.*

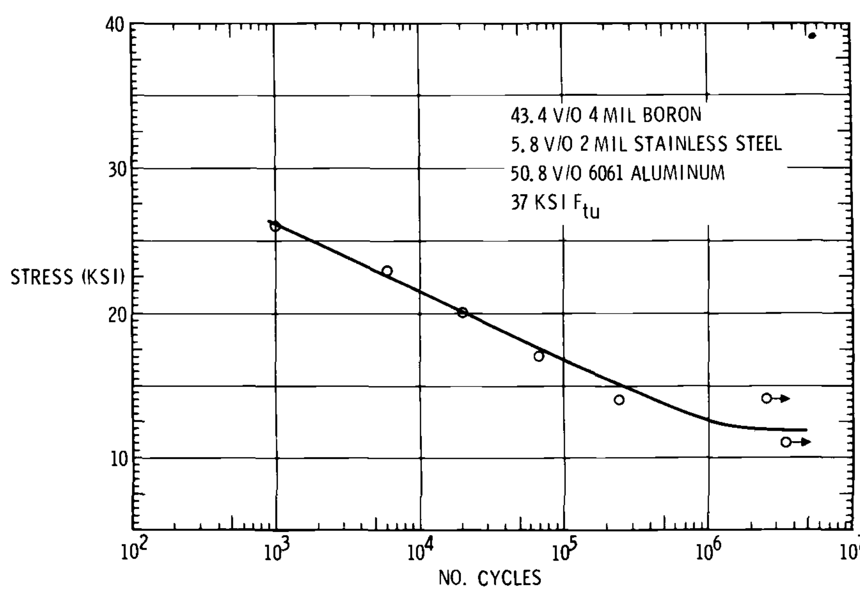

FIG. 5—*Fatigue properties of boron stainless steel aluminum, transverse.*

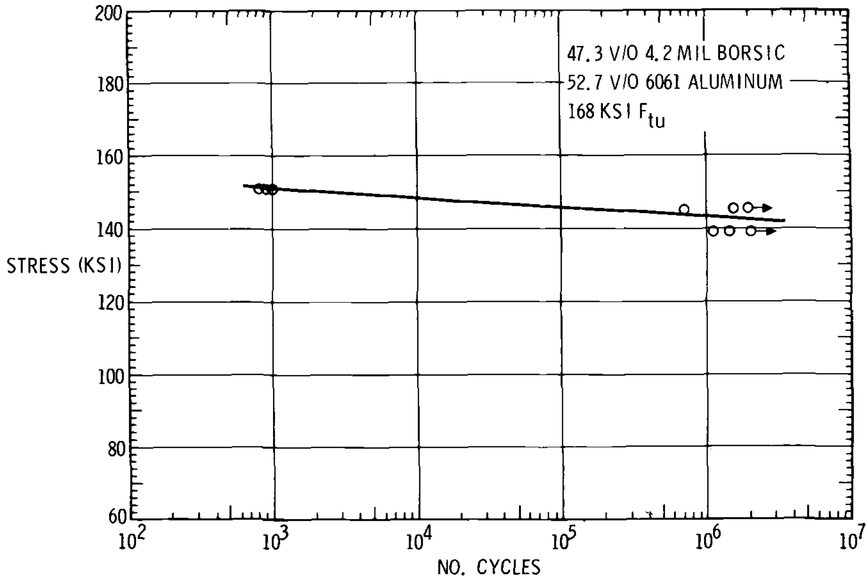

FIG. 6—*Fatigue properties of Borsic aluminum, longitudinal.*

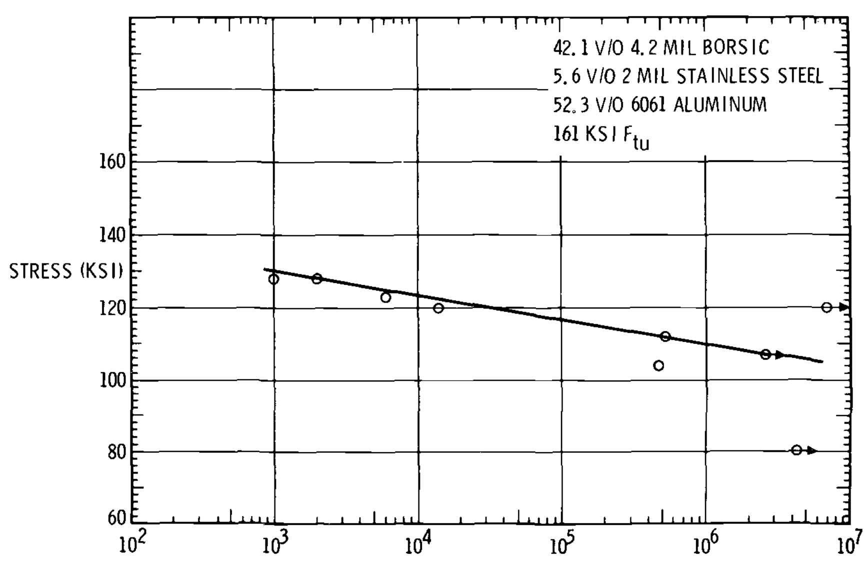

FIG. 7—*Fatigue properties of Borsic stainless steel aluminum, longitudinal.*

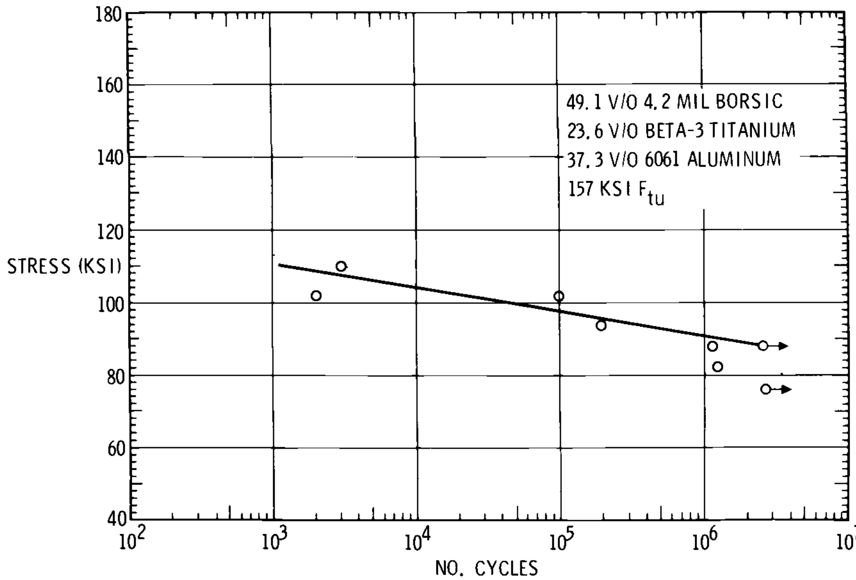

FIG. 8—*Fatigue properties of Borsic titanium aluminum, longitudinal.*

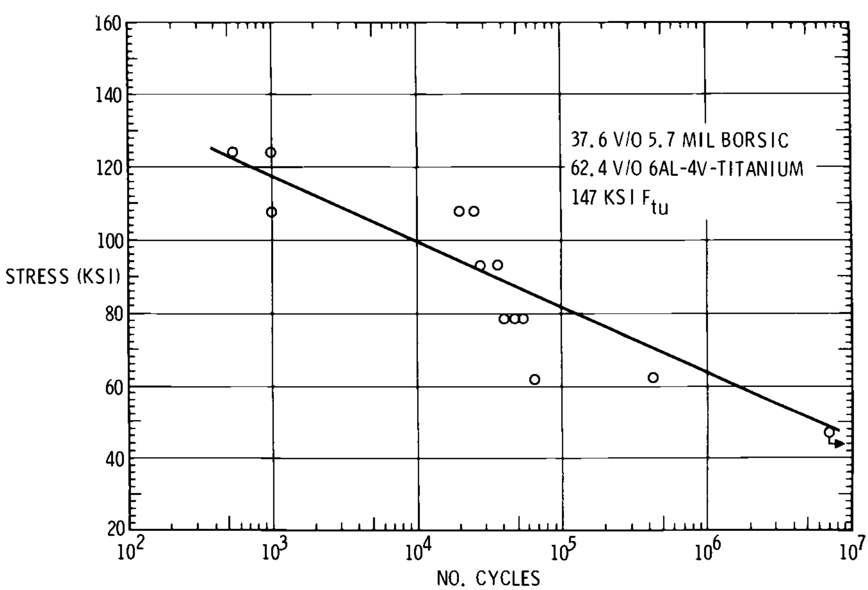

FIG. 9—*Fatigue properties of Borsic titanium, longitudinal.*

and 8 give longitudinal fatigue data on Borsic stainless steel aluminum and Borsic titanium aluminum, respectively. Figures 9 and 10 present the axial fatigue properties of Borsic titanium in the longitudinal and transverse directions. Figures 1 through 10 present actual fatigue data points as well as a best fit *S-N* curve for the test data and shows typical scatter obtained in fatigue tests of metal matrix composite materials.

Comparisons of the axial fatigue properties of metal matrix composite materials are given in Figs. 11–17. Figure 11 compares longitudinal fatigue properties as a function of filament type, filament size, and volume content of filament, while Fig. 12 makes a similar comparison for transverse fatigue properties. It is apparent from these figures that the fatigue strengths are considerably higher for the longitudinal direction than for the transverse direction in unidirectional boron-aluminum composites. Runouts (10^6 to 10^7 cycles) occur at 50 to 80 percent of the ultimate strength of the material in the longitudinal direction and at 25 to 50 percent for the transverse direction. It is also apparent that the fatigue strength is highly dependent upon the volume content. The longitudinal fatigue strengths of 50 volume percent boron aluminum are over twice as high as those for 25 volume percent boron aluminum. However, in the transverse direction the reverse is true. Also, as can be seen in Fig. 11, the 5.6-mil-diameter boron is superior to the 4.0-mil boron for the fatigue

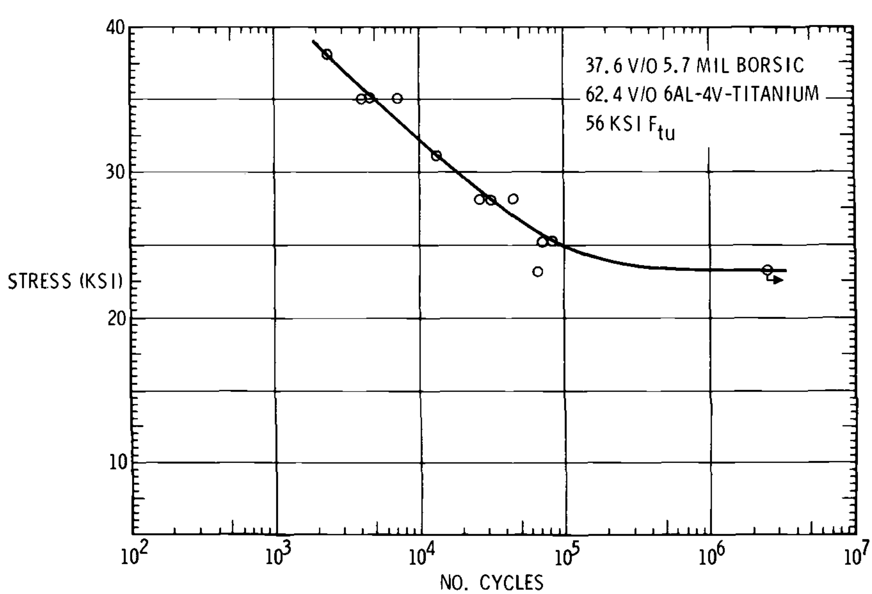

FIG. 10—*Fatigue properties of Borsic titanium, transverse.*

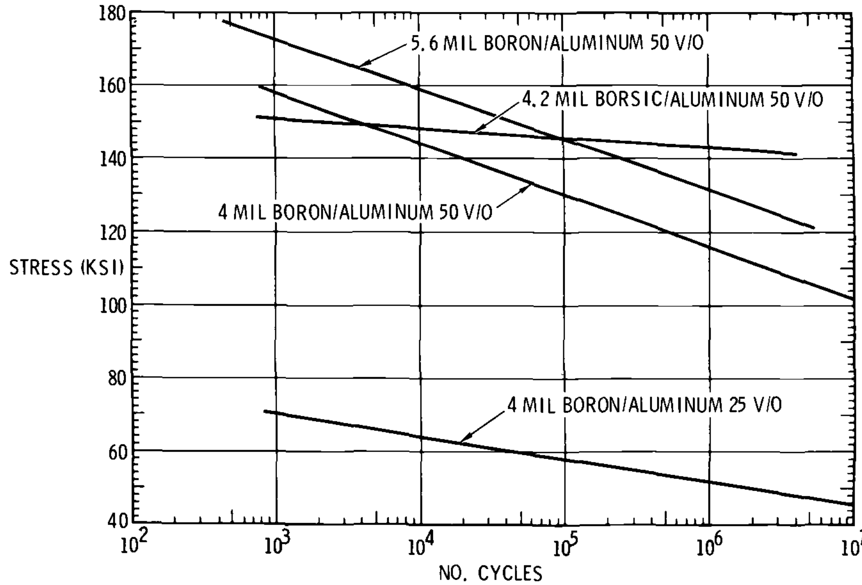

FIG. 11—*Effect of filament type, size, and volume on longitudinal fatigue properties.*

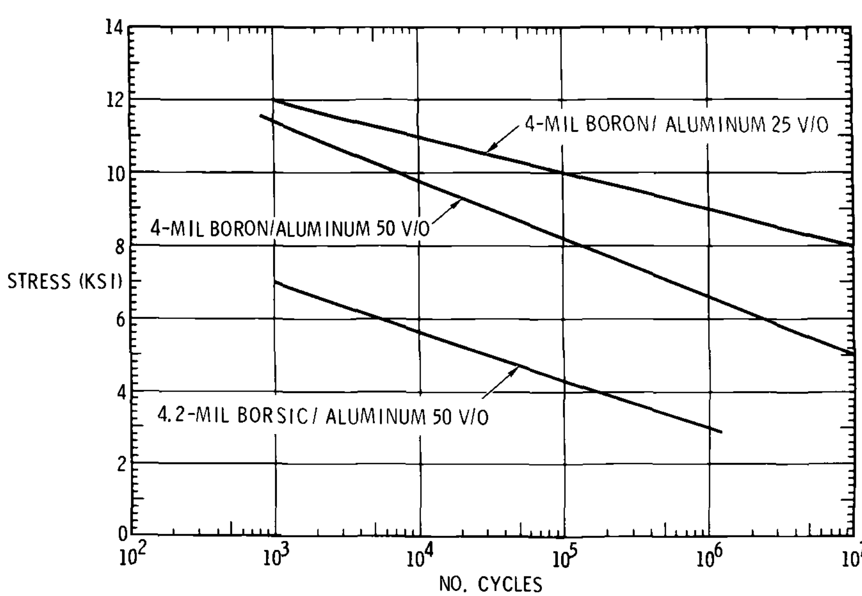

FIG. 12—*Effect of filament type and volume on transverse fatigue properties.*

properties of boron aluminum. Finally, boron aluminum has fatigue strengths superior to those of Borsic aluminum in the high-stress, low-cycle region for the longitudinal direction and at all stress levels for the transverse direction.

Figures 13 and 14 show the effect of heat treatment on the fatigue properties of metal matrix composites. There is little or no effect of heat treatment on longitudinal properties as can be seen from the data in Fig. 13, however, transverse properties can be significantly improved as shown for Borsic aluminum or essentially unaffected as shown for boron stainless steel aluminum in Fig. 14. The increase in the transverse fatigue strength of Borsic aluminum is to be expected due to the improvement in strength properties of the 6061 aluminum matrix material with heat treatment.

The effect of layup on the longitudinal fatigue properties of metal matrix composites is given in Fig. 15. The most obvious observation is that the fatigue strengths of unidirectional material are considerably higher than for 0 to 90 crossply material. Also, it is noted that the addition of small amounts (5 percent) of stainless steel wire to a boron-aluminum composite results in a slight decrease in longitudinal fatigue strengths, but significantly improves transverse fatigue strengths, as will be seen later in Fig. 17.

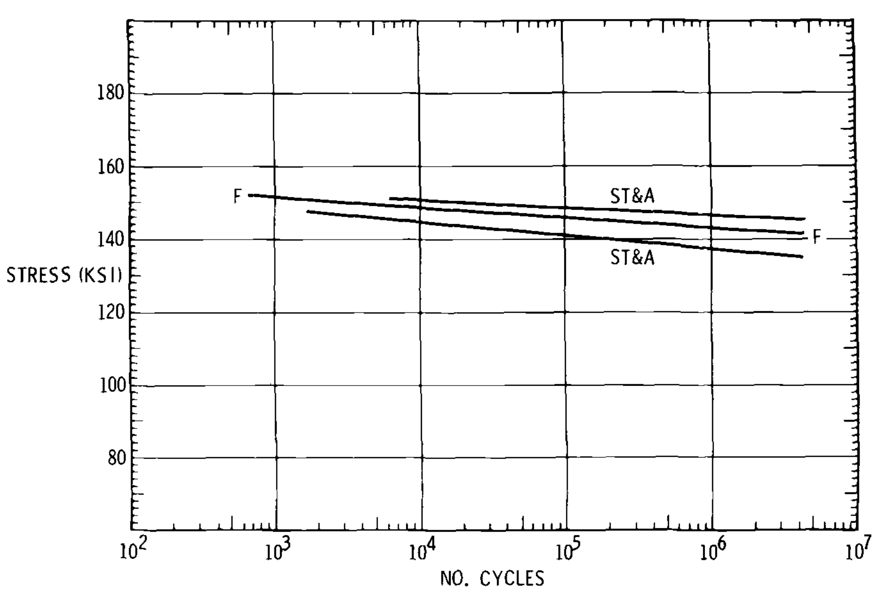

FIG. 13—*Effect of heat treatment on longitudinal fatigue of 4.2-mil Borsic aluminum.*

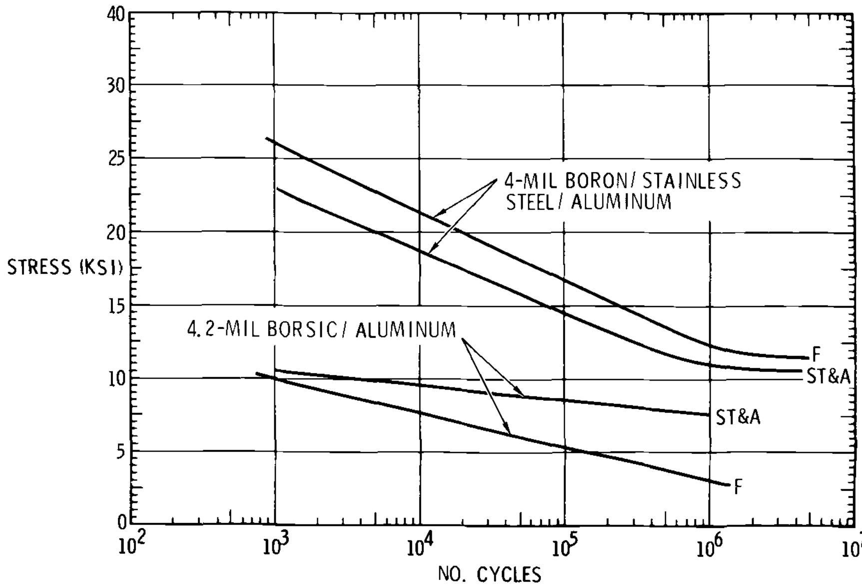

FIG. 14—*Effect of heat treatment on transverse fatigue.*

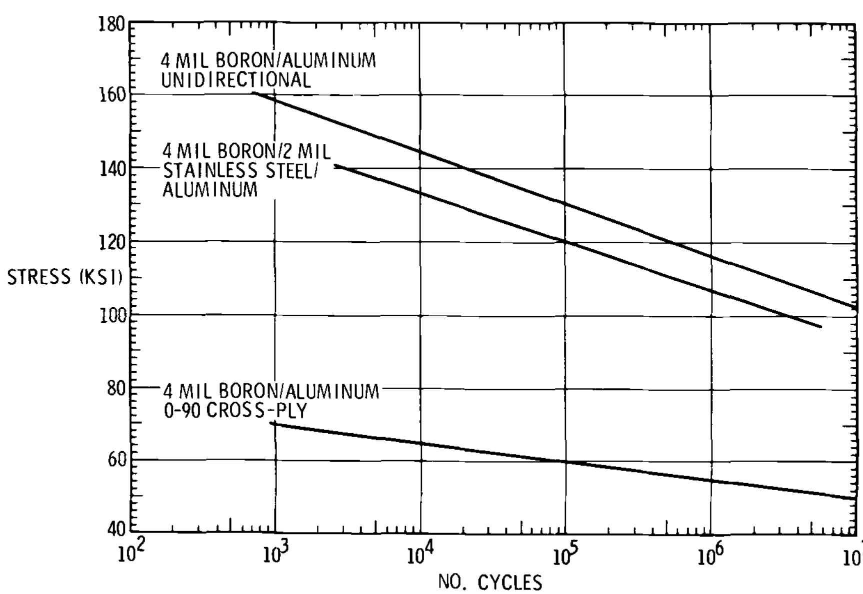

FIG. 15—*Effect of layup on longitudinal fatigue properties.*

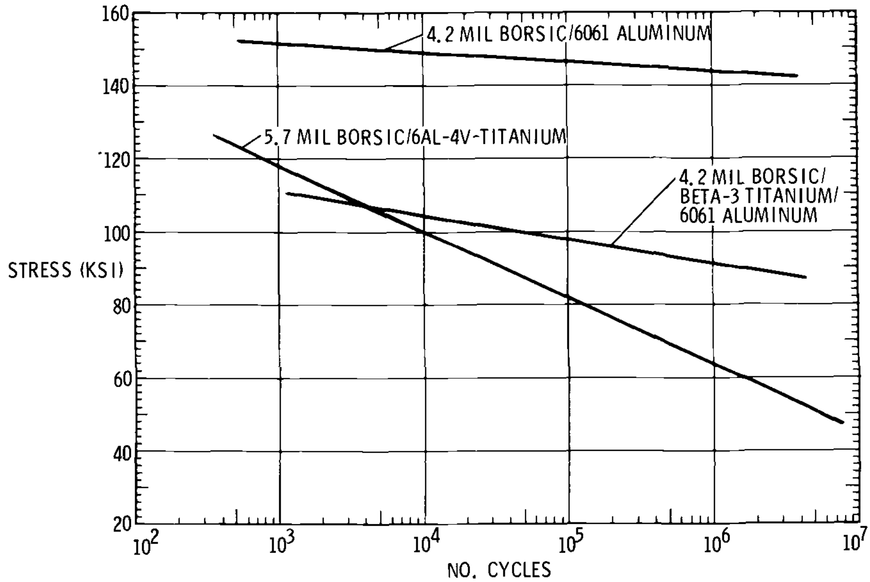

FIG. 16—*Effect of matrix material on longitudinal fatigue.*

Figures 16 and 17 present the effect of various matrix materials on the longitudinal and transverse fatigue properties of several composite materials. The highest longitudinal fatigue strengths are obtained with an aluminum matrix, whereas, the opposite is true for the transverse direction in which a 100 to 400 percent improvement in fatigue strengths is obtained for the titanium matrix or stainless steel wire additions as compared to the standard boron-aluminum material.

The *S-N* curves of a number of metal matrix composite materials have been presented and compared to facilitate their use by design and materials engineers in the selection of advanced composite materials for applications involving a fatigue environment.

Conclusions

Based upon the results of this study, the following conclusions are made:

1. Advanced metal matrix composite materials possess very high fatigue strengths in the longitudinal direction with runouts occurring at 50 to 80 percent of the ultimate strength.

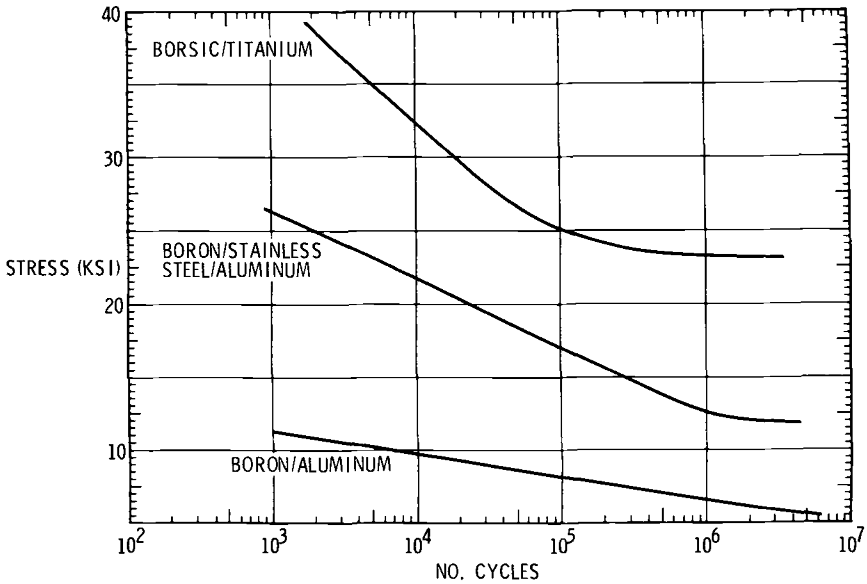

FIG. 17—*Effect of matrix material on transverse fatigue.*

2. The fatigue properties of 5.6-mil-diameter boron aluminum are superior to those of 4.0-mil boron aluminum.
3. Aluminum matrix composites possess higher fatigue strength properties in the longitudinal direction but lower in the transverse direction than titanium matrix composites.
4. Heat treatment significantly improves transverse fatigue strengths but has little or no effect on longitudinal fatigue properties.
5. Addition of stainless steel wires or titanium foils to a boron-aluminum composite significantly improves transverse fatigue strengths, but slightly reduces longitudinal fatigue strength properties.

Acknowledgments

The author wishes to acknowledge the assistance of his associates who contributed to this work, in particular to N. R. Adsit and C. J. Kropp, who developed the testing technique, and M. Spencer and E. Wehrhan, who performed the fatigue testing. The work was performed under the sponsorship of the Air Force Materials Laboratory and the Convair Aerospace Division of General Dynamics Corporation, whose permission to publish this work is gratefully acknowledged.

References

[1] Scahefer, W. H. et al, "Evaluation of the Structural Behavior of Filament Reinforced Metal Matrix Composites," Vol. 2, Technical Report AFML-TR-69-36, Air Force Materials Laboratory, Dayton, Ohio, Jan. 1969.

[2] Miller, M. F. et al, "Development of Improved Metal-Matrix Fabrication Techniques for Aircraft Structures," Technical Report AFML-TR-71-181, Air Force Materials Laboratory, Dayton, Ohio, July 1971.

[3] Hertz, J. et al, "Advanced Composite Applications for Spacecraft and Missiles," Phase I, Final Report, Vol. 2, Technical Report AFML-TR-71-186, Air Force Materials Laboratory, Dayton, Ohio, March 1972.

G. L. Roderick,[1] R. A. Everett,[1] and J. H. Crews, Jr.[2]

Debond Propagation in Composite-Reinforced Metals

REFERENCE: Roderick, G. L., Everett, R. A., and Crews, J. H., Jr., **"Debond Propagation in Composite-Reinforced Metals,"** *Fatigue of Composite Materials, ASTM STP 569,* American Society for Testing and Materials, 1975, pp. 295–306.

ABSTRACT: Strain energy release rates were used to correlate cyclic debonding between metal sheets and composite reinforcement. An expression for the strain energy release rate was derived and applied to fatigue test results for three material systems: graphite bonded to aluminum with both a room temperature and an elevated temperature curing adhesive; and, S-glass bonded to aluminum with an elevated temperature curing adhesive. For each material system, specimens of several thicknesses were tested with a range of fatigue loads. Cyclic debonding was monitored using a photoelastic technique. A close correlation was found between the observed debond rates and the calculated strain energy release rates for each material system.

KEY WORDS: fatigue tests, fatigue (materials), adhesive bonding, composite materials, structural engineering

Adhesive bonding is becoming widely used in aircraft structures for joining structural components and making efficient materials. In joints, it eliminates severe stress concentrations that are usually introduced with mechanical fasteners. Although it can be advantageous in metal-to-metal joints, it is particularly applicable to joining composite materials whose static strength is very sensitive to stress concentrations. Also, bonding is used to make more efficient structures by joining separate materials to form one system. For example, hybrid systems, formed by bonding metal and composite layers, have higher static strength for equal weight and stiffnesses [*1*][3] than metals while being more reliable than composites

[1] Aerospace technologists, United States Army Air Mobility Research and Development Laboratory-Langley Directorate, National Aeronautics and Space Administration, Langley Research Center, Hampton, Va. 23665.

[2] Aerospace technologist, National Aeronautics and Space Administration, Langley Research Center, Hampton, Va. 23665.

[3] The italic numbers in brackets refer to the list of references appended to this paper.

alone. Indeed, composites derive their high efficiency from bonded collections of constituent materials.

When these bonded structures are subject to fatigue loading they may be susceptible to a little-considered mode of fatigue failure, cyclic debonding [2]. Because most practical structures will be subject to fatigue loading, cyclic debonding should be considered in their design. Unfortunately, a designer has virtually no rationale to account for cyclic debonding; consequently, either the reliability or efficiency of his structure may suffer. As a first step in supplying a design rationale, the objective of this paper is to present a cyclic debond analysis.

The analysis was developed for simple laminated specimens made of aluminum alloy sheet bonded to graphite or fiberglass composites and tested under constant amplitude fatigue loading. It is based on the correlation of the observed debonding with the rate of releasing strain energy as the debond extended.

Nomenclature

The units for the physical quantities defined in this paper are given in the International System of Units (SI) [3]. The measurements and calculations were made in the U.S. Customary Units.

a	Debond length, m
da/dN	Debond propagation rate, m/cycle
c,n	Curve fit parameters
E	Young's modulus, MN/m^2
G	Strain energy release rate, J/m
L	Length, m
P	Applied load, N
R	Ratio of minimum-to-maximum applied stress
S	Stress in composite core of Region A, MN/m^2
t	Thickness, m
ΔT	Change in temperature, K
U	Strain energy, J
V	Volume, m^3
w	Specimen width, m
x,y	Cartesian coordinates, m
α	Thermal expansion coefficient, K^{-1}
δ	Deflection, m
ϵ	Strain
σ	Stress, MN/m^2
ϕ	Strain energy density, J/m^3

Subscripts

1 Aluminum cover
2 Composite core
A Region A
B Region B
C Region C

Experimental Procedure

Specimens and Loading

The specimen configuration used in the present study is shown in Fig. 1. The specimen was composed of two 7075-T6 aluminum alloy sheets bonded to a unidirectional composite core of graphite or S-glass (see Table 1). Two bonding materials were used for the graphite core specimens: EPON 927 which cures at room temperature (material system 1, Table 2), and AF 126 which cures at 394 K (material system 2, Table 2). The AF 126 was also used to bond the S-glass core specimens (material system 3, Table 2). The abrupt change in section of the specimen introduced a severe stress concentration in the bonding materials. Under cyclic loading, debonding started readily at this high stress concentration.

The specimens were tested axially under constant amplitude fatigue loading with $R = 0.1$. Maximum stresses in the unreinforced composite core range from 211 to 1210 MN/m^2. All of the tests were performed at a frequency of 10 Hz.

Measurement of Debond Rates

The debond front was monitored continuously by a photoelastic technique. Photoelastic coatings were bonded to the aluminum sheets, and the specimen was viewed through a polarizer and quarter-wave plate. Under loading, isochromatic fringes developed at the debond front due

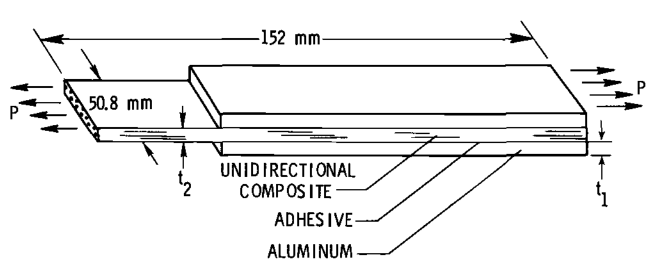

FIG. 1—*Specimen configuration.*

TABLE 1—*Material properties.*

Material	E	α
7075-T6 aluminum alloy	71×10^3	22.5×10^{-6}
Graphite-epoxy	131×10^3	-0.38×10^{-6}
S-glass-epoxy	61×10^3	3.60×10^{-6}

to the high strain gradient in that vicinity. Figure 2 shows the location of the photoelastic coatings on the specimen and typical isochromatic fringes. The isochromatic fringes were photographed at specified load cycle intervals to relate the debond front location to the number of applied load cycles.

Strain Energy Release Rate Equations

Fatigue crack propagation rates in metals have been correlated using the strain energy release rate, G, [*4*] where

$$G = P\left(\frac{d\delta}{da}\right) - \frac{dU}{da} \tag{1}$$

The term $P(d\delta/da)$ is the work done by the applied load as the crack extends and dU/da is the change in strain energy as the crack extends. Intuition suggests that a similar correlation may be valid for debond propagation. Consequently, an expression for G was developed for the specimen configuration used in this study. This expression was determined using a one-dimensional elasticity analysis described by the following discussion.

To simplify the analysis, the specimen was separated into three regions: A, B, and C (Fig. 3). In Regions A and C, only, uniform stresses in the x direction are significant. Consequently, these regions could be analyzed by an elementary elasticity method. Region B had a complex stress distribution and could not be analyzed using elementary methods. The stress distribution in Region B was assumed to remain constant as the debond

TABLE 2—*Specimen material systems.*

Material System	Composite	Bonding Material	Bonding Material Thickness, mm	Cure Temperature, K
1	Graphite-epoxy	EPON 927	0.13	RT[a]
2	Graphite-epoxy	AF 126	0.13	394
3	S-glass-epoxy	AF 126	0.13	394

[a] Room temperature (RT) = 294 K.

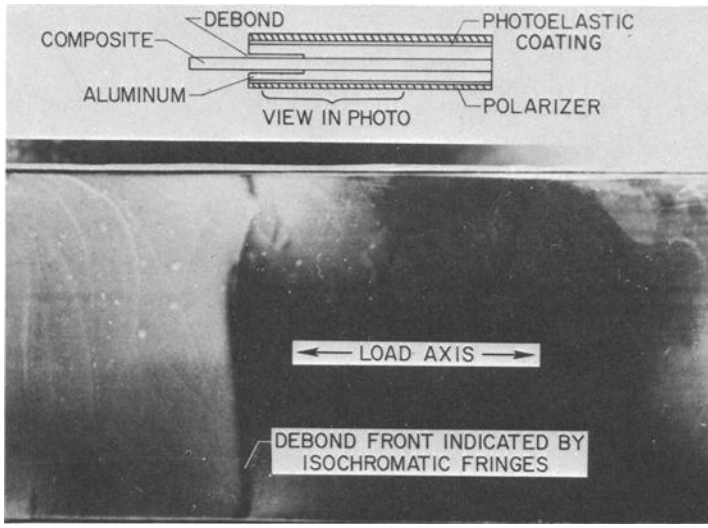

FIG. 2—*Partially debonded specimen.*

extended. As will be shown, this constancy eliminated the need to calculate the stress distribution in Region B.

An expression for $(d\delta/da)$ in Eq 1 was derived from the change in the end deflection of the specimen, $d\delta$, caused by an increment of debonding, da. Before debonding occurred, the end deflection was given by

$$\delta = \delta_A + \delta_B + \delta_C \tag{2}$$

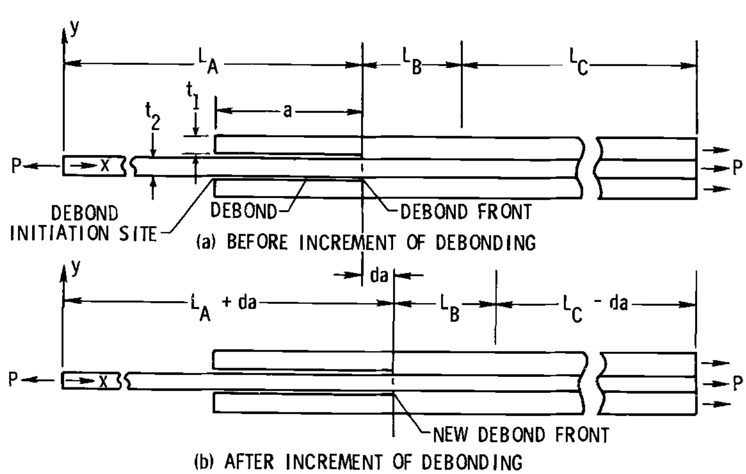

FIG. 3—*Test specimen before and after an increment of debonding.*

and after debonding by

$$\delta' = \delta'_A + \delta_B + \delta'_C \tag{3}$$

where the primes indicate deflection after debonding. The stress distribution in Region B was assumed to be the same before and after the region translated; thus, the δ_B term did not change with debonding. To find $d\delta$, Eq 2 was subtracted from Eq 3 yielding

$$\delta' - \delta = d\delta = (\delta'_A - \delta_A) + (\delta'_C - \delta_C) \tag{4}$$

The deflections on the right side of Eq 4 can be expressed in the general form

$$\delta = \epsilon L \tag{5}$$

Substitution of Eq 5 into Eq 4 yields

$$d\delta = [\epsilon_A(L_A + da) - \epsilon_A L_A] + [\epsilon_C(L_C - da) - \epsilon_C L_C] \tag{6}$$

$$d\delta = (\epsilon_A - \epsilon_C)\, da \tag{7}$$

or

$$\frac{d\delta}{da} = (\epsilon_A - \epsilon_C) \tag{8}$$

The expression for dU/da in Eq 1 was derived by calculating the change of strain energy in the specimen, dU, resulting from an increment of debonding, da. Employing the same reasoning used in the development of Eq 4, the change in strain energy is

$$U' - U = dU = (U'_A - U_A) + (U'_C - U_C) \tag{9}$$

The strain energies on the right side of Eq 9 can be expressed in the general form

$$U = \phi V \tag{10}$$

Substitution of Eq 10 into Eq 9 yields

$$\begin{aligned} dU = {} & \{\phi_{A2} w t_2 (L_A + da) - \phi_{A2} w t_2 L_A\} \\ & + \{[2\phi_{C1} w t_1 (L_C - da) + \phi_{C2} w t_2 (L_C - da)] \\ & - [2\phi_{C1} w t_1 L_C + \phi_{C2} w t_2 L_C]\} \end{aligned} \tag{11}$$

$$dU = w[\phi_{A2} t_2 - (\phi_{C2} t_2 + 2\phi_{C1} t_1)]\, da \tag{12}$$

or

$$\frac{dU}{da} = w[\phi_{A2} t_2 - (\phi_{C2} t_2 + 2\phi_{C1} t_1)] \tag{13}$$

Substituting Eqs 8 and 13 into Eq 1 yields

$$G = P(\epsilon_A - \epsilon_C) - w[\phi_{A2}t_2 - (\phi_{C2}t_2 + 2\phi_{C1}t_1)] \tag{14}$$

This equation is evaluated in the appendix in terms of applied stress, temperature change, material parameters, and specimen configuration and leads to

$$G = \frac{t_1 t_2 E_1 w}{E_2(2t_1E_1 + t_2E_2)} [S - \Delta T(\alpha_1 - \alpha_2)E_2]^2 \tag{15}$$

Results and Discussions

Figure 4 shows a sample plot of debond length against the number of applied load cycles. The shape of this debond curve was typical for all three material systems tested. Initially, debonding was nonlinear with respect to the number of applied load cycles, but became linear as the debond progressed. The main focus of this paper is on the linear portion of the debond behavior; however, a brief discussion of the nonlinear region is merited.

Nonlinear debonding occurred when the debond front was near the change in cross section of the specimen. The texture of the failure surface indicated that the failure mechanism changed as the debond extended. Figure 5 shows a photograph of the fracture surface of a typical debond specimen of material system 2. The graphite-composite core is shown on the left and the mating aluminum cover sheet is shown on the right. As the photograph indicates, the failure mechanism was initially cohesive but changed to predominantly adhesive as the debond extended. Similar behavior was observed for material system 3. However, for material

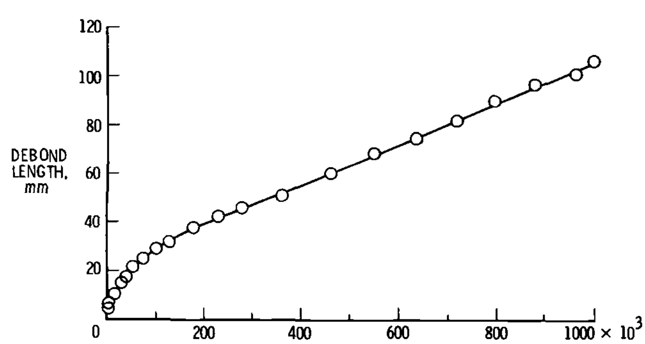

FIG. 4—*Typical variation of debond length with cycles for all three material systems.*

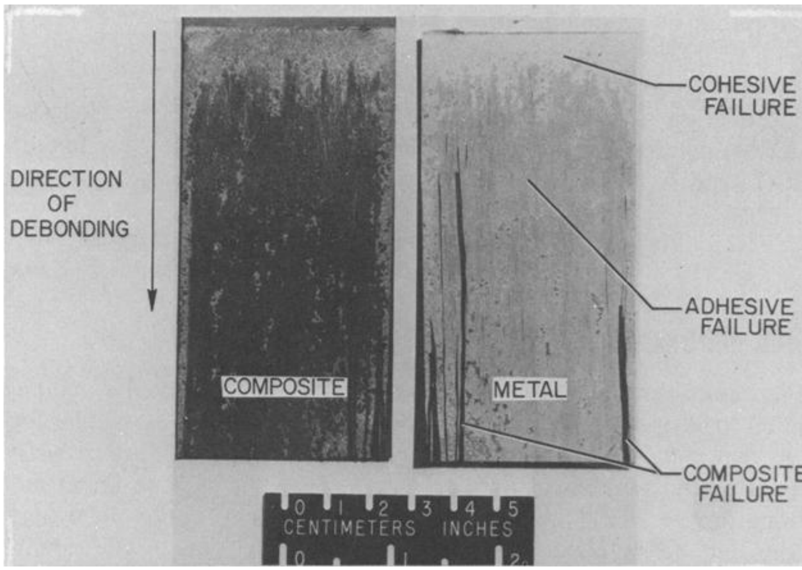

FIG. 5—*Debonded surfaces of a material system 2 specimen.*

system 1, the failure mechanism seemed to be reversed; initially the failure was adhesive but changed to cohesive as the debond extended. For all three material systems, the nonlinear portion of the debond behavior seemed to be related to a transition in failure mechanism.

Debond propagation rates were determined from the linear portion of debond versus cycle plot for each specimen. Figure 6 is a plot of rate against G, Eq 15, for the three material systems. This figure shows debond rate to be a single valued function of G for all material thicknesses. Table 3 presents these data in tabular form. An equation of a form which had successfully correlated fatigue crack propagation data for isotropic metals [5] is

$$\frac{da}{dN} = c(G)^n \tag{16}$$

This equation fits the data in Fig. 6 quite well (dashed curves). The constants, c and n, were determined using least-squares techniques and are given in the following table

Material System	c	n
1	1.19×10^{-9}	3.30
2	2.32×10^{-9}	2.15
3	5.63×10^{-9}	3.76

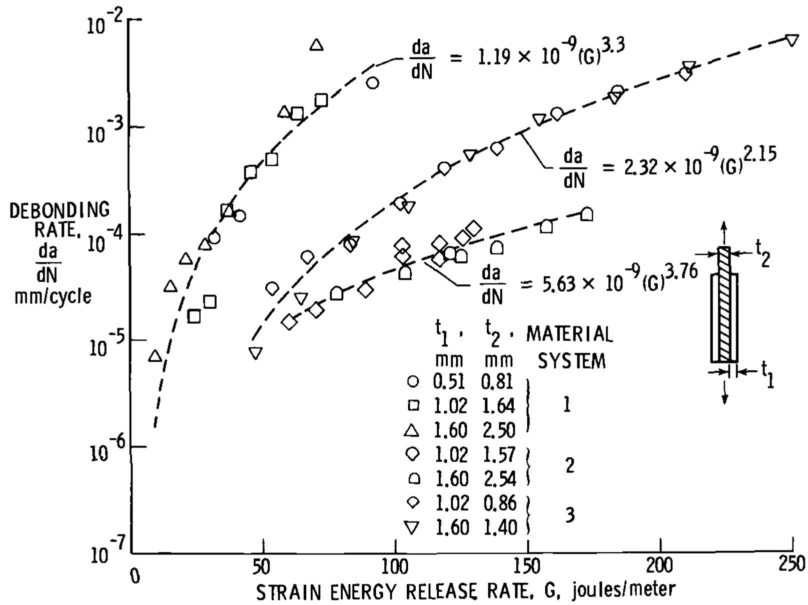

FIG. 6—*Variation of debond with strain energy release rate.*

TABLE 3—*Strain energy release rates and cyclic debond rates.*

Material System Type	Thickness, mm t_1	t_2										
			S[a]	504	706	807	1210	...	...	...	...	...
	0.51	0.81	da/dN[b]	0.000714	0.092	0.146	2.500	...	...	...	...	...
			G[c]	16.1	31.5	41.2	92.6	...	...	...	...	...
			S	426	475	527	590	639	698	746	...	...
Type 1	1.02	1.64	da/dN	0.0168	0.0229	0.166	0.373	0.498	1.32	1.78	...	...
			G	23.6	29.3	36.2	45.3	53.2	63.4	72.4	...	...
			S	211	270	324	376	429	543	598	...	...
	1.60	2.50	da/dN	0.00689	0.0315	0.0569	0.0785	0.163	1.32	5.59	...	...
			G	8.9	14.7	20.8	28.0	36.6	58.6	70.9	...	...
			S	390	445	541	605	605	667	667	703	716
	1.02	1.57	da/dN	0.015	0.0193	0.0302	0.0635	0.0779	0.0815	0.0592	0.0899	0.112
			G	60	70	89	103	103	117	117	126	130
Type 2			S	325	420	478	490	535	589	631	...	...
	1.60	2.54	da/dN	0.0279	0.0437	0.065	0.0627	0.0734	0.116	0.144	...	...
			G	78	104	121	125	139	158	173	...	...
			S	334	390	446	507	558	614	670	725	781
	1.02	0.86	da/dN	0.0305	0.0607	0.0772	0.184	0.409	0.605	1.26	2.03	2.95
			G	53	67	83	102	119	139	162	185	211
Type 3			S	217	274	328	384	438	492	547	595	658
	1.60	1.40	da/dN	0.0078	0.0254	0.0838	0.181	0.546	1.14	1.85	3.33	5.92
			G	47	64	84	105	129	155	184	212	251

[a] Stress, MN/m².
[b] Debond rate, μm/cycle.
[c] Strain energy release rate with thermal residual stresses, G, joules/meter.

Equation 16 may be useful to predict debond rates in composite reinforced structures subjected to fatigue loading for the systems studied. However, for other materials systems, appropriate values of c and n must be obtained from cyclic test data.

Figure 6 shows that c and n differ for each material system. This difference was probably due to the different bond strength and residual thermal stress of each system. The residual thermal stress in the graphite aluminum specimens bonded at elevated temperature was calculated to be as high as 120 MN/m^2 in the graphite core. Because residual thermal stresses of this magnitude are significant in comparison to the applied stress in the core, they were included in the derivation of the strain energy release rate. However, because both the residual thermal stresses and bond strength differed from system to system, isolation of either effect was not possible for the limited tests reported here.

Concluding Remarks

A fatigue analysis method was developed for cyclic debonding of laminates composed of metal and composite layers. The strain energy release rate, G, correlated the debond propagation rates from each of three series of laboratory tests for several applied loads and thicknesses. Specimens tested were graphite bonded to aluminum at room temperature, graphite bonded to aluminum at elevated temperature, and S-glass bonded to aluminum at elevated temperature. The test data were well represented by an equation of the form $da/dN = c(G)^n$. For the systems studied, a closed-form expression was developed for G, which included residual thermal stresses.

This study indicates that G promises to be a tractable tool with which to analyze the relations between cyclic debonding and fatigue loading in laminated structures. For simplicity in establishing G as a correlating parameter, tests were restricted to constant-amplitude loading at room temperature with a simple geometric configuration. The correlation achieved herein was on specific material systems that may be applicable to aircraft structures. However, to be useful for structural applications the model should be refined and verified for more complex fatigue environments and for complicated configurations. Also, since high residual thermal stresses may occur for some material systems, their effect on cyclic debonding should be established.

Appendix

Development of the Strain Energy Release Rate Equation

The strain energy release rate for debonding of a metal overlayed with a composite (Fig. 3) was given in the body of this paper by Eq 14

$$G = P(\epsilon_A - \epsilon_C) - w[\phi_{A2}t_2 - (\phi_{C2}t_2 + 2\phi_{C1}t_1)]$$

The strains in Eq 14 were found by requiring equilibrium, strain compatibility, and a constitutive relation between stress and strain in Regions A and C. Equilibrium is satisfied by

$$P = w\int \sigma \, dy \tag{17}$$

For the one-dimensional analysis used in this problem, strain compatibility was assured by assuming that the strain was constant through the thickness. The constitutive relation for the problem is given as [*6*]

$$\sigma = E(\epsilon - \alpha \, \Delta T) \tag{18}$$

Using these three relationships, the strains in Regions A and C can be calculated.

In Region A, compatibility is satisfied. Equilibrium is satisfied when

$$P = St_2w = \sigma_{A2}t_2w \tag{19}$$

The constitutive Eq for this region is

$$\sigma_{A2} = E_2(\epsilon_A - \alpha_2 \, \Delta T) \tag{20}$$

Substituting Eq 20 into Eq 19 and solving for ϵ_A yields

$$\epsilon_A = \frac{S}{E_2} + \alpha_2 \, \Delta T \tag{21}$$

For Region C, compatibility is satisfied when

$$\epsilon_{C1} = \epsilon_{C2} = \epsilon_C \tag{22}$$

Equilibrium is satisfied when

$$P = St_2w = 2t_1w\sigma_{C1} + \sigma_{C2}t_2w \tag{23}$$

The constitutive relationships for the metal and composite, respectively, are

$$\sigma_{C1} = E_1(\epsilon_C - \alpha_1 \, \Delta T) \tag{24}$$

$$\sigma_{C2} = E_2(\epsilon_C - \alpha_2 \, \Delta T) \tag{25}$$

Substituting Eq 24 and 25 into Eq 23 and solving for ϵ_C leads to

$$\epsilon_C = \frac{St_2 + \Delta T(2E_1t_1\alpha_1 + E_2t_2\alpha_2)}{2E_1t_1 + E_2t_2} \tag{26}$$

The strain energy density can be expressed as

$$\phi = \frac{\sigma^2}{2E} = \frac{[E(\epsilon - \alpha \, \Delta T)]^2}{2E} \tag{27}$$

or

$$\phi = \frac{E}{2} [\epsilon^2 - 2\epsilon\alpha \, \Delta T + \alpha^2(\Delta T)^2]$$

For Region A, substituting Eq 21 into Eq 27 yields

$$\phi_{A2} = \frac{E_2}{2} [\epsilon_A{}^2 - 2\epsilon_A\alpha_2 \, \Delta T + \alpha_2{}^2(\Delta T)^2] \tag{28}$$

Similarly for Region C, substitution of Eq 26 into Eq 27 for the metal yields

$$\phi_{C1} = \frac{E_1}{2} [\epsilon_C{}^2 - 2\epsilon_C\alpha_1 \, \Delta T + \alpha_1{}^2(\Delta T)^2] \tag{29}$$

and for the composite yields

$$\phi_{C2} = \frac{E_2}{2} [\epsilon_C{}^2 - 2\epsilon_C\alpha_2 \, \Delta T + \alpha_2{}^2(\Delta T)^2] \tag{30}$$

Substitution of Eqs 21, 23, 26, 28, 29, and 30 into Eq 14 yields

$$G = \frac{t_1 t_2 E_1 w}{E_2(2t_1E_1 + t_2E_2)} [S - \Delta T(\alpha_1 - \alpha_2)E_2]^2 \tag{31}$$

the expression for the strain energy release rate.

References

[1] Johnson, R. W. and June, R. R., "Application Study of Filamentary Composites in a Commercial Jet Aircraft Fuselage," NASA CR 112110, National Aeronautics and Space Administration, 1972.

[2] Blickfeldt, B. and McCarty, J. E., "Analytical and Experimental Investigation of Aircraft Metal Structures Reinforced with Filamentary Composites," NASA CR 2039, National Aeronautics and Space Administration, 1972.

[3] Mechtly, E. A., "The International System of Units," NASA SP-7012, National Aeronautics and Space Administration, 1969.

[4] Paris, P. C. and Sih, G. C., in *Fracture Symposium on Toughness Testing and Its Applications, ASTM STP 381*, American Society for Testing and Materials, 1965, pp. 30–38.

[5] Paris, P. C., "The Fracture Mechanics Approach to Fatigue," Sagmore Army Materials Research Conference, Aug. 1963, p. 116.

[6] Boley, B. A. and Werner, Jeromeh, *Theory of Thermal Stresses*, Wiley, New York, 1960, p. 259.

D. J. Wilkins,[1] *R. V. Wolff,*[1] *M. Shinozuka,*[2] *and E. F. Cox*[1]

Realism in Fatigue Testing: The Effect of Flight-by-Flight Thermal and Random Load Histories on Composite Bonded Joints

REFERENCE: Wilkins, D. J., Wolff, R. V., Shinozuka, M., and Cox, E. F., **"Realism in Fatigue Testing: The Effect of Flight-by-Flight Thermal and Random Load Histories on Composite Bonded Joints,"** *Fatigue of Composite Materials, ASTM STP 569,* American Society for Testing and Materials, 1975, pp. 307–322.

ABSTRACT: Current military specifications call for increased realism in fatigue testing. Criteria are discussed which recognize those portions of a spectrum that should be random and those that should be deterministic.

This paper documents a research program which included spectrum development, test facility setup, and a limited test series. The spectrum was a flight-by-flight random load history including realistic mission temperature exposures. The test facility utilized a small digital computer for closed-loop control of load and temperature.

Results of tests on three sets of five boron-epoxy-to-titanium bonded joints are discussed, and the effects of temperature exposure and time acceleration are investigated.

KEY WORDS: composite materials, laminates, joints (junctions), mechanical properties, fractures, fatigue tests, composite structures, reliability assurance, fatigue (materials)

Fatigue testing must be realistic. This simple conclusion has been reached after years of trying to sort out the effects of various simplifications made in testing. Now the Air Force, in its MIL-STD-1530, has specified that constant amplitude testing to prove airworthiness may only be used for those parts which have a constant amplitude service environment. Only a few aircraft parts, such as rotating machinery, can realistically be assumed to satisfy this requirement.

[1] Senior structures engineer, senior structures engineer, and project test engineer, respectively, General Dynamics, Fort Worth Division, Forth Worth, Tex. 76101.

[2] Professor, Department of Civil Engineering and Engineering Mechanics, Columbia University, New York, N.Y. 10027.

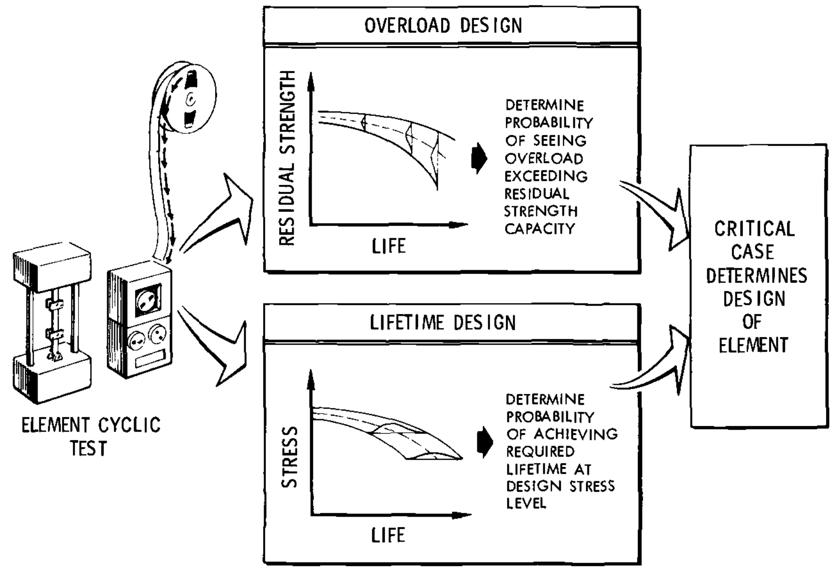

FIG. 1—*Reliability-based design.*

New fatigue test methods have been developed to simulate the service loads on aircraft hardware. The simulation must include the random nature of the load history in both amplitude sequence and frequency variation. Moreover, the flight-by-flight character of the load history and the presence of reversed loadings must also be included.

Realism in the test laboratory can be easily coupled with a reliability-based design approach where component strength and lifetime distribution parameters are of primary importance and test conditions must be assumed equivalent to real service conditions. This design approach is illustrated in Fig. 1 and has been presented elsewhere [*1*].[3]

The objective of this paper is to document a successful research program. The program was designed to bring together the fatigue analyst and the test engineer in developing a method to simulate and apply a realistic fatigue spectrum to an advanced composite bonded joint. The project required the development of a method for simulating the load history, a laboratory setup for economically applying the spectrum, a test specimen suitable for a real design problem, and an experimental test program with which to exercise the procedure.

[3] The italic numbers in brackets refer to the list of references appended to this paper.

Reality Defined

Reality cannot be duplicated but can only be simulated. Once this is understood, one can begin to formulate criteria for realism. Since a unique approach was formulated for this project, its genesis will be outlined.

An airplane is designed for a specific need as set forth in its required operational capability (ROC). This capability is exemplified by a set of mission types. The mission types realized are largely determined by where the aircraft is based so that the flight sequence of a given airplane may be reasonably assumed to be random.

Each mission is composed of several mission segment types, that, on the other hand, follow a rigid deterministic sequence. Each flight begins with a takeoff and climb, followed by a cruise or maneuver and, finally, a descent and landing. The landing load cannot be ignored in a spectrum simulation, since it causes a load reversal which is a significant factor in most fatigue-sensitive aircraft parts.

The individual loads which occur in a mission segment type, while constrained, are essentially random. The performance of a given maneuver under an existing atmospheric condition is a unique event which gives rise to a unique set of flight loads. The Air Force has tabulated service history data on aircraft operations by mission segment type in MIL-8866A in terms of frequency of occurrence versus acceleration level. The waveforms which produce these acceleration levels have not been preserved. Unfortunately, the lack of wave form information detracts from the attempt to simulate a service load history.

The realism criteria were, thus, formulated to:

1. Simulate an airplane lifetime as a set of randomly ordered missions.
2. Preserve the deterministic character of the mission segment sequence within a mission type, including at least one landing in each mission.
3. Model the individual loads occurring in a mission segment as a random half-cycle process which adheres to the cumulative service history occurrence relationship.
4. Model the relative temporal frequency as a stationary random process with an assumed spectral density.
5. Impose an individual load at the temperature corresponding to the altitude and speed at which it occurs.

Several significant assumptions still had to be made. For the purposes of this project, it was assumed that the loadings were uniaxial and that vertical accelerations translated into loads through a unity transfer function. A more subtle assumption, which pervades all fatigue testing, is that the real usage of the airplane will be the same as that supposed for it. Until fatigue analysis techniques are developed that allow us to predict lifetime performance based on changing service requirements, this assumption will remain.

Once the desired attributes of a realistic spectrum were agreed upon, the stage was set for the creation of a digital computer procedure to produce the spectrum.

Load and Thermal Histories

The objective of the spectrum generation task was to provide a load-temperature-time history based on the usual input, such as mission profile and load-occurrence data, in a form readily usable in the test facility. The resultant spectrum was for the lower wing skin root area of an air superiority fighter.

The operations analysts provided two mission profiles which represent the entire life of the aircraft very closely.

The two mission profiles are shown in Fig. 2. Mission I represents an air combat mission. Mission II represents an air combat training mission and, as such, contains one touch-and-go landing before the full stop landing.

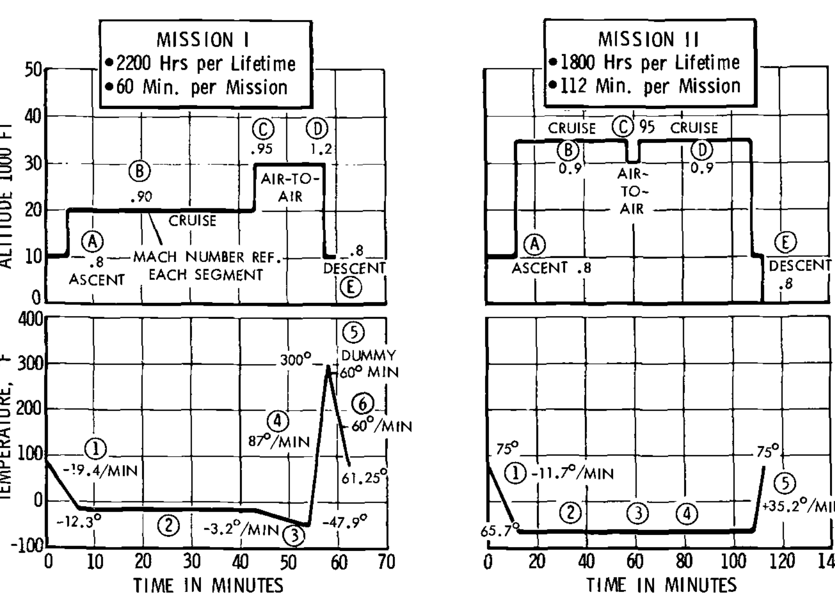

FIG. 2—*Mission and temperature profiles.*

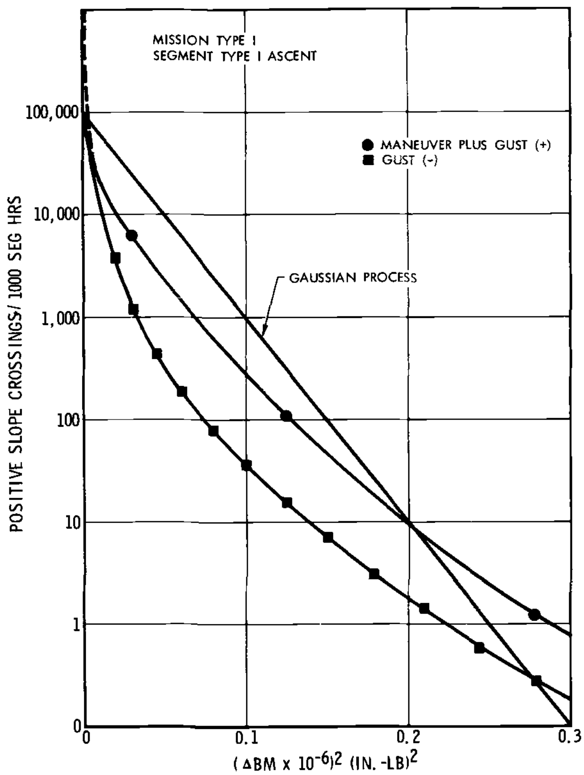

FIG. 3—*Typical occurrence curve.*

Load (in terms of wing root bending moment) versus occurrence plots were derived from MIL-8866A data for each mission segment type. A typical occurrence curve is shown as Fig. 3. These curves are often called exceedance curves, but, since the level-crossing occurrence count method was used and the load history, as simulated, does not return discretely to the segment mean load, occurrence is the proper term to use.

The only remaining piece of data to be defined is the power spectral density (PSD) of the force-time waveform. Due to the lack of actual waveform data, a bandwidth-limited white noise power spectrum was assumed along with an irregularity factor of 0.90. The irregularity factor is the ratio of positive slope crossings of the mean load per unit time (N_0) to peak occurrences per unit time (N_p).

In the computer program called Simulated History of Aircraft Missions (SHAM), random loads are generated which satisfy a Gaussian process with a mean of zero, standard deviation of one, and a prescribed

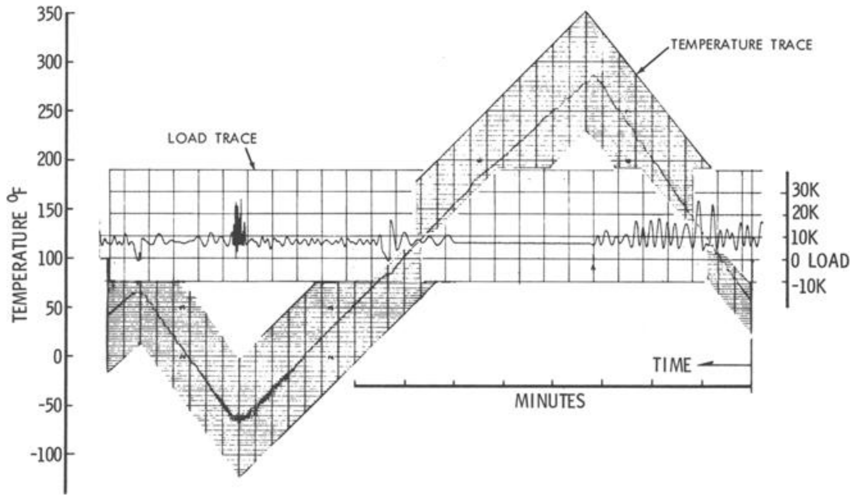

FIG. 4—*Load and thermal history.*

PSD shape. These loads are then searched for relative maxima and minima, and the highs and lows are transformed to real loads and written on magnetic tape each time 500 loads have accumulated. This procedure is continued through each segment and mission of the life. At the end of the lifetime, the cumulative occurrences and other lifetime statistics are compiled and printed.

The details of the Gaussian process simulation and its transformation into the actual non-Gaussian process are presented in Refs *2* and *3* and summarized in Appendix I. The major achievement of the present technique is the coupling of the simulation technique of Ref *3* with the fast Fourier transform (FFT) to make the procedure computationally efficient.

The magnetic tape produced by the IBM 370/155 for test laboratory use contains a sequence of digital values representing load value, temperature value, and time period to reach these values.

A portion of the load and thermal history is shown in Fig. 4. This figure illustrates a useful attribute of the program by which some segments may be accelerated up to 10 Hz if desired.

Laboratory Facility

A random-load/environment-fatigue testing capability was developed under the subject program by upgrading the previously developed loading facility that had been demonstrated under programs for composite bonded joints [*4,5*]. The computer-controlled system translates the

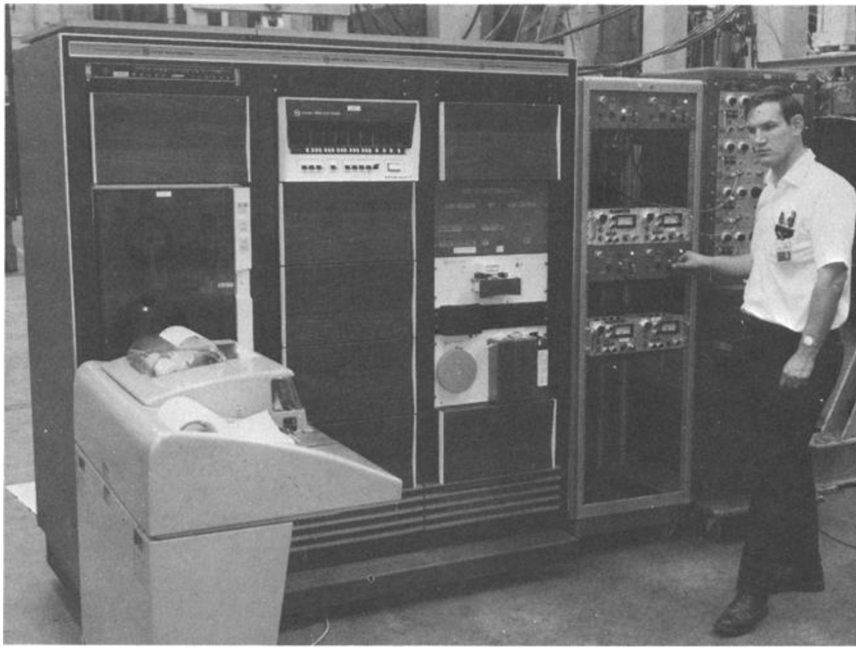

FIG. 5—*Control system.*

load-temperature history (stored on a magnetic tape) into a command signal to a closed-loop control system for both load and temperature.

Load Control System

The load control loop is closed in the analog form through a servo amplifier which is the current state of the art. The center of the system is a fatigue load control subsystem.[4] This computer-controlled system utilizes a Varian 620-i general purpose digital computer and an ASR 35 teletypewriter (see Fig. 5). The computer is connected to the fatigue machines through an interface unit developed by General Dynamics, and a unique program has been developed to control these machines from data supplied by the magnetic tape unit.

Environmental Control System

The environmental system uses forced air heating and cooling for specimen temperature requirements. The chamber-enclosed specimen is heated by plant air forced through an electrically powered heat ex-

[4] Designed and built by General Dynamics.

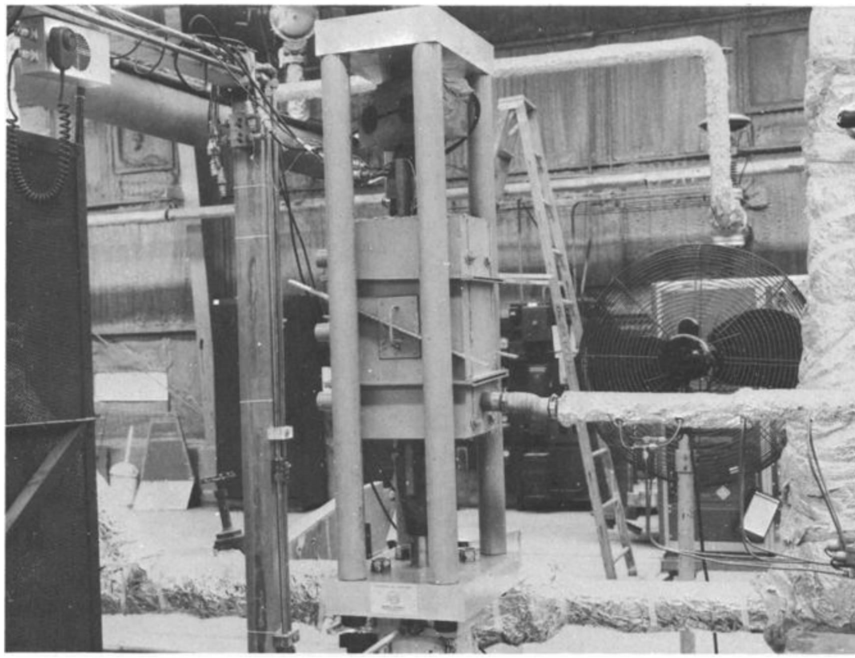

FIG. 6—*Environmental test chamber.*

changer. Cooling is accomplished by using a mixture of plant air and liquid nitrogen. Temperature sensors on the specimen provide a feedback signal to a servo amplifier for closed-loop control and verification. The environmental system heating and cooling rates were established at 90°F/min (50 K/min) and 60°F/min (33 K/min), respectively, for the subject program. The chamber and associated plumbing are shown in Fig. 6.

Empirical Program

The test facility capability was demonstrated by an empirical program on a full-scale boron-epoxy-to-titanium step-lap bonded joint component. The bonded joint design was selected as being typical for an air superiority fighter.

The test plan called for the exploration of three environmental conditions at one effective root mean square (RMS) load intensity. The three conditions required generating two versions of the loading spectrum. One version of the spectrum was real time during the elevated temperature mission exposures and accelerated time during ambient and low temperature mission exposures. The second version of the spectrum was accelerated time throughout. Specimens which were loaded using the accelerated spectrum were exposed to room temperature only. Two sets of specimens were loaded using the "real-time" spectrum. One of these sets was exposed to room temperature only. The other set was exposed to the mission segment temperature profiles which were correlated to the loads during the spectrum generation. Every specimen was subjected to an elevated temperature proof load to eliminate low strength members which could result from fabrication errors and to censor the fatigue population to ensure wearout rather than chance failures.

The selection of the proper RMS load intensity and truncation level were key factors in the test program. The procedure is discussed in Appendix II.

In addition to demonstrating the laboratory capability, the empirical program allowed comparisons on a mean value basis of real time and accelerated time fatigue loading, and room temperature and simulated service temperature fatigue loading.

Test Specimen

The test component is a composite laminate-to-metal step-lap bonded joint, representative of a composite wing skin joint in the region of a main spar. The test specimen is shown in Fig. 7. The titanium lug details were sized to have a net area approximately six times that of the test section to avoid a lug failure.

The laminate lay-up includes a combination of boron-epoxy and unidirectional E-glass/epoxy. The basic laminate is 50 percent, 0 deg; 40 percent, ±45 deg; and 10 percent, 90 deg boron-epoxy. However, in a region 1.8 in. (4.57 cm) wide through the center of the laminate the 0 deg boron lamina are replaced by 0 deg glass lamina that act as "softening" strips (reduce the stress concentration) around the bolts. The bolts are located at the center line of each step length of the bonded joint to permit attachment of the angles to which the stabilization assembly is bolted

FIG. 7—*Test specimen.*

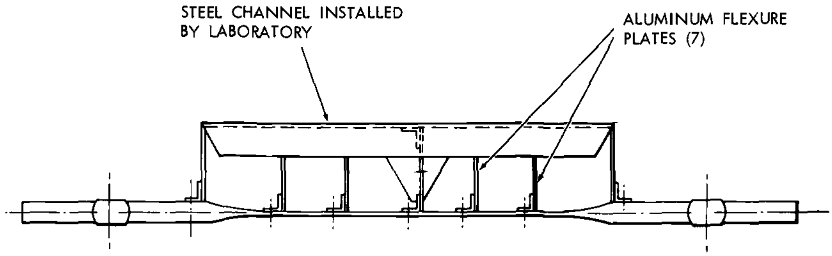

FIG. 8—*Stabilization assembly.*

before the joint is tested. The stabilization assembly, in effect, simulates a wing spar with the laminate simulating a skin. The stabilization assembly is shown in Fig. 8. The details of specimen fabrication are given in Ref 2.

Accelerated Random Fatigue

Five components were tested at ambient laboratory temperature using the random fatigue spectrum where time was accelerated throughout. The accelerated spectrum requires 24 h of loading time for one airplane lifetime and has an average "cyclic" rate of 3.7 Hz. All specimens were loaded until fatigue failure occurred. For specimens that reached one lifetime of loading without failure, the magnetic tape was restarted from the beginning and loading continued until the specimens failed.

The first fatigue specimen of the program was loaded until it failed at 2.8 lifetimes. A lifetime is 631 656 random loads. The failure was judged to have occurred within a reasonable time; hence, the maximum load of 40.5 kips (180 kN) which was 72 percent of mean ultimate room temperature strength was used throughout the program.

The accelerated spectrum test results are summarized in Table 1. The average result of the five specimens is 1.4 lifetimes. The failure loads shown in Table 1 are the magnetic tape command at the time of failure. The specimen may or may not have reached the command load. The fact that the command loads are not all equal to the truncation load indicates the speed of the degradation process near failure.

Real-Time Random Fatigue

Test components were tested using the random fatigue spectrum where the elevated temperature mission segments were loaded at real time. Specimens were tested using this spectrum where the loading was only at room temperature and in the environmental chamber where the mission temperature profiles were followed. The average cyclic rate of the real-time spectrum was 0.225 Hz and a lifetime of loading required 420 h.

TABLE 1 — *Test results.*

Spectrum Type	Temperature Exposure	Specimen Number	Lifetimes to Failure	Failure Load, kips (kN)
Accelerated:		1	2.80	34.0 (151)
24 test hours	room	2	1.13	38.8 (173)
631 656 loads	temperature	3	0.68	40.5 (180)
per life		4	1.91	37.7 (168)
		5	0.66	37.4 (166)
		1	0.53	38.8 (173)
	room	2	1.44	34.8 (177)
	temperature	3	0.75	40.4 (180)
Partial real-		4	0.49	39.0 (173)
time:		5	1.04	39.7 (177)
420 test hours		1	1.01	36.9 (164)
680 376 loads	varying	2	0.41	39.2 (174)
per life	(−65 to	3	0.60	39.5 (176)
	300°F)	4	0.54	38.6 (172)
		5	0.66	... ...

The load level for these tests was 40.5 kips (180 kN), which was identical to that used for accelerated spectrum loading.

Five specimens were tested at room temperature at real-time. The results of these tests are given in Table 1; the average lifetime observed was 0.85. Also shown are the results of specimens tested in the environmental chamber at real-time. The average lifetime observed for the four specimens that failed was 0.64. An additional specimen was run to 0.66 lives and stopped.

The maximum likelihood estimator values of the Weibull shape parameter, α_f, the scale parameter, β_f, and probability of survival, $P(s)$, versus log t are given in Fig. 9 and compared with accelerated and real-time room temperature fatigue results. Superposition of environment (temperature) upon fatigue loading results in a shift in the scale parameter to the left (decreased life) in comparison to both accelerated and real-time room temperature testing. In all real-time testing, the load spectrum input (giving the magnetic tape) was identical; hence, the only test variable was the mission temperature profile. The shift due to temperature is less than the shift observed between accelerated and real time ambient results.

Conclusions

Several significant conclusions have been drawn. An environmental random fatigue test facility has been established, and its capability has been proven.

CONDITION	PARAMETERS		
	α_f	β_f	μ_f
ACCELERATED	1.89	1.63	1.44
REAL TIME - ROOM TEMP	2.61	.96	.85
REAL TIME - MISSION TEMP	3.27	.76	.64

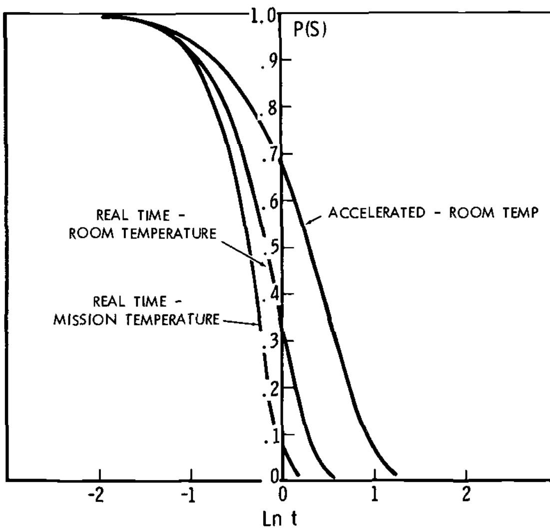

FIG. 9—*Probability of survival life time relationship for three test conditions.*

Random processes may be digitally simulated. The state of the art has been established to the degree that the laboratory capability is now more accurate than the data base, which is lacking in waveform and spectral density information.

The fatigue failure of a bonded joint has previously been shown to be dominated by crack growth in the adhesive. Specimens of the same population used for room temperature tests were tested under an identical load history, but mission temperature profiles were superimposed and mean life was reduced. The life reduction may be caused by an increase in the effective crack growth rate of the bonded joint above that observed at room temperature. There are many variables inherent in the "effective" crack growth rate observed when superimposing temperature and spectrum loading effects. No attempt is made here in assigning the lifetime degradation to particular segments of the load-temperature history.

The shortest fatigue life was obtained under the most realistic of the spectra. This result has been observed in the past. Indeed, such observations have led to the current emphasis on realistic testing. The more surprising result of the program was that the lifetime shift due to testing frequency was greater than that due to temperature effects. Of course, no strong conclusions can be drawn from so few specimens with scatter of this magnitude, especially since the data set ranges overlap each other. It is encouraging, in fact, that all of the data lie within one decade of life, considering the simplifications made for the accelerated tests.

The program has verified the feasibility of studying fatigue aspects of large-scale components under laboratory simulations of realistic service conditions. Such studies must be undertaken to understand lifetime characteristics.

Acknowledgments

The work reported here was performed under USAF Contract F33615-72-C-2060 for the Advanced Development Division, Air Force Materials Laboratory, Wright-Patterson Air Force Base, Ohio. The Air Force project engineers were R. M. Neff and A. W. Davis.

Max Waddoups was program manager and provided overall technical guidance. Test engineers who made major contributions were J. A. Mitchem, A. M. Arabian, and W. F. MacSwain.

APPENDIX I

Digital Random Process Simulation

The chief advantages of a PSD-based random process simulation are the preservation of the exceedance and frequency content of the process and the accommodation of any waveform. The full power of the method has not been realized, however, since airplane PSD information historically has not been retained. In the present study, the waveform was assumed to be bandwidth limited white noise, as shown in Fig. 10. The frequency cutoffs, ω_L and ω_u, on the

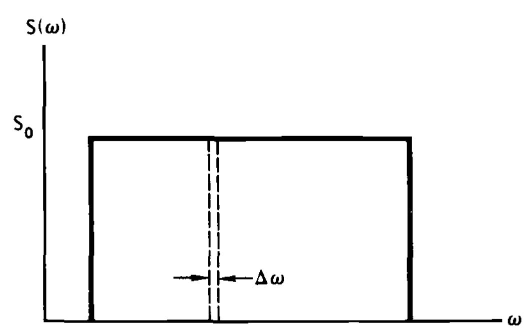

FIG. 10—*Rectangular power spectrum.*

rectangular PSD are defined by the N_o for the particular mission segment being simulated and the irregularity factor, R, which is defined as the ratio of N_o to N_p. Rice [6] has derived relationships between N_0, N_p and the PSD as

$$N_o = \frac{1}{2\pi} \left[\frac{\int_o^\infty \omega^2 S(\omega)\, d\omega}{\int_o^\infty S(\omega)\, d\omega} \right]^{1/2}$$

$$N_p = \frac{1}{2\pi} \left[\frac{\int_o^\infty \omega^4 S(\omega)\, d\omega}{\int_o^\infty \omega^2 S(\omega)\, d\omega} \right]^{1/2}$$

For the PSD shape used here, the frequency ratio ω_L/ω_u is completely determined by the irregularity factor R through the expression

$$R = \frac{\sqrt{5}}{3} [1 - \omega_L{}^3/\omega_u{}^3] / \sqrt{(1 - \omega_L/\omega_u)(1 - \omega_L{}^5/\omega_u{}^5)}$$

Since the irregularity factor for a fighter airplane is herein assumed to be 0.90, only the N_o for a particular mission segment needs to be specified to define the frequency cutoffs on the PSD.

Since the PSD frequency ratio depends only on R, and R is constant for all mission segments, the same nondimensionalized PSD shape can be used for all segments. Moreover, this permits the simultaneous generation of a large number of sample points covering many segments. The time base corresponding to a particular mission segment can subsequently be calculated from the segment N_o. This procedure has the effect of displacing the PSD to the left or right on the frequency axis.

The actual details of producing a force-time history from the PSD are due to Shinozuka [3]. The basic equation is

$$Y(t) = \sqrt{2} \sum_{k=1}^{N} \sqrt{2\, S_k\, \Delta\omega}\, \cos\, (\omega_k t + \phi_k)$$

where ϕ_k are random phase angles. The process may be nondimensionalized by its standard deviation

$$Y^*(t) = Y(t)/\sigma = \sqrt{\frac{2}{N}} \sum_{k=1}^{N} \cos\, (\omega_k t + \phi_k)$$

where

$$\sigma^2 = 2S(\omega_u - \omega_L) = 2\, S_o N \Delta\omega$$

Recognizing this transformation as a special case of the FFT [7] results in a considerable increase in efficiency with respect to the use of the cosine series directly. The appropriate equation then becomes

$$Y^*(t) = \sqrt{\frac{2}{N}}\, Re \sum_{k=1}^{N} \{e^{j\phi_k}\}\, e^{i\omega_k t}$$

where *Re* signifies "real part," and $e^{i\phi_k}$ is the complex array to be used in the FFT procedure.

Each half cycle obtained is multiplied by the RMS value corresponding to the Gaussian process represented in its segment occurrence curve (see Fig. 3). The resultant Gaussian delta-load value is transformed into a real delta-load value according to the appropriate segment occurrence curve. The delta load is then added to the segment mean load to arrive at a realized random load.

APPENDIX II

Load Level Selection

A primary program goal was to produce fatigue failures under realistic load environments and within an economically feasible test time. The current joint specimen and its spectrum were compared to a previously tested scarf joint and its spectrum to determine the relative lifetime capability of the current joint and the spectrum magnification factor.

Relationships defined in the Halpin-Waddoups "wearout" model were invoked to make the comparison [*8*,*9*,].

Calculations shown in Ref *2* indicate that the step lap joint could sustain a mean fatigue life of over 200 lifetimes under the reference air superiority fighter spectrum, with the peak spectrum load set at ⅔ of the elevated temperature strength. To obtain failures in a reasonable test time, the spectrum loads were magnified. The spectrum was magnified by a factor of 1.65 and truncated to prevent static failures as described as follows. The five accelerated spectrum specimens show an actual mean fatigue life of 1.4.

The proof load and spectrum truncation load were set on the basis of laminate strength at maximum temperature and a "risk" of 1 in 5 static failures. The static shape parameter was estimated from Ref *5* data as $\alpha_0 = 10$. The expected laminate strength retention is 85 percent at 300°F (422 K). Room temperature static strength of the specimen was 56 kips (249 kN). The load level for the proof test was calculated as the first failure of a sample $n = 5$ by

$$P_n = \beta_o(n)^{\frac{1}{-\alpha_o}}$$

Therefore

$$P_5 = (0.85)(56)(5)^{\frac{-1}{10}} = 40.5 \text{ kips (180 kN)}$$

References

[*1*] Eisenmann, J. R., Kaminski, B. E., Reed, D. L., and Wilkins, D. J., "Toward Reliable Composites: An Examination of Design Methodology," *Journal of Composite Materials*, Vol. 7, No. 3, July, 1973.

[*2*] Waddoups, M. E., Wolff, R. V., and Wilkins, D. J., "Reliability of Complex Large Scale Composite Structure-Proof of Concept," AFML-TR-73-160, Air Force Materials Laboratory, Dayton, Ohio, July, 1973.

[*3*] Shinozuka, M., *International Journal of Computers and Structures*, Vol. 2, 1972, pp. 855–874.

[4] Wolff, R. V., and Lemon, G. H., "Reliability Prediction for Adhesive Bonds," AFML-TR-72-121, Air Force Materials Laboratory, Dayton, Ohio, March 1972.
[5] Manning, S. D., Lemon, G. H., and Waddoups, M. E., "Structural Reliability Studies," AFFDL-TR-71-24, Air Force Flight Dynamics Laboratory, Dayton, Ohio, March 1971.
[6] Rice, S. O., "Mathematical Analysis of Random Noise," in *Selected Papers on Noise and Stochastic Processes,* N. Wax, Ed., Dover Publications, New York, 1954.
[7] Cooley, J. W. and Tukey, J. W., *Mathematics of Computers,* Vol. 19, April 1965, pp. 297–301.
[8] Halpin, J. C., Waddoups, M. E., and Johnson, T. A., *International Journal of Fracture Mechanics,* Vol. 8, 1972, pp. 465–468.
[9] Halpin, J. C., Jerina, K. L., and Johnson, T. A., "Characterization of Composites for the Purpose of Reliability Evaluation," AFML-TR-72-289, Air Force Materials Laboratory, Dayton, Ohio, Dec. 1972; also appears in *Analysis of the Test Methods for High Modulus Fibers and Composites,* ASTM STP 521. American Society for Testing and Materials, 1973.

J. R. Davidson[1]

Reliability After Inspection

REFERENCE: Davidson, J. R., "**Reliability After Inspection,**" *Fatigue of Composite Materials, ASTM STP 569,* American Society for Testing and Materials, 1975, pp. 323–334.

ABSTRACT: Because materials and structures cannot be made to always be perfect, they are inspected to determine if they contain flaws or defects large enough to influence their strength, reliability, or economic life. Inspection methods and procedures depend upon the part configuration, possible flaw type, orientation, location, and accessibility. The procedure will depend upon prior knowledge of possible defects and whether or not the inspector is to decide if a single flaw is at a specific location or if no significant flaws exist anywhere in some distributed area or volume.

Long-lived structures require that initial flaws be small so that the flaws will not grow to a critical size during the structure's life or between inspections. Consequently, nondestructive inspection methods are commonly pushed to their limits. For example, the size of a permitted flaw might be just less than the size flaw which will be detected 90 percent of the time. As a result, nondestructive engineering (NDE) methods are not infallible, and some flawed parts might pass inspection. The question, then, is how to calculate the reliability of a part or a structure that has passed inspection.

Three analyses have been developed to calculate this *a posteriori* reliability. Each handles an increasingly complex situation. The first and simplest gives the reliability based upon the efficiency of the detection method and the probability that the part was unflawed when it reached the inspector (*a priori* reliability).

The second deals with the problem where flaws are distributed over an area or throughout a volume. Here, the mean number of flaws per unit area or volume (*a priori*) is a parameter; the actual number in a part is assumed to be Poisson distributed.

The third analysis predicts the *a posteriori* reliability for a structure with distributed flaws but where some portions are inaccessible and cannot be inspected.

KEY WORDS: composite materials, nondestructive tests, inspection, reliability

[1] Head, Structural Integrity Branch, NASA-Langley Research Center, Hampton, Va. 23365.

Nomenclature

$P[A]$	Probability of event A occurring
$P[AB]$	Probability that both A and B occur
$P[A\|B]$	Probability of event A occurring, given that event B has occurred
A	Flaw exists
A'	Flaw does not exist
B	Flaw is indicated
B'	Flaw is not indicated
R	Reliability after inspection
ρ	Proportion of length, area, or volume of piece inspected
λ	Mean number of flaws per unit length, area, or volume; m^{-1}, m^{-2}, m^{-3}
L	Length which may contain flaws, m
S	Area which may contain flaws, m^2
V	Volume which may contain flaws, m^3
b	Number of subareas
n	Number of subareas with flaws
P_1	Probability when flaw site is known
P_2	Probability when flaw site unknown; many flaws; total inspection
P_3	Probability when flaw site unknown; many flaws; partial inspection
P_4	Probability when flaw site unknown; many flaws; partial inspection; flaw rate in uninspected region differs from rate in inspected region
P_5	Probability when flaw site unknown; many flaws; partial inspection; flaw rate varies among various regions
$p(n)$	Probability, as defined in specific equations
$p(0)$	Probability that no flaw exists
$p(1)$	Probability that one flaw exists
R_1,R_2,R_3,R_4,R_5	Reliabilities; subscripts denote cases like those for subscripted probabilities

Subscripts

a	Refers to parameters associated with the uninspectable portion of the structure
b	Refers to parameters associated with the inspectable portion of the structure

The chemical and physical processes used to form composite materials and structures are often complex and need careful control if the product is to be of acceptable quality. In a laminate, for example, gas bubbles may cause voids, nonuniform surface preparation may lead to debonded areas between layers, or improper wetting may leave fibers unattached to the matrix. However, finished products are inspected to screen out those which contain flaws so large that the product quality is impaired with respect to the intended product use. But flaws are occasionally overlooked during nondestructive inspections, and, consequently, such inspections are not 100 percent reliable.

The purpose of this paper is to derive the relationships among the probability of having manufacturing defects, the probability of detecting a flaw, and final reliability. Several specific situations are considered. First, equations for the simple situation where only one flaw can be present are used to introduce the relationships in a Bayes' theorem approach to the assessment of the final reliability. Next, situations that are prevalent in composites manufacturing are considered. These include a case where flaws may occur randomly on a laminate surface or throughout a volume, where only the mean number of flaws is known and where the actual number of flaws in a given product is a Poisson-distributed random number which varies about this mean. This solution is then expanded to include the more general instance where some area or volume may not be amenable to inspection and must go uninspected.

Quantification of the Inspection Procedures

Perhaps no inspection procedure can be 100 percent certain to find all flaws; but, to be useful in reliability calculations, the amount of certainty (or uncertainty) must be quantified, and to be quantified the inspection procedure itself must be tested.

One way to test the inspection procedure is to inspect specimens in which flaws are known to exist. Of course, the inspectors themselves should be ignorant about the introduced flaws if the test is to yield a fair measure of the inspection procedures.

If a maximum permissible flaw size is stated, then a "failure" can be defined as the failure to detect any flaw larger than the permitted maximum. A "success" occurs whenever such larger flaws are discovered. The probability of detection during inspection can be calculated from the relative number of successes and failures. The probability is stated by two terms, probability and confidence [*1*].[2] For example, if a total of 50

[2] The italic numbers in brackets refer to the list of references appended to this paper.

flawed parts are inspected, and 45 flaws are detected, one has 95 percent confidence that the future proportion of flaws detected will be

$$0.78 \leqslant p \leqslant 0.97$$

This proportion is taken as the probability of detecting a flawed part, and to be conservative, would establish the working probability at 0.78. The interval can, of course, be narrowed by testing more specimens or by finding a larger proportion of flaws, that is, having a more effective procedure.

Analysis

Flaw Site Known

The simplest situation occurs when the location of the potential flaw is known. The flaw, of course, may or may not exist. The problem is to decide whether or not a flaw is present at the specified location. All pieces in which flaws are indicated will be rejected or repaired. All pieces in which no flaws are indicated will be passed. The reliability of the final product is the ratio of flawless products to products passed, which is also the probability that no flaws exist, given that no flaws were indicated

$$R_1 = P[A'|B'] \tag{1}$$

An equation for R_1 is derived in Ref *2*; the derivation is sketched in Appendix I. The result is

$$R_1 = P_1[A'|B'] = \cfrac{1}{1 + \cfrac{(1 - P_1[B|A])P_1[A]}{(1 - P_1[A])P_1[B'|A']}} \tag{2}$$

In Eq 2, R_1 is expressed in terms of known quantities; the probability of detecting an existing flaw, $P[B|A]$; the probability that no flaws are indicated if they are not there, $P[B'|A']$; and, the unreliability before inspection or probability of a flaw existing before inspection, $P[A]$.

Equation 2 is a basic equation resulting from Bayes' theorem and is one of the simplest. It is suited for flaw detection when $P[B|A]$ is defined, for example, as the probability of detecting all flaws larger than a specified critical size. For an analysis where $P[B|A]$ varies with flaw size or where flaw growth is important, see Ref *3*.

Flaw Site Unknown; 100 percent of the Line, Area, or Volume Inspected

Distribution Function for the Number of Flaws—In a great many practical situations more than one flaw might possibly exist in a part. The distribution function for the number of flaws gives the probability that any specific number of flaws might exist in a part. Frequently, a flaw might be regarded as a "rare event" in the sense that most of the part length, area, or volume is unflawed. One of the first steps, then, is to establish a probability distribution for the total number of flaws in a part.

For the rare event situation and where a flaw is equally likely to be anywhere throughout the area, the probability distribution function for the number of flaws in a part is the Poisson distribution (see Appendix II)

$$p(n) = \frac{(\lambda S)^n e^{-\lambda S}}{n!} \tag{3}$$

where $p(n)$ is the probability that the part contains n flaws. For bond lines or line welds, λ is the mean number of flaws per unit length and S is the length; for laminates, λ is the mean number of flaws per unit area and S is the area; and, for large solids, λ is the mean number of flaws per unit volume and S is the volume of the part. Whereas n is, of course, an integer, λ may be a decimal. The product, λS, obviously, is the mean number of flaws per part; the product need not be an integer.

Reliability When Flaws are Distributed—When several flaws are distributed over a surface, only one flaw need be detected for the part to be rejected. If the detection of any flaw is assumed to be independent of any other existing flaw

$$P[AB'] = \sum_{n=1}^{\infty} P[A_n]P[B'|A_n] \tag{4}$$

where $P[A_n]$ is the probability that exactly n flaws are present over S, and $P[B'|A_n]$ is the probability that all of them escape detection. To get the total probability that a flawed part passes inspection, one must sum over all possible number of flaws, n.

Obviously, under the assumptions of the previous subsection

$$P[A_n] = p(n) = \frac{(\lambda S)^n}{n!} e^{-\lambda S} \tag{5}$$

Also, under the assumptions of flaw independence and detection independence, the rules of conditional probability hold, and

$$P[B'|A_n] = (P[B'|A_1])^n = (P[B'|A])^n \tag{6}$$

Consequently, Eq 4 becomes

$$P[AB'] = e^{-\lambda S} \sum_{n=1}^{\infty} \frac{(\lambda S)^n}{n!} (P[B'|A])^n \tag{7}$$

The remaining derivation is somewhat like that for R_1 (see Appendix III)

$$R_2 = \frac{1}{1 + \dfrac{\exp\{\lambda S P[B'|A]\} - 1}{P[B'|A']}} \tag{8}$$

which is analogous to Eq 2.

Flaw Site Unknown; Only Part of the Line, Area, or Volume is Inspectable

In many practical situations, portions of a structure are inaccessible for inspection. The portions may contain flaws. Because uninspectable areas may be conservatively constructed to compensate for uninspectability, the expected number of critical flaws per unit area within them may differ from the number within inspectable areas. In this section the equations for reliability when portions of the structure are uninspectable will be derived. The general case is where

$$\lambda_a \neq \lambda_b$$

that is, when the flaw rate of occurrence in the inspectable region differs from the rate in the uninspectable region.

The desired equation is easily derived from Eqs 3 and 8. The probability that no flaws exist in the uninspected region is

$$p(0) = \exp\{-(1-\rho)\lambda_a S\} \tag{9}$$

where $(1 - \rho)$ is the proportion of S which is not inspected. The probability that no flaw exists in the inspected region after inspection is

$$R_2 = \frac{1}{1 + \dfrac{\exp\{\rho\lambda_b S P[B'|A]\} - 1}{P[B'|A']}} \tag{10}$$

As long as the probability of occurrence of flaws in one region is independent from that in the other, the law of compound probability applies, so that

$$R_4 = p(0)R_2 = \frac{\exp\{-(1-\rho)\lambda_a S\}}{1 + \dfrac{\exp\{\rho\lambda_b S P[B'|A]\} - 1}{P[B'|A']}} \tag{11}$$

Case where $\lambda_a = \lambda_b$—If the flaw density is the same in the uninspected region as in the inspected region

$$\lambda_a = \lambda_b = \lambda$$

and

$$R_3 = \frac{\exp\{-(1-\rho)\lambda S\}}{1 + \dfrac{\exp\{\rho\lambda S P[B'|A]\} - 1}{P[B'|A']}} \tag{12}$$

Many sections—If a structure contains many sections with various flaw densities, the rules of compound probability can be applied in the same straightforward fashion as they were in deriving Eq 11. For m uninspectable regions and l inspectable regions the general form of the equation is

$$R_5 = \frac{\exp\left(-\sum_{k=1}^{m} \lambda_K S_K\right)}{\prod_{j=1}^{l} \left\{1 + \dfrac{\exp\{\lambda_j S_j P_j[B'|A]\} - 1}{P_j[B'|A']}\right\}} \tag{13}$$

where $P_j[\quad]$ is used to indicate that the probabilities of nondetection might vary among regions.

Results and Discussion

The dependence of reliability after inspection upon the reliability before inspection, the probability of detecting an existing flaw, the number of flaws, and the fraction of area inspectable can be illustrated by considering R_1, R_2, and R_3. Reliabilities R_4 and R_5 are simply compounded from the first three.

Figure 1 shows how R_1 varies with the reliability before inspection and the probability of detecting an existing flaw. If a highly reliable endproduct is desired, for example, with $R_1 = 0.99$ or greater, the figure shows that the reliability before inspection must be at least 0.9 when the probability of detection is 0.9, or that some way must be found to raise the probability of detection above 0.9. In general, if the probability of flaw detection is at least 0.9 and the reliability before inspection is at least 0.9, then the unreliability after inspection will always be almost an order of magnitude less than the unreliability before inspection.

When flaws are distributed over the surface of a molding or a laminate, the final reliability depends upon the flaw density and the total area. But this dependence can be discussed in terms of the mean number of total flaws, λS, as a single parameter. When high reliabilities ($R_2 \geqslant 0.95$) are desired, Fig. 2 shows that the probability of flaw detection, $P[B|A]$, must be very high (0.95 or greater) if the mean number of flaws is one or greater. To a large part, R_2 depends strongly upon detection probability

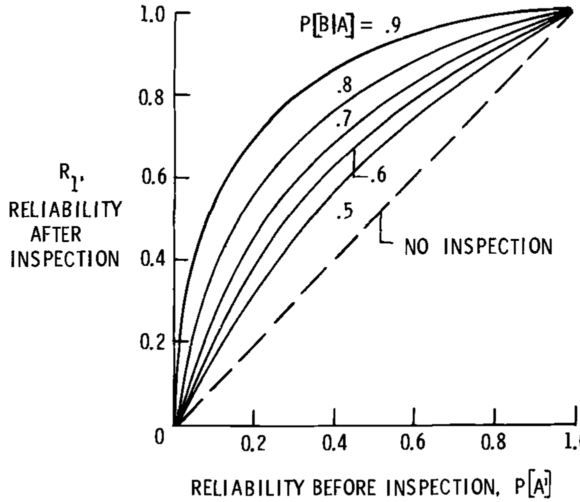

FIG. 1—*Variation of reliability after inspection as a function of reliability before inspection. The probability of identifying an existing flaw is a parameter. The false alarm rate,* $P[B|A'] = 0.02$.

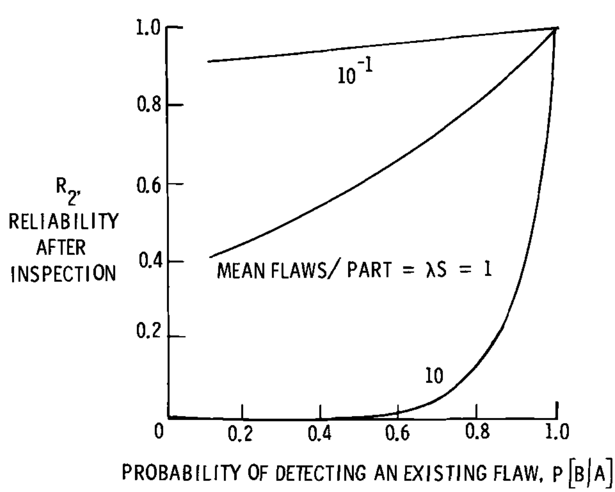

FIG. 2—*Variation of reliability as a function of the probability of detecting an existing flaw; the mean number of existing flaws is the parameter. False alarm rate,* $P[B|A'] = 0.02$.

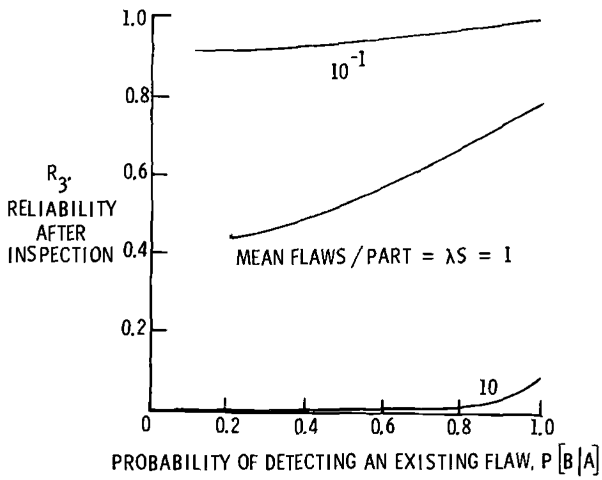

FIG. 3—*Variation of reliability as a function of the probability of detecting an existing flaw when only 75 percent of the total area is inspected; the mean number of existing flaws is the parameter, and* $\lambda_a = \lambda_b = \lambda$. *The false alarm rate* $P[B|A'] = 0.02$.

when more than one flaw is probable. Again, high reliabilities after inspection are associated with components that had high reliability before the inspection ($\lambda S < 10^{-1}$).

Figure 3 illustrates the effect of partial inspection. If only 75 percent of the surface can be inspected, high reliabilities after inspection can only be obtained when reliabilities were high before inspection, regardless of how certain the nondestructive inspection method is to find a crack in the inspectable portion. This situation happens because the uninspected region has a generally unacceptable probability of containing a flaw if $\lambda S \geq 1$.

Concluding Remarks

Equations were derived for the reliability of a composite material part after it was inspected. The equations related the reliability after inspection to the probability of detecting an existing flaw and the reliability before inspection. Equations were developed for many practical cases: where the potential flaw site was known; where a random number of flaws were distributed randomly over an area (or line, or throughout a volume); where only a fraction of the total area (length or volume) could be inspected; where various subsections were more likely to contain flaws than others; and, where some of these subsections may require nondestructive inspection techniques that have different probabilities of detecting existing flaws.

The numerical examples showed that an inspection procedure with a 0.9 probability of detecting an existing flaw can reduce unreliability by almost an order of magnitude if the part reliability is about 0.9 or higher before inspection. The examples also showed that a not very reliable laminate should be inspected over 100 percent of its surface if the final reliability is to be high.

The one consistent point brought out by the numerical calculations was that the surest way to have a reliable component after inspection was to start with a reliable component before inspection.

APPENDIX I

The probability that no flaws exist, given that no flaws were indicated during a nondestructive inspection, must be expressed in terms of known quantities. The derivation borrows directly from the concepts of probability theory. For example, the probability that both A' and B' occur is

$$P_1[A'B'] = P_1[A'|B']P_1[B'] \tag{14}$$

from which

$$P_1[A'|B'] = \frac{P_1[A'B']}{P_1[B']} \tag{15}$$

But, since B' can occur if either A or A' occurs,

$$P_1[B'] = P_1[B'|A]P_1[A] + P_1[B'|A']P_1[A'] \tag{16}$$

Also, by analogy with Eq 14

$$P_1'[A'B'] = P_1[B'|A']P_1[A'] \tag{17}$$

If Eqs 16 and 17 are substituted into Eq 15 the result is

$$R_1 = P_1[A'|B'] = \cfrac{1}{1 + \cfrac{P_1[B'|A]P_1[A]}{P_1[B'|A']P_1[A']}} \tag{18}$$

But, because some events are mutually exclusive

$$P_1[A'] = 1 - P_1[A] \tag{19}$$

and

$$P_1[B'|A] = 1 - P_1[B|A] \tag{20}$$

Consequently, Eq 18 can be expressed in terms of the unreliability before inspection, $P_1[A]$, and the probability of detecting a flawed part, $P_1[B|A]$

$$R_1 = \cfrac{1}{1 + \cfrac{(1 - P_1[B|A])P_1[A]}{P_1[B'|A'](1 - P_1[A])}} \tag{21}$$

APPENDIX II

The equation for the mass density function for the number of flaws over an area will be derived. The result will be easily converted to apply to line problems or volume problems, as is discussed in the body of the paper.

First, the number of flaws in a surface must be determined. The number of flaws over a surface, S, will be assumed to be a random number; consequently, an area under inspection might have 0, 1, 2, . . . or any number, n, flaws.

Suppose, for a moment, that the area, S, is subdivided into b, equal small areas and that the probability that an unacceptably large flaw is present in a specified subarea is proportional to the area of the subarea. Then, if λ is the constant of proportionality

$$p_1 = \lambda\left(\frac{S}{b}\right) \tag{22}$$

The probability of no flaws in (S/b) is

$$p_0 = 1 - \frac{\lambda S}{b} - \text{order}\left(\frac{\lambda S}{b}\right)^2 \tag{23}$$

where the third term is the probability that two or more flaws exist in the subarea; this term is of higher order than the second. If b is chosen to be large enough, the third term becomes negligible.

The probability of finding n subareas with flaws is a series of Bernoulli trials, where each subarea S/b is a trial with probability of success, p_1, and failure, p_0 [2].

$$\begin{aligned} p(n;b) &= \frac{b!}{(b-n)!n!}(p_1)^n(p_0)^{b-n} \\ &= \frac{b!}{(b-n)!n!}\left(\frac{\lambda S}{b}\right)^n\left(1-\frac{\lambda S}{b}\right)^{b-n} \end{aligned} \tag{24}$$

But the subdivision into subareas was arbitrary, and in no way can an arbitrary subdivision alter the mean number of unacceptable flaws (λS) contained in S. Therefore

$$p(n) = \lim_{\substack{b \to \infty \\ \lambda S = \text{constant}}} p(n;b) = \frac{(\lambda S)^n e^{-\lambda S}}{n!} \tag{25}$$

Equation 25 gives the probability that exactly n flaws are present over the area, S. From the derivation, λ can be seen to be the average number of flaws per unit area. Whereas λ and λS need not be integers, n, obviously, must be an integer. Equation 25 is the Poisson distribution and is tabulated in most elementary statistics texts.

APPENDIX III

Equation 7 can be related to Eq 8 through some of the relationships of elementary probability theory. As in Appendix I

$$P[AB'] = P[A|B']P[B'] = P[B'|A]P[A] \tag{26}$$

The "unreliability" is the probability of accepting a flawed part, and, parallel to Eq 15 is

$$1 - R_2 = P[A|B'] = \frac{P[AB']}{P[B']} \tag{27}$$

Also

$$\begin{aligned} P[B'] &= P[AB'] + P[A'B'] \\ &= P[AB'] + P[B'|A']P[A'] \end{aligned} \tag{28}$$

Equations 23, 24, and 16 can be combined to yield

$$R_2 = 1 - \frac{1}{1 + \dfrac{P[B'|A]P[A']}{P[AB']}} \tag{29}$$

Using Eq 7 in Eq 25, and noting that

$$P[A'] = p(0) = e^{-\lambda S} \tag{30}$$

and that

$$\sum_{n=1}^{\infty} \frac{x^n}{n!} = e^x - 1 \tag{31}$$

Eq 25 becomes

$$R_3 = \frac{1}{1 + \dfrac{\exp\{\lambda S P[B'|A]\} - 1}{P[B'|A']}} \tag{32}$$

References

[1] Dixon, W. J. and Massey, F. J., Jr., *Introduction to Statistical Analysis*, 2nd ed., McGraw-Hill, New York, 1957.
[2] Parzen, Emmanuel, *Modern Probability Theory and Its Applications*, Wiley, New York, 1962.
[3] Davidson, J. R., "Reliability and Structural Integrity," presented at the 10th Anniversary Meeting of the Society of Engineering Science, Raleigh, N. C., Nov. 1973.